Form Filling with Self-Compacting Concrete

Thrane, Lars Nyholm; Geiker, Mette Rica; Stang, Henrik; Szabo, Peter; Glavind, Mette; Skov, Jørgen

Publication date:
2007

Document Version
Publisher's PDF, also known as Version of record

Citation (APA):
Thrane, L. N., Geiker, M. R., Stang, H., Szabo, P., Glavind, M., & Skov, J. (2007). Form Filling with Self-Compacting Concrete.

Department of Civil Engineering DTU

Lars Nyholm Thrane

Form Filling with Self-Compacting Concrete

PHD THESIS

DANISH
TECHNOLOGICAL
INSTITUTE

unicon

BYG • DTU

Form Filling with Self-Compacting Concrete

Lars Nyholm Thrane

Ph.D. Thesis

Concrete Centre
Danish Technological Institute

Department of Civil Engineering
Department of Chemical Engineering
Technical University of Denmark

4K Beton A/S

2007

Form Filling with Self-Compacting
Concrete

Printed by Eurographic A/S
Department of Civil Engineering
Technical University of Denmark
ISBN 97-8877-8772-473
ISSN 1602-2917

Preface

This thesis is submitted as a partial fulfilment of the requirements for the Danish Ph.d. degree.

Acknowledgements

This Ph.D.-project is partly sponsored by: Danish Technological Institute (DTI), 4K Beton A/S (now Unicon A/S), and the Danish Academy of Technical Sciences. The author gratefully acknowledges their financial contributions.

I would like to thank my supervisors Mette Geiker (DTU), Henrik Stang (DTU), Peter Szabo (DTU), Mette Glavind (DTI), and Jørgen Skaarup (4K) as well as Anette Berrig (DTI, now The Danish Construction Association), and many of the staff members of 4K Beton A/S. There has been good discussions during the project ranging from mathematical details to matters of concrete manufacturing and handling in practice. I am grateful for my stays at the plants in Herning and Prøvestenen where I learned many useful things about concrete production and handling. Special thanks are given to the staff members at Prøvestenen for their help during form filling experiments.

Finally, I would like to thank the Danish SCC-Consortium for making it possible to perform full-scale form filling tests.

Abstract

The overall subject of this project was Self-Compacting Concrete. More specifically it has been to establish a modelling approach for prediction of the form filling behaviour of SCC in a vertical formwork.

Self-Compacting-Concrete (SCC) was first introduced in the 1980s. The purpose was to obtain flow properties which would make it possible to cast into a formwork without the need for subsequent compaction, e.g. by using poker vibrators. The possibility of not having to carry out vibration should encourage a wide use of SCC due to the prospects of improving the structural quality, working environment, productivity, and architectural appearance. However, especially in vertical applications there is a great unused potential.

Controlling the casting process is important in many different industries such as the metal, plastic, and food industry. The casting process may have a significant influence on the finished product and the challenges vary depending on the material characteristics and the type of flow.

Concrete may be regarded as a suspension defined as particles dispersed in a matrix phase. When the particles remain homogeneously distributed during form filling the important form filling characteristics comprise the form filling ability and flow patterns. The form filling ability describes the ability of the material to flow out into every corner of the formwork, and the flow patterns describe the intrinsic flow characteristics of the homogeneous flow, e.g. the direction and rate of flow at every point and time during placing, which may have a significant influence on the heterogeneous flow phenomena.

The heterogeneous flow phenomena comprise so-called blocking and dynamic segregation. Blocking refers to the situation where the flow of aggregates is disturbed by their interaction with the reinforcement bars, which may result in severe accumulation of the aggregates. Dynamic segregation refers to the situation, when particles segregate during flow. Compared to blocking, dynamic segregation is not caused by particle interactions with the solid boundaries, but it gradually evolves during flow over a larger scale of time and length. Any change in the particle volume fraction affects the local effective properties of the suspension and thus poses a threat to any process relying on flow of a homogeneous material.

In order to obtain a satisfactory form filling and thereby a satisfactory structural quality, it is necessary to develop theoretical tools to predict form filling with SCC. Trial and er-

ror is rarely an option, especially in-situ where the structural size and in-situ production often leave only one form filling attempt. Lack of theoretical prediction tools is one of the main reasons for the haltering use of SCC in vertical applications. A lack of prediction tools may lead to selection of concrete mix compositions and casting techniques that are not suitable for a given application.

This project proposes a modelling approach within the framework of Computational Fluid Dynamics (CFD). CFD is applied to simulate the homogeneous form filling characteristics, i.e. the form filling ability and flow patterns, taking into account the rheological properties and casting technique. It is assumed that the rheological properties of SCC follow a Bingham model with a yield stress and plastic viscosity. In this way the accuracy and ability of CFD to simulate the homogeneous flow on a realistic form filling scale is utilized compared to, e.g. a discrete particle flow approach which requires a much larger computer capacity, especially in three dimensions.

For the heterogeneous flow phenomena, this project focusses on the assessment of blocking, which is of special interest in relation to high quality and complicated structures with a dense reinforcement configuration. A phenomenological micro-mechanical model has been developed, which introduces a flow rate criterion below which blocking will occur. The model takes into account the flow domain dimension, particle size, rheological properties of the suspension and matrix, particle volume fraction, maximum particle volume fraction, and particle shape. Applying a flow rate criterion to the homogeneous form filling simulation provides a theoretical tool to assess parts of the formwork where there is a risk of blocking.

The modelling approach has been applied to selected flow domains comprising standard test methods, the slump flow test and the L-box test, and form filling applications. The latter comprise two vertical laboratory formwork with and without reinforcement and five full scale formwork.

Comparing the simulations with the experimental results, it shows that the modelling approach is applicable for simulation of the form filling ability and the flow patterns, and for identifying zones in the formwork with a risk of blocking. A similar modelling approach may also be applicable for assessment of the risk of dynamic segregation, and it is expected that a criterion can be developed based on theories for so-called shear-induced particle migration and gravity induced segregation due to differences in density.

In future constructions with Self-Compacting Concrete the proposed modelling approach may be applied to optimise the rheological parameters, particle configuration, and casting technique for a given application in order to obtain the structural quality required.

Resumé

Det overordnede emne for dette projekt var selvkompakterende beton (SCC). Mere specifict har det været at foreslå en modelleringsstrategi til at forudsige strømningsforløbet i en lodret støbning med SCC.

Selvkompakterende beton (SCC) blev udviklet i 1980'erne og gør det muligt at støbe beton i en form uden brug af vibrationsudstyr til at kompaktere betonen. SCC kan derved være medvirkende til at forbedre arbejdsmiljøet, produktiviteten, kvaliteten af den hærdnede beton og den arkitektoniske fremtoning. SCC bruges i væsentligt omfang; men især for lodrette konstruktioner er potentialet stort set uudnyttet.

At kontrollere støbeprocessen er vigtigt i mange forskellige industrier (levnedsmiddel, plastik, metal etc.). Støbeprocessen kan have stor indflydelse på kvaliteten af slutproduktet, og udfordringerne ved den enkelte støbeproces afhænger af materialeegenskaberne og strømningens karakter.

Beton kan opfattes som en suspension bestående af partikler (tilslag) i en væskefase. Når partiklerne forbliver homogent fordelt er formfyldningen beskrevet ved formfyldningsevnen og strømningsmønstret. Formfyldningsevnen beskriver betonens evne til at flyde ud i alle hjørner af formen, og strømningsmønstret beskriver bl.a. strømningshastigheden i ethvert punkt under formfyldningen. Strømningsmønstret kan have en betydelig effekt på risikoen for at opnå instabilitet af partiklerne.

Instabilitet forekommer enten ved at tilslagene blokerer bag armeringsstængerne eller ved såkaldt dynamisk seperation. Dynamisk seperation beskriver situation når tilslag separerer under strømningen. Enhver ændring i tilslagskoncentration udgør en risiko mod at opnå de forventede egenskaber af den hærdnede beton.

For at opnå et tilfredsstillende formfyldningsforløb, der sikrer at konstruktionen opnår den nødvendige kvalitet, er det nødvendigt at udvikle teoretiske værktøjer til at forudsige formfyldningsforløbet. Specielt in-situ er det vigtigt, da det ikke er muligt at forsøge sig frem til det mest optimale valg af betonegenskaber og støbeteknik. Manglen på teoretiske værktøjer er en af årsagerne til, at SCC kun er meget lidt udbredt i lodrette støbninger.

Dette projekt foreslår en modelleringsstrategi baseret på Computational Fluid Dynamics (CFD). CFD er benyttet til at simulere strømningen af SCC, når den forbliver homogen. Det er antaget, at SCC's reologiske egenskaber kan beskrives ved Bingham mod-

ellen, der indeholder en flydespænding og en plastisk viskositet. På denne måde bevares nøjagtigheden af en CFD beregning samt muligheden for at simulere over længere tid og længde sammenlignet med eksempelvis diskrete partikelmodeller. Specielt i tredimensionelle simuleringer er det en fordel.

Vedrørende instabilitet, er der i dette projekt valgt at fokusere på blokering, som er særlig relevant i lodrette støbninger med tæt armering. Der er udviklet en fænomenologisk model, som introducerer et flydekriterium for blokering dvs. blokering opstår under kritisk strømningshastighed. I modellen indgår de reologiske egenskaber af suspensionen og væskefasen, partikelkoncentrationen, den maksimale partikelkoncentration, partikelformen og indsnævringsforholdet. Dette kan anvendes sammen med CFD beregningen til at forudsige, hvor der er risiko for blokering under en formfyldning.

Modelleringsstrategien er blevet anvendt i udvalgte strømningsgeometrier, som omfatter de to standard testmetoder, flydesætmål og L-boks, to laboratorieforme og fem fuldskalaforme. For laboratorieformen er der gennemført forsøg og simulering af formfyldningen med og uden armering.

En sammenligning af simuleringerne med forsøgsresultaterne viser, at det er muligt at simulere formfyldningevnen, strømningsmønstret og identificere områder med risiko for blokering af tilslag. Det forventes, at en lignende modelleringsstrategi kan anvendes til at estimere risikoen for dynamisk separation baseret på teorier for partiklers bevægelse under påvirkning af forskydning og tyngdekraft.

I fremtidige SCC konstruktioner kan den foreslåede modelleringsstrategi anvendes til at udpege det mest hensigstmæssige valg af reologiske egenskaber, tilslagsfordeling og støbeteknik til en given konstruktion.

Table of Contents

List of Symbols

Basic dimensions used to express physical quantities:

Force (F), Length (L), Mass (M), Temperature (T), Time (t)

Volume ($V = L^3$), Area ($A = L^2$), Stress ($\sigma = \frac{F}{L^2}$), Velocity ($v = \frac{L}{t}$), Density ($\rho = \frac{M}{L^3}$), Flow rate ($Q = \frac{L^3}{t}$)

β	Slip coefficient $[\frac{v}{\sigma}]$
$[\eta]$	Intrinsic viscosity [dimensionless]
α	Confinement ratio defined as circular tube radius R over particle radius r_p [dimensionless]
α^*	Weighed confinement ratio of a polydisperse mix [dimensionless]
$\Delta v_{pm,2}$	Difference between the matrix and particle velocity at the outflow of a control volume in the x-direction $[v]$
Δx	Dimension of a control volume in x-direction $[L]$
Δy	Dimension of a control volume in y-direction $[L]$
Δz	Dimension of a control volume in z-direction $[L]$
δ_{ij}	The unit tensor where i and j refer to coordinate directions 1, 2, and 3 (e.g. x, y, z) [dimensionless]
$\dot{\epsilon}_{ij}$	Strain rate tensor where i and j refer to coordinate directions 1, 2, and 3 (e.g. x, y, z) $[t^{-1}]$
$\dot{\gamma}$	Shear rate or the magnitude of the strain rate tensor $\dot{\epsilon}_{ij}$ $[t^{-1}]$
ϵ	Penalty parameter [dimensionless]
η	Viscosity function or apparent viscosity of an ideal fluid $[\sigma \cdot t]$
η_m	Viscosity function or apparent viscosity of the matrix phase in a suspension $[\sigma \cdot t]$
η_s	Viscosity function or apparent viscosity of a suspension $[\sigma \cdot t]$
$\eta_{m,pl}$	Plastic viscosity of the matrix phase in a suspension $[\sigma \cdot t]$

$\eta_{m,pl}^{ref}$	Reference plastic viscosity of the matrix phase applied in a parameter study on blocking $[\sigma \cdot t]$
η_{pl}	Plastic viscosity of an ideal fluid $[\sigma \cdot t]$
$\eta_{s,pl}$	Plastic viscosity of a suspension $[\sigma \cdot t]$
Γ	Relative thickness of excess paste [dimensionless]
μ	Newtonian viscosity of an ideal fluid $[\sigma \cdot t]$
μ_m	Newtonian viscosity of the matrix phase in a suspension $[\sigma \cdot t]$
μ_s	Newtonian viscosity of a suspension $[\sigma \cdot t]$
Ω	Volume of container for slump test or slump flow test $[V]$
ω	Interpolation function [dimensionless]
Ω_e	Volume of a finite element e $[V]$
Ω_f	Differential volume of an infinitesimally small fluid element $[V]$
ϕ_m	Matrix volume fraction or porosity [dimensionless]
$\phi_p^{(2D)*}$	Particle area fraction of a cross-section of a packed bed at maximum particle volume fraction ϕ_p^* in the bulk region [dimensionless]
$\phi_{m,w}^*$	Matrix volume fraction at the maximum particle volume fraction $\phi_{p,w}^*$ in a circular tube [dimensionless]
$\phi_{p,i}$	Particle volume fraction of particle size fraction i [dimensionless]
$\phi_{p,i}^*$	Maximum particle volume fraction of particle size fraction i [dimensionless]
$\phi_{p,w}^*$	Maximum particle volume fraction in a circular tube [dimensionless]
$\phi_{p,w}^{(2D)*}$	Particle area fraction in a cross-section of a packed bed at maximum particle volume fraction $\phi_{p,w}^*$ in a circular tube [dimensionless]
ϕ_p	Particle volume fraction [dimensionless]
ϕ_p^*	Maximum particle volume fraction in the bulk region [dimensionless]
ρ_m	Matrix density $[\rho]$
ρ_s	Suspension density $[\rho]$
σ_t	Tangential component of the total stress vector at a solid boundary $[\sigma]$
σ_{ij}	Total stress tensor where i and j refer to coordinate directions 1, 2, and 3 (e.g. x, y, z) $[\sigma]$

τ	Shear stress or magnitude of the deviatoric stress tensor (τ_{ij}) [σ]
τ_0	Yield stress of an ideal fluid [σ]
τ_R	Shear stress at $r = R$ in a circular tube flow [σ]
τ_0^*	Dimensionless yield stress of an ideal fluid
τ_{ij}	Deviatoric stress tensor where i and j refer to coordinate directions 1, 2, and 3 (e.g. x, y, z) [σ]
$\tau_{m,0}$	Yield stress of the matrix phase in a suspension [σ]
$\tau_{m,0}^{ref}$	Reference yield stress of the matrix applied in a parameter study on blocking [σ]
$\tau_{m,r_{cap}}$	Shear stress at $r = r_{cap}$ of matrix flow in a straight circular capillary [σ]
$\tau_{s,0}$	Yield stress of a suspension [σ]
θ	The azimuthal coordinate in a cylindrical polar coordinate system
φ	Interpolation function [dimensionless]
ϱ_∞	Geometry function [dimensionless]
$\Delta\rho_{pm}$	Difference between the particle density and matrix density [ρ]
$\Delta P_{sep,cap}$	Pressure drop of capillary part in two-phase flow of a heterogeneous suspension [σ]
$\Delta P_{sep,sus}$	Pressure drop of suspension part in two-phase flow of a heterogeneous suspension [σ]
ΔP_{sep}	Total pressure drop in two-phase flow of a heterogeneous suspension [σ]
ΔP_{sus}	Total pressure drop in flow of a homogeneous suspension [σ]
Δz_{n-b}	Distance (z-direction) between node n and the cone boundary when it is turned upside down [L]
Δz_{n-n}	Distance (z-direction) between nodes of an element e in the cone lifting area when the cone is turned upside down [L]
A_i	Cross-sectional area i between reinforcements (e.g. A_1, A_2, or A_3 in the L-box setup A_{lbox})
A_1	Cross-sectional area between reinforcement in the L-box applying reinforcement setup A_{lbox}
A_2	Cross-sectional area between reinforcement in the L-box applying reinforcement setup A_{lbox}
A_3	Cross-sectional area between reinforcement in the L-box applying reinforcement setup A_{lbox}

A_b	Cross-section area of porous bed $[A]$
$A_{f,i}$	Cross-sectional area i between reinforcements occupied by material (e.g. A_1, A_2, or A_3 in the L-box setup A_{lbox})
a_i	Coefficient of the particle size fraction i in the compressible packing model [dimensionless]
A_{lbox}	Reinforcement setup in the L-box test
B_1	Cross-sectional area between reinforcement in the L-box applying reinforcement setup B_{lbox}
B_2	Cross-sectional area between reinforcement in the L-box applying reinforcement setup B_{lbox}
B_{lbox}	Reinforcement setup in the L-box test
c	Clear spacing between reinforcement $[L]$
$D100$	Abrams cone diameter of 100 mm facing the base plate in the slump flow test $[L]$
$D200$	Abrams cone diameter of 200 mm facing the base plate in the slump flow test $[L]$
d_c	Characteristic diameter of irregular shaped particles $[L]$
D_L	Diameter of the linear part of tube in the blocking test setup $[L]$
d_p	Particle diameter $[L]$
d_p^*	Corresponding particle diameter when applying the tube radius $R_{c,2}$ for flow between reinforcement $[L]$
d_{afi}	Diameter of aggregate size fraction i $[L]$
d_{bar}	Diameter of a reinforcement bar $[L]$
d_{cap}	Capillary diameter $[L]$
$d_{L,i}$	Lower particle diameter of particle size fraction i $[L]$
$d_{p,i}$	Diameter of particle size fraction i $[L]$
$d_{u,i}$	Upper particle diameter of particle size fraction i $[L]$
e	Element number [dimensionless]
E_1	First Ergun constant [dimensionless]
E_2	Second Ergun constant [dimensionless]
F	Marker concentration [dimensionless]
f/k	Shape factor [dimensionless]

f_e	Fractional fill state of element e [dimensionless]
F_i	Volume forces per unit mass where i refer to coordinate directions 1, 2, and 3 (e.g. x, y, z) $[\frac{F}{M}]$
F_L	Piston load $[F]$
f_n	Fill value of node n of a finite element e [dimensionless]
F_{drag}	Drag force on particles in a flow of a suspension $[F]$
$F_{p-b,n}$	Normal component of the interaction force between particles and solid boundaries in a flow of a suspension $[F]$
$F_{p-b,t}$	Tangential component of the interaction force between particles and solid boundaries in a flow of a suspension $[F]$
F_{p-b}	Interaction force between particles and solid boundaries in a flow of a suspension $[F]$
$F_{p-p,n}$	Normal component of the interaction force between particles in a flow of a suspension $[F]$
$F_{p-p,t}$	Tangential component of the interaction force between particles in a flow of a suspension $[F]$
F_{p-p}	Interaction force between particles in a flow of a suspension $[F]$
g	gravity $[L/t^2]$
$g_i(y,z)$	Concentration of material between reinforcement bars at cross-sectional area i (e.g. A_1, A_2, or A_3 in the L-box setup A_{lbox}) [dimensionless]
H	Cone or cylinder height $[L]$
h	Distance between parallel plates in pure shear flow $[L]$
h_0	Height of material in the slump flow test $[L]$
H_1	Height of material in the L-box at $x = 0$ mm $[L]$
H_2	Height of material in the L-box at $x = 700$ mm $[L]$
h_{gate}	Height of gate above the bottom in the L-box test $[L]$
$II_{\dot{\epsilon}_{ij}}$	Second invariant of the strain rate tensor $\dot{\epsilon}_{ij}$ $[(t^{-2})]$
$II_{\dot{\tau}_{ij}}$	Second invariant of the deviatoric stress tensor τ_{ij} $[\sigma^2]$
K	Compaction index in the compressible packing model [dimensionless]
k	Permeability of a porous medium $[A]$

k_0	Coefficient which depends on the shape of the capillary ($k_0 = 2$ for circular shape) [dimensionless]
K_c	Compaction index of the cement fraction in the compressible packing model [dimensionless]
K_g	Compaction index of the gravel fraction in the compressible packing model [dimensionless]
K_i	Compaction index of particle size fraction i in the compressible packing model [dimensionless]
k_k	Kozeny constant [dimensionless]
K_s	Compaction index of the sand fraction in the compressible packing model [dimensionless]
k_{ck}	Carman-Kozeny constant [dimensionless]
L_b	Length of packed bed [L]
L_c	Characteristic length used to calculate the Reynolds number [L]
L_e	Effective path length of packed bed [L]
L_L	Length of the linear part of the tube applied in the blocking tests [L]
L_T	Length of the tapered tube applied in the blocking tests [L]
m_i	Individual particle in the discrete particle approach where $i = 1, 2..M$ and M is the total number of particles [dimensionless]
n	Node number [dimensionless]
n_j	Components of the normal vector at a solid boundary where j refer to coordinate directions 1, 2, and 3 (e.g. x, y, z) [dimensionless]
n_{cap}	Number of capillaries [dimensionless]
p	Pressure [σ]
Q_0	Suspension flow rate [Q]
Q_m	Matrix flow rate [Q]
$Q_{cap,Bingham}$	Flow rate of Bingham matrix through a single capillary [Q]
$Q_{cap,Newton}$	Flow rate of Newtonian fluid through a single capillary [Q]
$Q_{m,1}$	Matrix flow rate into a control volume [Q]
$Q_{m,2}$	Matrix flow rate out of a control volume [Q]
$Q_{p,1}$	Particle flow rate into a control volume [Q]

$Q_{p,2}$	Particle flow rate out of control volume [Q]
$Q_{x,i}$	Flow rate in the x-direction over the cross-sectional area i between reinforcements (e.g. A_1, A_2, or A_3 in the L-box setup A_{lbox}) $[Q]$
R	Circular tube radius $[L]$
r	Radial direction in a cylindrical polar coordinate system $[L]$
R_1	Upper radius of the slump cone $[L]$
r_1	Normalized coordinate for a finite element [dimensionless]
R_2	Bottom radius of the slump cone $[L]$
r_2	Normalized coordinate for a finite element [dimensionless]
R_a	Tube radius applied in a parameter study $[L]$
R_b	Tube radius applied in a parameter study $[L]$
r_h	Hydraulic radius in infinite flow domain (bulk region) $[L]$
$r_h^{(1)}$	Hydraulic radius when including the circular tube wall area in calculation of the wetted surface area $[L]$
R_L	Radius at linear tube in blocking test setup $[L]$
r_p	Particle radius $[L]$
R_T	Radius at outlet of tapered tube in blocking test setup $[L]$
$R_{c,1}$	Corresponding tube radius when it is equal to the clear spacing c between the reinforcement bars $[L]$
$R_{c,2}$	Corresponding tube radius when it is equal to the radius of the circumscribed circle of a quadrant with side lengths equal to the clear spacing between the reinforcement bars $[L]$
$r_{cap,w}^{(2)*}$	Capillary radius $r_{cap,w}^{(2)}$ at the maximum particle volume fraction $\phi_{p,w}^*$ $[L]$
$r_{cap,w}^{(2)}$	Capillary radius when including the circular tube wall area in calculation of the wetted surface area, the assumption of $d_{cap} \sim d_p$ at $\phi_p = \phi_p^*$, and the channeling effect of the wall $[L]$
r_{cap}	Capillary radius in infinite flow domain (bulk region) $[L]$
$r_{cap}^{(1)*}$	The capillary radius $r_{cap}^{(1)}$ at the maximum particle volume fraction ϕ_p^* $[L]$
$r_{cap}^{(1)}$	Capillary radius when including the circular tube wall area in calculation of the wetted surface area $[L]$

$r_{cap}^{(2)*}$	The capillary radius $r_{cap}^{(2)}$ at the maximum particle volume fraction ϕ_p^* $[L]$
$r_{cap}^{(2)}$	Capillary radius when including the circular tube wall area in calculation of the wetted surface and the assumption of $d_{cap} \sim d_p$ at $\phi_p = \phi_p^*$ $[L]$
Re	Reynolds number [dimensionless]
S_0	Specific surface area of a single spherical particle $[L^{-1}]$
S_w	Wetted pore surface area $[A]$
S_{cap}	Surface area of a single straight circular capillary $[A]$
S_{tube}	Surface area of a circular tube $[A]$
SF	Slump flow (or spread) value in the slump flow test $[L]$
SL	Slump value in the slump test $[L]$
SL^*	Dimensionless slump value in the slump test [dimensionless]
SP	Superplastizicer dosage [solid content + water % weight of powder]
SP^*	Superplastizicer dosage [solid content % weight of powder]
$T50$	Time to reach a slump flow of 500 mm in the slump flow test $[t]$
t_i	Components of tangential vector at a solid boundary where i refer to coordinate directions 1, 2, and 3 (e.g. x, y, z) [dimensionless]
U	Mean or superficial velocity $[v]$
u_i	Components of the velocity vector where i refers to coordinate directions 1, 2, and 3 (e.g. x, y, z) $[v]$
u_i^b	Components of the velocity vector at boundary for which the tangential stress is zero where i refers to coordinate directions 1, 2, and 3 (e.g. x, y, z) $[v]$
U_m	Average velocity $[v]$
u_r^n	Velocity of node n in the radial direction $[v]$
u_x^n	Velocity of node n in the x-direction $[v]$
u_y^n	Velocity of node n in the y-direction $[v]$
u_z^n	Velocity of node n in the z-direction $[v]$
U_{crit}	Critical velocity below which blocking of particles occurs $[v]$
U_{fill}	Inlet velocity applied in simulation of form filling $[v]$
U_{lift}	Lifting velocity of slump cone or gate in the L-box $[v]$

U_{piston}	Piston velocity in circular tube flow test setup $[v]$
U_{shear}	Velocity of upper plate in pure shear flow $[v]$
$U_{x,i}$	Velocity in the x-direction over the cross-sectional area i between reinforcements (e.g. A_1, A_2, or A_3 in the L-box setup A_{lbox}) $[v]$
$U_{x,i}^{av}$	Average velocity in the x-direction over the cross-sectional area i between reinforcements (e.g. A_1, A_2, or A_3 in the L-box setup A_{lbox}) $[v]$
$u_{x,lub}$	Velocity in the x-direction in the lubrication slip model $[v]$
$u_{x,slip}$	Velocity in the x-direction in the Navier slip model $[v]$
V_c	Control volume $[V]$
v_f	Velocity of an infinitesimal small fluid element moving along a streamline $[v]$
v_m	Average matrix velocity $[v]$
v_s	Average suspension velocity in and out of a control volume $[v]$
V_{abi}	Critical volume for aggregate size fraction i $[V]$
V_{ai}	Volume of aggregate size fraction i $[V]$
V_{cap}	Volume of single circular straight capillary $[V]$
$v_{m,1}$	Average matrix velocity into a control volume $[v]$
$v_{m,2}$	Average matrix velocity out of a control volume $[v]$
$v_{p,1}$	Average particle velocity into a control volume $[v]$
$v_{p,2}$	Average particle velocity out of a control volume $[v]$
$v_{s,1}$	Average suspension velocity into a control volume $[v]$
$v_{s,2}$	Average suspension velocity out of a control volume $[v]$
V_{tube}	Volume of circular tube $[V]$
W	Weighing constant used in calculation of the weighed confinement ratio α^* [dimensionless]
x	Axis in the Cartesian coordinate system $[L]$
x_i	Cartesian coordinates in the i-direction normally referred to as x, y, z $[L]$
y	Axis in the Cartesian coordinate system $[L]$
z	Axis in the Cartesian coordinate system $[L]$
Z_a	Specific z-coordinate in a circular tube at a confinement ratio of $\alpha = 2$ $[L]$

Z_b	Specific z-coordinate in a circular tube at a confinement ratio of $\alpha = 2$ $[L]$
z_b	Z-coordinate of a moving boundary $[L]$
Z_c	Specific position in the z-direction in a circular tube at a confinement ratio of $\alpha = 2$ $[L]$
Z_d	Specific position in the z-direction in a circular tube at a confinement ratio of $\alpha = 2$ $[L]$
Z_L	Theoretical piston travel length $[L]$
z_n	Z-coordinate of node n $[L]$
$\mathbf{a}$	Global vector of unknowns
$\mathbf{F}$	Vector including body forces and boundary conditions
$\mathbf{K}$	Global system matrix [dimensionless]
$\mathbf{P}$	Column vector of pressure at nodal points of a finite element e $[\sigma]$
$\mathbf{R}_1$	Residual of mass in the finite element method
$\mathbf{R}_2$	Residual of momentum in the finite element method
$\mathbf{U}_i$	Column vector of the velocity component u_i of nodal points in a finite element e $[v]$

Chapter 1

Introduction

This Chapter gives the background of the work presented in this thesis on simulation of form filling with Self-Compacting Concrete (SCC). A short historical review on the development of SCC is given in Section 1.1. The present status on application of SCC and the necessity of models to predict form filling with SCC are discussed in Section 1.2 and 1.3, respectively. Computational methods to assess the flow of fluids and suspensions are described in Section 1.4. This leads to the basic hypothesis applied in this project for simulation of form filling with SCC (Section 1.5). The objectives, research strategy, and outline of this thesis are given in Section 1.6, 1.7, and 1.8.

1.1 Self-Compacting Concrete

Concrete is the most common construction material used throughout the world for infrastructure, civil engineering and housing applications, followed by wood, steel and a number of miscellaneous materials. Worldwide, over ten billion tons of concrete are being produced each year (Mehta 2002)(Lafarge.com 2005).

Fresh concrete is an inorganic material consisting of a mixture of particles suspended in water. Particles include hydraulic and inert powders, and fine to coarse aggregates. Hydraulic powders comprise Portland cements and semi-hydraulic mineral admixtures like fly ash and silica fume, which react with the water and solidifies into a matrix phase bonding the components together to create a stone-like material. Chemical admixtures may be applied to enhance the control of the workability, hardening process, and air void distribution (Herholdt, Justesen, Christensen & Nielsen 1985)(Neville & Brooks 1990).

Casting of conventional concrete involves placing and subsequent compaction which is essential for the purpose of ensuring the requirements of strength, impermeability, and durability of the hardened concrete in the actual structure (Neville & Brooks 1990). Vibration is often part of the compaction and is carried out to eliminate entrapped air and force the particles into a closer configuration (Neville & Brooks 1990)(Frandsen & Schultz 1997). Incorrect compaction will result in a lower structural quality; for instance, too long time of vibration might damage the macrostructure, microstructure, and air void structure of the concrete (Frandsen & Schultz 1997).

The first initiative to change the paradigms of concrete casting came in the 1980s in Japan. At this time durability of concrete structures was of major concern because the reduced number of skilled workers in the construction industry had led to a reduction in the quality of construction in the 1970s and 1980s (Ouchi 1999)(Okamura & Ouchi 2003).

In 1986, Professor Hajime Okamura proposed a new type of concrete, the Self-Compacting Concrete (SCC) (Ouchi 1999). SCC should be able to fill every corner of a formwork, purely by means of its own weight and without the need for vibrating compaction.

The development of Self-Compacting Concrete has been closely related to the development of chemical cement dispersing plasticizers. Today, the ”new generation” of superplasticizers, the polycarboxylate ethers (PCE), gives improved workability retention to the cementitious mix. These superplasticizers disperse the cement by steric stabilization, which is more powerful compared to the electrostatic repulsion of older types of plasticisers (Sakai & Daimon 1995)(Collepardi 1998)(Yamada, Takahashi, Hanehara & Matsuhisa 2000)(Flatt 2004*a*).

In general, the main motivations for applying SCC are:

- Structural quality
    - There is lower risk of getting non-filled zones, poor compaction, and an inhomogeneous air void structure.
- Productivity
    - It is possible to apply higher casting rates, reduce manpower, and leave out safety measures normally required to the formwork when vibrating conventional concrete. The productivity, though, must take into account the possibility of extra costs e.g. to tighten and design the formwork for higher formwork pressures.
- Working environment
    - The working environment is significantly improved when vibration is eliminated. For instance, recent results have shown that the concrete worker carrying out vibration is exposed to approximately 90 unhealthy lifts per hour, which is clearly above the recommended maximum of 20 lifts per hour (BriteEuram 2000)(Nielsen 2006).
- Architectural design
    - SCC brings new possibilities into architectural design of concrete structures. There is a growing demand for increased individuality in structural design (a view which was presented by Rottig (2003) at a Nordic Mini-Seminar on ”Form Filling Ability of SCC” under the topic ”Industry and Individualism” (Thrane 2004)). For instance, in the post-war period a lot of effort was put into the pre-cast industry where the main target was to carry out construction at low costs, an effort which left out the individuality of craftsmen work. Nowadays, the stereotype appearance of these structures brings negative associations to many people’s mind leaving the concrete industry with a serious image problem.

1.2 Status on Application of Self-Compacting Concrete

Thus, there are significant benefits from applying SCC, which should encourage a wide use. In the 1990s SCC was introduced in Europe, and Holland and Sweden were among the first to apply SCC (Bennenk 2005)(Billberg & Osterberg 2002). In the beginning of the 21^{st} century SCC started to be of interest in the US (Ouchi, Nakamura, Österberg, Hallberg & Lwin 2003).

However, the annual production of SCC indicates that challenges still need to be overcome. According to the European Ready Mixed Concrete Organization, SCC amounted for less than 1 % of the ready mix concrete production in Europe in 2004 (ermco.org 2005). This estimate may be influenced by a lack of conformity on the definition of SCC. According to the definition by Ouchi (1999), SCC can be cast and compacted without the use of vibration. Others may define SCC according to flow criteria in workability test methods, e.g. a minimum slump flow value.

As an example of applying the no-vibration definition, the situation in Denmark shows an annual ready mix production of approximately 20-25 % in 2005, but it is almost only applied in simple horizontal applications such as floors for housing (Thrane 2005)(voscc.dk 2006). Approximately 80 % of such applications are being cast with SCC, almost replacing conventional concrete. It is likely that the situation is somewhat similar in other countries in such applications. SCC is not applied in complicated horizontal applications, e.g industrial floors with high planeness requirements.

Compared to horizontal applications, the development seems to be halting or is even being recessive in vertical in-situ applications. The strongest interest seems to be found in connection to complicated castings, in repair etc., where conventional concrete is impossible to apply (Skarendahl 2003). The future potential of SCC in vertical applications may be as high as 70 % of the total ready mix production (Thrane 2005)(voscc.dk 2006).

In the precast industry SCC has adapted well in many countries where pre-cast producers now use SCC for a considerable part of their production (Skarendahl 2003)(Lauritsen & Thrane 2003)(Walraven 2003)(Bennenk 2005)(voscc.dk 2006). A large part of SCC in the pre-cast industry is also applied in simple horizontal applications, often replacing conventional concrete.

1.3 Modelling of Form Filling with Self-Compacting Concrete

In many industries where the manufacturing process involves casting of a fluid or suspension, it is essential to have tools to assess under what conditions the required product quality is obtained. The assessment may be based on trial and error, theoretical prediction or a combination.

Trial and error may be applied to optimize the casting process when a large number of small samples have to be produced.

When casting concrete, especially in-situ, trial and error is rarely an option. The structural size and in-situ production often only leaves one attempt to obtain a satisfactory form filling and thereby structural quality.

Therefore, it is absolutely necessary to develop theoretical models to predict form filling with SCC. Lack of theoretical assessment tools are one of the main reasons for the haltering use of SCC in vertical applications. This may lead to selection of concrete mix compositions and casting techniques that are not suitable for a given application.

1.4 Numerical Methods to Assess Flow of Fluids and Suspensions

Numerical methods have been developed for the simulation of transient arbitrary free surface flow, which is of interest in many industries. The challenges vary depending on the type of flow and material characteristics.

The applicability of two different approaches for simulation of the form filling ability, flow patterns, and heterogeneous flow phenomena associated with casting of SCC is discussed below. These two approaches are referred to as the discrete particle flow and homogeneous fluid approach.

1.4.1 Discrete Particle Approach

Three discrete particle flow methods are described below; the distinct element methods (DEM), the dissipative particle dynamics (DPD), and the viscoplastic suspension element method (VSEM).

The aim of these methods is to carry out detailed studies of the movement, trajectory, rotation, and interaction of particles.

- Distinct element method (DEM):

    - It was initially developed to better understand the behavior of dry granular materials of interest in numerous industries (chemistry, agricultural processing, mining etc.). The behavior of dry granular media involves characteristic properties as dilatancy, localization of deformation, or segregation in dynamic applications such as chutes, hoppers and belt conveyers (Cleary 1998)(Quoc, Zhang & Walton 2000)(Kruse & Lemmon 2005)(Fortin, Millet & d. Saxce 2005). DEM consists in modelling the granular medium as a collection of particles whose trajectories are studied separately. When contacts occur between particles, a local constitutive law determines the inter-particle contact forces and consequently the resulting motions of the particles involved in the contact. The DEM method evolved from early molecular dynamic algorithms and Cundall & Strack (1979) and Walton (1982) developed the first simple contact algorithms between two-dimensional circular disks. Much research has focused on the development and improvement of contact laws and particle shape flexibility as well as extension to three dimensions e.g. see (Lin & Ng 1995), (Langston, Al-Awamleh, Fraige & Asmar 2004), and (Zhao, Nezami, Hashash & Ghaboussi 2006).

      Based on work by Chu, Machida & Suzuki (1996), a three-dimensional particle flow code program, PCD3D, was applied in a preliminary study by Noor & Uomoto (1999) to simulate the flow of SCC in the slump flow, L-box, and V-funnel test, respectively. DEM was observed to reproduce the qualitative behavior of fresh concrete. As a compromise between modelling of aggregate movement and limitation of the computational time, the material was divided into mortar and coarse aggregates larger than 7.5 mm. The method proposed by Noor & Uomoto (1999) was adopted by Petersson & Hakami (2001) and Petersson (2003) to simulate SCC flow in the slump flow, J-ring, and L-box test, respectively. However, the applicability of DEM to simulate the form filling ability, flow patterns, and heterogeneous flow phenomena is not clear from these investigations.

- Dissipative particle dynamics (DPD):
  - DPD were originally mesoscopic models for complex fluids, e.g. emulsions, where the mesoscopic particles represent clusters of molecules (The mesoscopic particles are not to be confused with particles in suspensions, which are called rigid bodies or objects in connection with DPD)(Martys & Mountain 1999). The particles are subjected to pair-wise forces which comprise: Soft repulsion, stochastic noise and a dissipation (conceptually similar to a viscous drag). Navier-Stokes behavior is obtained with a suitable choice of functional form of these potentials, thus the method captures hydrodynamics. Based on work by Koelman & Hoogerbrugge (1993) the mesoscopic models have been extended to cover rigid bodies by freezing a part of the fluid particles (the fluid phase). Martys & Mountain (1999) proposed a so-called velocity Verlet algorithm for a DPD based model describing the motion of rigid body inclusions. Compared to the originally used Euler algorithm the velocity Verlet algorithm is claimed to significantly improve the numerical accuracy at little computational costs. Examples of applications of DPD to the SCC technology are given in (Ferraris, Larrard & Martys 2001), (Martys & Farraris 2002), and (Ferraris & Martys 2003). DPD has been used to model the sphere movement and interaction of monosized and polysized spheres (between 200-500 spheres depending on the solid fraction)(Ferraris et al. 2001)(Ferraris & Martys 2003). The viscosity of the suspensions was calculated based on the average stresses at a given strain rate. The calculated relative viscosities were observed to correlate well with measured data. DPD may in combination with knowledge on the forces between the colloidal particles in the matrix allow numerical modelling of the actual viscosity of the suspension (E.S.Boek, Coveney, Lekkerkerker & Schoot 1997).

    A few studies of monodisperse spheres passing reinforcement bars under the influence of gravity indicated that blocking occurs when the particle diameter to bar spacing is above 1/5 (Martys & Farraris 2002). However, the effect of flow, mix proportions and properties are not evident from these simulations. Finally, Martys & Farraris (2002) have studied flow in a co-axial rheometer and the results indicate that it is possible to simulate particle migration.

- Viscoplastic Suspension Element Method (VSEM):
  - Mori & Tanigawa (1992) developed a so-called viscoplastic suspension element method (VSEM) to simulate the flow of concrete in various tests. The concrete was divided into mortar and coarse aggregates, and the aggregates were approximated as monodisperse spheres. The rheological properties of the concrete (suspension) was calculated based on the rheological properties of the matrix and the coarse aggregate content. The motion of stiff spheres in a viscoplastic body was simulated by cylindrical so-called suspension elements with viscoplastic properties between pairs of particles being closer than a given distance. Kurokawa, Tanigawa, Mori & Nishinosono (1996) compared simulated (two-dimensional) and measured flow during a so-called L-flow and slump test for concretes with yield stresses between 50 and 300

> Pa. They found the numerical approach to overestimate the initial rate and underestimate the final flow. Detection of heterogeneous flow phenomena was not evident from these studies. Mori & Tanigawa (1992) tested concretes with a minimum yield stress at 100 Pa and claimed the method applicable for the simulation of complex behavior of concrete such as collapse, separation, and mixing, however, verification is limited.

In summary, the discrete particle flow approaches DEM, DPD and VSEM aim at simulating both the macroscopic and local behaviour of granular materials and suspensions.

In respect of simulating the form filling ability, flow patterns, and heterogeneous flow phenomena, the main advantage of the discrete particle approach is the ability to carry out detailed studies of the particle flow and thereby simulate the heterogeneous flow phenomena. Simulation of the form filling ability and flow patterns on a larger scale of length and time, similar to form filling scales, requires a very large computer capacity, especially in three dimensions.

Presently, limited analyses have been performed on the form filling ability and flow patterns, and the relation between simulations and experiments is not clear.

Blocking can be studied at a smaller scale of length and time, and attempts to model the flow past reinforcement have been carried out. However, the effect of flow and mix proportions is not clear and verification of the analyses has not been carried out.

Results have indicated the possibility of simulating particle migration which is related to dynamic segregation. However, in form filling applications dynamic segregation occurs over scales of time and length similar to studies of the filling ability and flow patterns which impose the same very large requirements to the computational capacity.

In its present state the discrete particle approach does not seem applicable for the simulation of the form filling characteristics of SCC on a larger scale of time and length. Also, one of the important aspects concerns the input parameters to the models describing the contact laws between particles. These are not measurable quantities for which reason they need to be fitted in order to get the best comparison between numerical predictions and experiments. Further research in ways to select and measure the input parameters is needed.

1.4.2 Homogeneous Fluid Approach

The homogenous fluid approach refers to simulation of ideal fluids without particle inclusions and is included in the overall framework of Computational Fluid Dynamics (CFD) (Wendt 1992). The flow characteristics (velocity, pressure, and temperature) are obtained by solving the governing equations of mass, momentum and energy using a numerical solution method. The material properties comprise, e.g. density, viscosity, specific heat, and thermal conductivity.

Important issues are the discretisation method and handling of free surfaces. The discretization methods comprise the finite volume method, the finite element method, and finite difference method (Wendt 1992). Various techniques have been developed for treatment of the free surface and the most appropriate technique rely on the material and deformation characteristics. The mesh may be fixed and combined with a volume of fluid technique (Hirt & Nichols 1981) or the mesh may be deforming (Lewis, C. & Taylor 1997)(Souli & Zolesio 2001).

The CFD technology has proven to be applicable for simulation of mould filling of food, metal, and plastics as well as to study e.g. the drag on cars and aeroplane wings (Tome, McKee, Barratt, Jarvis & Patrick 1999)(Luoma & Voller 2000)(Xu 2003)(Mirbagheri, Shrinparvar, Ashory & Davami 2004)(Lewis, Postek, Han & Gethin 2006)(Tie, Dequn & Huamin 2006)(Kieffer, Moujaes & Armbya 2006)(Epstein, Peigin & Tsach 2006).

Tome et al. (1999) studied two-dimensional filling of a Newtonian sirup in a square container (50·50 mm^2) with an inlet of 3, 4, or 5 mm. Simulations and experiments were compared for three different inlet velocities and, in general, good correlation was found between the experimental and simulated free surface.

The casting of metal and polymers is a rather complex flow problem and includes filling of a cavity, heat transfer, and solidification typically within a few seconds. Studies can be found in (Luoma & Voller 2000), (Xu 2003), (Mirbagheri et al. 2004), (Lewis et al. 2006), and (Tie et al. 2006). In general, it seems CFD is capable of simulating the filling ability, flow patterns, and temperature distribution in the material during the filling and solidification period.

Compared to the moulding processes in the food, plastic and metal industry only limited studies have been carried out on the process of casting concrete using a homogeneous fluid approach.

Mori & Tanigawa (1992) developed a so-called Viscoplastic Finite Element Method (VFEM) and a Viscoplastic Divided Element Method (VDEM) for two-dimensinoal fluid flow, however, based on an approximation of the dynamic behavior and using a mono-dimensional plasticity criterion. In VFEM the mesh deforms to describe the free surface. In VDEM the mesh is fixed, and the flow is described as displacement of markers.

Experimental verification of the proposed procedures is limited and simulations using measured rheological properties have not been carried out. Kurokawa, Taniwawa, Mori & Komura (1994) compared one experimental slump flow test with a simulation using VFEM, which resulted in fitted Bingham parameters of $\tau_0 = 100$ Pa and $\eta_{pl} = 800$ Pa·s. Kitaoji, Tanigawa, Mori, Kurokawa & Urano (1996) compared two form filling experiments without reinforcement with a two-dimensional simulation of the free surface using VDEM, and a reasonable agreement was found using $\tau_0 = 50$ Pa and $\eta_{pl} = 800$ Pa·s in the first and $\tau_0 = 300$ Pa and $\eta_{pl} = 1100$ Pa·s in the second form filling. These fitted Bingham values seem to be relatively high compared to experimental studies on the rheological properties of SCC. For instance, Wallevik (2003*b*) showed a yield stress range from approximately 10 to 80 Pa and a plastic viscosity range from approximately 20 to 150 Pa·s obtained from measurements in a co-axial viscometer.

In summary, a homogeneous fluid approach seems promising for the simulation of the form filling ability and flow patterns on a larger scale of length and time compared to the discrete particle approach. Also, it is an advantage that input to the simulations is given in terms of physical measurable quantities, such as the viscosity.

Compared to the moulding processes in other industries using a homogeneous fluid approach, only limited studies have been carried out on concrete casting.
Thus, there is a need to carry out detailed studies of the transient behavior and the correlation between simulations and experiments in various flow domains with and without reinforcement. Simulations should be based on the complete three-dimensional set of governing equations and use measured rheological properties.

The homogeneous fluid approach does not simulate particle blocking or dynamic segregation. Therefore, additional tools are needed to assess under which flow conditions there is a risk of blocking and dynamic segregation. The use of numerical approaches to study blocking and dynamic segregation was discussed in Section 1.4.1. A few analytical methods have been proposed for blocking and segregation of SCC. These are discussed below.

Heterogenous Flow Phenomena (Analytical Approach)

A semi-empirical model to assess blocking was proposed by Bui (1994) and Tangtermsirikul & Bui (1995) based on the concept of a critical volume for each aggregate fraction which is determined from experiments, see also (Billberg 1999) and (Olsen, Thrane, Nielsen & Brandl 2001). Then, for a given aggregate composition (grading and shape), the model estimates a critical volume fraction of the specific aggregate composition or a minimum amount of paste necessary to avoid blocking. This approach focuses on a blocking criterion based on bar spacing and mix composition - in particular aggregate size and volume fraction. A criterion for the blocking resistance based only on the mix composition may be referred to as a static criterion, i.e. the possible effect of dynamic behavior is not considered.

Modelling of particle segregation in cementitious materials has focused on the static segregation (the concrete is not flowing). Saak, Jennings & Shah (2001) suggested a criterion to the particle diameter based on the force equilibrium of one particle in a Bingham matrix. Bethmont, Schwarzentruber, Stefani & Leroy (2003) showed that this equation underestimates the critical diameter by approximately a factor of 10 because the movement of a particle has to overcome the yield stress over an area that is larger than the projected surface area of the particle as shown by Beris, Tsamopoulos, Armstrong & Brown (1985). Bethmont et al. (2003) modified the equation based on experimental results to find good agreement between the theoretical estimate and experimental results of the critical diameter. The effect of the granular skeleton has been studied by Bethmont (2005) and Roussel (2006a) in a static matrix phase (cement paste or mortar) and group effects are positive as far as they enhance the segregation resistance of SCC. Roussel (2006a) has written a stability criterion taking into account the mechanical interactions between the particles, and found good agreement with experimental results.

The methods proposed so far on blocking and segregation have focused on static criteria, e.g. to the particle volume fraction and particle size. Further improvements to the assessment of blocking and dynamic segregation may look into the effect of flow and the possibility of developing models with a limited need for empirical calibration.

1.5 Basic Hypothesis for Simulation of Form Filling with Self-Compacting Concrete

Based on the present state of computational modelling of flow of suspensions, it is decided to apply the following basic hypothesis for simulation of form filling with SCC. It is assumed that form filling with SCC may be simulated within a CFD framework based on:

- Homogeneous flow properties of SCC:
  - The rheological parameters characterize the homogenous flow properties of fluids and suspensions. The rheological parameters depend on the viscosity function chosen to describe the relation between the shear stress and shear rate (Bird, Armstrong & Hassager 1987).
- Casting technique:
  - The casting technique includes the type of placing (pump or conveyor belt), inlet placement (static or dynamic), and casting rate.
- Resistance to heterogeneous flow phenomena:
  - Analytical models on the heterogeneous flow phenomena are essential in order to take into account possible heterogeneity in the homogeneous form filling simulation. Different mix compositions may have the same rheological properties, but not the same resistance to the heterogeneous flow phenomena (see below).

Combining the choice of a viscosity function (and thereby the rheological parameters) and the casting technique with analytical models for the heterogeneous flow phenomena, it is expected that the three important form filling characteristics can be simulated in a CFD framework:

- Filling ability:
  - The form filling ability expresses the ability of the concrete to homogenously flow out into every corner of the formwork. The rheological properties and casting technique determines the form filling ability if heterogeneous flow phenomena are avoided.
- Flow patterns:
  - The flow patterns express the flow characteristics of the homogeneous flow e.g. the direction and rate of flow at every point and time during placing. The flow patterns depend on the rheological properties and casting technique, and may be used to identify e.g. particle paths (plug flow zones and dead zones) and shear rates. Field observations indicate that the flow patterns have a significant influence on the heterogenous flow phenomena.

- Heterogeneous flow phenomena:
    - The heterogeneous flow phenomena refer to blocking and dynamic segregation of aggregates. Blocking and dynamic segregation are defined as aggregate accumulation behind reinforcement during flow (confined flow) and segregation during flow (non-confined flow), respectively. On a form filling scale blocking and dynamic segregation mainly concern the coarse aggregate ($d_p > 4$ mm). Blocking and dynamic segregation causes, e.g. honeycombing, poor form filling, and mortar rich top layers, which are significant reasons for the recessive use of SCC in vertical applications. Blocking is of special interest in high quality and complicated structures with a dense reinforcement configuration.

1.6 Objective

The objectives of this project are:

- Homogeneous flow:
    - Establish and demonstrate the capability of models in relation to simulating the form filling ability and flow patterns of SCC in selected flow domains of various form geometry and reinforcement configuration.
- Heterogeneous flow phenomena:
    - Develop a phenomenological model for blocking of particles in the confined flow of a suspension taking into account the flow rate, flow domain dimension, particle size, rheological properties of the suspension and matrix, particle volume fraction, maximum particle volume fraction, and particle shape.

For the heterogeneous flow phenomena, it is decided to focus on blocking, which is of special interest in complicated castings with a high reinforcement density.

Modelling dynamic segregation is not included in this project, but a qualitative description of the phenomenon is included and discussed in relation to the experimental observations.

1.7 Research Strategy

The homogeneous fluid approach is applied to simulate the filling ability and flow patterns in selected flow domains. Assuming isothermal conditions the governing equations derived from continuity of mass and momentum are applied. The Bingham constitutive law is applied to describe the rheological properties. The numerical approach is based on a combined Galerkin finite element method and volume of fluid technique adapted in Fidap (FIDAP 2000). Routines are developed to handle moving boundaries in the selected flow domains.

The selected flow domains include standard test methods and vertical form filling applications. The test methods comprise the slump flow test and the L-box test with reinforcement. The form filling applications comprise two laboratory formworks (with and without reinforcement), and five full-scale form works with a light reinforcement.

The homogenous flow simulations are compared with the experimental results with respect to the filling ability and flow patterns. The correlation between measured rheological properties and those applied in simulations is discussed. Independent measurements of the rheological properties are undertaken in a commercially available concrete rheometer, the BML rheometer (Wallevik 1998*b*).

For assessment of blocking, a phenomenological model is proposed. A blocking criterion is formulated for the flow of a monodisperse suspension in a finite circular tube flow domain introducing a flow rate criterion. The model takes into account the tube radius, particle radius, rheological properties of the suspension and matrix, particle volume fraction, maximum particle volume fraction, and particle shape. The model applies capillary theories and pressure drop-flow rate relations for a circular tube flow domain. The experimental results from piston driven flow of a monodisperse suspension in a circular tube are compared with the behaviour of the phenomenological model. The piston velocity, tube radius, particle volume fraction, and particle shape are varied. Particle shapes include spherical glass beads and cube shaped aluminium particles suspended in a matrix phase consisting of water, lime stone filler, fly ash, and silica fume dispersed with a superplastizicer. A procedure is proposed to extend the model to the flow of a suspension between reinforcement to illustrate the principles of applying a flow rate criterion in a homogeneous flow simulation for assessment of blocking. This approach is applied in simulations of the selected flow domains including reinforcement (L-box test and form filling applications).

Finally, the dynamic segregation and surface quality are discussed in relation to the simulated flow patterns.

1.8 Outline of the Report

This thesis is divided into eight chapters. The content of the chapters are described below and Figure 1.1 illustrates the structure of the report.

- Chapter 1: "Introduction"
  - The history, application, and challenges of SCC are discussed. Possible strategies for simulating the form filling ability, flow patterns, and heterogeneous flow phenomena are discussed leading to the basic hypothesis and objectives of this thesis.
- Chapter 2: "Examples of Application"
  - Examples of vertical and horizontal applications of SCC are presented. Implementation of a rheological approach for characterization of the homogeneous flow properties is discussed.
- Chapter 3: "Flow and Flow Properties of Self-Compacting Concrete"
  - The properties of homogeneous suspensions and possible heterogeneous flow phenomena are presented and discussed. The homogeneous properties include the viscosity function, the applicability of the Bingham model, composite modelling of the rheological properties, rheological measuring techniques, and the relation between standard test methods and the rheological properties. The heterogeneous flow phenomena include a description and discussion of blocking and dynamic segregation.
- Chapter 4: "Homogeneous Flow: Mathematical Formulation"
  - The governing equations of for homogeneous flow are presented.
- Chapter 5: "Homogeneous Flow: Numerical Solution Method"
  - The numerical approach for solving the velocity field and capturing the free surface location is presented. For each of the selected flow domains, the numerical model is presented and discussed including ways of handling moving boundaries such as lifting the slump cone and the gate of the L-box. A relation is proposed to simulate a slip boundary condition.
- Chapter 6: "Heterogeneous Flow: Blocking"
  - A phenomenological model for blocking is presented and discussed, and experiments are carried out to investigate the model behavior. A procedure is proposed to extend the flow rate criterion to flow between reinforcement, which is applied in Chapter 7.
- Chapter 7: "Simulation and Testing of Form Filling with Self-Compacting Concrete"
  - Simulation and testing of SCC flow in the selected flow domains; the slump flow test, L-box test, and form filling applications are presented. In the cases including reinforcement, the model outlined in Chapter 6 is applied to estimate a critical flow rate.

- Chapter 8: "Conclusions and Future Perspectives"
  - The conclusions on the selected modelling approach to simulate the form filling ability, flow patterns and blocking are given. The future perspectives of simulating form filling with SCC are discussed.

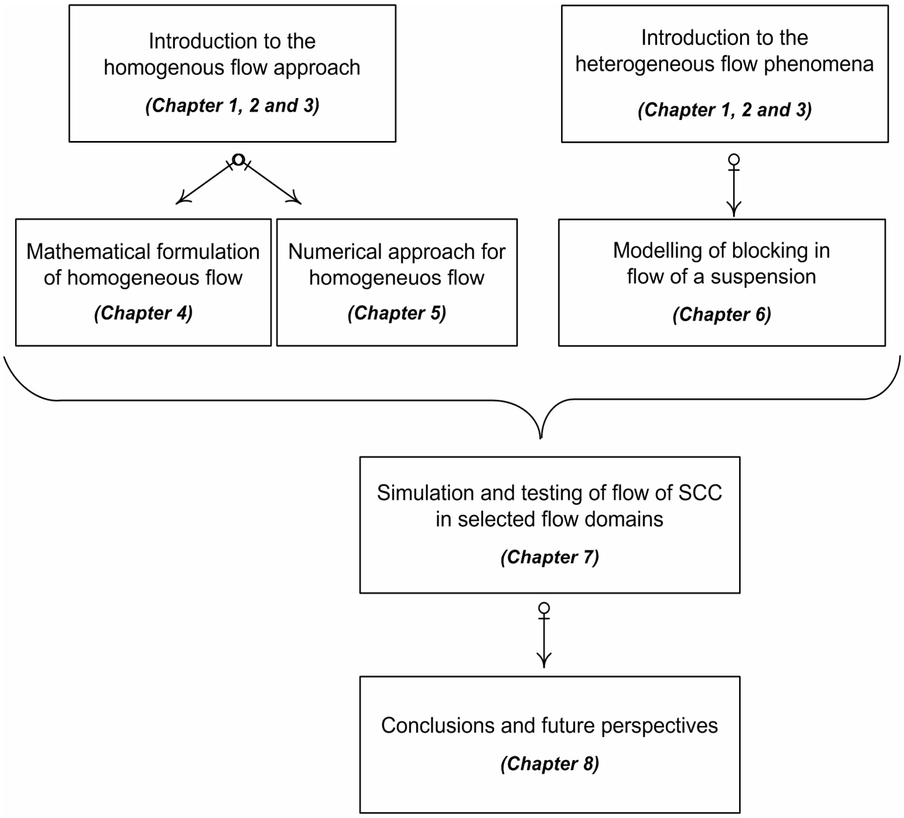

Figure 1.1 *Illustration of the structure of the thesis.*

1.9 Limitations

This project focuses on simulation of the form filling ability, flow patterns and blocking of aggregates.

Modelling of the dynamic segregation, intrinsic air void stability, and surface quality are not included.

However, the dynamic segregation and surface finish are discussed in relation to the experimental observations.

Assumptions for the modelling procedures are described in each of the relevant chapters.

Chapter 2

Examples of Self-Compacting Concrete Applications

This Chapter presents examples of SCC applications. The cases were presented on the Nordic Mini-Seminar: ”Form Filling Ability of Self-Compacting Concrete” (Thrane 2004). It shows examples of horizontal and vertical castings both from in-situ and the precast industry.

The observations from the castings are briefly discussed. Instead of the rheological properties, results from the slump flow test are reported (Efnarc 2002). The slump flow test and other empirical test methods are quick and easy-to-use compared to the commercial rheometers. However, the empirical test methods provide test specific results. Measuring procedures, accuracy, repeatability, reproducibility, and correlation to rheology are important to consider to obtain a valid characterization of the homogeneous flow properties in order to obtain usable experiences from field observations of SCC castings. The rheological properties of SCC and correlation to the standard test methods are discussed in Section 3.1.2 and 3.1.5, respectively.

2.1 In-Situ Applications

2.1.1 Horizontal Castings

As mentioned in Section 1.2 most SCC is applied in simple horizontal applications (at least in Denmark). An example of a simple in-situ floor casting is shown in Figure 2.1. The use of SCC has made casting much easier, but much care must be taken during casting and finishing to avoid surface defects.

- Casting
    - The concrete is either placed by pumping or conveyor belt depending on the area of the application, and drainpipes are often used to level the surface (see Figure 2.1). The form geometry and light reinforcement configuration are rarely a problem to the form filling ability due to the flexibility of positioning the inlet. The main challenge

is to avoid dynamic segregation. Observations indicate an increased risk of dynamic segregation when increasing the distance between the inlet position and the free surface of the concrete. It seems preferable to aim at a slump flow of $SF \sim 550$ mm. In terms of the Bingham parameters, the total spread only gives an indication of the yield stress and not the plastic viscosity. Increasing the plastic viscosity is likely to increase the dynamic segregation resistance. Experiences from the concrete workers show that there can be a significant difference on how easy different SCCs may be to work with (for leveling, shoveling etc.), and it is not only linked to the slump flow in the sense that a higher slump flow decreases the efforts needed to handle the concrete. Also, the plastic viscosity is important to consider, and it is beneficial to decrease the plastic viscosity. Thus, to obtain a proper flow, segregation resistance, and easiness to handling the concrete, it is important to address both the yield stress and plastic viscosity.

- Finishing
  - Many of the challenges of horizontal castings relate to the surface finishing period. Increasing casting rates, variations in consistency from batch to batch, the retarding effect of the superplasticizers, and difficulties with obtaining uniform curing conditions can result in uneven surface properties. For instance, sometimes a dense top layer of paste is created which captures the rising air voids beneath the surface. This may result in weak zones, which may deform or spall when exposed to loading e.g. mechanical trowelling (Jacobsen 2004).

Figure 2.1 *An example of a simple horizontal SCC application, in this case an in-situ floor. Drainpipes are typically used to level the surface (Wallin 2003).*

SCC is not applied, e.g. in industrial floors, because the procedure applied in simple horizontal applications cannot satisfy the planeness requirement to such floors.

2.1.2 Vertical Castings

As mentioned in Chapter 1, the use of SCC in vertical in-situ applications is very limited due to the lack of tools to assess and control the form filling ability, flow patterns, and heterogeneous flow phenomena. The motivation for its use is mostly found when the complexity of the structure makes conventional casting difficult.

The castings of concrete arches as part of the Södra Länken project in Sweden are examples of complicated castings (Österberg 2002). The two parallel tunnels did not have a full rock cover at a section of about 20 meters, and the only possible way to stabilize it was by concrete arches (see Figure 2.2).

Figure 2.2 *The final tunnel lining for the Södra Länken project. The concrete arches were cast with SCC due to the complexity of the structure. To the left the arrangement for continuous discharge, and to the right a view of the south arch (Österberg 2002).*

To ensure the structural quality improved control of the organization, production, quality control, casting technique, and surveillance during form filling were applied.

In general, the results from the casting were positive. In the arch section the homogeneity was better than for those cast when using conventional concrete and vibration. A strict quality control showed that about 30 % of the arriving batches had to be either corrected or rejected. Acceptance was based on measurement of the slump flow, where the desired slump flow was set to $SF \sim 700$ mm, and visual observations of the segregation resistance. During casting, visual observations of the filling ability and heterogeneous flow phenomena were applied to adjust the casting technique if needed. Continuous discharge was obtained by ensuring that two trucks could unload after each other without interruption.

For details about the experiences from the casting, see Österberg (2002).

2.2 Pre-Cast Applications

2.2.1 Horizontal Castings

As mentioned in Chapter 1, SCC is widely used in simple horizontal applications in the precast industry. An example of the casting of a wall element is shown in Figure 2.3.

Figure 2.3 *Example of a simple horizontal casting (wall element) in the precast industry. Filling and finishing are shown to the left and right, respectively (Rottig 2003).*

In general, the comments from the horizontal in-situ casting apply to the precast castings. Some of the supplement experiences are given below.

For instance, casting joints can be avoided by casting relatively quickly while moving the bucket from side to side in the longitudinal direction (Bennenk 2005). If a break occurs between two batches, additional energy should be applied in the contact surface, e.g. by lifting the bucket and ensure an overlap by casting behind the first layer.

Besides the risk of dynamic segregation, also the risk of blocking increases when increasing the distance between the inlet position and the free surface of the concrete (Lauritsen & Thrane 2003).

Regarding the finishing, it is often more easy to control the surface properties compared to the in-situ castings. Smaller areas and an indoor climate is a great advantage (Skarendahl 2003).

2.2.2 Vertical Castings

Two examples of vertical precast applications are presented.

The first example shows the form filling procedure applied for the casting of a vertical L-element (see Figure 2.4). The casting procedure and the desired slump flow range ($SF \sim 650$ mm) were the results of numerous trial and error tests (Lauritsen

& Thrane 2003).

The form work was turned upside-down to eliminate the surface finishing procedure of the final upper surface. Casting starts at point 1 slowly moving to point 2. Filling continues with the bucket fixed in this position, and the concrete flows down the slope until it reaches the height at point 3. Then the casting rate is reduced until the height of point 4 is reached. Now the bucket is placed right above the vertical part of the element at point 5, and filling is completed. The casting procedure aims to let the concrete slide slowly over the edge, because a direct drop through the reinforcement have proved to increase the risk of dynamic segregation.

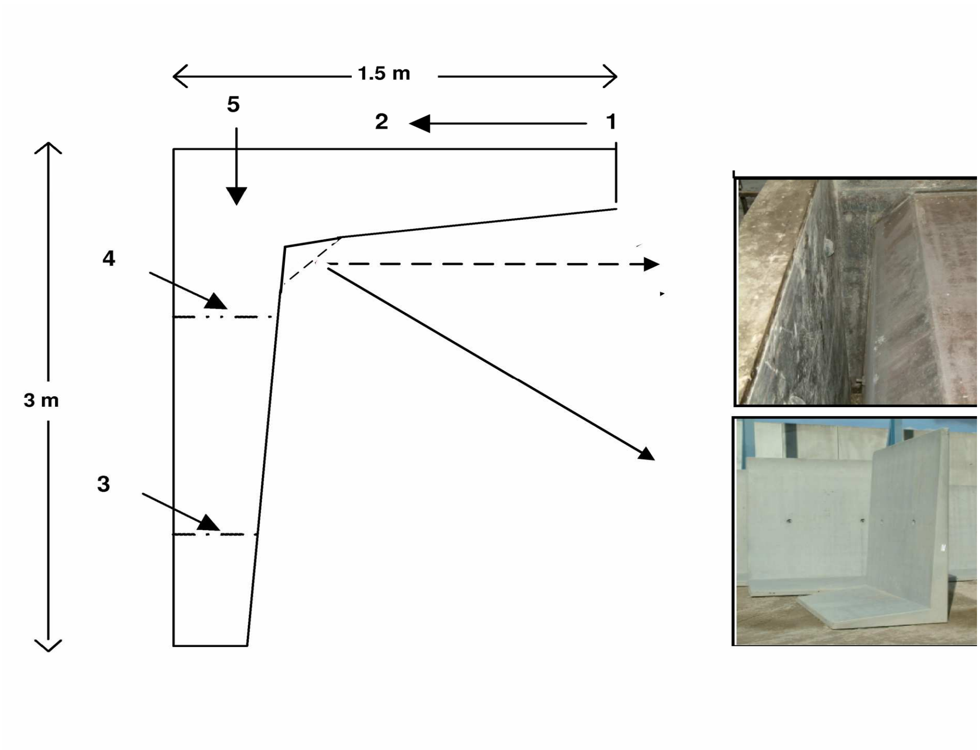

Figure 2.4 *Example of a vertical precast application. The numbers 1-5 refer to the filling procedure (see text). The bend and final element are shown to the right (Lauritsen & Thrane 2003).*

The second example is from a wall casting as part of a full-scale study of SCC for housing applications in Stockholm (see Figure 2.5)(Carlsward 2003). SCC was placed from the top of the formwork which introduced a free falling height of 2.5 m. A complete filling was not a problem due to the flexibility of positioning the inlet, the simple form geometry, and the light reinforcement configuration. However, for SCC with slump flow values of approximately $SF \sim 570$ mm more work was required to level off the upper surface. Compared to the first example (Figure 2.4), the free fall did not result in any clear signs of dynamic segregation.

The surface quality, though, was influenced by the casting technique. In the casting zone numerous surface pores were observed, which may have been due to the capture of entrapped air in the previous cast layers.

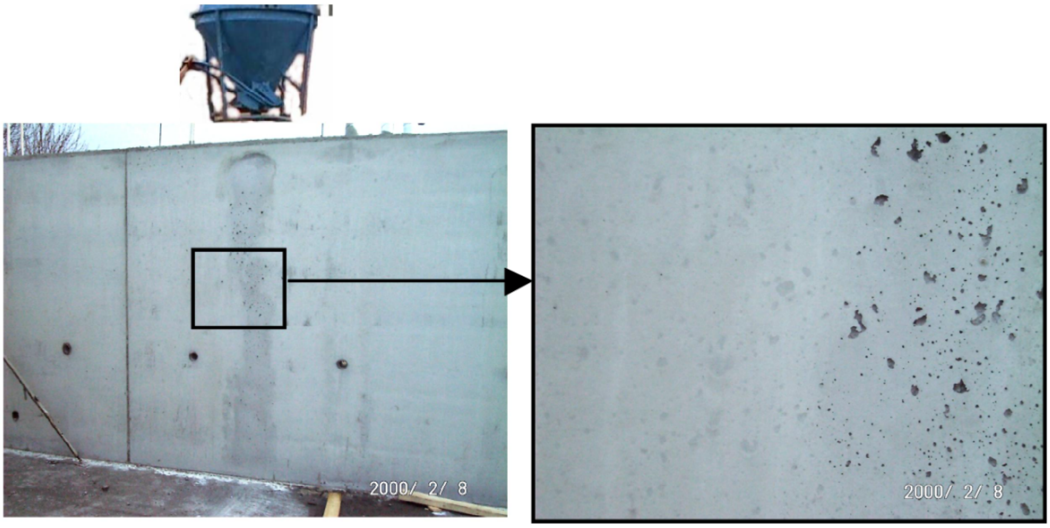

Figure 2.5 *Example of a wall cast with SCC in Stockholm (Carlsward 2003).*

2.3 Remarks on Self-Compacting Concrete Applications

The examples of applications presented illustrate some of the challenges of SCC in practice. The examples indicate that SCC castings are presently carried out based on individuals interpretation of qualitative experiences. On this point, the precast industry has an advantage e.g. as Skarendahl (2003) describes it: ”an indoor production of a repetitive nature with a personnel gaining experience through repetitive work under constant condition is likely to efficiently support the implementation of a new technology. Another important condition is that the organizational structure in pre-casting is such that a single actor normally is of full control from acceptance of a constituent material to the delivery of a finish component”.

However, valid quantitative experiences from trial and error can only be obtained and used when it is possible to measure and control the rheological properties from production to casting, and monitor the form filling characteristics. For instance, only the final slump flow (SF) was reported in the examples presented. It does relate to the yield stress, but no information is gained on the dynamics of flow. Rheological evaluations are still primarily used for research and development and not yet to any significant degree as a tool in quality assurance procedures (Skarendahl 2003). Improved test methods for assessment of the rheological properties will improve the quality control and make decisions less dependent on the experience of the personnel on site.

In mixers, most methods to assess the flow properties are based on measurements of the power consumption. However, a single power consumption value is also inadequate to address both the yield stress and the plastic viscosity. One measurement will neither give indication of the yield stress nor the plastic viscosity, and it is important to look into ways of measuring both parameters. Online control of the rheological properties will make it possible to adjust the mix continuously before released into the truck and reduce batch variations. Ongoing work on this subject is carried out within the framework of the Danish SCC-Consortium.

Chapter 3

Flow and Flow Properties of Self-Compacting Concrete

This Chapter discusses the flow and flow properties of SCC. The first part considers the flow and flow properties of homogenous suspensions, and the second part describes the possible heterogeneous flow phenomena in flow of suspensions.

The first part includes a

- general introduction to the rheology of suspensions introducing the viscosity function and the Bingham rheological model.
- description of the applicability of the Bingham model to describe the rheological properties of SCC in form filling simulations.
- description of the principles of measuring the rheological properties and the rheometer applied in this study.
- description of composite models for assessment of the rheological properties of suspensions.
- presentation of standard test methods and previous work on the relation between the results from these tests and the Bingham parameters, yield stress and plastic viscosity.

The second part includes the

- definition of blocking and a description of existing models to assess blocking of SCC and other types of suspensions.
- definition of dynamic segregation and a qualitative assessment of some likely causes for dynamic segregation, e.g. phase separation due to particle migration.

3.1 Homogeneous Suspensions

In this project the term suspension refers to a two-phase material consisting of particles suspended in a matrix phase compared to so-called ideal fluids which are single phase materials.

Assuming isothermal conditions, the viscosity and density define the properties of ideal fluids. Water, polymeric liquids, and oils may be thought of as ideal fluids. Suspensions, on the other hand, depend on the properties of the particles and matrix phase on a local scale. However, when the particles remain homogeneously distributed, suspensions are comparable to ideal fluids on a macroscopic scale for which reason the viscosity and density may also characterize the material properties of homogeneous suspensions.

Concrete can be regarded as a complex suspension, and in the next sections the Bingham rheological model is introduced and discussed in relation to SCC.

3.1.1 The Bingham Rheological Model

Rheology is the science of the deformation of flow of matter and it is concerned with relationships between stress, strain, rate of strain and time (Bird et al. 1987)(Tattersall & Banfill 1983).

The deviatoric stress tensor (τ_{ij}) of a viscous fluid is part of the total stress tensor (σ_{ij}) applied in the governing equation of motion (see Chapter 4). In arbitrary flow the deviatoric stress tensor (τ_{ij}) of an incompressible fluid is given by

$$\tau_{ij} = 2\eta\dot{\epsilon_{ij}} \tag{3.1}$$

where η is the viscosity function (apparent viscosity) and $\dot{\epsilon_{ij}}$ is the strain rate tensor given by

$$\dot{\epsilon}_{ij} = \frac{1}{2}\left(\frac{\partial u_i}{\partial x_j} + \frac{\partial u_j}{\partial x_i}\right) \tag{3.2}$$

where u_i are the components of the velocity vector, and x_i are the variables associated with the 1, 2, 3 axes, i.e. the x_1, x_2, x_3 are the Cartesian coordinates referred to as x, y, and z.

If the apparent viscosity is constant ($\eta = \mu$) the fluid is referred to as a Newtonian fluid (Bird et al. 1987).

If η is not constant, the fluid is referred to as a non-Newtonian fluid (Bird et al. 1987).

The generalized equation for the viscosity (η) incorporates the idea of a shear rate dependent viscosity and Equation 3.1 becomes

$$\tau_{ij} = 2\eta(\dot{\gamma})\dot{\epsilon_{ij}} \tag{3.3}$$

where $\dot{\gamma}$ is the shear rate (or magnitude of the strain rate tensor). The shear rate is given by

$$\dot{\gamma} = \sqrt{\tfrac{1}{2} II_{\dot{\epsilon}_{ij}}} \tag{3.4}$$

where the term $II_{\dot{\epsilon}_{ij}}$ is known as the second invariant of the strain rate tensor. In the same way the magnitude of the deviatoric stress tensor (shear stress) is given by $\tau = \sqrt{\frac{1}{2} II_{\tau_{ij}}}$ where $II_{\dot{\tau}_{ij}}$ is the second invariant of the deviatoric stress tensor.

Different viscosity functions have been proposed to describe the non-Newtonian rheological properties. One of them is the Bingham model with a yield stress (τ_0) and a plastic viscosity (η_{pl}). Applying a yield criterion, Equation 3.3 for a Bingham plastic law can be written

$$\begin{aligned} \tau_{ij} &= 2\eta(\dot{\gamma})\dot{\epsilon_{ij}} & \\ \tau_{ij} &= 2\left(\frac{\tau_0}{2\dot{\gamma}} + \eta_{pl}\right)\dot{\epsilon_{ij}} & \text{if } \tau > \tau_0 \\ \dot{\epsilon_{ij}} &= 0 & \text{if } \tau \leq \tau_0 \end{aligned} \tag{3.5}$$

where $\eta = \frac{\tau_0}{2\dot{\gamma}} + \eta_{pl}$ is the apparent viscosity of a Bingham fluid (Hohenemser & Prager 1932)(Oldroyd 1947)(White 1977).

In pure shear flow, e.g. two parallel plates move relatively to each other as shown in Figure 3.1, the only non-zero components of the deviatoric stress and strain rate tensor are τ_{xy} and $\dot{\epsilon}_{xy}$, respectively.

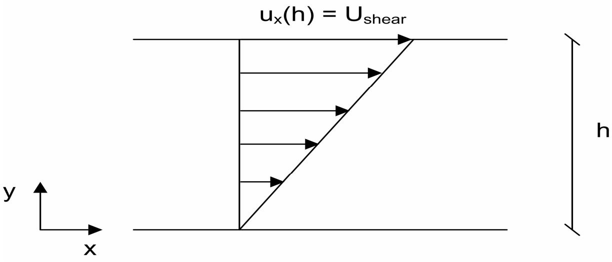

Figure 3.1 *Illustration of pure shear flow between two parallel plates separated by a distance of h where the upper plate moves at constant velocity U_{shear} (Bird et al. 1987).*

Thus, $\dot{\gamma} = \dot{\epsilon}_{xy} = \frac{1}{2}\frac{V}{h}$, and $\tau = \tau_{xy}$. Inserting this into Equation 3.5 gives

$$\begin{aligned} \tau_{xy} &= \tau_0 + 2\eta_{pl}\dot{\gamma} && \text{if } \tau \geq \tau_0 \\ \tau_{xy} &= \tau_0 + \eta_{pl}\frac{U_{shear}}{h} && \text{if } \tau \geq \tau_0 \\ \dot{\epsilon}_{xy} &= 0 && \text{if } \tau < \tau_0 \end{aligned} \tag{3.6}$$

which is a form often seen in the literature when referring to a Bingham fluid.

3.1.2 Applicability of the Bingham Model to describe the Rheological Properties of Self-Compacting Concrete

A wide number of studies have been carried out on the rheological properties of cementitious materials, and some of the initial studies can be found in (Tattersall 1955) and (Uzomaka 1974).

In general, cementitious materials exhibit shear rate and time-dependent behaviour, i.e. the cement paste undergo a structural built-up and break down of particle clusters when it is subjected to deformation and is left at rest, respectively. When the progress of break down and rebuilt is fully reversible, it is referred to as thixotropy (Tattersall 1955)(Tattersall & Banfill 1983)(Cheng 1987)(Barnes 1997)(Hackley & Ferraris 2001)(Billberg 2006).

Subjecting a cement paste to a given shear rate the shear stress depends on the interparticle forces and the energy being put into breaking down the structure. The net force between particles is a function of particle size, surface properties, and shape (Wallevik 2003*a*)(Flatt 2004*b*).

In SCC both the superplasticizer and the aggregate tend to reduce the thixotropic behaviour. The superplasticizer creates a better deflocculation between the colloid and cement particles as mentioned in Section 1.1. For instance, Fernandez-Altable & Casanova (2006) found that increasing the superplasticizer dosage from 0.2 to 0.9 % (weight of cement), the thixotropic behaviour would decrease 50 %. The thixotropic behaviour was quantified as the integrated area between the upwards and downwards shear stress-strain rate curves. By adding aggregates to the cement paste the shear rate of the cement paste increases on a local scale, which has a positive effect on breaking down the structure of the cement paste (Helmuth, Mills, Whiting & Bhattacharja 1995)(Banfill 2003). The macroscopic and local velocity field are shown in Figure 3.2.

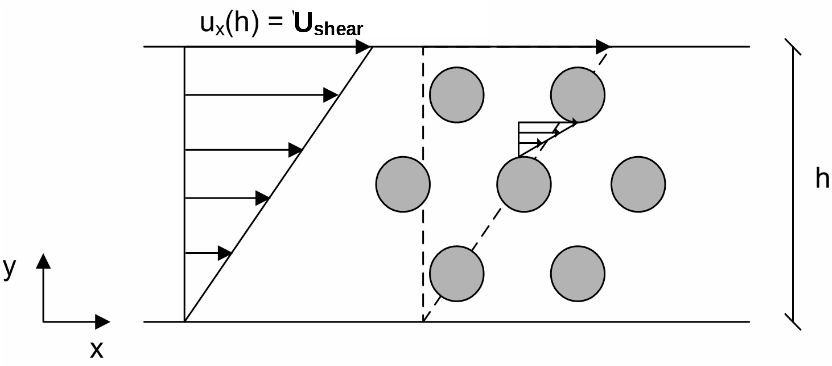

Figure 3.2 *Illustration of a monodisperse suspension of spherical particles subjected to pure shear flow between two parallel plates separated by a distance of h where the upper plate moves at constant velocity U_{shear}. The local shear rate in the matrix phase is higher than the macroscopic shear rate and depends on the distance between the particles.*

Studies of the rheological properties of SCC and concrete in general have focused on the Bingham and the Herschel-Bulkley model respectively, see e.g. (Tattersall & Banfill 1983), (Hu & Larrard 1996), (Larrard, Ferraris & Sedran 1998), (Geiker, Brandl, Thrane, Bager & Wallevik 2002), (Beaupre, Chapdelaine, Domone, Koehler, Shen, Sonebi, Struble, Tenke, Wallevik & Wallevik 2003), (Nielsson & Wallevik 2003), (Banfill 2003), and (Wallevik 2003*b*). The Herschel-Bulkley equation has been applied to describe shear thickening behaviour by introducing a power law exponent to the strain rate of the Bingham model.

An overview of the measured values of yield stress and plastic viscosity of SCC at steady state has been presented by Wallevik (2003*b*). The measurements were conducted on SCC in eleven countries using a co-axial viscometer (the BML viscometer, see Section 3.1.4). The results show a yield stress range of approximately 0 to 80 Pa and a plastic viscosity range of approximately 20 and 150 Pa·s.

However, the Bingham parameters depend on the viscometer applied, which was shown in comparative studies carried out in 2000 and 2003, and reported in (Ferraris, Brower, Banfill, Beaupre, Chapdelaine, de Larrard, Domone, Nachbaur, Sedran, Wallevik & Wallevik 2000) and (Beaupre et al. 2003). In general, it was shown that the rheometers gave different values of the yield stress and plastic viscosity, and it was concluded that more research is needed to obtain a good correlation between any two rheometers. Especially, the plastic viscosity cannot be easily and uniquely measured (Ferraris & Martys 2003). Instead it was found that the relative plastic viscosity does not seem to depend on the geometry of the rheometer, but only on the amount of coarse aggregate that was added to the matrix. Therefore, the relative plastic viscosity may be used to compare data from various instruments even when a calibration with a standard material is not available and the results from the rheometers are given in different units (Ferraris & Martys 2003)(Tattersall & Banfill 1983).

The Bingham model describes the steady state relation between shear stress and strain rate. In order to describe the transient shear stress-strain rate relation, analytical models have been proposed based on the general concept of a scalar structure parameter, first introduced by Moore (1959) to explain flow behaviour of ceramic pastes (Mujumdar, Beris & Metzner 2002). The Moore model was extended by Worrall & Tuliani (1964) to account for yield stress during their study of aging phenomena in clay-water suspensions. Cheng & Evans (1965) generalized the Moore model and developed conditions for thixotropy and antithixotropy. Based on this model, Coussot, Nguyen, Huynh & Bonn (2002) proposed a four parameter phenomenological model for a Hershel-Bulkley material based on the structure parameter. It proved to provide a good qualitative and to some extent quantitative description of the response of typical paste materials in a co-axial viscometer (Roussel, Roy & Coussot 2004)(Roussel 2005). However, due to the low number of parameters it was not possible to quantify the structuration state at rest, and a fifth parameter was therefore proposed to the model.

Recently, Roussel (2006*b*) extended the thixotropic model to a Bingham material to include the most important aspects of thixotropy in relation to SCC casting; the flocculation state at rest given by the flocculation state parameter, and the deflocculation during flow given by an index parameter included in a decaying exponential function fitted from shear stress measurements at constant shear rate. Flocculation during flow is neglected as it is assumed that the characteristic time of flocculation is long compared to the characteristic time of deflocculation (Papo 1988).

As Roussel (2006*b*) points out, most interest to practical applications is the understanding and measuring of the flocculation state parameter at rest. Billberg (2005) developed a new methodology to measure the so-called static yield stress which relate to the flocculation state parameter at rest, and showed that the static yield stress is a linear function of the resting time. For tests on twelve mixes the static yield stress was found to increase at a rate ranging from 42 to 80 Pa/min. Increasing the static yield stress can have a positive effect on lowering the form pressure (Billberg 2006)(Leemann, Hoffmann & Winnefeld 2006). Today, it is recommended to apply a hydrostatic pressure loading condition, which means that is often necessary to enhance the stress capacity of existing formworks (Glavind & Frederiksen 2001)(Billberg & Osterberg 2002).

Ovarlez & Roussel (2006) proposed a theoretical model for the formwork pressure based on the flocculation rate at rest, and it was found that the model corresponded well to the results found in (Assaad, Khayat & Mesbah 2003) and (Billberg 2003). On the other hand, Roussel (2006*b*) showed that an increase in the static yield stress has a negative effect in discontinuous castings e.g. delay between truck arrivals, which can result in a poor mixing of cast layers.

Another approach to model the thixotropic behaviour of cement paste was given by Wallevik (2003*a*) based on the comprehensive flocculation/dispersion theory by Hattori & Izumi (1990). The transient shear stress-shear rate relation in a co-axial viscometer was predicted from numerical simulations where the flow history is taken into account using fading memory integrals. Five parameters goes into the numerical model which are fitted using the numerical simulations.

In summary, the Bingham model seems applicable for describing the steady state relation between shear stress and strain rate and recently a model has been proposed to describe the transient behaviour. However, if the flocculation rate during flow can be neglected compared to when at rest, and the characteristic time of deflocculation is relatively low, it may be assumed that that the rheological properties of SCC remain unaffected by thixotropy during continuous castings. Therefore, as a first approximation to the simulation of the form filing ability and flow patterns, it seems reasonable to assume an ideal Bingham behaviour. However, in discontinuous castings, the thixotropic behaviour has to be taking into account as shown by Roussel (2006*b*).

3.1.3 Composite Models on the Rheological Properties

The development of models to predict form filling with SCC based on the rheological properties and casting technique provide a tool to assess the most appropriate rheological parameters for a given form filling application. Therefore, it becomes increasingly important to be able to predict the rheological properties in the mix design phase.

Predicting the rheological properties of concrete is a complicated task because particles cover a wide range of particle sizes ranging from the sub-micron scale to the millimetre scale (colloid particles to coarse aggregate), and the macroscopic response of a suspension is a result of many different types of forces within the suspension. The importance of these forces depend on the scale of matter and are discussed in details in Flatt (2004*b*) and Coussot & Ancey (1999). The forces of the system include gravity, inertia, viscous drag, dispersion (van der Waals), electrostatic, and Brownian forces. For the colloid particles (silica fume) and the cement particles the dominant forces are the dispersion (van der Waals), electrostatic, and Brownian forces as well as gravity is of importance to the cement particles depending on the separation distance between the particles. Gravity, viscous forces, and inertia are of most importance to the aggregates.

From a modelling point of view, the composite theory is one way to approach the rheology of suspensions. It assumes that a suspension can be divided into a particle phase and a matrix phase.

In the classic composite theory the suspension is considered to consist of hard non-interacting spheres where the surface forces between the particles are neglected. However, when the surface forces become relevant these may cause flocculation of the particles causing a change in the geometrical configuration of the particles and a physically different system (Buscall, Mills, Stewart, Sutton, White & Yates 1987)(Kapur, Scales, Boger & Healy 1997)(Scales, Johnson, Healy & Kapur 1998)(Zhou, Solomon, Scales & Boger 1999)(Flatt 2004*b*). Furthermore, it is assumed that the interaction between the particles in the suspension and matrix phase is purely viscous, i.e. the matrix rheology remain undisturbed by the particles of the suspension. This is of concern when the matrix phase itself includes particles. This may be compared to the situation of measuring the viscosity of a particle suspension in a viscometer where the gap somewhat corresponds to the distance between the particles of the suspension. According to Barnes (1995) it is often recommended as a "rule of thumb" to apply a ratio of particle size to gap size in a viscometer of 1 to 10.

Assuming that the surface forces between particles are negligible, Einstein was the first to propose a relation for the Newtonian viscosity (μ_s) of a suspension of hard spheres at very low volume fractions ($\phi_p < 0.03$) given by

$$\mu_s = \mu_m(1 + 2.5\phi_p) \tag{3.7}$$

where μ_m is the Newtonian viscosity of the matrix phase.

Equation 3.7 is only valid when the suspension is dilute enough so the flow field around one sphere is not influenced by the neighboring spheres, and later the Krieger-Dougherty equation was proposed as a general empirical expression for the apparent viscosity of suspensions (η_s) (Krieger 1972)(Larson 1999). For a Newtonian suspension the apparent viscosity $\eta_s = \mu_s$. Otherwise the apparent viscosity depends on the applied shear rate. The Krieger-Dougherty relation is given by

$$\eta_s = \eta_m \left(1 - \frac{\phi_p}{\phi_p^*}\right)^{-[\eta]\phi_p^*} \tag{3.8}$$

where ϕ_p^* is the maximum particle volume fraction, and $[\eta]$ is the so-called intrinsic viscosity.

The maximum particle volume fraction (ϕ_p^*) represents the particle volume fraction in a packed bed after a given process of packing the particles, and depends on the shape and polydispersity of the particles. For instance, for monodisperse spheres the packing degree range from 0.06 for the loosest possible packing, 0.52 for simple cubic packing, and 0.74 for the theoretical cubic close packing (face-centered) (Gardner 1966)(Steinhaus 1999). A random close packing of monodisperse spheres is approximately 0.64 (Jaeger & Nagel 1992). As the maximum particle volume fraction depends on the energy put into the process of packing the particles it is also a function of the shear rate applied in a viscometer (Krieger 1972)(Larrard 1999).

The intrinsic viscosity $[\eta]$ is a measure of the effect of individual particles on the viscosity and depends on the shape of the particles (Krieger 1972)(Struble & Sun 1995). Hinch & Leal (1972) studied the variation in the intrinsic viscosity as a function of shear rate. They found that the intrinsic viscosity does not vary with the shear rate level for spherical particles compared to other particle shapes.

According to Equation 3.8 the apparent viscosity of a suspension increases as a function of the particle volume fraction ϕ_p until the maximum particle volume is reached (ϕ_p^*), and the viscosity goes toward infinity. Qualitatively, this may be explained by more interactions between particles and the generation of higher shear rates in the matrix under a given macroscopic shear rate (see Figure 3.2). According to Frankel & Acrivos (1967), the latter is the main contribution to the viscous dissipation of suspensions.

Equation 3.8 has showed to correlate well with the experimental data for monodisperse model suspensions see, e.g. (Papir & Krieger 1970), (Woods & Krieger 1970), (Kruif, van Iersel, Vrij & Russel 1985), and (Candau, Buchert & Krieger 1990).

According to a summary of experimental studies given by Barnes, Hutton & Walters (1989), the maximum particle fraction varies approximate between 0.60 and 0.70 for monodisperse spherical particles, and the intrinsic viscosity is approximately 2.5 for spherical shaped particles, and in the range of 3.0 to 5.0 for angular shaped particles.

Recently, Ovarlez, Bertrand & Rodts (2006) studied non-colloidal monodisperse spherical particles (d_p = 0.30 mm) immersed in a Newtonian fluid (silicone oil) at particle volume fractions from 0.55 to 0.60. From measurements in a Couette viscometer they found the Krieger-Dougherty relation to fit the experimental results when using values of 0.603 and 2.5 for the maximum particle volume fraction and the intrinsic viscosity, respectively. This corresponds to the previous results for monodisperse suspensions with spherical particles. However, the study focused on measuring in detail the velocity and particle volume fraction profiles in the gap between the inner and outer cylinder using magnetic resonance imaging (MRI) techniques. The particle volume fraction throughout the gap varies from the average macroscopic particle volume fraction as a result of shear induced particle migration (see Section 3.2.2). Correlating the measurements of the particle volume fraction and shear rate on a local scale to the macroscopic measurements, they found that a Krieger-Dougherty relation applies when using a maximum packing fraction of almost the same value of 0.605, but an intrinsic viscosity of 3.3.

An example of a study on the apparent viscosity in which the surface forces are not negligible can be found in Struble & Sun (1995). Three types of cement were applied and samples were prepared at similar water cement ratios. To study the effect of surface forces, superplastixser were added to one of two identical samples in order to obtain a fully dispersed and flocculated system, respectively. Tests were carried out at particle volume fractions from approximately 0.45 to 0.60. It was found that the Krieger-Dougherty relation described the results well with water as the matrix phase. For instance, for one type of cement the fitted values of the maximum particle volume fraction and the intrinsic viscosity were 0.76 and 6.2 for the dispersed system, and 0.64 and 6.3 for the flocculated system. Thus, the intrinsic viscosity is almost the same in the two systems, however, dispersion of the cement has a positive effect on the maximum particle volume fraction. The particle shape and particle size distribution of the cement have not been reported, and as the authors note more research is needed to compare the intrinsic viscosity fitted in these studies to the values found for model systems, e.g. 2.5 for spherical shaped particles.

In general, the Krieger-Dougherty relation have proved to describe the apparent viscosity of different systems as a function of the matrix viscosity, the particle volume fraction, the maximum particle volume fraction, and the intrinsic viscosity. For monodisperse model systems, it seems that the intrinsic viscosity is somewhat constant, e.g. 2.5 for spherical particles, though, results by Ovarlez et al. (2006) have indicated a higher value from studies of the local particle volume fraction and velocity field in the gap in a co-axial viscometer. The maximum particle volume fraction depends on the energy put into the process of packing the particles, and the fitted values of the maximum particle volume fraction are within the theoretical close packing densities for monodisperse spheres ranging from 0.52 to 0.74.

Some examples of the Krieger-Dougherty relation are shown in 3.3.

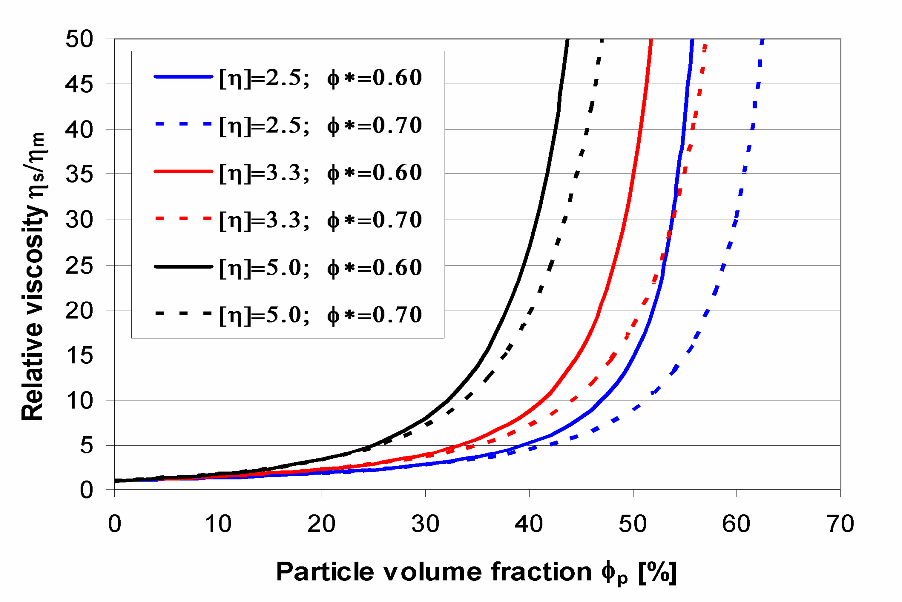

Figure 3.3 *The Krieger-Dougherty relation for the relative viscosity (η_s/η_m) as a function of the particle volume fraction ϕ_p. It is shown for three values of the intrinsic viscosity $[\eta]$ = 2.5, 3.3, and 5.0, and two values of the maximum particle volume fraction ϕ_p^* = 0.60 and 0.70.*

It shows the relative apparent viscosity as a function of the particle volume fraction for three values of the intrinsic viscosity (2.5, 3.3, and 5.0) and two values of the maximum particle volume fraction (0.60 and 0.70). It shows that the relative apparent viscosity increases when increasing the intrinsic viscosity (shapes different from the spherical shape) and/or decreasing the maximum particle volume fraction.

As mentioned, the Krieger-Dougherty relation describes the apparent viscosity and for non-Newtonian suspensions the apparent viscosity is a function of the shear rate. Inserting the apparent viscosity of the Bingham model in Equation 3.8, it is possibly to derive expressions for the constitutive Bingham parameters yield stress and plastic viscosity assuming that also the matrix phase follows a Bingham plastic law. This gives

$$\eta_{s,pl} + \frac{\tau_{s,0}}{2\dot{\gamma}} = \left(\eta_{m,pl} + \frac{\tau_{m,0}}{2\dot{\gamma}}\right)\left(1 - \frac{\phi_p}{\phi_p^*}\right)^{-[\eta]\phi_p^*} \tag{3.9}$$

where the apparent viscosity of the suspension and matrix are $\eta_s = \eta_{s,pl} + \frac{\tau_{s,0}}{2\dot{\gamma}}$ and $\eta_m = \eta_{m,pl} + \frac{\tau_{m,0}}{2\dot{\gamma}}$, respectively (see Equation 3.5).

The plastic viscosity ($\eta_{s,pl}$) is found by letting the shear rate go towards infinity. This gives

$$\eta_{s,pl} \quad = \quad \eta_{m,pl}\left(1-\frac{\phi_p}{\phi_p^*}\right)^{-[\eta]\phi_p^*} \qquad \text{for} \qquad \dot{\gamma}\rightarrow\infty \tag{3.10}$$

which inserted in Equation 3.9 gives a similar relation for the yield stress:

$$\tau_{s,0} \quad = \quad \tau_{m,0}\left(1-\frac{\phi_p}{\phi_p^*}\right)^{-[\eta]\phi_p^*} \tag{3.11}$$

Thus, inserting the Bingham model in the Krieger-Dougherty equation yields similar expressions for the relative plastic viscosity and the relative yield stress.

The Krieger-Dougherty relation is probably the most general composite model describing the rheology of suspensions. Later, other models have been proposed for the Bingham parameters yield stress and plastic viscosity based on the principles of the composite theory, e.g. Larrard (1999), Oh, Noguchi & Tomosawa (1999), and Nielsen (2003). These expressions show the same fundamental relations for the plastic viscosity and yield stress as Equation 3.10 and 3.11, e.g. the plastic viscosity and yield stress increase as a function of the particle volume fraction and for shapes different from the spherical shape.

Larrard (1999) has proposed expressions for the plastic viscosity and yield stress based on the so-called compressible packing model. The compressible packing model is a extension of the so-called linear packing model developed to calculate the packing density of polydisperse grain mixtures (Stovall, Larrard & Buil 1986). The compressible packing model takes into account the energy put into the compaction of the particles. For the plastic viscosity a semi-empirical expression was proposed as

$$\eta_{s,pl} \quad = \quad \exp\left(C_1\left(\frac{\phi_p}{\phi_p^*}-C_2\right)\right) \tag{3.12}$$

where C_1 and C_2 are fit parameters determined from experimental calibration. Based on experimental results from mortars and concrete with and without superplasticizer, it was found that $C_1 = 26.75$ and $C_2 = 0.7448$ resulted in a mean error of 61 Pa·s.

For the yield stress, an expression was proposed as $\tau_{s,0} = \exp\left(\sum_{i=1}^{n} a_i K_i\right)$ where $K_i = \frac{\phi_{p,i}/\phi_{p,i}^*}{1-\phi_{p,i}/\phi_{p,i}^*}$ is the contribution of particle size fraction i to the so-called compaction index K, and a_i is a coefficient which is supposed to increase when the particle diameter ($d_{p,i}$) decrease. Using experimental data of 25 mixtures, containing a saturation dosage of superplasticizer, fitted values of a_i were found to give an expression of the yield stress by

$$\tau_{s,0} \quad = \quad \exp(2.537 + 0.540K_g + 0.854K_s + 0.224K_c) \tag{3.13}$$

where K_g, K_s, and K_c are the contribution to the compaction index from the gravel, sand, and cement. The mean error between the predictions and the experiments is equal to 177 Pa, and according to the authors further experimental validation and developments are needed.

Oh et al. (1999) evaluate the relative Bingham parameters as a function of the so-called relative thickness of excess paste (Γ), which takes into account the relative particle volume fraction and the particle shape. Based on experimental calibration they found

$$\begin{aligned} \eta_{s,pl} &= \eta_{m,pl}\,(0.0705\,\Gamma^{-1.69}+1) \\ \tau_{s,0} &= \tau_{m,0}\,(0.0525\,\Gamma^{-2.22}+1) \end{aligned} \tag{3.14}$$

where the relative thickness of excess paste $\Gamma = \frac{1-\frac{\phi_p}{\phi_p^*}}{f/k\cdot\phi_p}$, and f/k is the so-called shape factor. Theoretically the shape factor is the specific surface area of a particle with a projected diameter of 1. Thus for spheres, $f/k = 6$, and larger for angular and irregular shapes.

The model by Oh et al. (1999) have also been applied by (Hasholt, Pade & Winnefeld 2005) in studies of SCC when using the cement paste as the matrix phase providing other suggestions for the fit parameters.

Nielsen (2003) has proposed models for the relative Bingham parameters on the basis of the maximum particle volume fraction and the particle geometry. The expressions are given by

$$\begin{aligned} \eta_{s,pl} &= \eta_{m,pl}\left(\frac{1+\varrho_\infty\phi_p}{1-\phi_p}\right) \\ \tau_{s,0} &= \tau_{m,0}\left(\frac{1+\varrho_\infty\phi_p}{1}\right) \end{aligned} \tag{3.15}$$

where ϱ_∞ is the so-called geometry function, which is expressed in terms of the so-called shape factors, the shape function power index, the particle volume fraction, and the maximum particle volume fraction. The shape factors depend on the aspect ratio of the particles which is 1 for spheres. Experiments were carried out in Geiker, Brandl, Thrane & Nielsen (2002) in studies of SCC when using the mortar phase as the matrix phase. It was found that the experimental results could be simulated when using fitted values of the aspect ratio and the power shape index. The best correlation between the theoretical estimate and the experimental results was found using glass bead particles where the plastic viscosity was fitted reasonable well when using the theoretical values of the aspect ratio (value of 1) and the power shape index (value of 1).

As previously mentioned, the applicability of a composite model depends on the choice of matrix phase, e.g. water, cement paste, and mortar may be applied as the matrix phase. For the yield stress, a composite model only makes sense over the cement paste scale as water have a zero yield stress value. The yield stress of cement pastes depend on the structural arrangement of the particles, and the nature and magnitude of the surface forces operating between them. Modelling of the yield stress of cement paste has to take into account the surface forces and fundamental modelling approaches, and experimental studies can be found in Buscall et al. (1987), Kapur et al. (1997), Scales et al. (1998), Zhou et al. (1999), and Flatt (2004*b*).

Buscall et al. (1987) carried out extensive studies of the shear rheology, sedimentation behaviour, and compressibility of strongly flocculated dispersions of colloid particles at various particle volume fractions and particle size. Suspensions consisted of monodisperse polystyrene lattices of particle diameter 0.49 to 3.4 μm at particle volume fractions between 0.05 and 0.25. Results for the shear yield stress show that the yield stress increases for increasing particle volume fractions and decreasing particles sizes. At low particle volume fractions, the flocs of particles are discrete but above a critical particle volume fraction continuous networks start to form. This critical particle volume fraction is strongly dependent on the size (and shape) of the particles.

Kapur et al. (1997) developed a model for the yield stress of concentrated, flocculated particulate suspensions at the isoelectric point, i.e. the net surface charge on the particle is zero (no repulsive interaction between the particles) and the interparticle forces are dominated by the van der Waals forces. The final expression for the yield stress is given as a function of generally accepted values of the Hamaker constant, a so-called coordination number of the particle, the surface separation distance between two particles, and the particle size distribution. The coordination number and the surface separation distance between two particles are both functions of the particles volume fraction. For the coordination number, the linearly increasing relationship of Gotoh is applied (Suzuki, Michitaka, Yamada & Iinoya 1981). For the surface separation distance, a constant value times the so-called crowding factor is proposed. The constant value represents the closest distance between particles and the crowding factor is a function of the particle volume fraction. The crowding factor decreases toward unity at the maximum particle volume fraction. When using experiments to fit the constant value and the function for the crowding factor, the model is in reasonable agreement with the experimental results of flocculated suspensions at the isoelectric point.

The model by Kapur et al. (1997) was further developed by Scales et al. (1998) to include the effect of charges of the particles and thereby include the repulsive interaction between particles. Zhou et al. (1999) compared experimental results of alumina suspensions with the model predictions by Kapur et al. (1997) and Scales et al. (1998). Tests were carried out for different particle size distribution at the vicinity of the isoelectric point and for a range of particle volume fractions. They found a reasonable agreement between the models and the test results below a particle volume fraction of 0.42 where the surface forces dominate the yield stress. The deviations between the model predictions and the experimental results were explained in terms of network structural effects and a simplified yield stress model was proposed.

Recently, Flatt (2004*b*) presented a yield stress model of suspensions taking into account the effect of steric stabilization which has become important with the development of the "new generation" of superplastizizers. The model predicts the yield stress as a function of the particle volume fraction, the maximum particle volume fraction, a so-called particle volume percolation threshold, and a prefactor that is a function of the volume mean particle size, the particle size distribution, and the interparticle force parameter. When using fitted values of the percolation threshold, a reasonable agreement between experimental results of cement paste and the model was obtained. However, it was concluded that further research are needed for ways to predict and measure the percoloation threshold value.

In summary, different composite models have been proposed to predict the rheological properties of suspensions as a function of the rheological properties of the matrix phase and the particle configuration (particle volume fraction, maximum particle volume fraction, and shape). These expressions assume that surface forces can be neglected and possible surface forces are included in the properties of the matrix phase, which need to be determined from experiments or estimated from models. The Krieger-Dougherty relation have been extended to a Bingham material, and other models proposed for estimation of the yield stress and plastic viscosity have been presented. Experimental verifications show that fitting of parameters are needed to some extend, and it is important to note that fit parameters depend on the choice of materials and the rheometers applied in the experiments. However, for perfect model systems, the Krieger-Dougherty relation have been found to express the apparent viscosity reasonable well.

The composite modelling concept breaks down when estimating the yield stress of cement paste where the surface forces dominate, and different models have been proposed. In the future, the combined use of composite models and a yield stress model for the cement paste may provide a complete theoretical tool to determine both the plastic viscosity and yield stress of SCC.

3.1.4 Rheological Measurements

In different types of flow domains, it is possible to apply the constitutive law to the governing flow equations and analytically derive the velocity field, e.g. pipe flow, tangential annular flow, flow between parallel planes, cone and plate etc (Bird et al. 1987).

In a rheometer, based on one of these principles, it is possible to derive the rheological parameters in fundamental units from measurements of the stress - strain rate relation.

Different types of commercial rheometers have been developed to measure the rheological properties of cement pastes and concrete.

For instance, the BTHRHEOM rheometer applies the parallel-plate geometry, and the CEMAGREF-IMG and BML rheometers apply the co-axial cylinder geometry (Ferraris et al. 2000).

Other rheometers such as the IBB rheometer and the Two-Point rheometers are based on rotating an impeller in fresh concrete contained within a cylindrical vessel. The flow patterns are not easily modelled, and to give rheological properties in fundamental units calibration with known fluids are needed (Tattersall & Banfill 1983)(Ferraris et al. 2000).

Some of the important aspects of experimental rheology include:

- Plug flow:
  - If the material exhibits yield stress behaviour, a plug flow may occur when the shear stresses in the material become lower than the yield stress. The equations typically used to derive the rheological properties assume that the material is fully subjected to shear. For instance, Wallevik (1998*a*) studied plug flow behaviour in a co-axial viscometer, and an iterative scheme was proposed to handle plug flow. However, it is preferable to avoid plug flow by applying sufficient deformation rates that ensures a complete shear of the material.
- Slip:
  - The governing flow equations used to derive the rheological properties assume a no-slip condition between the fluid and the solid boundaries of the flow domain. Slip may occur if the boundary layer is not representative of the bulk material properties (Bird et al. 1987).
- Thixotropy:
  - If the fluid exhibits thixotropic behaviour, this should be taking into account in the measuring procedure. The ideal rheological behaviour refers to rheological parameters derived from steady-state stress - strain rate relations (Tattersall & Banfill 1983). For instance, in Geiker, Brandl, Thrane & Nielsen (2002) it was shown that the apparent shear thickening behaviour obtained in previous investigations on SCC may be due to the lack of steady state.

In this project measurements of the rheological properties have been measured using the BML viscometer based on the co-axial cylinder principle (Wallevik 1998*b*), which is shown in Figure 3.4.

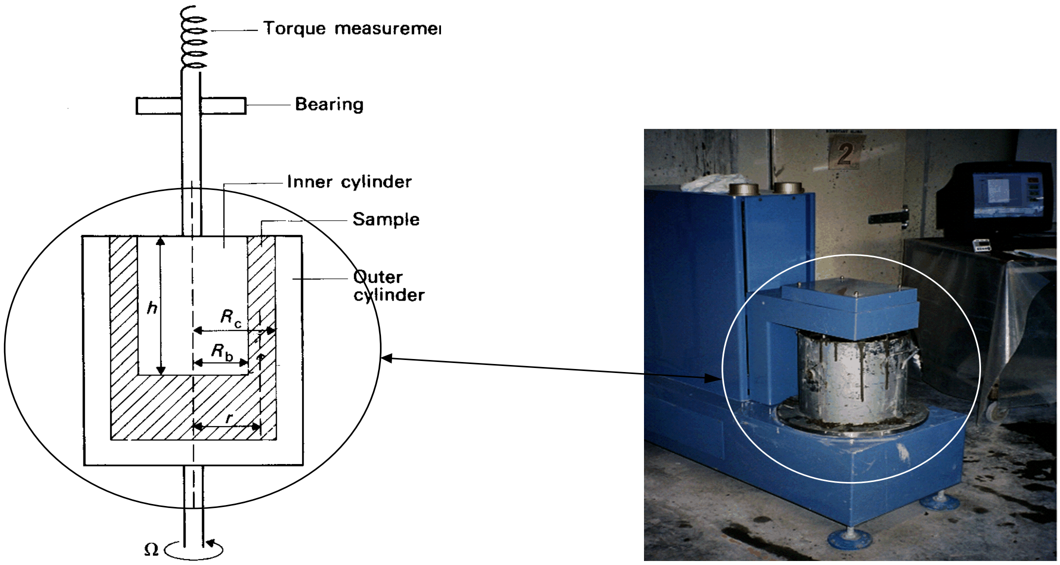

Figure 3.4 *Illustration of the geometry of a co-axial rheometer to the left (Tattersall & Banfill 1983) and the BML rheometer to the right applying this principle (Wallevik 1998*b*).*

It consists of two cylinders mounted co-axially, and the gap between them is filled with material. The outer cylinder is rotated at a known angular velocity with the result that the inner cylinder also tends to turn because of the viscous drag exerted by the material. The torque required to prevent it from turning is measured. The torque as a function of time is measured for selected rotation velocities. For a Bingham fluid the relation between the torque and angular velocity of the outer cylinder is given by the so-called Reiner-Riwlin equation which gives a means for determining the yield stress and the plastic viscosity (Reiner & Riwlin 1927).

3.1.5 Standard Test Methods

In general, standard test methods are widely used in various industries for assessment of the workability of suspensions due to their low costs and easiness of use.

One of the most used test methods for strongly flocculated suspensions like conventional concrete is the slump test. A container (cone or cylinder) is placed on a plate and filled with the material. After lifting the container, the material deforms (see Figure 3.5). In strongly flocculated suspensions the slump (SL) is measured. However, when the deformability is increased, the focus changes from slump to spreading flows where also the transient deformation is widely important for description of the flow properties. In concrete testing, the Abrams cone is widely used ($H = 300$ mm, $R_1 = 50$ mm, and $R_2 = 100$ mm). Typically the slump (SL) is measured if it is smaller than 250 mm, otherwise the slump flow (SF) is measured (Roussel & Coussot 2005). For characterization of the transient flow, it has been proposed to measure the time to reach a diameter of 500 mm (the so-called T50 value) (Efnarc 2002). Other cone dimensions have been applied to test pastes, e.g. the mini-cone ($H = 50$ mm, $R_1 = 35$ mm, and $R_2 = 50$ mm).

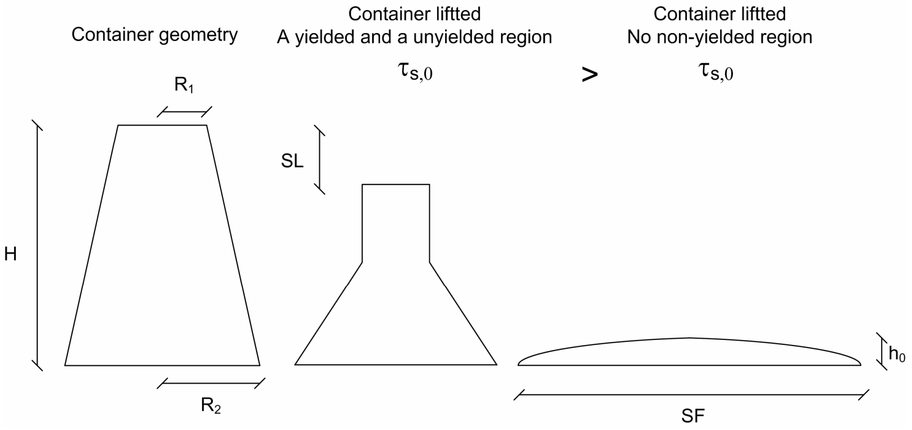

Figure 3.5 *Illustration of the principles of the slump and slump flow test, respectively. Lifting the container, the material deforms and the shape of deformation is directly related to the yield stress when neglecting inertia. The slump (SL) is measured at high yield stresses and the slump flow (SF) is measured at low yield stresses.*

In general, much work has been carried out on linking the yield stress to the stoppage shape of the deformed material as knowledge of the yield stress is essential in engineering design and operation where the handling and transport of industrial suspension are involved (Pashias, Boger, Summers & Glenister 1996). When it is possible to neglect inertia and surface forces, the final shape of a stoppage flow test is directly linked to the yield stress.

The work include analytical derivations, numerical simulations, and empirical expressions.

The relations are often presented as dimensionless slump (SL^*) versus dimensionless yield stress. The slump is normalized by the height of the container, $SL^* = SL/H$, and the yield stress is normalized as $\tau_0^* = \tau_0/\rho_s g H$, where ρ_s is the density and g is the gravity.

For yield stresses in the range of 0-100 Pa and a density of 2300 kg/m^3, this corresponds to a dimensionless yield stress of approximately 0 - 0.015. For flocculated suspensions the yield stress is much higher ($\tau_0 > 1000$ Pa) leading to a dimensionless yield stress of approximately 0.150 - 0.400.

Murata (1984) was the first to study the deformation of concrete due to its own weight in a slump test of cone shape ($R_2 = 2R_1$). It was assumed that the two-dimensional deformation of the material can be divided into a yielded and a non-yielded region as shown in Figure 3.5. The yielded region deforms until the shear stress acting on the cross-sectional area is higher than the yield stress. When the shear stress equals the yield stress, the flow stops. Based on these assumptions, a relation was derived between the slump, yield stress, height, and density.

Similar assumptions were applied by Christensen (1991), Pashias et al. (1996), Schowalter & Christensen (1998), Clayton, Grice & Boger (2003), and Saak, Jennings & Shah (2004).

Christensen (1991) and Schowalter & Christensen (1998) corrected a simple integration error in the original theory by Murata (1984) and derived an expression between the dimensionless slump value and the dimensionless yield stress for axisymmetric flow. Pashias et al. (1996) extended the theory by Murata (1984) to a cylindrical geometry ($R_1 = R_2$), and Saak et al. (2004) generalized the previous relations by Murata (1984) to write an equation taking into account top and bottom radius in the relation. Clayton et al. (2003) also derived a generalized equation for the cone geometry introducing a dimensionless parameter relating the top and base radius, which for $R_2 = 2R_1$ yields the same result as, e.g. Schowalter & Christensen (1998).

Comparison of the theoretical estimates with experimental results shows that a reasonable correlation is obtained for the cylinder geometry for a range of dimensionless yield stresses from approximately 0.05 to 0.40 (corresponding to concrete yield stresses from 300 to 3000 Pa). However, for the cone models, there is lack of consistency between the theoretical estimate and the measured values (Clayton et al. 2003)(Saak et al. 2004).

All of the above analytical expressions have applied a one-dimensional expression of the constitutive equation including a one-dimensional yielding criterion, i.e. $\dot{\gamma} = 0$ when $\tau < \tau_0$ where $\dot{\gamma}$ is the shear rate, and τ is the shear stress (see Section 3.1.1). In the context of a three-dimensional constitutive equation and yielding criterion, Roussel & Coussot (2005) have studied separately the two asymptotic flow regimes, $SF >> h_0$ and $SF << h_0$ (see Figure 3.5). In the regime, $SF >> h_0$, the three-dimensional flow reduces to a one-dimensional flow where the flow is governed by shear stresses. This corresponds to the assumptions of the previous analytical results, which also found a better correlation between the cone models and the experiments for high slumps. However, as pointed out by Roussel & Coussot (2005), the assumption of a non-yielded region is likely not to apply, since for large slumps, there is no undeformed region. In this regime, the flow may be described within the frame of the so-called long-wave approximation, which was first applied by Ko & Mei (1989) in two dimensional flow and extended to three dimensions by Coussot, Proust & Ancey (1996). Then Roussel & Coussot (2005) derived an expression for the dimensionless yield stress as a function of the dimensionless slump, which compared to the previous analytical relations takes into account also the volume of the sample. A similar approach has been undertaken by Piau (2005). In this pure shear flow regime the dimensionless yield stress is given by

$$\tau_0^* = \sqrt{\frac{2\pi}{15\Omega}} H^{3/2} (1 - SL^*)^{5/2} \qquad SF >> h_0 \tag{3.16}$$

where Ω is the sample volume.

An expression was also derived for the yield stress as a function of the slump flow (SF) given by:

$$\tau_0 = \frac{225\rho_s g \Omega^2}{4\pi^2 (SF)^5} \qquad SF >> h_0 \tag{3.17}$$

For the Abrams cone, the slump flow (SF) as a function of the ratio (ρ/τ_0) is then given by:

$$SF \;=\; 0.278 \left(\frac{\rho_s}{\tau_0}\right)^{1/5} \qquad [m] \tag{3.18}$$

In a similar way an equation was derived for pure elongational flow corresponding to high yield stresses where it is assumed that the diagonal stresses of the stress tensor dominates over the shear stresses. Neglecting the stress variation in the radial direction Roussel & Coussot (2005) found:

$$\tau_0^* \;=\; \frac{1 - SL^*}{\sqrt{3}} \qquad SF << h_0 \tag{3.19}$$

The analytical expressions by Roussel (2004) and Roussel & Coussot (2005) were validated using numerical simulations, and the results were also compared to the previous results for the cone geometry. They found the expression for pure shear flow (Equation 3.16) for both the Abrams cone geometry and the mini-cone geometry to agree well with the numerical simulations over a range of dimensionless yield stress of 0.001 up to approximately 0.020. For concrete this corresponds to a range of yield stresses from approximately 10 to 1300 Pa. The results show the importance of including both the volume and height in the model. As expected, the previous results for the cone geometry, in this case the expression by Clayton et al. (2003), did not correlate with the numerical results, though better for the Abrams cone than the mini-cone. For the elongational flow, given by Equation 3.19, the slump is overestimated and the model only becomes valid for very small slumps or large yield stresses approaching the critical yield stress where no flow occurs.

In all of the expressions derived for the relation between the slump and yield stress, the effect of inertia and surface tension have been neglected. The effect of inertia depends on the plastic viscosity, density, and the lifting velocity of the cone. The experimental results of Tattersall & Banfill (1983), Murata (1984), and Pashias et al. (1996) as well as the assumptions for the slumping behaviour made by Roussel & Coussot (2005) indicate that inertia may be neglected, i.e. the yield stress is the only rheological parameter influencing the stoppage behaviour. For instance, Pashias et al. (1996) found in their studies of flocculated suspensions that the lifting velocity did not have any effect on the final slump height provided it remained less than approximately 10 m/s. However, for proper validation of the effect of inertia numerical simulations of the transient flow are required. To be certain that inertia was not affecting the final slump behaviour in the numerical studies by Roussel (2004), the plastic viscosity was set at high values ($\eta_{pl} = 200$ Pa·s in the Abrams cone and 1 Pa·s in the mini-cone), where it was assumed that the cone was lifted instantly (infinite lifting velocity). The effect of surface tension was studied in Roussel, Stefani & Leroy (2005) on cement paste flow in the mini-cone test. It was found that the surface tension had to be included for small values of the yield stress and plastic viscosity where the surface tension may be of the same order as the yield stress of 1-2 Pa.

All of the above mentioned studies have focused on estimation of the yield stress. For estimation of the plastic viscosity of SCC, the transient flow must be studied. As mentioned, it has been proposed to measure the $T50$ value when using the Abrams cone for assessment of the transient flow characteristics. However, empirical investigations correlating the $T50$ value with the plastic viscosity from rheological measurements have not shown a clear relationship, see e.g. (Nielsson & Wallevik 2003). For further understanding of the transient flow characteristics, numerical simulations are needed. Besides the plastic viscosity, the transient flow in the slump flow test depends on the cone lifting velocity, cone orientation, yield stress, and boundary conditions.

Kurokawa et al. (1994) carried out transient simulations using the Viscoplastic Finite Element Method (VFEM) (see Section 1.4.2), and suggested a relation between the $T50$ value, the plastic viscosity (η_{pl}), and the slump flow (SF), however independent on the lifting velocity. The relation is given by

$$T50 \quad = \quad \frac{\eta_{pl}}{0.0545\rho_s\left(1-\frac{40000}{SF^2}\right)\left(1-\frac{25000}{SF^2}\right)} \tag{3.20}$$

where SF, η_{pl}, and ρ_s are inserted in [mm], [Pa·s] and [kg/m^3], respectively.

Sedran (2000) compared Equation 3.20 to the results of an experimental program and a mean error of 65 Pa·s was obtained. When fitting the multiplying coefficient, from 0.0545 to 0.0414, this resulted in a mean error of 50 Pa·s. Also, an empirical linear relation was suggested based on 25 tests given by

$$T50 \quad = \quad \frac{1000\eta_{pl}}{\rho_s(0.026SF-2.39)} \tag{3.21}$$

which gave a mean error of 35 Pa·s in a range of plastic viscosities from 50 to 350 Pa·s, however, as previously mentioned, empirical relations depend on the choice of materials and the viscometer applied.

The expressions proposed for estimation of the yield stress and plastic viscosity based on the slump flow test assumes a homogeneous suspension. Depending on the particle size and volume fraction limits may exists to which this assumption is valid. However, further research into modeling discrete flow and/or experimental testing are needed to assess the effect of particle size and particle volume fraction to, e.g. set up criteria to the slump flow (SF) for which the homogeneous approach is valid.

Recently, Nguyen, Roussel & Coussot (2006) derived analytical expressions relating the yield stress and the so-called H_2/H_1 ratio in the L-box test for which the ratio of material thickness to particle size is higher than in the slump flow test (See Section 5.3.2 for the geometry of the L-box). Relations were derived for the L-box with and without reinforcement. The expression assumes that inertia can be neglected, and it is emphasized that the gate in the L-box must be lifted slowly based on the results of Thrane, Szabo, Geiker, Glavind & Stang (2004), which are reported in Chapter 7. The expressions for the H_2/H_1 ratio are given by

$$\begin{aligned} \frac{H_2}{H_1} &\cong \frac{\rho_s g - 84\tau_0}{\rho_s g + 84\tau_0} && \text{without bars} \\ \frac{H_2}{H_1} &\cong \frac{\rho_s g - 100\tau_0}{\rho_s g + 100\tau_0} && \text{with bars} \end{aligned} \tag{3.22}$$

where the reinforcement consists of three bars with a diameter of 14 mm separated by a distance of 40 mm from the center of the bars. However, experiments need to be carried out to verify these expressions. This could include a comparison with viscometric measurements, a comparison with numerical simulations, and a comparison between the slump flow (SF) and the H_2/H_1 ratio at various particle sizes and particle volume fractions.

For other test methods proposed for empirical assessment of the flow properties of SCC, see e.g. (ermco.org 2005) and (Efnarc 2002).

In summary, much work have been carried out on estimating the yield stress from the slump test and slump flow test, and recently also a relation for the yield stress in the L-box was proposed. These expressions assume that inertia can be neglected. For estimation of the plastic viscosity, numerical simulations of the transient flow are needed. An attempt has been made to correlate the so-called $T50$ value in the slump flow test to the plastic viscosity, however verification is limited. Fitted parameters to this equation have been proposed based on viscometric measurements, however, these may depend on the choice of materials and the viscometer applied.

In Chapter 7, the results of the transient numerical simulations carried out in this project on the slump flow test and the L-box test are presented. The simulations include moving boundaries and the results are compared to the results presented in this section.

3.2 Heterogeneous Flow Phenomena

The heterogeneous flow phenomena of blocking and dynamic segregation are described below.

The changes in particle volume fraction associated with blocking and dynamic segregation affect the local effective properties of the suspension causing changes in velocity and particle volume fraction profiles and thus poses a threat to any process relying on flow of a homogeneous material.

3.2.1 Blocking

By definition, one of the main advantages of SCC is the ability to cast narrow and confined zones where it could be difficult or even impossible to cast and compact conventional types of concrete, e.g. formwork sections with a complicated and dense reinforcement configuration. One of the challenges of SCC is to avoid blocking of aggregates behind reinforcement bars which may result, e.g. in honey combing and a poor form filling ability.

In this report the term blocking is defined as accumulation of aggregates behind reinforcement bars, which is illustrated in Figure 3.6 showing two form filling scenarios. In the upper situation, the concrete remain homogeneous during form filling and in the lower situation blocking occurs behind some of the reinforcement resulting in aggregate accumulation.

If a suspension is not able to pass through a narrow gap due to the viscous resistance this is referred to as a low passing ability, i.e. retained material will include both the particle and matrix phase respectively. From a modelling point of view, this should be captured in the simulation of homogeneous flow.

In the codes and norms, the existing criteria to bar spacing are restricted to guidelines for conventional concrete. The recommendation for bar spacing according to Eurocode 2 (2002) is

- ”The main purpose is to assure that the bars of spacing shall be such that the concrete can be placed and compacted satisfactorily for the development of adequate bond.”

Besides a qualitative specification, no other requirements are outlined, and nothing specific for SCC.

Therefore, it is important to obtain quantitative tools to assess under which conditions there will be a risk of blocking.

In order to predict blocking, two-phase flow models are required to study the particle flow and matrix flow separately.

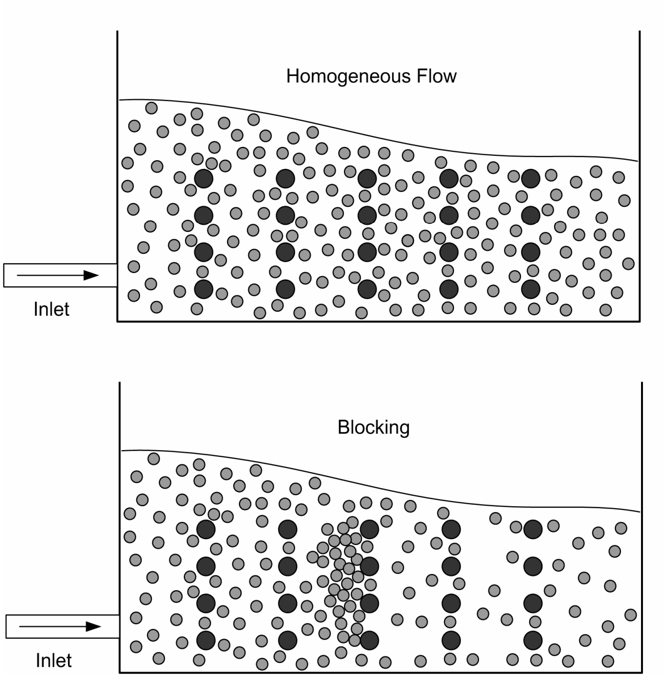

Figure 3.6 *Illustration of two form filling situations with SCC. In the upper situation the concrete remains homogeneous during form filling. In the lower situation the heterogeneous flow phenomena of blocking occurs i.e. aggregates are retained due to interactions with the reinforcement.*

Blocking of aggregates have been studied by Bui (1994), Tangtermsirikul & Bui (1995), and Martys & Farraris (2002).

Bui (1994) and Tangtermsirikul & Bui (1995) have proposed an empirical model for assessment of the blocking resistance based on the concept of a critical volume (V_{abi}) for each aggregate size fraction (i). For a given aggregate composition (grading and shape), the model may be used to assess a critical volume fraction of the specific aggregate composition (V_{abi}).

The criterion is written as a summation of the ratio between the volume of aggregate size fraction i (V_{ai}) and its critical blocking volume.

$$\sum_{i=1}^{N} \frac{V_{ai}}{V_{abi}} \begin{cases} < \ 1 : \text{No blocking} \\ = \ 1 : \text{Critical ratio} \\ > \ 1 : \text{Blocking} \end{cases} \tag{3.23}$$

The critical blocking volume (V_{abi}) is determined experimentally as a function of the ratio of the clear spacing (c) to the aggregate diameter of fraction i (d_{afi}).

This procedure provides an estimate of a minimum amount of paste necessary to avoid blocking, see also (Billberg 1999).

Examples of relations between the critical blocking volume (V_{abi}) and the ratio of clear spacing to aggregate diameter (c/d_{afi}) for natural rounded and crushed aggregate can be found in (Bui 1994), (Billberg 1999), (Tangtermsirikul & Bui 1995), and (Olsen et al. 2001). For instance, for natural rounded aggregate Billberg (1999) proposed values of the critical volumes (V_{abi}) of 0, 0.55, and 0.82 at a ratio c/d_{afi} of 1, 2.4, and 15, respectively. A linear relation is proposed between these points.

Martys & Farraris (2002) have carried out numerical simulations using dissipative particle dynamics. A few simulations have been carried out on monodisperse spheres passing reinforcement under the influence of gravity. The results showed blocking when the particle diameter to bar spacing was above 1/5. However, the effect of flow, mix proportions and properties are not evident from these simulations.

For empirical assessment of the risk of blocking of SCC, several test methods have been developed, such as the L-box (Billberg 1999), J-ring (ermco.org 2005), ring penetration test (Kurokawa, Taniwawa, Kim & Teranishi 1995), and the passing ability tester (Noguchi, Oh & Tomosawa 1999). These test methods introduce SCC flow under the force of gravity, and the blocking resistance is assessed by letting it pass a setup of reinforcement bars.

To the authors knowledge, only limited literature is available on blocking of suspensions in other types of finite flow domains. Sharp & Adrian (2005) has investigated dilute suspension flow through a circular tube, and Pandya, Bhuniya & Khilar (1998) have investigated dilute suspension flow through a packed bed of monodisperse spheres, thus, the suspension flow takes place in the porosity of a packed bed.

Sharp & Adrian (2005) have carried out an experimental study of dilute monodisperse suspension flow in tubes at confinement ratios (α) from 2.0 to 4.2 (tube radius over particle radius). The neutrally buoyant spherical particles (22 to 136 μm) were suspended in a Newtonian liquid (DI water, sugar water, or a glycerol solution in order to match the specific gravity of the particles). Experiments were carried out at low particle volume fractions (ϕ_p) from 0.005 to 0.031 and at Reynolds number approximately between 15-600. Most of the tests were carried out at Reynolds numbers between 75-300. However, only the particle size (d_p), confinement ratio (α), the particle volume fraction (ϕ_p), and the number of times blocking were observed have been reported. In this study, pH was varied in order to minimize the attractive surface forces between the particles so blocking would only be due to hydrodynamic interactions and not a cause of flocculation during flow (Gregory 1981). This assumption was verified, e.g. samples of the material at the outlet did not show agglomeration. From the experimental program, it seems that blocking is more likely to occur when the confinement ratios are approximately 2.5 to 3.3, however, the results indicate that blocking due to hydrodynamic interactions is not only a function of the particle volume fraction and confinement ratio. For instance, at $d_p = 136$ μm, $\alpha = 2.98$, and $\phi_p = 0.028$ blocking was observed in one out of two tests. In other two tests carried out at $d_p = 22$ μm, but at a higher confinement ratio of $\alpha = 3.41$, and at a lower particle volume $\phi_p = 0.005$, blocking was observed in both tests. As the authors also note, there is a need to understand fundamentally the effect of e.g. the flow rate, viscosity, and size distribution.

Pandya et al. (1998) studied the existence of a critical particle volume fraction of dilute suspensions plugging a packed bed. The suspensions consisted of neutrally buoyant spheres (40 and 63 μm) in a Newtonian liquid (water), and the packed bed consisted of glass beads (bead diameter of 0.5, 1.1, 1.6, and 3.0 mm). Instead of the confinement ratio defined for a tube flow, the confinement is given as the ratio of bead diameter to particle diameter. A relation for the smallest constriction diameter of the packed bed is proposed as the bead diameter divided by 6.49. This may be used to compared the confinement of the packed bed to the confinement ratio (α) for a circular tube. Then it is seen that the critical particle volume fraction is e.g. 0.004 and 0.090 at a confinement ratio of 1.92 and 6.16, respectively. A geometrical model has been proposed for the critical particle volume fraction as a function of the bead diameter to particle diameter ratio (or the equivalent confinement ratio). It seems that a reasonable correlation is obtained between the experimental results and the model up to a confinement ratio of approximately 3.80 where the critical particle volume fraction is found to be 0.02. For increasing confinement ratios, the model underestimates the critical particle volume fraction. For instance, at a confinement ratio of 15, the model estimates a critical particle volume fraction of approximately 0.18, which is underestimated. This correlates with the results discussed in the next section on particle migration in finite circular tube flow domains. Here, studies of suspension flow at similar confinement ratios and particle volume fractions of 0.50 do not show blocking. As the authors also note, the model clearly requires improvements, and the effect of suspension flow rate, viscosity, size distribution, and electric charges are not included in the model.

Experimentally, Pandya et al. (1998) carried out six tests with varying flow rates at $\alpha = 2.69$, $\phi_p = 0.01$, and $d_p = 63$ μm. The results showed that the risk of plugging the packed bed decreased when decreasing the flow rate. The effect of hydrodynamics and surface forces are not clear from these investigations, however, in another study by Ramachandran, Venkatesan, Tryggvason & Fogler (2000) it was shown that at high velocities the hydrodynamic forces acting on the particles at the pore entrance can overcome the inter-particle colloidal repulsion and result in the particles flocculating and plugging the pore. These studies included 0.22 μm particles arriving at pores with a confinement ratio of 3.7.

From the dry granular flow literature (only particles) examples of studies on blocking may be found in (Hong & McLennan 1992), (To, Lai & Pak 2002), and (Tsai, Losert, Voth & Gollub 2002). Hong & McLennan (1992) studied glass beads being discharged through a hole at the bottom of a two-dimensional tank and blocking was observed at a confinement ratio of 3. To et al. (2002) studied round disks exiting a vertical two-dimensional channel (angle of 75 %) and, for instance, the probability of blocking was found to be 0 and 50 % at confinement ratios of 3 and 2.5, respectively. Tsai et al. (2002) studied spherical beads in a straight two-dimensional channel and found, for instance, consistent and occasional blocking at confinement ratios of 5 and 6.25, respectively.

Though blocking of particles in a dry granular flow at low confinement ratios is similar to blocking of particles in the flow of a suspension, the general physics of flow are significantly different, e.g. for neutrally buoyant particles in a suspension, the particles are driven by drag forces from interaction with the matrix phase, whereas particles in a dry granular flow are driven by gravity and their mutual interactions.

In summary, experiments and modelling of the blocking phenomena have been undertaking. The studies of flow between reinforcement have focused on a blocking criterion based on bar spacing and mix composition - in particular aggregate size and volume fraction. A criterion for the blocking resistance based only on the mix composition may be referred to as a static criterion, i.e. the possible effect of dynamic behaviour is not considered.

In the studies of circular tube flow and flow through a packed bed only dilute monodisperse suspensions have been considered. Again, the results mainly report the relation between the particle volume fraction and the confinement ratio. However, the results indicate that other effects, such as the flow rate, viscosity, and electric charges may affect the risk of blocking.

In order to come closer to understanding the combined effect of the suspension flow rate, rheological properties of the suspension and matrix, confinement ratio, and particle volume fraction a phenomenological model to estimate blocking is proposed in Chapter 6. The model is formulated based on the hypothesis of a critical flow rate below which blocking will occur assuming only hydrodynamic interactions.

3.2.2 Dynamic Segregation

Dynamic segregation refers to the situation where particles segregate during flow. Compared to blocking, dynamic segregation is not caused by particle interactions with the solid boundaries. Instead, dynamic segregation seems to gradually evolve during flow over a larger scale of time and length and is governed by the flow patterns and the intrinsic properties of the suspension. Dynamic segregation is illustrated in Figure 3.7 showing two form filling scenarios in which dynamic segregation has occurred in the lower situation resulting a top layer without particles. Mortar or paste rich top layers may lead to a higher shrinkage, lower strength, and a lack of rough surfaces in casting joints.

Phase separation during flow is of interest in many industries, and much attention has been paid to the so-called shear induced particle migration where particles tend to migrate from regions of high shear rates to regions of low shear rates due to hydrodynamic interactions. Particle migration has been well documented from experimental studies in a tube flow domain, Couette flow domain (counter rotating concentric cylinders), and in a rectangular duct geometry (Goldsmith & Mason 1962)(Karnis, Goldsmith &

Mason 1966)(McMahon & Parker 1975) (Sinton & Chow 1991)(Hampton, Mammoli, Graham, Tetlow & Altobelli 1997)(Altobelli, Fukushima & Mondy 1997)(Han, Kim, Kim & Lee 1999)(Moraczewski, Tang & Shapley 2005) (Gadala-Maria & Acrivos 1980)(Leighton & Acrivos 1987)(Graham, Altobelli, Fukushima, Mondy & Stephens 1991)(Abbott, Tetlow, Graham, Altobelli, Fukushima, Mondy & Stephens 1991)(Chow, Sinton, Iwamiya & Stephens 1994)(Tetlow, Graham, Ingber, Subia, Mondy & Altobelli 1998)(Koh, Hookham & Leal 1994)(Shauly, Averbakh, Nir & Semiat 1997).

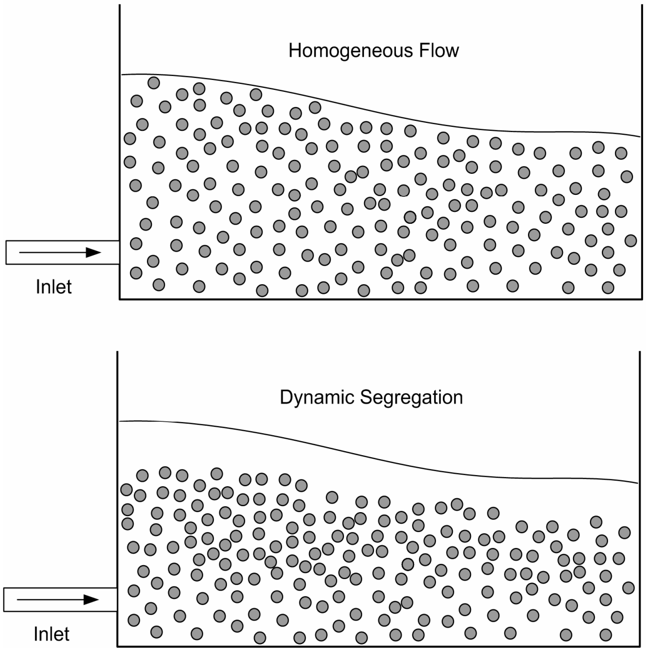

Figure 3.7 *Illustration of two form filling situations with SCC. In the first case the concrete remains homogeneous during form filling. In the second case the heterogeneous flow phenomena of dynamic segregation has occurred, which results in a top layer without particles.*

In pressure driven tube flow, the particles tend to migrate towards the tube axis where the shear rate is minimal. In the Couette domain (counter rotating concentric cylinders) particles migrate towards the outer wall where the shear rate is minimal.

Compared to blocking, phase separation due to particle migration occurs perpendicular to the streamlines whereas, e.g. in the tube flow domain, blocking would be observed as particles being retained in the direction of the streamlines due to the interaction with the solid boundaries.

In the above mentioned studies, the applied suspensions consist of neutrally buoyant particles suspended in an incompressible Newtonian liquid and it has been assumed that inertial, electrostatic and Brownian motion forces are negligible. The particle volume fractions have varied from approximately 0.10 to 0.50 and the confinement ratios in, e.g.

the tube flow domain vary from approximately 10 to 150.

Barentin, Azanza & Pouligny (2004) have studied suspensions where the particles are heavier than the interstitial fluid in a parallel plate rheometer. Experiments show that particle segregation is sensitive to both hydrodynamic interactions and gravity especially for large gaps between the parallel plates.

To describe particle migration mathematically, a phenomenological diffusive flux model has been proposed by Phillips, Armstrong, Brown, Graham & Abbott (1992) to predict the particle volume fraction profiles resulting from shear-induced migration of monodisperse particles in a Newtonian liquid. Quantitatively, the particle-migration flux is proportional to gradients of the particle volume fraction, gradients of the local shear rate, and gradients of effective viscosity (depending on the particle volume fraction). The model comprise two diffusion coefficients associated with the particle collisions and gradients in the relative suspension viscosity. These are fitted against experimental results. For instance, Tetlow et al. (1998) and Hampton et al. (1997) studied the model in the Couette and tube flow domain, respectively. Tetlow et al. (1998) found a good correlation with the experimental profiles of the particle volume fraction in a Couette device. They found that instead of using constant values for the diffusion coefficients, the experimental results were better fitted when the coefficients were modeled as functions of the local particle volume fraction. Hampton et al. (1997) found that for appropriate tuned empirical coefficients, the model provides good quantitative estimation of the particle volume fraction profiles. Two confinement ratios of 40 and 16 were studied and the best correlation was found at 40.

Flow rate dependent particle migration, in which particle migration occurs below a critical value has been observed in studies of concentrated and highly viscous pastes in a squeeze flow test by Delhaye, Poitou & Chaouche (2000) and Poitou & Racineux (2001).

Poitou & Racineux (2001) have developed a numerical scheme to describe the squeeze flow test. Conservation laws of mass and momentum were written for each phase and the suspension (particle) rheology was modelled using a shear-thinning power law expression, while the matrix followed that of Newtonian liquid. The numerical scheme seems to simulate the behaviour observed in the experiments. Furthermore, a qualitative analytical expression was developed to estimate a critical squeeze flow velocity below which migration of particles occurs. It is based on an energy criterion dividing the total viscous dissipation into an intrinsic viscous dissipation caused by friction between particles (particles and matrix move at the same velocity), and interaction dissipation due to the viscous drag (particles and matrix do not move at the same velocity). The concept of a critical velocity is based on the assumption that particles migrate to zones where the intrinsic viscous dissipation is low, i.e. where the solid shear rate is low. They assume that a critical velocity may be estimated when the viscous dissipation due to friction and drag are equal. For a quantitative estimate they select a matrix velocity relative to the particles velocity, which is set at the same value as the squeezing velocity.

The squeeze flow test has also been applied by Phan & Chaouche (2005) to study the behaviour of cement paste used in SCC. The results are in good correlation to the observations by Delhaye et al. (2000) and Poitou & Racineux (2001). They found that above a certain critical velocity the force is an increasing function of the velocity indicating a homogenous viscous behaviour. Below the critical velocity, phase separation was observed.

Flow rate dependent has also been observed in ram extrusion of high solid volume microcrystalline cellulose pastes by Rough, Wilson & Bridgwater (2002). Here, phase separation is a result of the compaction process and the development of pore pressures in the liquid phase (water).

A one-dimensional model was proposed by Rough et al. (2002) to describe the compaction and ram extrusion of highly concentrated pastes exhibiting high yield stresses. This type of material deforms as a stiff suspension, where the particle stress is responsible for the deformation of the particles, whereas the liquid stress (pore pressure) is the driving force for the flow of the liquid phase. The model includes several estimates of material parameters which are based on existing results in the solids and soils literature. An important feature of the model is the use of experimentally determined parameters for the extrusion work parameters, the solids compressibility, and reference particles permeability.

To date, limited fundamental research on dynamic segregation of SCC has been carried out. As mentioned in Section 1.4.2, most studies have focused on the static resistance of either a single or group of particles in a static paste material with a yield stress (Beris et al. 1985)(Saak et al. 2001)(Bethmont et al. 2003)(Roussel 2006*a*).

For instance, based on the work by Beris et al. (1985) and Saak et al. (2001), Bethmont et al. (2003) modified the equation for the critical diameter of a single particle in a yield stress matrix to give

$$d_p \leq 20.97 \frac{\tau_{m,0}}{\Delta\rho_{pm} g} \tag{3.24}$$

where d_p is the particle diameter, $\Delta\rho_{pm}$ is the difference between the matrix density and particle density, $\tau_{m,0}$ is the matrix yield stress, and g is gravity. The inequality expresses the critical diameter of a single particle, i.e. when the diameter is lower than the term on the right side, static segregation will not occur.

Bethmont et al. (2003) carried out experiments where one particle was placed at the top of a cylinder filled with cement paste. The cement pastes had different yield stresses, and the particle sizes applied were 5, 6, 8, 9, 10 and 16 mm. The samples were later split to detect the particle position and determine whether segregation had occurred or not. The results of these test show that Equation 3.24 gives a reasonable estimate of the critical diameter, whereas the previous equation of Saak et al. (2001) underestimates the critical diameter by approximately a factor of 10.

In order to come closer to understanding and modelling of dynamic segregation, it is likely that it can be back-traced to the combined effect of shear induced particle migration and gravity induced segregation due to differences in density.

In Chapter 7, dynamic segregation is discussed in relation to the experimental observations from the vertical form filling applications.

Chapter 4

Homogeneous Flow: Mathematical Formulation

Computational modelling of the transient flow of suspensions may be conducted according to a homogenous suspension or discrete particle flow approach, respectively. The applicability of these methods for simulating the transient flow was discussed in Section 1.4.

The application of the two approaches is illustrated in Figure 4.1 showing SCC being cast into a vertical formwork with reinforcement. The homogeneous suspension approach aims to describe the bulk flow behavior, neglecting the structure of material on a smaller scale (Lai, Rubin & Krempl 1996). The viscosity function comprises the interactions between the different phases, i.e. fluid-particle and particle-particle interactions (Wallevik 2003*b*). The discrete particle flow aims to simulate the motion of individual particles based on specific choices of contact laws for the particle interactions.

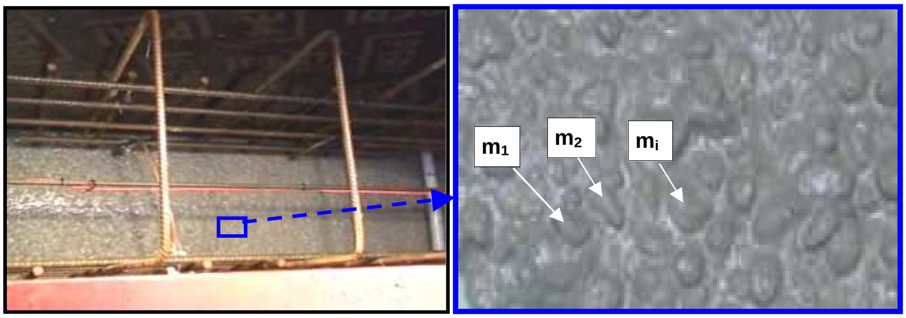

Figure 4.1 *Vertical SCC casting. In the homogeneous fluid approach (left) only one phase is considered whereas the discrete particle flow approach (right) considers individual particles* m_i *where* $i=1,2..M$ *and* M *is the number of particles.*

In this project a homogeneous fluid approach is applied to simulate the transient flow of SCC on a larger scale of time and length. The current Chapter presents the governing equations, and Chapter 5 presents the numerical approach applied to solve the governing equations in the selected flow domains. Chapter 6 presents a model for the heterogeneous flow phenomena of blocking relevant to flow between the reinforcement.

4.1 Homogeneous Suspension Approach

The homogenous suspension approach assumes only one phase for which reason it may also be referred to as a single fluid approach. The governing equations are derived from conservation of mass, momentum, and energy (Bird, Stewart & Lightfoot 1960).

For a region of space occupied by the fluid, the fluid is characterized by a velocity field, density field, pressure field and a temperature field. The latter is derived from the energy equation, but in the ongoing, it is assumed that temperature variations during castings are negligible and flow takes place under isothermal conditions. For the energy equation, see e.g. Bird et al. (1987).

The mathematical formulation of the physical principles may be constructed from a infinitesimal fluid element, which is illustrated in Figure 4.2 showing flow of a fluid represented by streamlines. If an infinitesimally small fluid element with a differential volume $d\Omega_f$ is considered, it may be either fixed in space (to the left) or it may be moving along a streamline with a velocity equal to the flow velocity at each point (to the right). The partial equations obtained directly from the fluid element fixed in space are called the conservation form of the equations, and those obtained directly from the moving fluid element are called the non-conservation form of the equations (Wendt 1992).

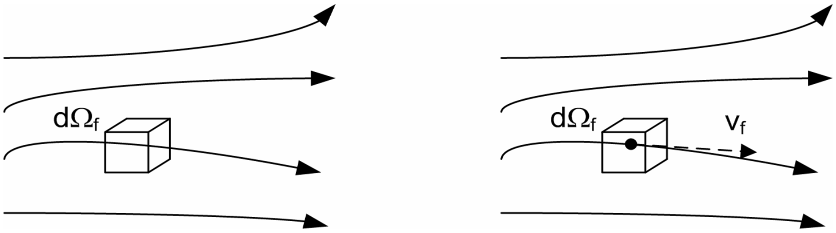

Figure 4.2 *Infinitesimal small fluid element approach from which the governing equations are derived. The fluid element has a differential volume $d\Omega_f$. To the left the fluid element is fixed in space and the fluid moves through the element. To the right, the fluid element is moving along a streamline with a velocity equal to the flow velocity at each point (v_f) (Wendt 1992).*

The continuity equation is based on the physical principle that mass is conserved and it is given by

$$\frac{\partial \rho}{\partial t} + \frac{\partial (\rho u_i)}{\partial x_i} = 0 \tag{4.1}$$

If incompressibility is assumed ($\rho =$ constant), this reduces to

$$\frac{\partial u_i}{\partial x_i} = 0 \tag{4.2}$$

where ρ is the density, x_i are the coordinates, and u_i the components of the velocity vector in each of the coordinate directions.

The momentum equation is formulated based on the work by the French Mathematician Cauchy who formulated a generalized three-dimensional stress state (Lai et al. 1996). Combined with Eulers law of mechanics he constructed a general theoretical framework for motion of any continuous medium given by

$$\rho\left(\frac{\partial u_i}{\partial t}+u_i\frac{\partial u_i}{\partial x_j}\right)=\frac{\partial \sigma_{ij}}{\partial x_j}+\rho F_i \tag{4.3}$$

where σ_{ij} is the stress tensor and F_i the volume forces per mass unit.

The rate of change of momentum is described through the convective term on the left side and the stress tensor and the body forces (gravity) on the right side.

The stress tensor consists of two parts, the pressure (p) and the deviatoric stress tensor (τ_{ij}) associated with the deformation of the fluid element. In the viscoplastic state, the stress tensor is given by

$$\sigma_{ij}=-p\delta_{ij}+\tau_{ij} \tag{4.4}$$

where δ_{ij} is the unit tensor.

The constitutive relation between the deviatoric stress tensor (τ_{ij}) and the strain rate tensor $(\dot{\epsilon_{ij}})$ for viscous incompressible fluids was presented in Section 3.1.1.

Substituting the constitutive law of an incompressible Newtonian fluid into the Cauchy's equation results in the well-known Navier-Stokes equations (Bird et al. 1987)(Wendt 1992).

4.1.1 Reynolds Number

The governing equations presented in the above section assume laminar flow. A laminar flow is a orderly flow in which the fluid particles move in smooth layers, and occurs at slow speed. Turbulent flow, on the other hand, is recognized by the flow becoming increasingly sensitive when the velocity of flow increases (Bird et al. 1960)(Lai et al. 1996).

The dimensionaless Reynolds number (Re) can be used to assess the importance of the convective term (inertia) in the momentum equation and whether a flow will be laminar or turbulent. The Reynolds number is the ratio of inertial forces to viscous forces given by

$$Re = \frac{\rho V_m L_c}{\mu} \tag{4.5}$$

where V_m is the mean velocity, L_c is the characteristic length, μ is the viscosity, and ρ is the density.

The laminar flow regime may divided into regions according to the relative importance of the viscous and inertial forces, respectively. At low Reynolds numbers, only the viscous forces are relevant.

For a Bingham fluid a reference viscosity may be applied instead of the Newtonian viscosity in Equation 4.5. The reference viscosity may be estimated based on the apparent viscosity, and to be on the safe side, the viscosity may be set equal to the plastic viscosity (η_{pl}).

Chapter 5

Homogeneous Flow: Numerical Solution Method

In Chapter 4, the mathematical formulation for flow of homogeneous fluids was presented. This Chapter presents the numerical solution method applied to solve the governing equations. First, a brief description of the Galerkin Finite Element Method (GFEM) is given. Next, calculation of the homogeneous form filling characteristics is presented; the characteristics comprise the form filling ability, flow patterns, and shear rates. Finally, the discretization of each of the selected flow domains is presented including the methods applied to handle moving boundaries.

5.1 Galerkin Finite Element Method

The Galerkin finite element method adapted in Fidap has been applied to solve the governing equations of viscous fluid flow (FIDAP 2000). The objective of the finite element method is to reduce the continuum problem (infinite number of degrees of freedom) to a discrete problem (finite number of degrees of freedom) described by a system of algebraic equations (Chung 1978)(Gresho & Sani 2000). The finite element procedure begins with the division of the continuum region of interest into a number of elements.

Applying a so-called Eulerian description of fluid motion the elements are assumed to be fixed in space. Within each element, the dependent variables velocity (u_i) and pressure (p) are interpolated by functions of compatible order in terms of values to be determined at a set of nodal points. For the purpose of developing the equations for these unknown nodal points, an individual element may be separated from the assembled system. Within each element, the velocity and pressure fields are approximated by,

$$\begin{aligned} u_i(x,t) &= \varphi^T \mathbf{U}_i(t) \\ p(x,t) &= \omega^T \mathbf{P}(t) \end{aligned} \tag{5.1}$$

where $\mathbf{U}_i$ and $\mathbf{P}$ are column vectors of element nodal point unknowns and φ and ω are column vectors of the interpolation functions (FIDAP 2000).

Substitution of these approximations into the differential equations for conservation of mass and momentum (Eq. 4.2 and 4.3), and the boundary conditions yields a set of residuals (errors) $\mathbf{R}_1$ and $\mathbf{R}_2$:

$$\begin{aligned} \mathbf{f}_1(\varphi, \mathbf{U}_i) &= \mathbf{R}_1 \qquad \text{Conservation of Mass} \\ \mathbf{f}_2(\varphi, \omega, \mathbf{U}_i, \mathbf{P}) &= \mathbf{R}_2 \qquad \text{Conservation of Momentum} \end{aligned} \tag{5.2}$$

An approximate solution of the boundary value problem is now obtained by finding a way to make this residual small. In the finite element method, this is done by requiring that an appropriate number of weighted integrals of the residual is zero. The Galerkin form seeks to reduce these errors to zero in a weighted sense by making the residuals orthogonal to the interpolation functions of each element (Chung 1978)(Gresho & Sani 2000). This is written

$$\begin{aligned} (\mathbf{R}_1, \varphi) = 0 \\ (\mathbf{R}_2, \omega) = 0 \end{aligned} \tag{5.3}$$

where, e.g. ($\mathbf{R}_1$,φ) denotes the inner product given by $\int_{\Omega_e} \mathbf{R}_1 \cdot \varphi$ and Ω_e is the volume of the element e (FIDAP 2000).

The application of the GFEM procedure to the governing equations results in a set of nonlinear algebraic equations that may be represented in a matrix form as

$$\mathbf{K}(\mathbf{a})\mathbf{a} = \mathbf{F} \tag{5.4}$$

where $\mathbf{K}$ is the global system matrix, $\mathbf{a}$ is the global vector of unknowns (velocities, pressures, temperatures, etc.), and $\mathbf{F}$ is a vector that includes the effects of body forces and boundary conditions. The boundary conditions may include specification of velocity components and surface stresses (FIDAP 2000).

The adequate choice of the interpolation functions is one of the important steps of a finite element analysis (Chung 1978).

In Fidap, various elements are available in both two-dimensional and three-dimensional flow studies. An example of a four-node quadrilateral iso-parametric element is shown in

Figure 5.1. The term iso-parametric refers to the use of the same interpolation functions to describe the shape of the element and the velocity.

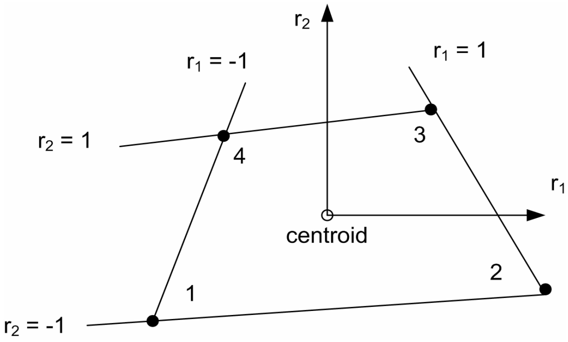

Figure 5.1 *An isoparametric four-node quadrilateral element (FIDAP 2000).*

The interpolation functions are expressed in terms of the normalized coordinates for the element (r_1 and r_2), which vary from -1 to 1. For this element, the velocity components (u_i) are approximated using a bilinear interpolation function defined by:

$$\varphi = \begin{pmatrix} \frac{1}{4}(1-r_1)(1-r_2) \\ \frac{1}{4}(1+r_1)(1-r_2) \\ \frac{1}{4}(1+r_1)(1+r_2) \\ \frac{1}{4}(1-r_1)(1+r_2) \end{pmatrix} \tag{5.5}$$

Two pressure discretizations are possible with this element, a bilinear continuous approximation ($\omega = \varphi$) with the pressure degrees of freedom located at the four corner nodes, or a piecewise constant discontinuous pressure approximation ($\omega = 1$). The pressure degree of freedom in the latter case is usually associated with the element centroid (FIDAP 2000).

Two different numerical approaches can be used for the incompressibility constraint and the discretization of the pressure variable, a so-called penalty and a mixed formulation approach. If a penalty approach is chosen, the continuity equation is discarded and the pressure is eliminated from the momentum equation where ϵ is the so-called penalty parameter. The pressure is recovered by post processing from the velocity field by $p = -\frac{1}{\epsilon}\frac{\delta u_i}{\delta x_i}$. In a mixed formulation, the pressure variable is discretized and contributes to an additional degree of freedom to the system of unknowns to be solved for. A mixed formulation can be used together with either a continuous or a discontinuous pressure approximation

(Gresho & Sani 2000)(FIDAP 2000).

For further details with regard to the manipulations involving the integrals resulting in the algebraic matrix equations, and the solution methodologies, see (FIDAP 2000). For a thorough overview of the finite element technique in fluid mechanics see e.g. (Gresho & Sani 2000), (Anderson, Degrez, Dick & Grundmann 1995), and (Chung 1978).

5.1.1 Boundary Conditions

The different types of boundary conditions involved in simulation of the homogeneous flow are presented in the sections below and comprise:

- constrained nodal degrees of freedom
- a shear stress slip boundary condition
- the free surface boundary condition

Handling of moving boundaries are discussed for each of the specific cases considered in this study (see Section 5.3).

Constrained nodal degrees of freedom

The velocity components of the boundary nodes may be constrained to a predefined value. This results in the field equation for that particular degree of freedom being deleted, and the specified value being imposed for that degree of freedom in the other equations. For instance, for a no-slip condition the velocity at the boundary is set to to zero.

Shear stress boundary condition

It is possible to apply a shear stress boundary condition in which the shear stress is proportional to the relative tangential velocity at the boundary. This is the so-called Navier slip boundary condition at the liquid solid interface. It is given by

$$\sigma_t = \sigma_{ij} n_j t_i = \tfrac{1}{\beta}(u_i - u_i^b) t_i \tag{5.6}$$

where σ_t is the tangential component of the total stress vector at a boundary, σ_{ij} is the stress tensor, n_j and t_i are components of the normal and tangential vectors at the boundary, β is the slip coefficient, u_i is the velocity, and u_i^b is the velocity of the boundary for which the tangential stress is zero. When $u_i = u_i^b$ the boundary condition reduces to a full slip boundary condition.

The Navier slip model may be associated with the existence of a non homogeneous region of fluid near the wall, a lubrication of the interface (Bird et al. 1987). The thin film near the wall has a lower viscosity than the bulk region. For instance, possible particle migration in a viscometer may result in a thin layer of paste at the boundaries which may lead to incorrect interpretations of the results. Normally a constant velocity is applied to one of the boundaries (e.g. outer cylinder in a co-axial viscometer) and thus a given shear rate is assumed to be imposed on the suspension. However, due to the slipping behavior the shear rate of the bulk suspension will be lower than expected resulting in an incorrect interpretation of the shear stress-shear rate relationship.

Figure 5.2 shows the three different types of fluid-solid boundary conditions, i.e. the no-slip, the Navier slip, and the lubricating slip model under steady shear flow over the height h. The viscosities of the suspension and matrix are assumed to be μ_s and μ_m, respectively. In the lubrication model the thickness of the lubricating matrix phase and the bulk phase are denoted h_1 and h_2, respectively. At $y = h$ the velocity of the no-slip, and slip models are denoted U_{shear}.

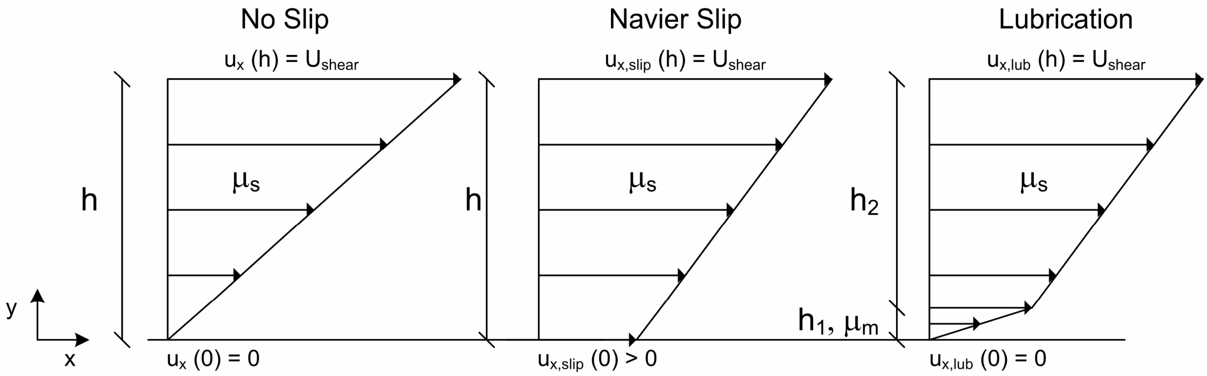

Figure 5.2 *Three different types of boundary conditions i.e. the no slip condition (left), the Navier slip (middle), and the lubricating slip model (right).*

In order to determine the slip coefficient in the Navier slip model, the velocity distributions in the lubrication model and the Navier slip model are derived. In general, the Navier-Stokes equation in the x-direction yields

$$\rho(\frac{\delta}{\delta t} + u_x\frac{\delta u_x}{\delta x} + u_y\frac{\delta u_x}{\delta y} + u_z\frac{\delta u_x}{\delta z}) = -(\frac{\delta \tau_{xx}}{\delta x} + \frac{\delta \tau_{yx}}{\delta y} + \frac{\delta \tau_{zx}}{\delta z}) - \frac{\delta p}{\delta x} + \rho g_x \tag{5.7}$$

which for steady state shear flow reduces to

$$\frac{\delta \tau_{yx}}{\delta y} = 0 \Rightarrow \tau_{yx} = T \tag{5.8}$$

which show that the shear stress is constant over the height h with a value of T.

The lubrication model

The constitutive equation for shear flow is given by $\tau_{yx} = -\mu \frac{\partial u_x}{\partial y}$ which gives

$$T = -\mu_i \frac{\partial u^{"i"}_{x,lub}}{\partial y} \tag{5.9}$$

where $i = 1, 2$ refer to the domains over height h_1 and h_2, respectively. Integration yields:

$$\begin{aligned} u^{"1"}_{x,lub} &= -\frac{T}{\mu_m} y + K_1 \\ u^{"2"}_{x,lub} &= -\frac{T}{\mu_s} y + K_2 \end{aligned} \tag{5.10}$$

where K_1 and K_2 are constants. It is assumed that $u_{x,lub}(y = 0) = 0$ which results in:

$$u^{"1"}_{x,lub}(0) = 0 \Rightarrow K_1 = 0 \tag{5.11}$$

The velocity distribution in the x-direction in the domain over height h_1 can now be written as

$$u^{"1"}_{x,lub} = -\frac{T}{\mu_m} h_1 \tag{5.12}$$

which then gives K_2:

$$-\frac{T}{\mu_m} h_1 = -\frac{T}{\mu_s} h_1 + K_2 \Rightarrow K_2 = T h_1 \left(\frac{1}{\mu_s} - \frac{1}{\mu_m}\right) \tag{5.13}$$

Finally, the velocity distribution in the x-direction in the domain over height h_2 is given by:

$$u^{"2"}_{x,lub}(y) = -\frac{T}{\mu_s} y + T h_1 \left(\frac{1}{\mu_s} - \frac{1}{\mu_m}\right) \tag{5.14}$$

Navier slip model

The velocity distribution ($u_{x,slip}$) is found for the Navier slip boundary condition. The velocity $u_{x,slip}$ is given by

$$u_{x,slip}(y) = -\frac{T}{\mu_s}y + K_3 \tag{5.15}$$

where K_3 is a constant. At $y = 0$ the slip condition yields $u_{x,slip}(0) = \beta T$. This gives

$$K_3 = \beta T \tag{5.16}$$

and the velocity distribution is given by:

$$u_{x,slip}(y) = \beta T - \frac{T}{\mu_s}y = T(\beta - \frac{y}{\mu_s}) \tag{5.17}$$

Slip coefficient

The slip coefficient β is now derived from

$$u_{x,slip}(h) = u_{x,lub}(h) = U_{shear} \tag{5.18}$$

where $h = h_1 + h_2$. The slip coefficient is then given by:

$$\begin{gathered} T(\beta - \frac{h_1 + h_2}{\mu_s}) = T(-\frac{h_2}{\mu_s} - \frac{h_1}{\mu_m}) \\ \beta = (\frac{h_1}{\mu_s} - \frac{h_1}{\mu_m}) \end{gathered} \tag{5.19}$$

The effect of a slip boundary condition is illustrated in Section 7.1 in a parameter study of the slump flow test where a slip condition is applied on the base plate.

Free surface boundary condition

In general, concrete flow includes a free surface of arbitrary shape, which vary in time.

To be able to simulate the deformations of the free surface, the fluid is characterized by a volume-of-fluid representation on the computational mesh. A volume tracking method is applied to determine advection (transport) of the fluid (FIDAP 2000). The fluid volume is represented by means of a marker concentration F. The advection of the marker concentration is governed by

$$\frac{\partial F}{\partial t} + u_i \frac{\partial F}{\partial x_i} = 0 \tag{5.20}$$

where F is equal to unity within the tracked volume and zero outside. Sharp interfaces are maintained by ensuring sharp gradients in F. This requires special treatment of the advective term in the transport equation (Equation 5.20), which is achieved under the framework of a volume tracking method.

The marker concentration is discretised by

$$f_e = \frac{1}{\Omega_e} \int_e F d\Omega_e \tag{5.21}$$

where f_e is referred to as the fractional fill state of element e and Ω_e is the volume of element e. The fractional fill states (f_e) vary between zero and unity. An element in which $f_e = 1$ refers to a full fluid element and $f_e = 0$ refers to an empty void element. A partial element has a fractional fill between zero and unity. Partial elements are regions of transition between the fluid and the void. It is assumed, in this case, that there is no interaction between the fluid and the void; no force is imposed on the fluid from the void. Empty elements are in that way ignored in the assembly of the element contributions to the governing equations. These equations are only assembled for partial and full elements only (FIDAP 2000).

The volume tracking method consists of two steps. In the first step, the fluid volume within an element is reconstructed based upon its fill state and the fill state of its neighbors and represents an estimate of the spatial location of the fluid within the mesh. In the second step, the finite element equations are used to calculate the kinematics based on the fluid boundary, and from the velocity field, the fluid is advected leading to new fractional fill states (FIDAP 2000).

5.2 Modelling of Homogeneous Form Filling Characteristics

5.2.1 Form Filling Ability

The location of the free surface is visualized by plotting contours of the fractional fill state (f_e) within the mesh. The fill states are discontinuous across elements and are not defined at nodes. For contouring purposes, nodal values of the fractional fill states are interpolated from nodal fill values (f_n) determined as

$$f_n = \frac{\sum_e f_e \Omega_e}{\sum_e \Omega_e} \tag{5.22}$$

for all elements e touching node n.

An example of a two-dimensional free surface plot is shown in Figure 5.3.

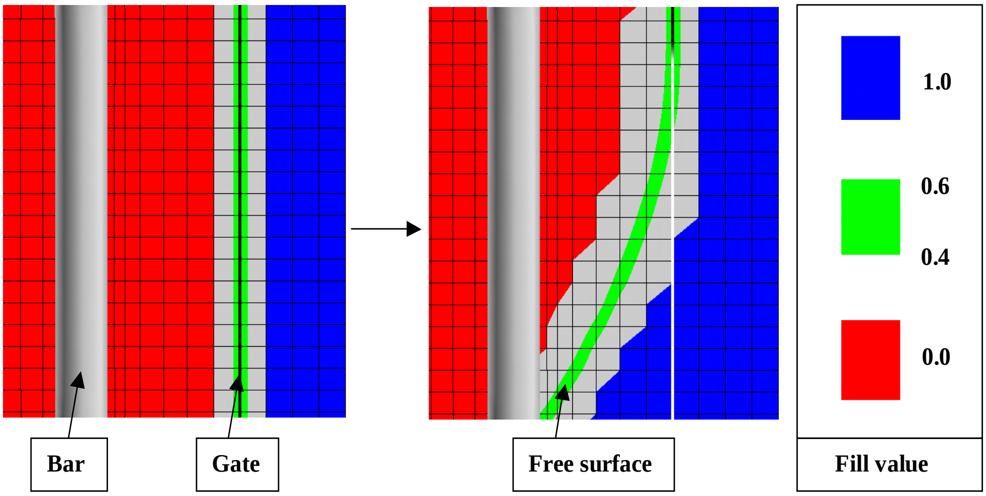

Figure 5.3 *An example of the two-dimensional free surface detection from an L-box simulation. To the left, at time $t = 0$, the gate has not been lifted. To the right, at time $t = t_1$, the gate has been lifted and flow is initiated. The free surface is plotted from calculation of nodal values of the fractional fill state (f_n). For a node n, a value of $f_n = 1$ and 0 corresponds to every element surrounding node n being completely filled and empty, respectively. The free surface location is detected by plotting contours at $f_n = 0.5$. The green color represents f_n from 0.4 to 0.6* .

It shows the free surface before and after lifting the gate in an L-box simulation. The blue and red color are plotted for nodal fill values (f_n) of 1 and 0, respectively. The actual location of the free surface is interpreted for nodal values $f_n = 0.5$. The green color represents the area between nodal values of 0.4 and 0.6, respectively.

5.2.2 Flow Patterns

The flow patterns are one of the relevant properties to study during form filling.

The homogeneous flow simulation provides an opportunity to compute the flow patterns in terms of the path of so-called massless particles released at a specific location and time during filling. The particle path of a particle is determined by integrating through the current velocity field using a second order Runge-Kutta method with an adaptive step size (Fieldview 2002).

5.2.3 Shear Rate

The magnitude of the strain rate tensor (shear rate) at a specific location and time during placing is calculated according to Equation 3.4.

5.3 Selected Flow Domains

5.3.1 Slump Flow Test

The geometry of the slump flow test is shown in Figure 5.4 (ermco.org 2005). In the standard procedure it is carried out with an upright cone where the large diameter faces the base plate. In manual operations, the cone is sometimes turned upside down in order for one person to carry out the test because the concrete pressure on an upright cone has a tendency to lift it. When the large and small diameter faces the base plate, this is denoted $D200$ and $D100$, respectively.

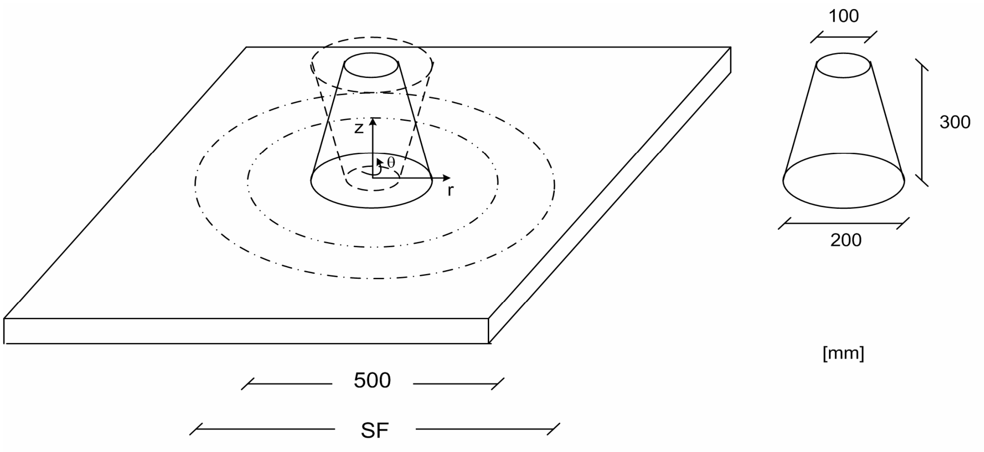

Figure 5.4 *The geometry of the slump flow test (ermco.org 2005). When the large and small diameter faces the base plate, this is denoted $D200$ and $D100$, respectively.*

It is assumed that the flow exhibits symmetry around the z-axis, i.e. velocity and pressure are independent on θ and u_θ is zero. The continuity and momentum equation is then described according to cylindrical polar coordinate directions r and z.

Figure 5.5 shows the computational mesh for the slump flow test with an upright cone. The computational domain allows for advection of the fluid into the free space outside the cone.

The computational flow domain has been divided into 4-node quadrilateral and 3-node triangular elements (bilinear interpolation). This provides a better resolution of the free surface compared to, for instance, fewer elements with a bi-and triquadratic interpolation.

In Figure 5.5, the dense mesh (dark area in top figure) represents the space where the cone passes through when it is lifted. To obtain a smooth solution, the sides of the elements are parallel to the side of the cone.

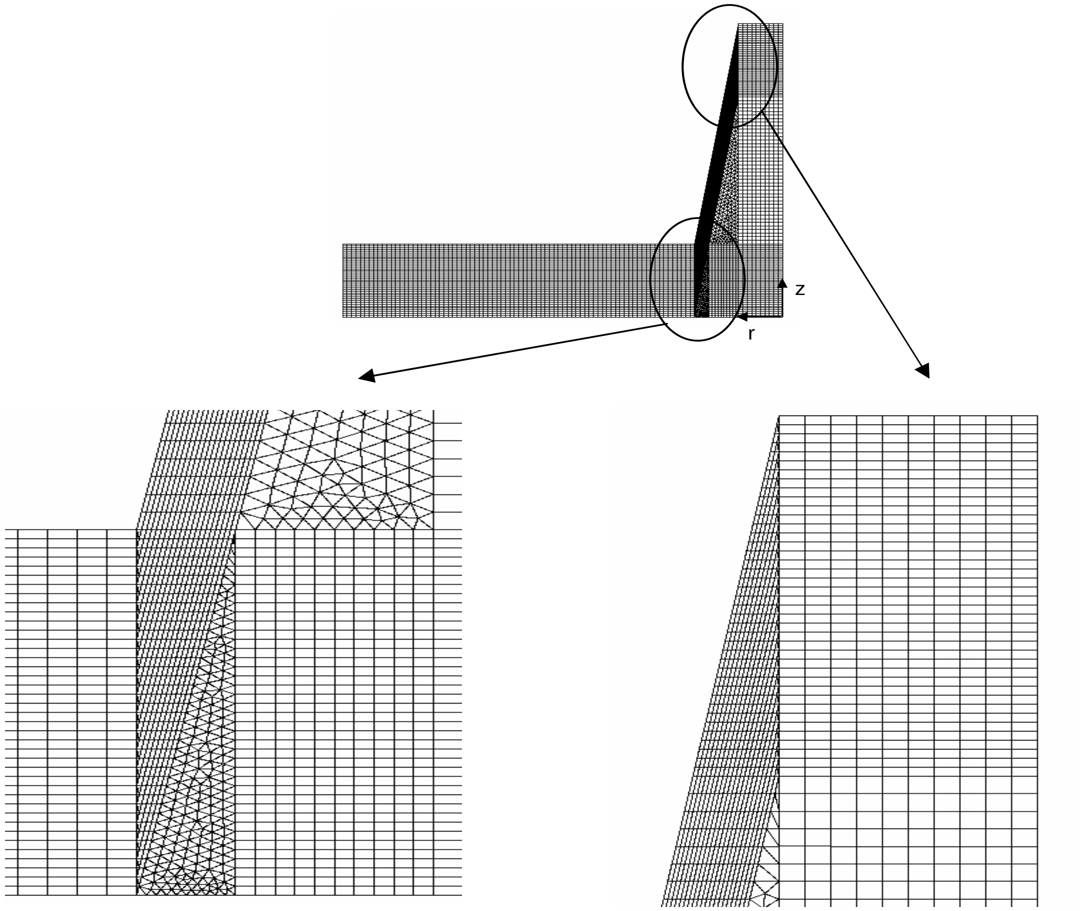

Figure 5.5 *The computational mesh of the slump flow test with an upright cone (D200). The top figure shows the mesh of the complete computational flow domain. The dense mesh (dark area) is highlighted in the bottom figures, and represents the area where the cone passes through when it is lifted.*

A subroutine has been written to handle lifting of a cone associated with a moving boundary. When the moving boundary passes through the elements, the radial velocity (u_r^n) and vertical velocity velocity (u_z^n) of the nodes are constrained to zero if $z_b(r,t) \leq z_n$ for n =1, 2, ..N, where z_b is the z-coordinate of the moving boundary, z_n is the z-coordinate of node n, and N is the total number of nodes which are passed by the cone when lifted. If $z_b(r,t) > z_n$, the velocities u_r^n and u_z^n are solved for.

A similar procedure is not applicable when the cone is turned upside down ($D100$) as the lifting of the cone results in a upward movement on the fluid. Instead, a pseudo boundary is introduced in which a node is part of this boundary when it is within a certain distance. Figure 5.6 shows the mesh of the part where the cone passes through when it is turned upside down. The blue line illustrates cone boundary at a given time, and to the right a part of the mesh is highlighted.

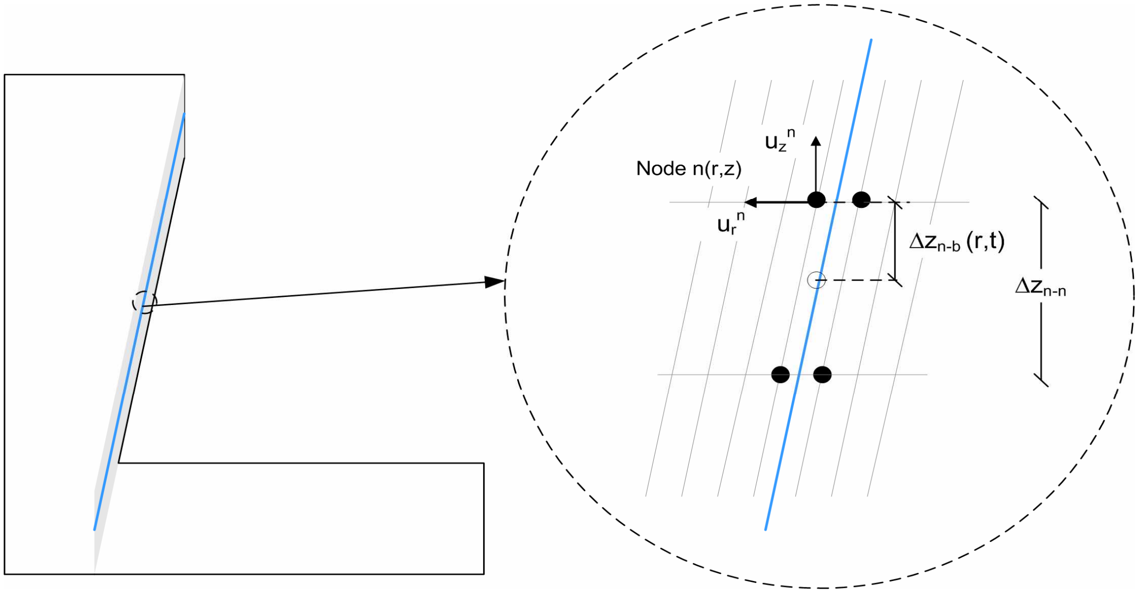

Figure 5.6 *Illustration of the principles for simulating the lifting of the slump cone when it is turned upside down (D100). To the left is shown the computational mesh in the part which the cone passes through, and the blue line represents the cone boundary at given time t. To the right, the mesh is highlighted and illustrates the principles for computing the moving boundary.*

Nodes are considered part of the boundary if $\Delta z_{n-b}(r,t) \leq \frac{1}{2}\Delta z_{n-n}$ where $\Delta z_{n-b}(r,t)$ is the distance from node n to the cone boundary in the z-direction and Δz_{n-n} is the distance between nodes of an element in the z-direction. When nodes are part of the cone boundary, the velocities $v_z^n = U_{lift}$ and $v_r^n = 0$, where U_{lift} is cone lifting velocity in the z-direction. Therefore, the lifting of the cone is modelled as a moving fluid boundary with a thickness of approximately $\frac{1}{2}$ times the element thickness (~ 0.4 mm) .

Simulations have been carried out with both a constrained and a shear stress type of boundary condition for the bottom plate.

5.3.2 L-Box

Figure 5.7 shows the geometry of the L-box. A moveable gate divides the vertical and the horizontal section. The vertical section is filled with concrete and the gate is lifted to allow concrete to flow past the reinforcement bars and into the horizontal section.

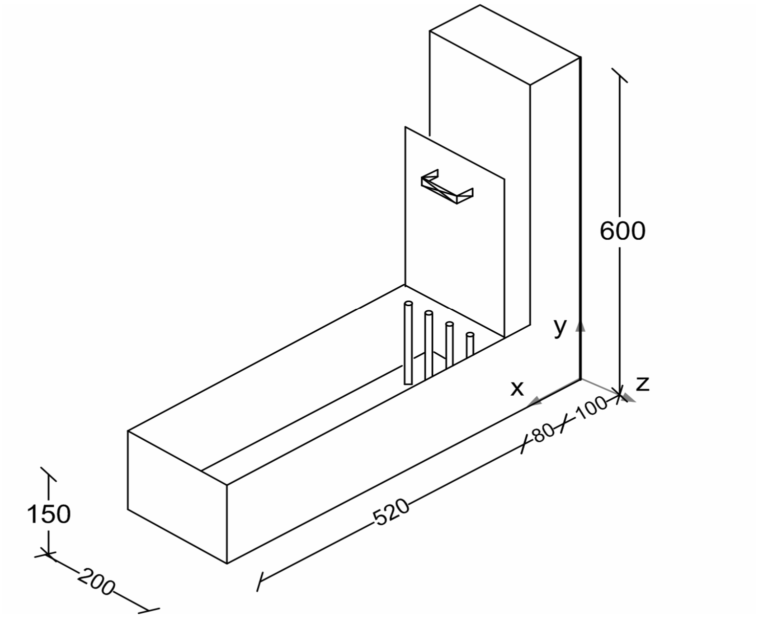

Figure 5.7 *The geometry of the L-box applied in this study (measures in mm). Four bars with a diameter d_{bar} = 10 mm are placed so the closest distance between the center of two bars is 40 mm.*

In Chapter 7, it is investigated whether it is reasonable to assume that the transient flow in the x-direction may be modelled in two dimensions (channel flow) in order to limit the requirements for computational capacity. In two dimensional flow there is no effect from the boundaries in the xy-plane. Simulations of the L-box without reinforcement are carried out in two and three dimensions for particular choices of viscosity. Figure 5.8 shows the two-dimensional model of the L-box.

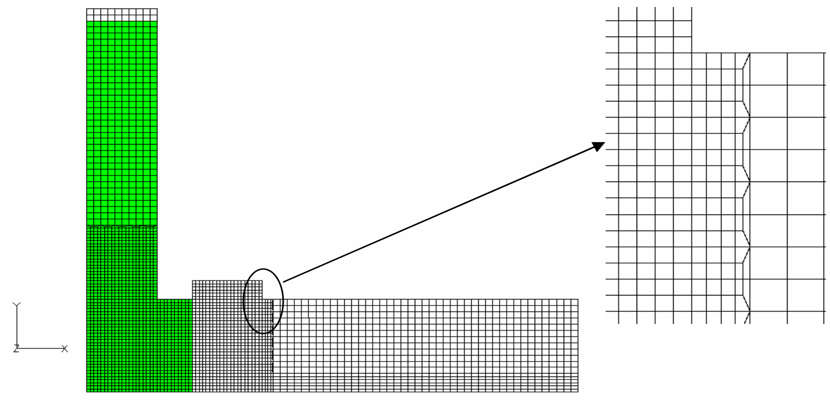

Figure 5.8 *The two-dimensional computational mesh of the L-box model without reinforcement.*

As for the slump flow test, linear interpolation for the velocity has been selected. The flow domain consists of four-node quadrilateral elements.

In three dimensions it is assumed that the flow is symmetric across the xy-plane at $z =$ -100 mm. Figure 5.9 shows a section of the three-dimensional computational mesh of the L-box. It shows the surface at the boundaries, and the three-dimensional eight-node brick elements are created by propagating the boundary mesh in the direction of the normal vector.

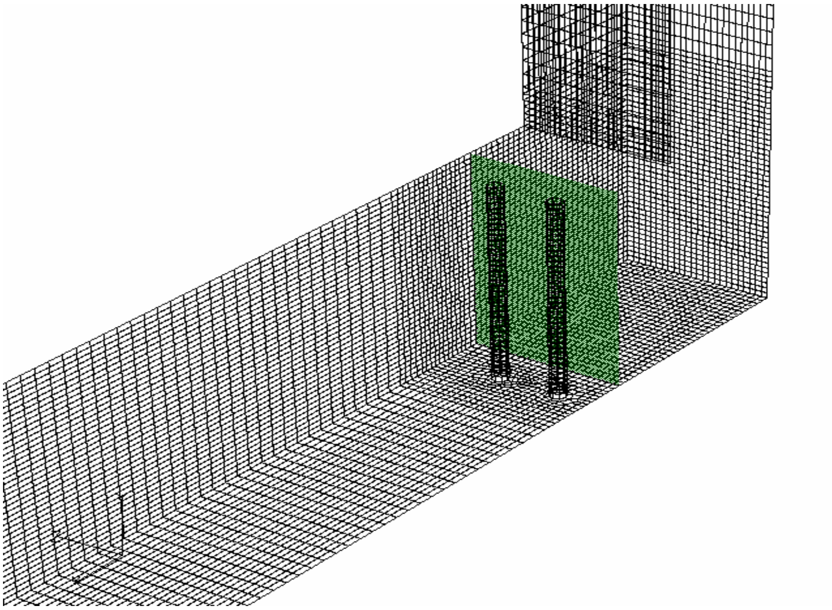

Figure 5.9 *A section of the three-dimensional L-box model showing the computational mesh at the surface boundaries. Eight-node bricks elements are created from these surface meshes by propagating them in the direction of the normal vector.*

The lifting velocity of the gate is written into a subroutine. The velocities u_x^n, u_y^n, and u_z^n of a node n belonging to the face of the gate are constrained to zero if $z_n \geq h_{gate}$ for n = 1, 2, ..N, where z_n is the z-coordinate of node n, $h_{gate} = U_{lift} \cdot t$ is the height the gate above the bottom of the L-box ($z = 0$) at time t, and N is the number of nodes at the face of the gate. If $z_n < h_{gate}$, the velocities u_x^n, u_y^n, and u_z^n are solved for.

At all interfaces between the concrete and the sides of the L-box, a constrained boundary condition has been applied where the velocity is constrained to zero (no-slip).

5.3.3 Form Work - Laboratory

A vertical formwork was produced to test the form filling behaviour on a larger scale of time and length than in the slump flow test and the L-box test. Figure 5.10 shows the geometry of the formwork. The formwork has a length of 3.00 m, a height of 1.20 m, and a width of 0.30 m. An inlet is placed at the lower bottom corner from which pumping of the concrete is possible. The location of its center is $(x, y, z) =$ (0.35 m, 0.20 m, 0 m).

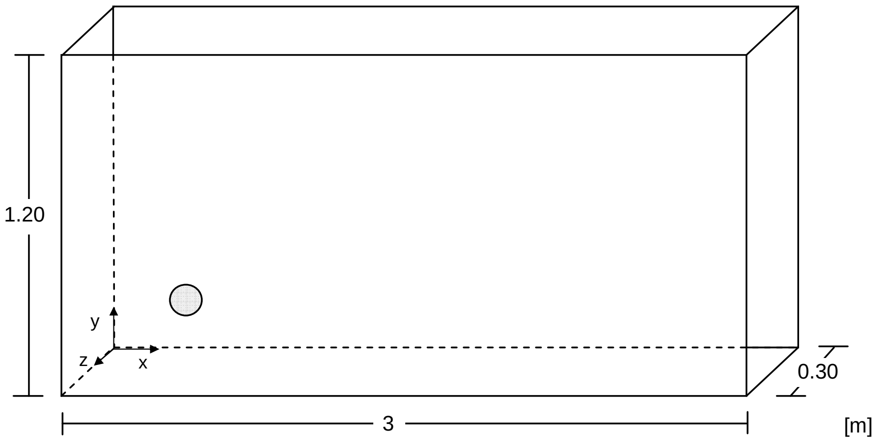

Figure 5.10 *The geometry of the laboratory form work. An inlet is placed on one side at the lower bottom corner with the center at* $(x, y, z) = (0.35\ m, 0.20\ m, 0\ m)$.

Experiments have been carried out with and without reinforcement.

The numerical model without reinforcement is shown in Figure 5.12. The elements consist of eight-node brick elements with linear interpolation for the velocity. It shows the surface mesh which is propagated in the direction of the normal vector to the surface to create the brick elements. The inlet is rectangular instead of the actual cylindrical shape in order to reduce the size and complexity of the mesh which is shown to the right in Figure 5.11. It is assumed that this does not have any significant influence on the results of the simulations.

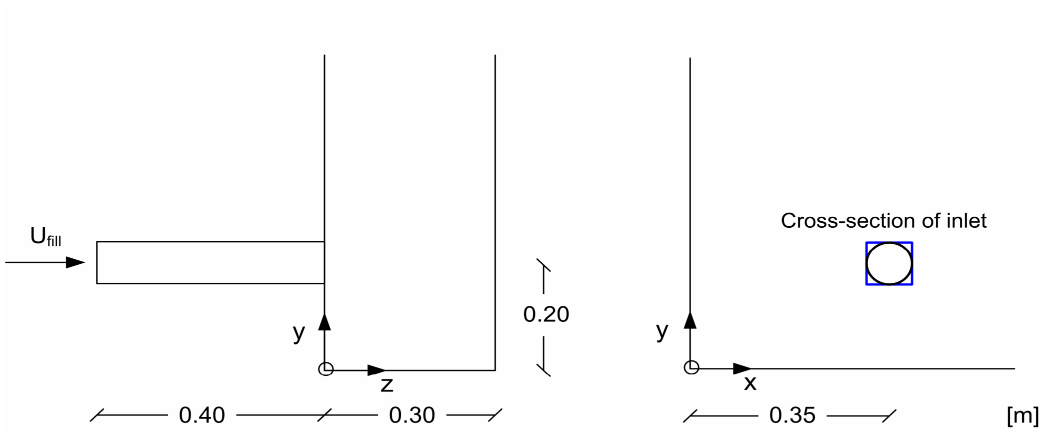

Figure 5.11 *The geometry of the inlet applied in the model of the laboratory formwork. To the left, a constant velocity* $u_z = U_{fill}$ *is applied over the cross-section at* $z = -0.40$ *m. To the right, the cross-section geometry of the inlet applied in the model (blue) and in the experiment (black).*

To capture the flow behavior of the fluid entering the formwork an inlet with a length of 0.40 m has been applied. During the initial filling, the inlet cross-section at $z = 0$

is not completely covered with fluid. A constant velocity $u_z = U_{fill}$ is applied over the cross-section at $z = -0.40$ m corresponding to the filling rate applied in the experiment (see Figure 5.11 to the left).

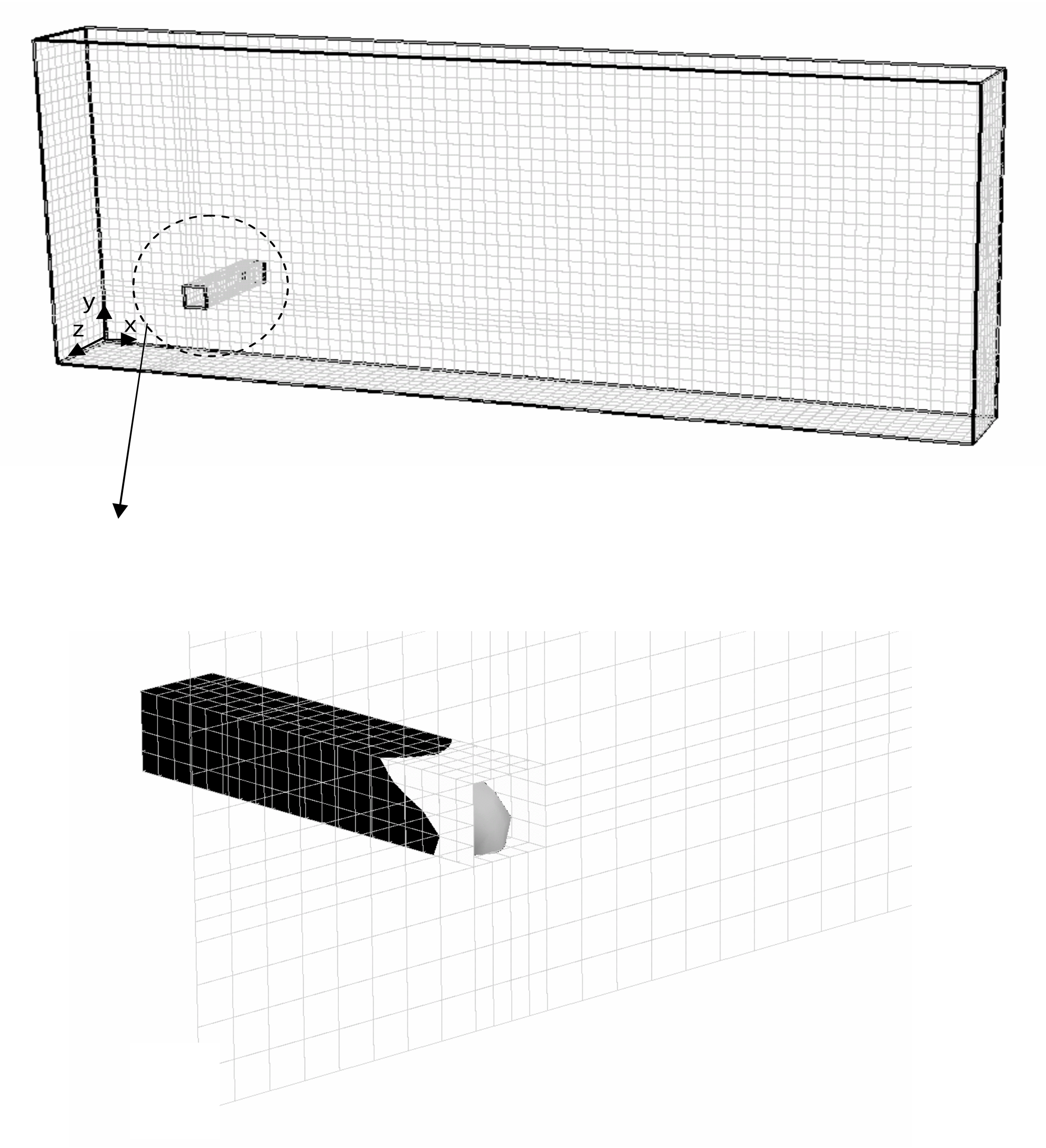

Figure 5.12 *The three-dimensional model of the laboratory formwork without reinforcement showing the computational mesh of the surface boundaries. Eight-node bricks elements are created from these surface meshes by propagating them in the direction of the normal vector.*

For the experiment carried out with reinforcement, the configuration is shown in Figure 5.13. The reinforcement consists of four reinforcement grids. The inner dimensions of the grids are $0.15 \cdot 0.15$ m^2. Additional bars have been applied between two of the grids to vary the clear spacing and thereby the ratio between the clear spacing and particle size.

When placed in the formwork, the reinforcement has been placed so it starts at $x = 0.70$ m and end at $x = 1.45$ m.

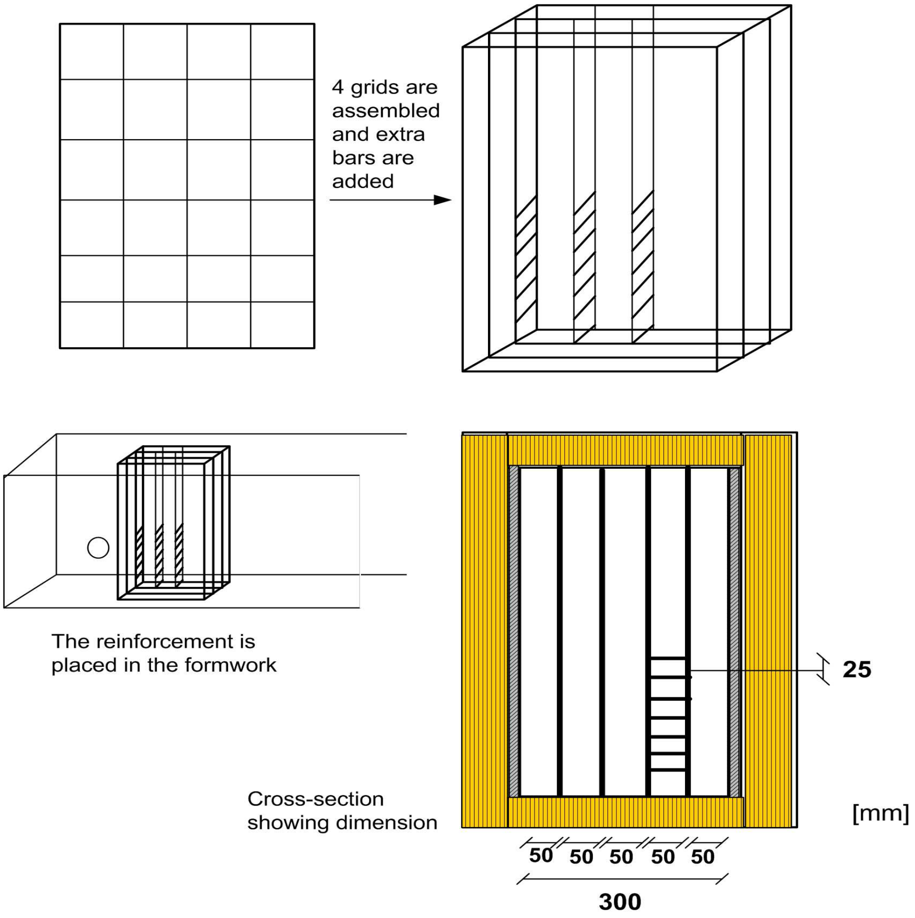

Figure 5.13 *Reinforcement configuration applied in the laboratory form.*

The computational model of the formwork with reinforcement is shown in Figure 5.14. The gap between the surface of the bars is equal to the minimum size between the cylindrical bars used in the experiment. Figure 5.15 shows the surface mesh in the part of the formwork where the reinforcement is placed. In order to reduce the complexity and number of elements, the cross-section of the reinforcement is assumed to be quadratic instead of cylindrical with a side length corresponding to the diameter of the reinforcement bars.

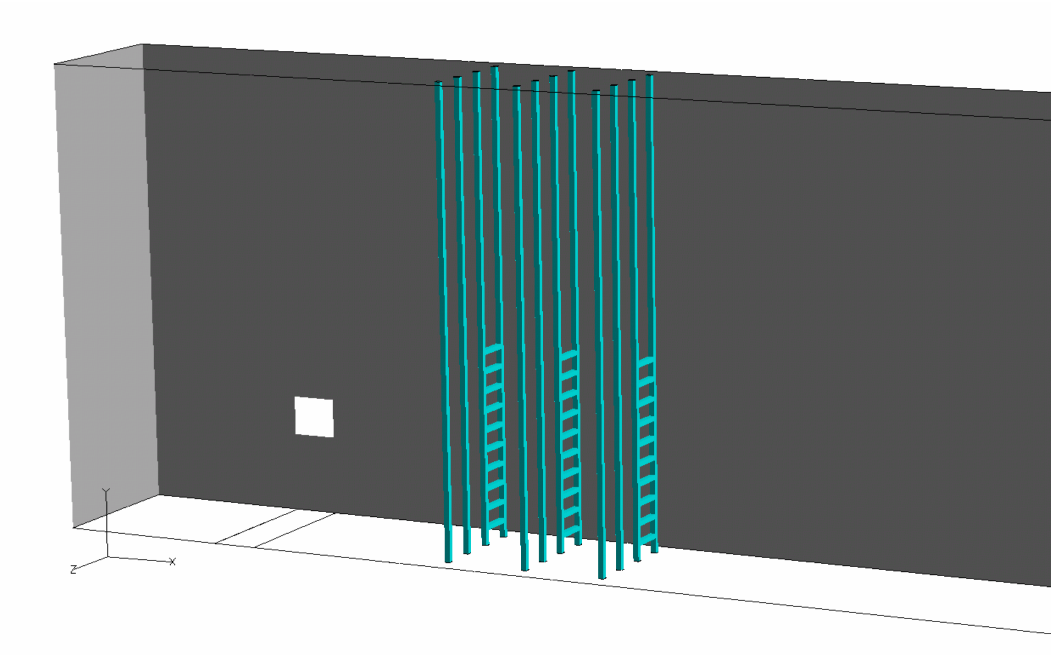

Figure 5.14 *The three-dimensional model of the laboratory formwork with reinforcement.*

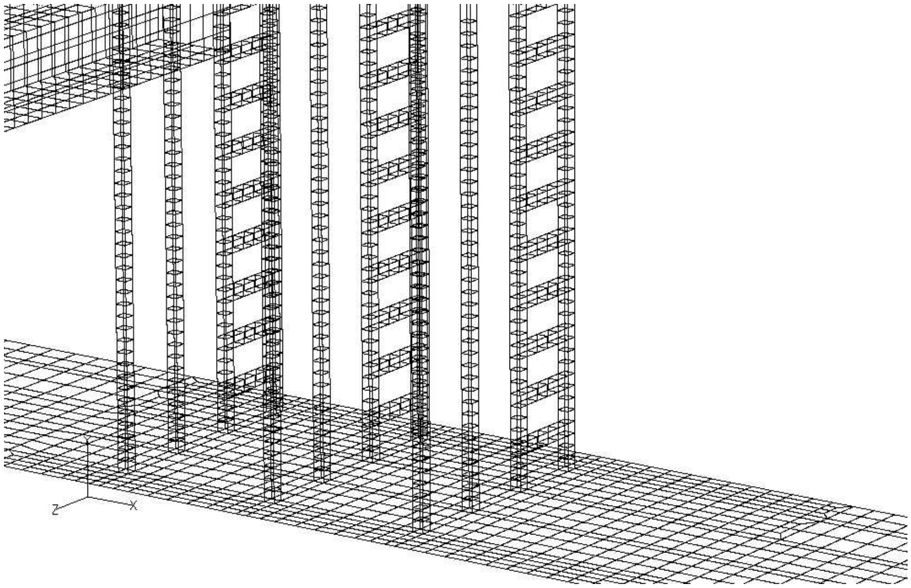

Figure 5.15 *Example of the computational surface mesh near the reinforcement in the three-dimensional model of the laboratory formwork with reinforcement.*

5.3.4 Form Work - Full-Scale

Five different full scale form filling tests have been carried out applying the same formwork geometry, however, different casting techniques. The form geometry is shown in Figure 5.16 and has a length of 5.0 m, height of 4.0 m, and a width of 0.50 m. A light reinforcement grid is placed approximately 5 cm from each side of the formwork. The initial position of the inlet in the five form filling experiments is approximately 0.20 m above the bottom of the formwork.

During filling, the inlet is either placed 0.50 m below the free surface, placed 0.50 m above the free surface, or 0.20 m above the bottom corresponding to situations A, B, and C in Figure 5.17, respectively. In Chapter 7, the five tests are referred to as Fu_1, Fu_2, Fu_3, Fu_4, and Fu_5. Tests Fu_1 and Fu_4 apply the casting technique of situation A. Tests Fu_2 and Fu_5 apply the castings technique in situation B, and test Fu_3 apply the casting technique in situation C.

As the inlet is placed in the plane of symmetry, the flow is also symmetric across the plane of symmetry. In order to limit the size of the model, it is assumed that the z-component of the velocity field is negligible compared to the x and y components, respectively. The two-dimensional model is shown in Figure 5.18. The inlet velocity in the two-dimensional model is chosen so it corresponds to the three-dimensional filling rate in the experiments. A subroutine has been written to handle the lifting of the concreting pipe in situations A and B, similar to the procedures outlined for the cone and gate in the slump flow and L-box test, respectively.

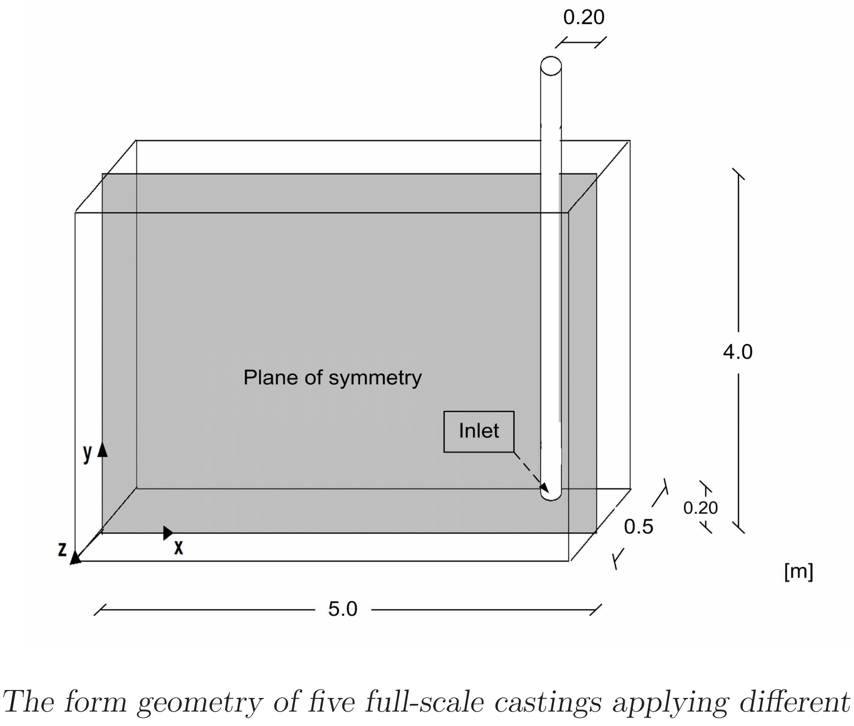

Figure 5.16 *The form geometry of five full-scale castings applying different castings techniques and the initial position of the inlet. The inlet diameter is 0.08 m.*

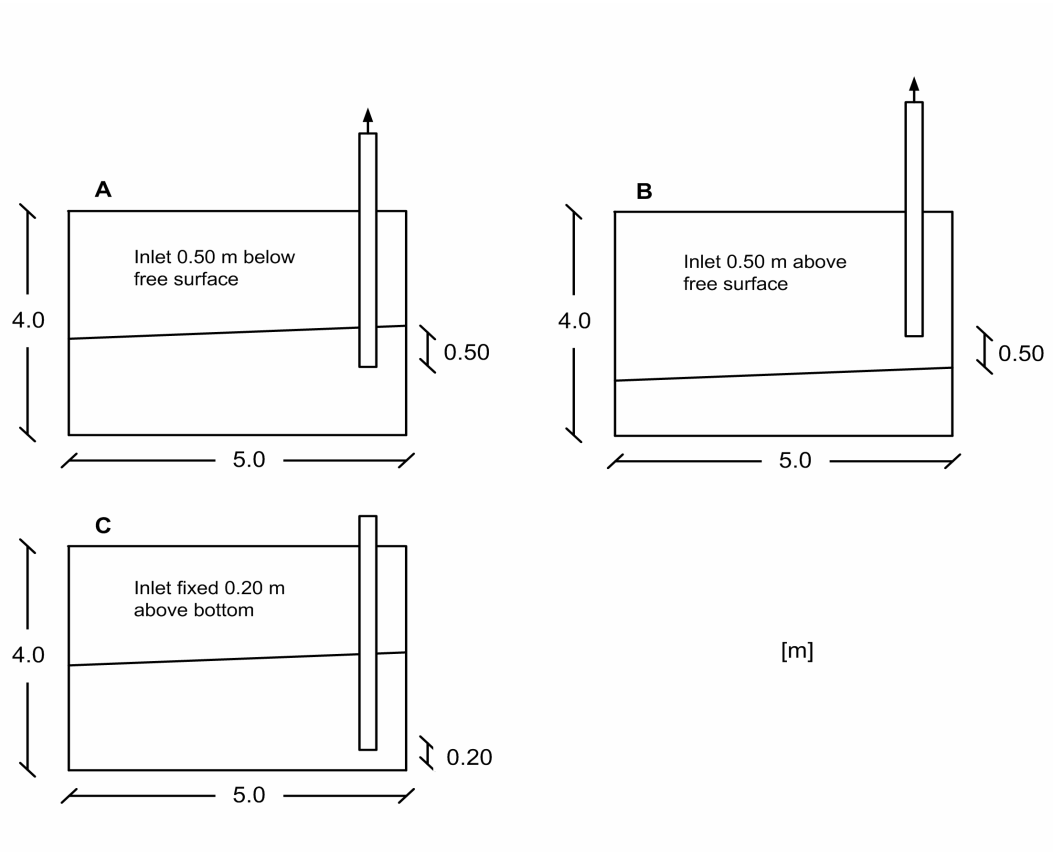

Figure 5.17 *The three casting techniques (A, B, and C). The five full-scale castings Fu_1, Fu_2, Fu_3, Fu_4, and Fu_5 apply casting technique A, B, C, A, and B, respectively.*

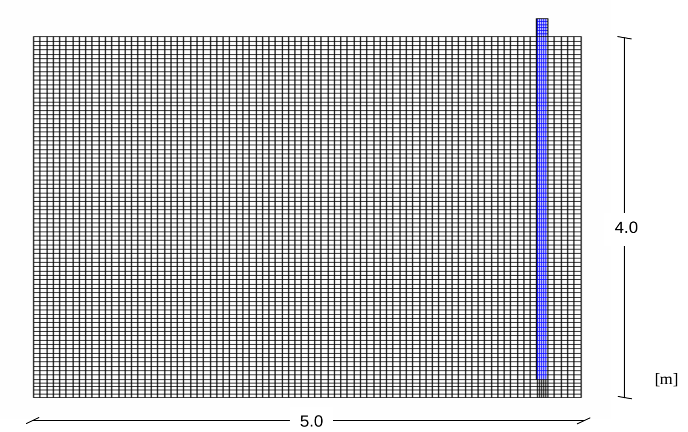

Figure 5.18 *The two-dimensional model of the full-scale castings consisting of four-node quadrilateral elements. The blue area represents the concreting pipe. A subroutine is applied to handle the position of the inlet when the concreting pipe is lifted.*

Chapter 6

Heterogeneous Flow: Blocking

Chapters 4 and 5 presented the computational fluid dynamics approach applied to simulate homogeneous flow. This included the mathematical formulation of flow and the numerical solution to the selected flow domains; the slump flow test, the L-box test, the two laboratory formwork, and the five full-scale formwork.

SCC has to flow past reinforcement, and it is important to assess under which conditions blocking of aggregates occurs. Blocking of aggregates occurs when the aggregates are retained by reinforcement bars as illustrated in Figure 3.6 in Chapter 3. The flow in the L-box and in the form filling applications include flow between reinforcement.

Previous studies of blocking were discussed in Section 3.2. In general, existing methods for assessment of the blocking of a suspension have focused on a criterion based on geometrical considerations - the ratio of flow domain geometry to the particle size, and the particle volume fraction. The effect of flow dynamics and material properties, such as the viscosity, has not been considered in these approaches.

This Chapter proposes a theoretical framework for evaluation of the risk of blocking in the flow of a suspension in a confined flow domain. The aim is to obtain a relatively simple analytical and phenomenological model to describe blocking, taking into account the dynamics of flow, which is considered by introducing a flow rate criterion. The phenomenological model may be used for parameter studies on the effect of, e.g. the suspension viscosity, matrix viscosity, and particle volume fraction on the critical flow rate.

This Chapter is outlined as follows:

- The hypothesis of blocking occurring below a critical flow rate is discussed (Section 6.1).
- The modelling approach is presented, which consider the flow of a monodisperse suspension in a finite circular tube flow domain (Section 6.2).
- The overall mathematical formulation of the flow rate criterion is described. It includes the modelling of homogenous suspension flow where the matrix flow is

equal to the particle flow, and heterogeneous flow where the matrix flows relative to the particles (Section 6.3).

- Modelling the homogeneous suspension flow is based on existing pressure drop - flow rate relations for a finite circular tube flow domain (Section 6.3.1).
- Modelling of matrix flow relative to particle flow is discussed (Section 6.3.2). Existing theories for fluid flow through a packed bed are presented, and the approach applied in this study for flow in a finite circular tube flow domain is discussed.
- The matrix flow relative to the particles depends on the interparticular configuration of the particles. The interparticular configuration in a finite circular tube flow domain is discussed, and a modified theory for the interparticular configuration is proposed (Section 6.3.3). The proposed modifications are based on assumptions of the particle configuration of a packed bed of monodisperse spheres and existing models for the porosity of packed bed in a finite circular tube flow domain at low confinement ratios (tube radius over particle radius).
- The flow rate criterion is illustrated in Section 6.4, and a parameter study on the effect of the confinement ratio, absolute tube radius, and the rheological properties are carried out and discussed in Section 6.5.
- The experimental results from piston driven flow of monodisperse suspensions in a circular tube are presented. Tests are carried out for varying piston velocity, tube radius, particle volume fraction, and particle shape. The experimental results are discussed in relation to the phenomenological behavior of the model (Section 6.6).
- The model is discussed in relation to assessment of SCC flow between reinforcement. A procedure is proposed to assess a corresponding circular tube radius for flow between reinforcement.

The proposed procedure for assessment of a corresponding tube radius is applied in Chapter 7 for estimation of a critical flow rate of SCC flow between reinforcement in the L-box and form filling applications.

6.1 Hypothesis

In the studies presented in Section 3.2 on blocking and dynamic segregation, flow rate dependent phase separation was observed in some of the investigations.

Assuming only hydrodynamic interactions, it is assumed that blocking occurs below a critical flow rate. The results of Ramachandran et al. (2000) (and partly Pandya et al. (1998)) indicate that this assumption may only be valid when the particle interaction is not influenced by surfaces forces, such as repulsion between colloid particles.

Qualitatively, the critical flow rate in a finite flow domain may be described as follows.

In two-phase flow, the particles flow due to the hydrodynamic drag force (F_{drag}) exerted by the matrix on the particles. Hydrodynamic forces in a collection of spheres in a viscous creeping flow have been studied by many researchers. For instance, Liu, Muller & Denn (2003) investigated the interactions of two collinearly spheres in creeping flow with a Bingham material and recently Jie & Zhu (2006) applied numerical modelling to calculate the drag forces of an interacting coaxial sphere chain suspended in a Herschel-Bulkley fluid flow.

It is assumed that the drag force must overcome the particle interactions (F_{p-p}), and in finite domains also the interaction between particles and fixed solid boundaries (F_{p-b}), to maintain a homogeneous flow of the suspension. Figure 6.1 illustrates, in principle, the collision forces acting on a particle divided into their normal and tangential components $F_{p-p,n}$, $F_{p-p,t}$, $F_{p-b,n}$, and $F_{p-b,t}$.

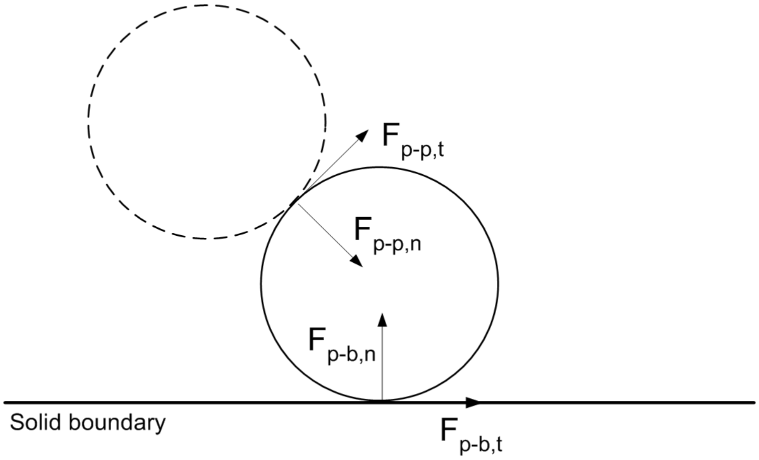

Figure 6.1 *Illustration of collision forces acting on a particle in a suspension flow where* F_{p-p} *is the force acting on a particle from collision with other particles and* F_{p-b} *is the force acting on a particle from collision with the solid boundaries. The forces are divided into normal (n) and tangential (t) components.*

As the gap narrows, it is assumed that the resistance to flow due to particle-solid boundary interactions increases. The solid boundaries are fixed in space for which reason the risk of initiating blocking increases if not overcome by the drag force.

The drag force on the particles depends on the local shear rate at the particle interface and the matrix viscosity (see Figure 3.2). The shear rate is a function of the suspension flow rate (Q_0) and the distance between the particles. The latter depends on the particle volume fraction (ϕ_p), the maximum particle volume fraction (ϕ_p^*), the particle size (d_p), and the particle shape. At a given shear rate, the drag force increases by increasing the matrix viscosity. Factors, such as slip at the particle interface, may reduce the drag force.

Regarding the particle shape, it is assumed that spherical particles require less drag than irregular particles to avoid interlocking of particles due to the ball bearing effect and a smaller contact area between the particles.

6.2 Modelling Approach

It is assumed that blocking of particles is flow rate dependent, i.e. blocking occurs below a critical flow rate. A phenomenological model for estimation of the critical flow rate is derived for the flow of a suspension in finite circular tube flow domain. It is assumed that

- the suspension consists of two phases, a monodisperse particle phase of spherical shape, and a viscous matrix phase.
- a critical flow rate may be formulated by comparing the pressure drop required to retain a constant flow rate (Q_0) in the two situations; homogenous flow and heterogeneous flow. The procedure is independent on a specific choice of the matrix velocity relative to the particles.
- only hydrodynamic interactions influence the blocking phenomena, i.e. the non-hydrodynamic influences, such as inertial, electrostatic, and Brownian motion forces are assumed negligible.
- the apparent viscosity of the suspension and matrix follows a Bingham model with a yield stress and plastic viscosity.
- a composite model may be applied for estimation of the suspension yield stress and plastic viscosity when assuming only hydrodynamic interactions.

The homogeneous flow of the suspension is modelled using the existing Buckingham-Reiner equation for the pressure drop - flow rate relation of a Bingham fluid in a circular tube (Buckingham 1921)(Bird et al. 1960).

Heterogeneous flow consists of matrix flow relative to particle flow. The matrix flow is formulated based on existing packed bed theories and considerations of the effect of the interparticular particle configuration and the wall effect on the capillary radius.

In the outline of the phenomenological model, the input parameters for estimation of a critical flow are:

- Matrix viscosity ($\tau_{m,0}$, $\eta_{m,pl}$)
- Particle radius (r_p)
- Tube radius (R)
- Particle volume fraction (ϕ_p)
- Maximum particle volume fraction (ϕ_p^*)

Finally, a method is proposed for assessment of a corresponding tube radius for flow between reinforcement.

6.3 Mathematical Formulation of a Flow Rate Criterion

The overall mathematical concept for deriving of a critical flow rate is presented.

First, a control volume, $V_c = \Delta x \Delta y \Delta z$, is considered as shown in Figure 6.2. It consists of a matrix and a particle phase, respectively. A constant flow rate (Q_0) is imposed in the x-direction.

The average velocities of the suspension, particle, and matrix in the x-direction are given by $v_{s,i}$, $v_{p,i}$, and $v_{m,i}$, respectively. The index i = 1, 2 denotes flow in and out of the control volume. At a given flow rate, the average suspension velocity $v_{s,1} = v_{s,2}$ in both the homogeneous and heterogeneous flow for which reason the average suspension velocity will be denoted v_s in the following.

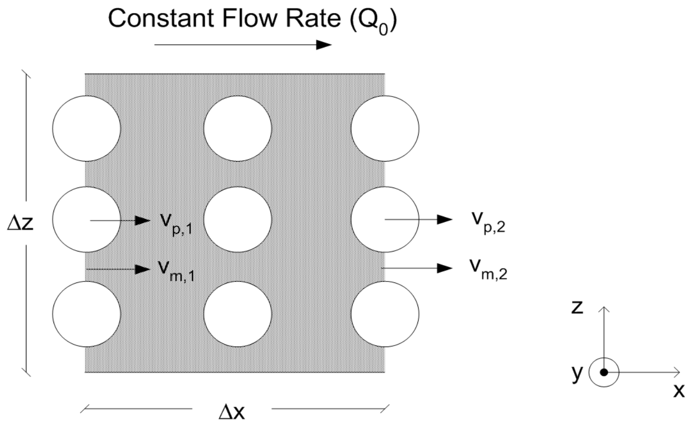

Figure 6.2 *Illustration of average matrix and particle velocities, $v_{m,i}$ and $v_{p,i}$, in and out of a control volume $V_c = \Delta x \Delta y \Delta z$. Indexes i = 1, 2 denotes flow in and out of the control volume. A constant flow rate (Q_0) is imposed in the x-direction. Blocking is initiated if $v_{p,2} < v_{p,1}$.*

If a constant particle flow rate ($Q_{p,1}$) and matrix flow rate ($Q_{m,1}$) into the control volume is assumed, these are given by

$$\begin{aligned} Q_{p,1}(t) &= Q_0 \phi_p(t_0) \\ Q_{m,1}(t) &= Q_0(1 - \phi_p(t_0)) \end{aligned} \tag{6.1}$$

where it is assumed that the particle volume fraction is equal to the particle area fraction of a cross-section and $\phi_p(t_0)$ is the particle volume fraction at $t = 0$.

In homogeneous flow, the average suspension, particle, and matrix velocities are given by

$$v_s = v_{p,i} = v_{m,i} = \frac{Q_0}{\Delta y \Delta z} \tag{6.2}$$

In heterogeneous flow, the average particle ($v_{p,i}$) and matrix ($v_{m,i}$) velocities vary. For instance, assuming a constant particle velocity gradient in the x-direction ($\frac{\Delta v_p}{\Delta x}$), the transient particle and matrix velocities coming in and out of the control will be given by

$$\begin{aligned}
v_{p,1}(t) &= \frac{Q_0 \phi_p(t_0)}{\phi_p(t)\Delta y \Delta z} \\
v_{m,1}(t) &= \frac{Q_0(1-\phi_p(t_0))}{(1-\phi_p(t))\Delta y \Delta z} \\
v_{p,2}(t) &= \frac{Q_0 \phi_p(t_0)}{\phi_p(t)\Delta y \Delta z} + \frac{\Delta v_p}{\Delta x}\Delta x \\
v_{m,2}(t) &= \frac{Q_0(1-\phi_p(t_0))}{(1-\phi_p(t))\Delta y \Delta z} - \frac{\phi_p(t)}{(1-\phi_p(t))}\frac{\Delta v_p}{\Delta x}\Delta x
\end{aligned} \tag{6.3}$$

where the particle volume fraction at $t_{j+1} = t_j + dt$ is given by:

$$\begin{aligned}
\phi_p(t_{j+1}) &= \phi_p(t_j) + \frac{d\phi_p(t_j)}{dt}dt \\
&= \phi_p(t_j) + \frac{\Delta v_p}{\Delta x}\phi_p(t_j)dt \quad j = 1:n, \;\; \phi_p \leq \phi_p^*
\end{aligned} \tag{6.4}$$

Particle accumulation continues until the particle volume fraction reaches the maximum particle volume fraction (ϕ_p^*). If $v_{p,2} = 0$, complete blocking occurs, i.e. only matrix flow through, and the system may be described as a consolidation process. If $0 < v_{p,2} < v_{m,2}$, the heterogeneous flow describes an intermediate stage between the consolidation process and a completely homogeneous flow.

It is assumed that blocking is initiated if it is possible for heterogeneous flow to exist at a pressure drop (ΔP_{sep}) which is lower than the pressure drop required for the flow of a homogeneous suspension (ΔP_{sus}):

$$\begin{aligned}
&\Delta P_{sep} > \Delta P_{sus} : \text{No blocking} \\
&\Delta P_{sep} < \Delta P_{sus} : \text{Blocking} \\
&\Delta P_{sep} = \Delta P_{sus} : \text{Critical flow rate}
\end{aligned} \tag{6.5}$$

Particle accumulation continues if ΔP_{sep} remains less than ΔP_{sus}.

The pressure drop in heterogeneous flow (ΔP_{sep}) is assumed to consist of a suspension part ($\Delta P_{sep,sus}$) and a capillary part ($\Delta P_{sep,cap}$). The suspension part refers to the part in which the matrix flows at the same velocity as the particles ($v_{p,2}$) over the cross section area $\Delta y \Delta z$. The capillary part refers to the part where the matrix flow at a velocity $\Delta v_{pm,2} = v_{m,2} - v_{p,2}$ higher than the particles over the cross section area $(1 - \phi_p)\Delta y \Delta z$.

Homogeneous flow and heterogeneous flow at the initiation of blocking ($t = 0$) are illustrated in Figure 6.3. The heterogeneous flow consists of a suspension part and a capillary part, respectively.

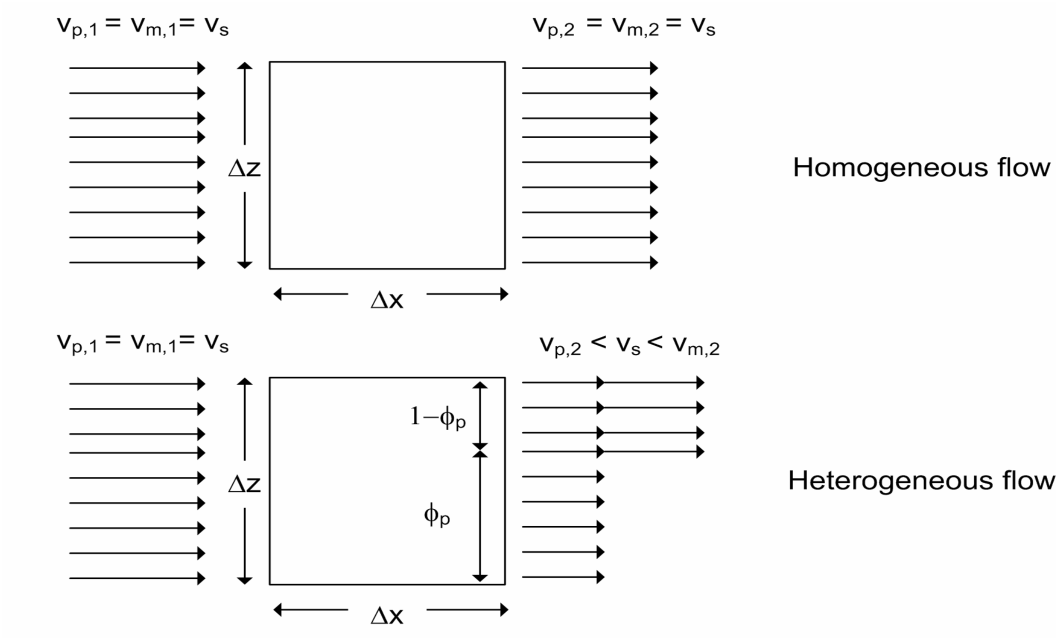

Figure 6.3 *Illustration of homogeneous and heterogeneous flow through a control volume at the initiation of blocking (t=0). The heterogenous flow consist of a suspension and capillary part, respectively. The suspension part flows at a velocity* $v_{p,2}$ *over the cross section area* $\Delta y \Delta z$*, and the capillary part flows at a velocity* $\Delta v_{pm,2} = v_{m,2} - v_{p,2}$ *over the cross section area* $(1 - \phi_p)\Delta y \Delta z$.

In order to determine the pressure drop of a homogeneous suspension flowing in a finite flow domain at a given flow rate, it is decided to consider a circular tube flow domain for which well-known pressure drop - flow rate relations have been developed.

It is assumed that the pressure drop - flow rate relation for matrix flow relative to the particles can be estimated based on capillary theories.

6.3.1 Matrix Flow Equal to Particle Flow

Homogeneous suspension flow occurs when the matrix and particle phase flow at the same velocity.

In a finite circular tube flow domain, the pressure drop - flow rate relation for a Bingham fluid is given by the Buckingham-Reiner equation

$$Q_0 = \frac{\pi R^3 \tau_R}{4\eta_{pl}} \left(1 - \frac{4}{3}\frac{\tau_0}{\tau_R} + \frac{1}{3}\left(\frac{\tau_0}{\tau_R}\right)^4\right) \qquad \tau_R \geq \tau_0 \tag{6.6}$$

where $\tau_R = \frac{\Delta P R}{2L_t}$, R is the tube radius, and L_t is the tube length (Buckingham 1921)(Bird et al. 1960).

Equation 6.6 will be applied to determine ΔP_{sus} in the homogenous suspension flow and $\Delta P_{sep,sus}$ for the suspension part in the heterogenous flow. Thus, τ_0 and η_{pl} are replaced by $\tau_{s,0}$ and $\eta_{s,pl}$.

The yield stress ($\tau_{s,0}$) and plastic viscosity ($\eta_{s,pl}$) are functions of the particle volume fraction (ϕ_p). In Section 3.1.3 it was shown that both the plastic viscosity and yield stress are increasing functions of the particle volume fraction, and different composite models have been proposed. The simple Krieger-Dougherty relation has proven to be able to describe the apparent viscosity of various monodisperse model suspensions. Considering that the blocking model is initially phenomenological and taking into account that most of the other proposed models rely on experimental calibration, it is decided to apply the expressions derived for a Bingham suspension based on the Krieger-Dougherty expression for the apparent viscosity. Equation 3.10 and 3.11 are rewritten here in Equation 6.7.

$$\begin{aligned} \eta_{s,pl} &= \eta_{m,pl}\left(1 - \frac{\phi_p}{\phi_p^*}\right)^{-[\eta]\phi_p^*} \\ \tau_{s,0} &= \tau_{m,0}\left(1 - \frac{\phi_p}{\phi_p^*}\right)^{-[\eta]\phi_p^*} \end{aligned} \tag{6.7}$$

where $\eta_{s,pl}$ is the plastic viscosity of the suspension, $\eta_{m,pl}$ is the plastic viscosity of the matrix, $\tau_{s,0}$ is the yield stress of the suspension, $\tau_{m,0}$ is the yield stress of the matrix, ϕ_p^* is the maximum particle volume fraction, and $[\eta]$ is the intrinsic viscosity. The maximum particle volume fraction and intrinsic viscosity were discussed in Section 3.1.3. It is assumed that the maximum particle volume fraction of the bulk suspension is equal to 0.64 for a random close packing of spheres and the intrinsic viscosity is set to a value of 2.5, which is often applied for spherical particles.

6.3.2 Matrix Flow Relative to Particle Flow

As part of estimating the pressure drop of heterogeneous flow (ΔP_{sep}), the pressure drop from the capillary part ($\Delta P_{sep,cap}$) has to be estimated. This corresponds to the part in which the matrix flows relative to the particles.

Estimating the pressure drop - flow rate relation for matrix flow through a packed bed is of relevance to the design of many different processes in the industry.

Darcy was the first to develop an empirical equation to describe the one-dimensional flow of a Newtonian fluid through a uniform incompressible porous media. Darcy's law is defined as

$$\frac{Q_0}{A_b} = U = -\frac{k}{\mu_m}\frac{\Delta P}{L_b} \tag{6.8}$$

where Q_0 is the volume flow rate, U the mean linear fluid velocity (or superficial velocity as introduced by Bird et al. (1960)), μ_m is the Newtonian matrix viscosity, A_b is the cross sectional area, L_b is the length of the sample, ΔP the pressure drop, and k is the coefficient of permeability (Darcy 1856).

The permeability (k) of a porous medium is a measure of the matrix conductivity through the particles and depends on factors, such as the particle volume fraction, the particle size, the particle shape, the morphology, the chemical properties, and the pore connectivity (Darcy 1856).

Capillary theories have been proposed to estimate the permeability k. Blake (1922) was the first to suggest that the particle skeleton could be thought of as a single pipe with a complicated cross section with a hydraulic radius (r_h), which is defined as the ratio of volume filled with liquid over the wetted surface. If it is accepted that the wetted surface area is equal to the particle surface area and the area lost to the contact between particles is negligible, it may be expressed in terms of the specific surface area of a single spherical particle ($S_0 = 3/r_p$) to give

$$r_h = \frac{\phi_m}{S_0(1-\phi_m)} = \frac{(1-\phi_p)r_p}{3\phi_p} \tag{6.9}$$

where r_p is the particle radius, ϕ_m is the void volume fraction (porosity), and ϕ_p is the particle volume fraction.

The hydraulic radius (Eq. 6.9) is illustrated for three different particle radius in Figure 6.4. The hydraulic radius is shown as a function of the normalized particle volume fraction (ϕ_p/ϕ_p^*) where $\phi_p^* = 0.64$ is the maximum particle volume fraction for random close packing of spheres (Jaeger & Nagel 1992). It shows that the hydraulic radius decreases as a function of the particle volume fraction, i.e. the bed resistance to matrix flow increases, and approaches infinite for $\phi_p \to 0$ where the bed resistance is zero. Also, at a given particle volume fraction, the hydraulic radius decreases for decreasing particle sizes which also results in a higher bed resistance.

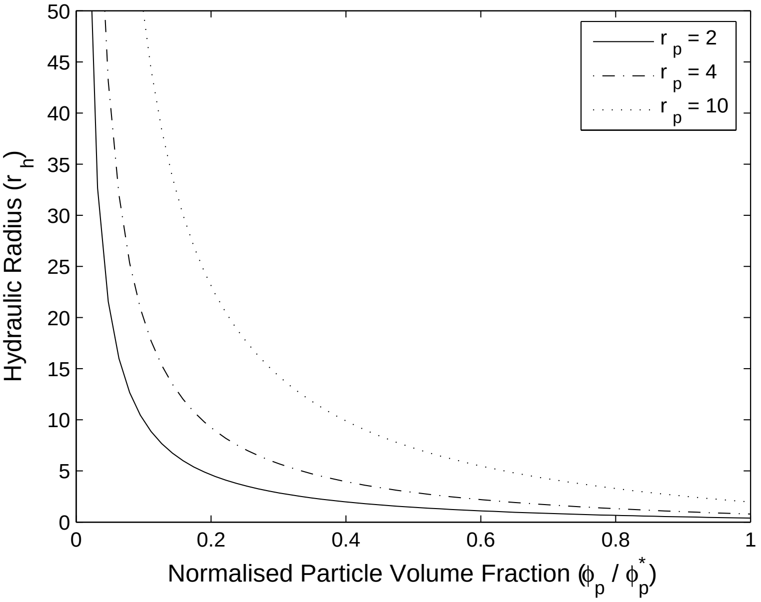

Figure 6.4 *The hydraulic radius (r_h) calculated according to Equation 6.9 for an infinite packed bed of monodisperse spheres as a function of the normalized particle volume fraction (ϕ_p/ϕ_p^*) for three different particle radius r_p = 2, 4, and 10 [length dimension].*

Based on the hydraulic radius, Kozeny (1927) and Carman (1937) proposed a general equation for Newtonian flow through any non-circular capillary given by

$$v_m = \frac{r_h^2}{k_0 \mu_m} \frac{\Delta P}{L_e} \tag{6.10}$$

where v_m is the average velocity of matrix flow, k_0 is a coefficient which depends on the shape of the capillary ($k_0 = 2$ for circular cross sections), and L_e is the length of the path through the pore space, which is assumed to be tortuous and therefore of a greater length than the sample length L_b.

The so-called Carman-Kozeny equation is derived by writing the relation between the mean linear velocity (U) and the average matrix velocity (v_m), which gives

$$\begin{aligned}
U &= v_m \phi_m \\
U &= \frac{r_h^2}{k_0 \mu_m} \frac{\Delta P}{L_e} \phi_m \\
U &= \frac{\phi_m^3 r_p^2}{9(1-\phi_m)^2 k_0 \mu_m} \frac{\Delta P}{L_e} \frac{L_b}{L_b} \\
U &= \frac{\phi_m^3 d_p^2}{36(1-\phi_m)^2 k_0 (\frac{L_e}{L_b}) \mu_m} \frac{\Delta P}{L_b}
\end{aligned} \tag{6.11}$$

where $k_k = k_0(\frac{L_e}{L_b})$ is known as the Kozeny constant and the ratio $(\frac{L_e}{L_b})$ is known as the tortuosity. Later Carman suggested that the time to pass through L_e is greater than L_b by a amount of $(\frac{L_e}{L_b})$ to obtain the Carman-Kozeny constant $k_{ck} = \left(\frac{L_e}{L_b}\right)^2 k_0$. The Carman-Kozeny equation is then given by

$$U = \left(\frac{\phi_m^3 d_p^2}{36(1-\phi_m)^2 k_0 (\frac{L_e}{L_b})^2 \mu_m} \right) \frac{\Delta P}{L_b} \tag{6.12}$$

where the term in the brackets is the permeability for a Newtonian matrix flowing through a packed bed of monodisperse spheres.

Equation 6.12 may also be obtained by considering n_{cap} number of straight cylindrical capillaries of radius, r_{cap}, intersecting the sample (Scheidegger 1974). For a laminar stationary flow, the total flux (Q_m) through the capillaries is given by multiplying n_{cap} by the flow rate of a single circular capillary $(Q_{cap,Newton})$ given by the Hagen-Poiseuille equation (Bird et al. 1987). Thus,

$$\begin{aligned}
Q_m &= n_{cap} \cdot Q_{cap,Newton} \\
Q_m &= \frac{\phi_m \Delta y \Delta z}{\pi r_{cap}^2} \cdot \frac{\pi r_{cap}^4}{8\mu_m} \frac{\Delta P}{L_e} \frac{L_b}{L_b} \\
U &= \phi_m \cdot \frac{r_{cap}^2}{8\mu_m} \frac{\Delta P}{L_e} \frac{L_b}{L_b}
\end{aligned} \tag{6.13}$$

The capillary radius (r_{cap}) for a single straight circular capillary may be written in terms of the hydraulic radius which gives

$$r_h = \frac{V_{cap}}{S_{cap}} = \frac{\pi r_{cap}^2 L_e}{2\pi r_{cap} L_e} = \frac{r_{cap}}{2} \tag{6.14}$$

where V_{cap} is the volume and S_{cap} is the surface area of a straight circular capillary, respectively. Assuming that this can be extended to multiple capillaries using Equation 6.9, the capillary radius (r_{cap}) can then be inserted into Equation 6.13 to give

$$\begin{aligned} U &= \phi_m \cdot \frac{(\frac{2(\phi_m)r_p}{3(1-\phi_m)})^2}{8\mu_m} \frac{\Delta P}{L_e} \frac{L_b}{L_b} \\ U &= \frac{\phi_m^3 d_p^2}{72(1-\phi_m)^2(\frac{L_e}{L_b})\mu_m} \frac{\Delta P}{L_b} \qquad (6.15) \\ U &= \frac{\phi_m^3 d_p^2}{36(1-\phi_m)^2 k_0(\frac{L_e}{L_b})\mu_m} \frac{\Delta P}{L_b} \end{aligned}$$

or the same result as Equation 6.11 with the Kozeny constant $k_k = k_0(\frac{L_e}{L_b})$.

Equations 6.11 and 6.15 give a relation between the pressure drop and flow rate for laminar viscous flow without the effect of inertia, i.e. low Reynolds number.

In order to cover flow over a large number of Reynolds number, Ergun (1952) proposed a combination of the Carman-Kozeny equation with an empirical Burk-Plummer relation to include both viscous and inertia effects. The equation is given by

$$\frac{\Delta P}{L_b} = \left(\frac{E_1(1-\phi_m)^2\mu_m}{d_p^2\phi_m^3}\right) U + \left(\frac{E_2(1-\phi_m)\rho_m}{d_p^2\phi_m^3}\right) U^2 \tag{6.16}$$

where E_1 and E_2 are the first and second Ergun constants, respectively. The equation may also be written in dimensionless form in terms of the so-called bed friction factor and the modified Reynolds number see, e.g. Ergun (1952). The first term on the right side corresponds to the Carman-Kozeny equation for Darcy flow, i.e. $E_1 = 36k_0(\frac{L_e}{L_b})^2$. The second term includes the inertia effect and are relevant at higher Reynolds numbers. For instance, for flow through a packed bed of monodisperse spheres, Fand & Thinakaran (1990) found that the upper bound for Darcy flow was for $Re = 2.3$ where $Re = \frac{d_p U \rho_m}{\mu_m(1-\phi_m)}$). The so-called Forchheimer flow regime including both the viscous and inertial term was found for approximately $5 \leq Re \leq 80$, and turbulent flow was found for $Re > 120$.

The general Equation 6.16 considers Newtonian flow through a packed bed in an infinite flow domain.

The next step is to consider a Bingham matrix flow through a packed bed in a finite circular tube flow domain. In the following, the Bingham extension, the bed parameters (k_0, $\frac{L_e}{L_b}$), the wall effect, and the capillary radius (r_{cap}) are discussed, and the assumptions for the further modelling are described.

Most work on Non-Newtonian fluid flow through packed beds has considered a power law fluid see, e.g. Kozicki, Hsu & Tiu (1967), Kemblowski & Michniewicz (1979), Cohen & Metzner (1981), and Hayes, Afacan, Boulanger & Shenoy (1996).

The Bingham correlation in an infinite domain may be derived in the same way as the Ergun equation, and Chase & Dachavijit (2005) showed it in dimensionless form in terms of the bed friction factor and modified Reynolds number. This include three constants, two of them are assumed equal to the Ergun constants and a third needs empirical calibration depending on the specific material, the packed bed geometry, and surface roughness.

Considering laminar viscous flow at low Reynolds number, the pressure drop - flow rate relation for a Bingham matrix may also be written in the same way as the derivation following Equation 6.13. Thus,

$$\begin{aligned}
Q_m &= n_{cap} \cdot Q_{cap,Bingham} \\
Q_m &= \frac{\phi_m \Delta y \Delta z}{\pi r_{cap}^2} \cdot \frac{\pi r_{cap}^3 \tau_{m,r_{cap}}}{4\eta_{m,pl}} \left(1 - \frac{4}{3}\frac{\tau_{m,0}}{\tau_{m,r_{cap}}} + \frac{1}{3}\left(\frac{\tau_{m,0}}{\tau_{m,r_{cap}}}\right)^4 \right) && \tau_{m,r_{cap}} \geq \tau_{m,0} \\
U &= \phi_m \cdot \frac{r_{cap} \tau_{m,r_{cap}}}{4\eta_{m,pl}} \left(1 - \frac{4}{3}\frac{\tau_{m,0}}{\tau_{m,r_{cap}}} + \frac{1}{3}\left(\frac{\tau_{m,0}}{\tau_{m,r_{cap}}}\right)^4 \right) && \tau_{m,r_{cap}} \geq \tau_{m,0}
\end{aligned} \tag{6.17}$$

where $\tau_{m,r_{cap}} = \frac{\Delta P r_{cap}}{2L_e}\frac{L_b}{L_b} = \frac{r_{cap}}{2\frac{L_e}{L_b}}\frac{\Delta P}{L_b}$ (Buckingham 1921) (Bird et al. 1960).

The packed bed factors $\frac{L_e}{L_b}$ and k_0 are unique parameters for the particular packed bed and refer to the tortuosity of the pore length and the pore cross-sectional geometry. However, these need to be determined from experimental calibration to include also factors, such as the pore connectedness, the rheological properties of the matrix phase, the particle shape, the particle roughness, the particle size distribution, and the confinement ratio of the packed bed.

Cohen & Metzner (1981) presents a review of the numerous experimental investigations that have been carried out for estimation of these factors for Newtonian flow through a packed bed of spherical particles. If it is assumed that $k_0 = 2$, it seems $1.41 \leq \frac{L_e}{L_b} \leq 1.58$ results in a Carman-Kozeny constant $4.166 \leq k_0(\frac{L_e}{L_b})^2 \leq 5$, which is also supported in later studies, e.g. by (Fand & Thinakaran 1990). Basu (2001) studied laminar non-Newtonian power law fluid through a packed bed confined in a circular tube at a low confinement ratio of 3.8 and found values of $k_0 = 1.5$ and $\frac{L_e}{L_b} = 1.2$ corresponding to a Kozeny constant of $k_0(\frac{L_e}{L_b}) = 1.80$ and a Carman-Kozeny constant of $k_0(\frac{L_e}{L_b})^2 = 2.16$ or approximately half of the value for Newtonian flow in an infinite domain.

Most studies consider a large bed length to particle size, e.g. 75 (Basu 2001), 250 (Fand & Thinakaran 1990), 62 (Sodre 1998), 33 (Lin & Miller 1999) and (Montillet 2004), and 2000 (Matveev, Barysheva, Koptyug, Khanaev & Noskov 2006). Considering the blocking phenomena, it may be assumed that matrix flow relative to particle flow initially will occur over a distance corresponding to a few times the particle size, and it is likely that the bed length to particle size may also have an influence on the bed parameters $\frac{L_e}{L_b}$ and k_0. At a low bed length to particle size, it may be assumed that the tortuosity is less pronounced so $L_e \approx L_b$. Assuming that $k_0 = 2$, this gives a Kozeny constant of $k_0(\frac{L_e}{L_b}) = 2$ and a Carman-kozeny constant of $k_0(\frac{L_e}{L_b}) = 2$. The assumptions of $\frac{L_e}{L_b} = 1$ and $k_0(\frac{L_e}{L_b}) = 2$ will be applied in the ongoing, however, experiments should determine the validity of this assumption.

The pressure drop - flow rate relations for Newtonian flow (Eq. 6.16) and Equation 6.17 for Bingham flow do not consider the wall effect (Mehta & Hawley 1969)(Cohen & Metzner 1981)(Fand & Thinakaran 1990)(Larrard 1999)(Basu 2001). Physically, the wall effects the flow in two ways. Firstly, the wall contributes to the wetted surface and thereby friction of the flow, especially at low confinement ratios. Mehta & Hawley (1969) proposed a correction to the Ergun equation to account for the contribution of the wall area to the wetted surface area used in calculation of the hydraulic radius (r_h) given by Equation 6.9. The hydraulic radius ($r_h^{(1)}$) and capillary radius ($r_{cap}^{(1)}$) may then be written as

$$\begin{aligned} r_h^{(1)} &= \frac{(1-\phi_p)R}{\frac{3\phi_p R}{r_p}+2} = \frac{(1-\phi_p)R}{3\phi_p\alpha+2} = \kappa(\phi_p,\alpha)R \quad && \phi_p \leq \phi_p^* \\ r_{cap}^{(1)} &= 2\kappa(\phi_p,\alpha)R && \phi_p \leq \phi_p^* \end{aligned} \tag{6.18}$$

where $\alpha = \frac{R}{r_p}$ is the confinement ratio. The hydraulic radius ($r_h^{(1)}$) and capillary radius ($r_{cap}^{(1)}$) are illustrated in Figure 6.5 for the same parameters applied in Figure 6.4 and at a confinement ratio of $\alpha = 20$. By including the tube surface area in calculation of the hydraulic radius, it does not exceed the tube radius R at $\phi_p = 0$, and the boundary condition $r_{cap}^{(1)} = R$ at $\phi_p = 0$ is obtained. In the next section, the capillary radius at $\phi_p = \phi_p^*$ is discussed in relation to the geometrical considerations of a packed bed of monodisperse spheres at a low bed length to particle diameter ratio, and a modification to Equation 6.18 is proposed.

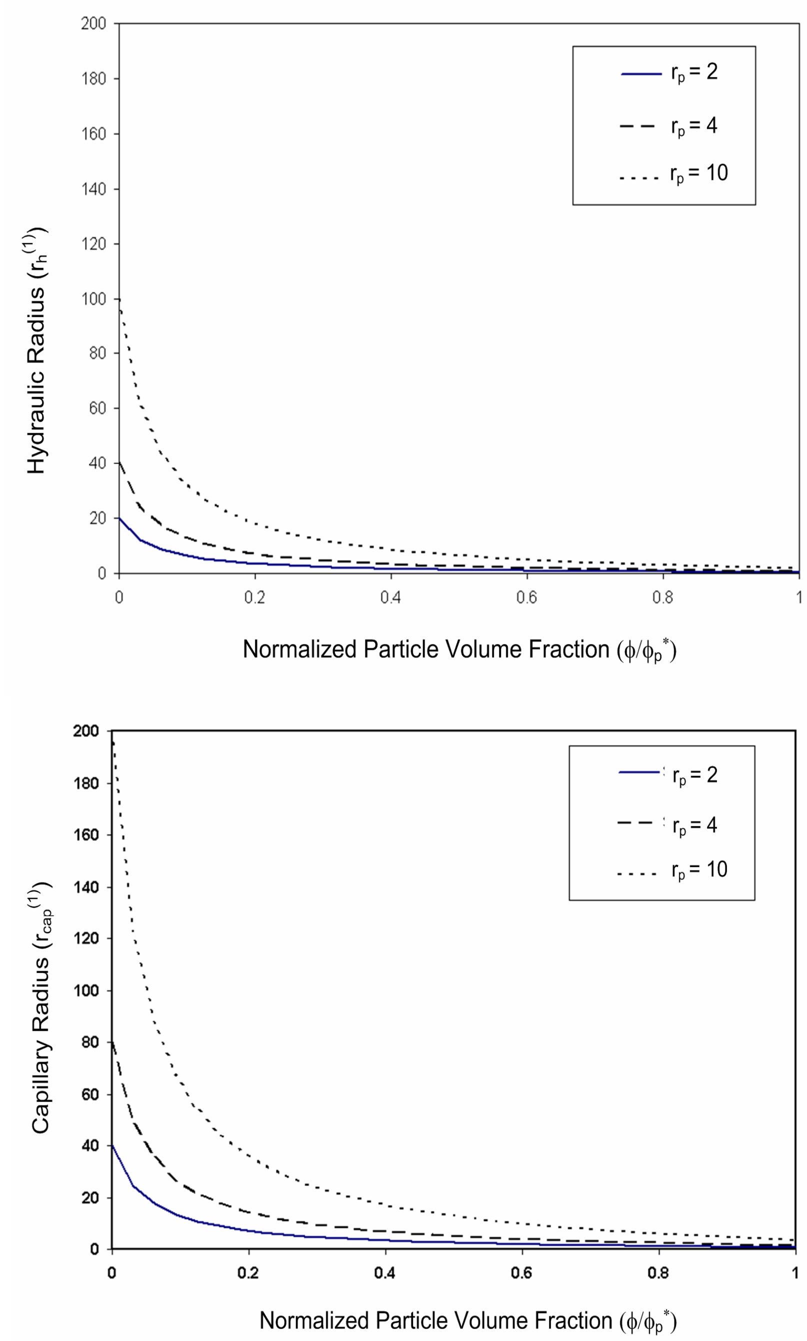

Figure 6.5 *The hydraulic radius ($r_h^{(1)}$) and capillary radius ($r_{cap}^{(1)}$) calculated according to Equation 6.18 for a packed bed of monodisperse spheres in a finite circular tube flow domain (confinement ratio $\alpha = 20$) as a function of the normalized particle volume fraction (ϕ_p/ϕ_p^*) and for three different particle radius $r_p =$ 2, 4, and 10 [length dimension].*

Secondly, the wall effect contributes to a change of the porosity in the region of the wall where it will be larger than in the bulk region. When solid particles are confined near the wall it will affect the local magnitude of the porosity, because the spatial distribution of the particles must conform with the shape of the wall (Larrard 1999). Within this annular "zone of the wall", the average porosity is greater than it is without, and hence in the presence of a uniform pressure gradient, the average velocity of flow is higher within the zone than without. This effect is commonly referred to as channeling (Fand & Thinakaran 1990).

Carman (1937) derived equations for the average porosity as a function of the confinement ratio in the range $1 \leq \alpha \leq 1.866$ and at $\alpha = 2$. In the range between $1.866 \leq \alpha \leq 2$ Carman (1937) suggested that the average porosity was calculated from linear interpolation. For higher confinement ratios, $\alpha \geq 2.033$, Fand & Thinakaran (1990) have proposed a hyperbola equation based on experimental work of random packed monodisperse spheres. This intersects with the Carman equation at $\alpha = 2.033$ and goes toward 0.36 for high confinement ratios corresponding to a maximum particle volume fraction of $\phi_p^* = 0.64$.

In Cohen & Metzner (1981), a so-called tri-regional model was proposed to calculate the flow rate dividing the bed into a wall, transition, and bulk region, respectively. The porosity was expressed as function of the distance from the wall (normalized by particle diameter). The flow velocity was then obtained from each of these regions by integration of the porosity. In the wall region, the wetted surface of the wall was included for calculation of the hydraulic radius as proposed by Mehta & Hawley (1969). Cohen & Metzner (1981) compared the method to a so-called single region model given by the Ergun equation (Eq. 6.16), but using the average porosity instead of the bulk porosity, and the Ergun equation modified by (Mehta & Hawley 1969) and using the bulk porosity. The highest and lowest flow rate was obtained from the single region model and the Ergun equation modified by (Mehta & Hawley 1969), respectively. The single region model seems to overestimate the flow by not taking the surface area of the wall into account, and the Ergun equation modified by (Mehta & Hawley 1969) seems to underestimate the flow by not taking the increased porosity into account. Basu (2001) compared the tri-regional model to experiments on power law fluids through a packed bed at confinement ratio of 3.8 and found for the fitted values of k_0 and $(\frac{L_e}{L_b})$ a reasonable agreement between the experimental results and the model estimate. Sodre (1998) extended the model to an annular cross section flow domain and compared the model to experiments of turbulent flow of air through an annular bed with an outer radius over inner radius of 1.349 and a bed size to particle diameter ratio of 8.258. They found a good agreement in this flow regime when using values of 150 and 1.75 for the first and second Ergun constant, respectively (Equation 6.16).

As mentioned, the next section discusses the capillary radius of a packed bed of monodisperse spheres at a low bed length to particle size ratio. As proposed by (Mehta & Hawley 1969), the wall surface area is included in calculation of the capillary radius (Equation 6.18). The channeling effect is taking into account through geometrical considerations of the capillary radius in a confined packed bed of monodisperse spheres.

6.3.3 Modified Matrix Flow Relative to Particle Flow

This section discusses the capillary radius ($r_{cap}^{(1)}$) given by Equation 6.18 for a finite circular tube domain in relation to the geometrical configuration of a packed bed of monodisperse spheres at a low bed length to particle diameter. The geometrical configuration of the particles are studied for high and low confinement ratios.

At a high confinement ratio (infinite domain), three different types of systematic three dimensional packing of monosized spheres are shown in Figure 6.6. It shows the face-centered cubic, hexagonal, and simple cubic packing for which it is possible analytically to derive the packing density (Gardner 1966)(Steinhaus 1999). The face-centered and hexagonal packing of spheres gives approximately the same value of 0.74 and the simple cubic packing gives 0.52. A random close packing of monodisperse spheres has been found to lie between the hexagonal and simple cubic packing with a value of 0.64 (Jaeger & Nagel 1992)(Jalali & Li 2004).

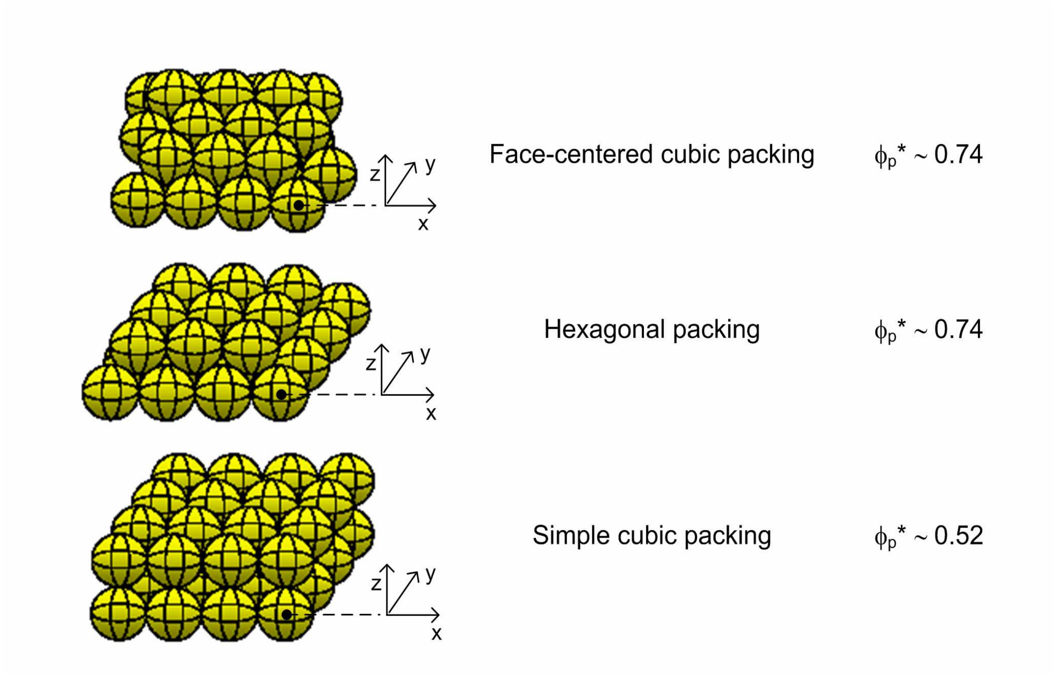

Figure 6.6 *Illustration of the face-centered cubic, hexagonal, and simple cubic packing of monodisperse spheres in an infinite domain.*

According to Equation 6.14, the capillary radius (r_{cap}) of randomly packed bed ($\phi_p^* = 0.64$) in an infinite domain is given by:

$$r_{cap} = \frac{2(1-\phi_p)r_p}{3\phi_p} = 0.375 \cdot r_p \quad \text{for} \quad \phi_p = \phi_p^* = 0.64 \tag{6.19}$$

In Figure 6.7 and Figure 6.8 the capillary radius given by Equation 6.19 is compared to cross-sections of the simple cubic and hexagonal packing, respectively. The figures show the geometrical configuration of six cross-sections corresponding to distances of $Z = 0 \cdot r_p$, $0.3 \cdot r_p$, $0.6 \cdot r_p$, $0.9 \cdot r_p$, $1.2 \cdot r_p$, and $\sqrt{2} \cdot r_p$.

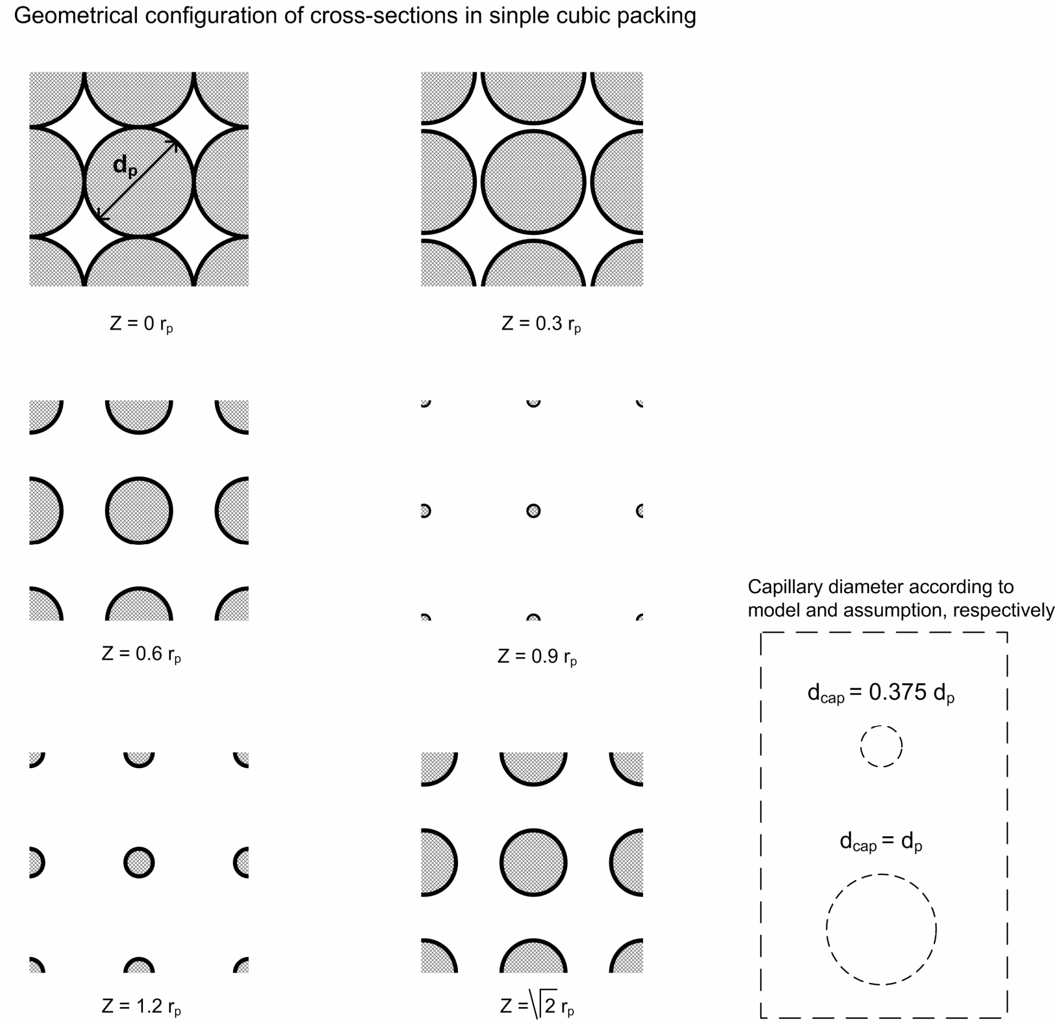

Figure 6.7 *To the left, the geometrical configuration of different cross-sections through a simple cubic packing of monodisperse spheres ($\phi_p^* = 0.52$). To the right, the calculated capillary radius according to Equation 6.19 ($d_{cap} = 0.375 \cdot d_p$) and the assumption applied of $d_{cap} = d_p$ [length dimension].*

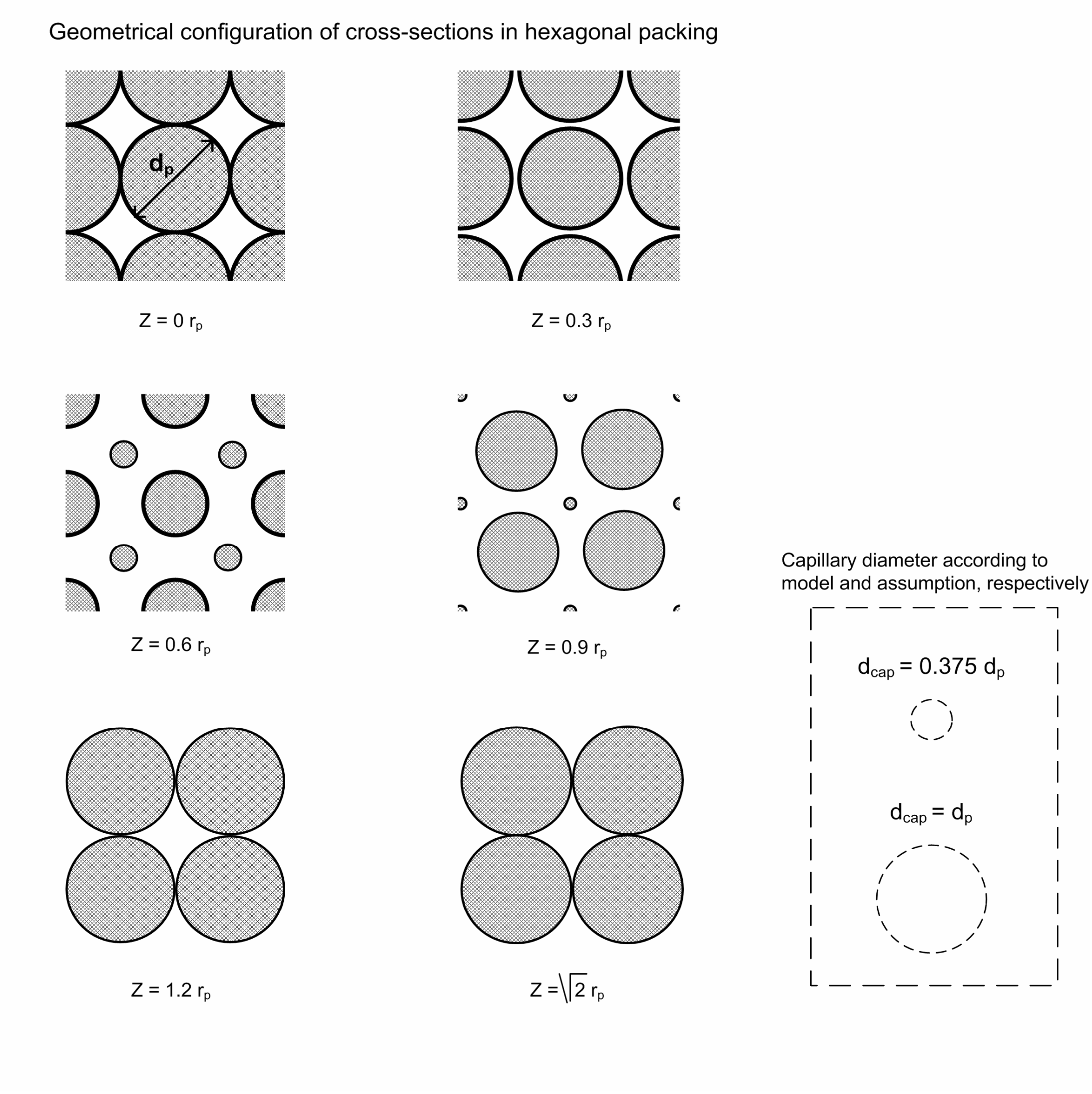

Figure 6.8 *To the left, the geometrical configuration of different cross-sections through a hexagonal packing of monodisperse spheres ($\phi_p^* = 0.74$). To the right, the calculated capillary radius according to Equation 6.19 ($d_{cap} = 0.375 \cdot d_p$) and the assumption applied of $d_{cap} = d_p$ [length dimension].*

Comparing the capillary diameter ($d_{cap} = 0.375 \cdot d_p$) to the cross-section of the simple cubic packing, it seems that d_{cap} is somewhat underestimated. Only at the closest constriction at $Z = 0 \cdot r_p$ the capillary diameter seem to be a reasonable estimate. For $Z = r_p$ the capillary diameter goes toward infinity. Therefore, it may seem reasonable that the average capillary diameter is higher than $d_{cap} = 0.375 \cdot d_p$, and it may be assumed that the capillary diameter is of the same order as the particle diameter ($d_{cap} \sim d_p$).

For the hexagonal packing in Figure 6.8 which represents the highest possible packing of monodisperse spheres (0.74), the pore space is reduced in the sections where the particles overlap in the z-direction compared to the simple cubic packing. Based on a qualitative assessment it also seems reasonable that $d_{cap} > 0.375\ d_p$, though, the assumption of $d_{cap} \sim d_p$ may be an overestimation. However, considering that the maximum packing is equal to the random close packing of $\phi_p^* = 0.64$, it is assumed in the ongoing that $d_{cap} \sim d_p$ at $\phi_p = \phi_p^*$.

In the ongoing, the modified capillary radius, with the assumption of $d_{cap} \sim d_p$ at $\phi_p = \phi_p^*$, is denoted $r_{cap}^{(2)}$. Thus, at the maximum particle volume fraction

$$\frac{r_{cap}^{(2)*}}{r_p} = 1 \quad \text{at} \quad \phi_p = \phi_p^* \tag{6.20}$$

where $r_{cap}^{(2)*}$ represents the modified capillary radius at the maximum particle volume fraction ϕ_p^*.

This may now be compared to the capillary radius $r_{cap}^{(1)*}$ given by Equation 6.18 at $\phi_p = \phi_p^*$. The ratio $\frac{r_{cap}^{(2)*}}{r_{cap}^{(1)*}}$ is given by:

$$\frac{r_{cap}^{(2)*}}{r_{cap}^{(1)*}} = \frac{3\phi_p^*}{2(1-\phi_p^*)} + \frac{1}{(1-\phi_p^*)\frac{R}{r_p}} \tag{6.21}$$

Figure 6.9 shows Equation 6.21 as a function of the confinement ratio ($\alpha = \frac{R}{r_p}$) for $\phi_p^* = 0.64$.

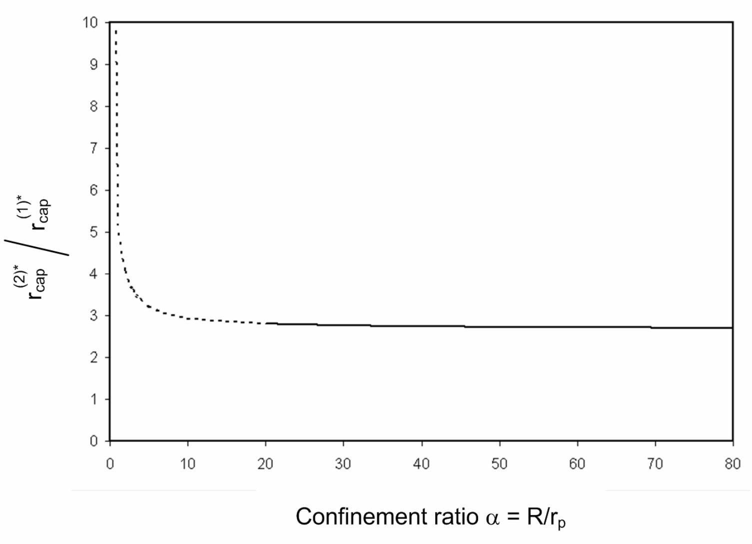

Figure 6.9 *The ratio of capillary radius* $\frac{r_{cap}^{(2)*}}{r_{cap}^{(1)*}}$ *as a function of the confinement ratio* $\alpha = \frac{R}{r_p}$ *according to Equation 6.21 for a random packed bed of monodisperse spheres* ($\phi_p^* = 0.64$). *The solid line represents* $\alpha \geq 20$.

For $\alpha = \frac{R}{r_p} \rightarrow \infty$, the ratio $\frac{r_{cap}^{(2)*}}{r_{cap}^{(1)*}} \rightarrow 2.66$ for a random packed bed of monodisperse spheres in a infinite domain.

Assuming that Equation 6.21 applies for $\alpha \geq 20$, the modified capillary radius at maximum packing ($r_{cap}^{(2)*}$) may be extended to include particle volume fractions $\phi_p \leq \phi_p^*$. The modified capillary radius for $\alpha \geq 20$ in a finite tube flow domain is then given by

$$\begin{aligned} r_{cap}^{(2)} &= \left((\frac{r_{cap}^{(2)*}}{r_{cap}^{(1)*}} - 1)\frac{\phi_p}{\phi_p^*} + 1 \right) r_{cap}^{(1)} & \phi_p \leq \phi_p^* \quad \text{and} \quad \alpha \geq 20 \\ &\approx \left(1.66\frac{\phi_p}{\phi_p^*} + 1 \right) r_{cap}^{(1)} & \phi_p \leq \phi_p^* \approx 0.64 \quad \text{and} \quad \alpha \geq 20 \end{aligned} \tag{6.22}$$

where $r_{cap}^{(1)}$ is given by Equation 6.18.

The capillary radius ($r_{cap}^{(2)}$) according to Equation 6.22 and the capillary radius ($r_{cap}^{(1)}$) according to Equation 6.18 are shown in Figure 6.10 for the same parameters as applied in Figure 6.5.

It is now seen that the boundary conditions $r_{cap}^{(2)*} = r_p$ at $\phi_p = \phi_p^*$ and $r_{cap}^{(2)} = R$ at $\phi_p = 0$ are obtained.

The next section discusses the modified capillary radius when taking the channeling effect of the wall into account ($\alpha < 20$). This will be denoted $r_{cap,w}^{(2)}$.

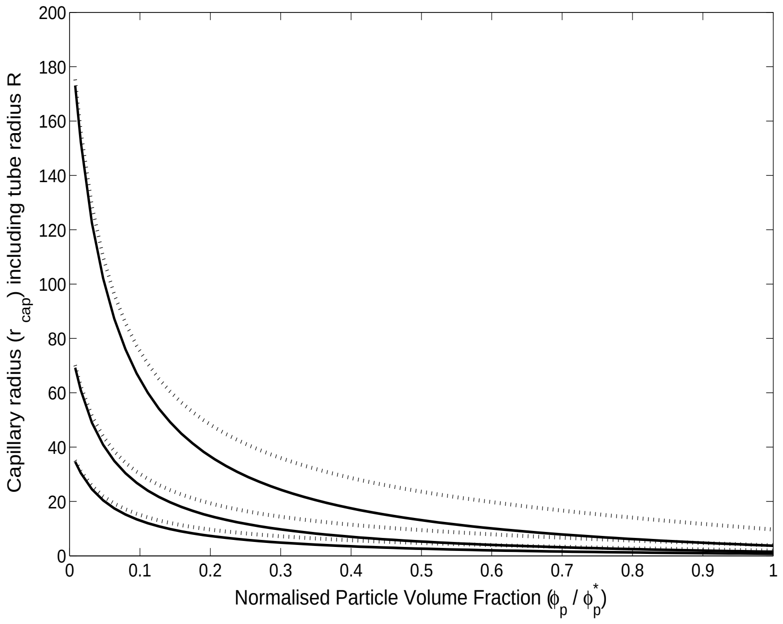

Figure 6.10 *The capillary radius* $r_{cap}^{(1)}$ *(solid lines) according to Equation 6.18 and the modified capillary radius* $r_{cap}^{(2)}$ *(dotted lines) according to Equation 6.22 of a suspension of randomly packed monodisperse spheres in a finite circular tube flow domain as a function of the normalized particle volume fraction* $\frac{\phi_p}{\phi_p^*}$*. It is shown for three different particle radius* $r_p = 2$*, 4, and 10 [length dimension] and an confinement ratio* $\alpha = \frac{R}{r_p} = 20$*. It is assumed* $\phi_p^* = 0.64$ *(*$r_{cap}^{(1)}$ *was also shown in the bottom figure of Figure 6.5).*

Finite Circular Tube Flow Domain Including the Channelling effect

As mentioned in Section 6.3.2, the local magnitude of the porosity near the wall increases because the spatial distribution of the particles must conform with the shape of the wall (Larrard 1999).

In the procedure for estimating the pressure drop of heterogeneous flow, the wall effect influences on the suspension part and capillary part. In the suspension part, the rheological properties is a function of the maximum particle volume fraction (ϕ_p^*) which will be lower than in the bulk region. In the capillary part, the dimension and number of capillaries in the confined region may be higher than in the bulk region.

Fand & Thinakaran (1990) have studied the porosity ($\phi_{m,w}^*$) of a packed bed of monodisperse spheres in a finite circular tube flow domain as a function of the confinement ratio. Three different regions have been identified and writing them in terms of the maximum particle fraction ($\phi_{p,w}^*(\alpha)$) these are given by:

$$
\begin{aligned}
\phi^*_{p,w}(\alpha) = 1 - \phi^*_{m,w}(\alpha) &= 1 - \left(1 - \frac{\frac{2}{3}(\frac{1}{\alpha})^3}{\sqrt{\frac{2}{\alpha} - 1}}\right) && 1.0 \leq \alpha \leq 1.866 \\
\phi^*_{p,w}(\alpha) = 1 - \phi^*_{m,w}(\alpha) &= 1 - \left(\frac{0.151}{\alpha - 1} + 0.360\right) && \alpha \geq 2.033 \qquad (6.23) \\
\phi^*_{p,w}(\alpha) = 1 - \phi^*_{m,w}(\alpha) &= 1 - (-0.6649\alpha + 1.8578) && 1.866 \leq \alpha \leq 2.033
\end{aligned}
$$

The maximum particle volume fraction ($\phi^*_{p,w}(\alpha)$) according to Equation 6.23 is shown in Figure 6.11.

It shows that for confinement ratios $\alpha \geq 20$, the maximum particle volume fraction within the confined tube ($\phi^*_{p,w}(\alpha)$) approaches the bulk value of randomly packed monodisperse spheres, i.e. $\phi^*_{p,w} \approx \phi^*_p = 0.64$.

For $\alpha \leq 20$, the maximum particle volume fraction ($\phi^*_{p,w}$) decreases to 0.47 at $\alpha = 2$ and 0.32 at $\alpha = 1.67$ before increasing to 0.65 at $\alpha = 1$.

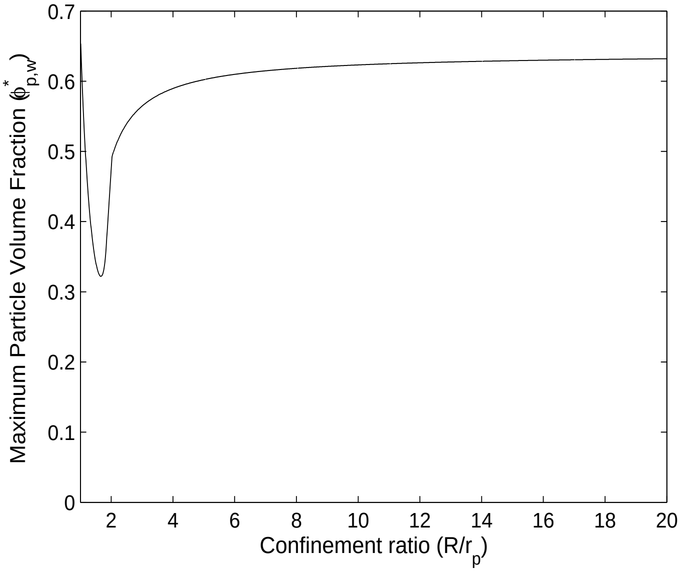

Figure 6.11 *The maximum particle volume fraction ($\phi^*_{p,w}$) for monodisperse spheres confined within a finite circular tube flow domain as a function of the confinement ratio $\alpha = R/r_p$ given by Equation 6.23 (Fand & Thinakaran 1990).*

In the previous section it was assumed that the capillary radius $r^{(2)*}_{cap} = r_p$ at $\phi_p = \phi^*_p$ in a packed bed of monodisperse spheres in the bulk region. However, for a confinement ratio approximately below 20 it may be assumed that $r^{(2)*}_{cap,w} \geq r_p$. A method for determining $r^{(2)*}_{cap,w}$ for confinement ratios $\alpha \leq 20$ is outlined below.

An expression must fulfil the following requirements:

- $\frac{r^{(2)*}_{cap,w}}{r_p} = 1 \quad \text{when } \phi^*_{p,w} = \phi^*_p \approx 0.64$
- $\frac{r^{(2)*}_{cap,w}}{r_p} = 0 \quad \text{when } \alpha = 1$
- $\frac{r^{(2)*}_{cap,w}}{r_p} \leq \alpha = \frac{R}{r_p}$

Initially, it is suggested to let the capillary radius $r^{(2)*}_{cap,w}(\alpha)$ be given by:

$$\frac{r^{(2)*}_{cap,w}(\alpha)}{r_p} = \frac{\phi^*_p}{\phi^*_{p,w}(\alpha)} \tag{6.24}$$

which is illustrated in Figure 6.12 together with $\frac{r^{(2)*}_{cap,w}}{r_p} = \alpha$.

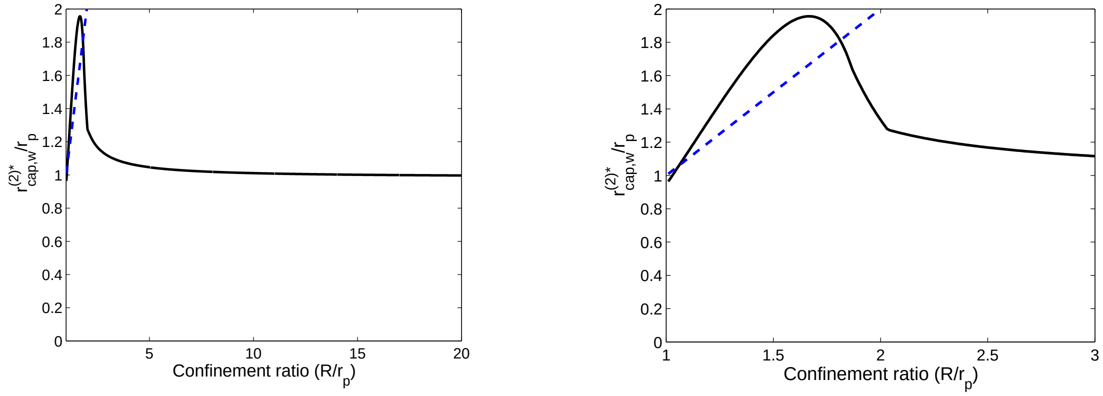

(a) (b)

Figure 6.12 *The ratio $r^{(2)*}_{cap,w}/r_p$ in a finite circular tube flow domain as a function of the confinement ratio according to Equation 6.24 (black line). To the left it is shown in the range $0 \leq \alpha \leq 20$ and to the right in the range $0 \leq \alpha \leq 3$. The blue line shows $r^{(2)*}_{cap,w}/r_p = \alpha$.*

It shows that the requirement $\frac{r^{(2)*}_{cap,w}}{r_p} \leq \alpha$ is only fulfilled for confinement ratios approximately larger than 1.8.

Furthermore, Equation 6.24 assumes that the three-dimensional particle volume fraction applies to a two-dimensional cross section, thus:

$$\frac{\phi_p^*}{\phi_{p,w}^*(\alpha)} \approx \frac{\phi_p^{(2D)*}}{\phi_{p,w}^{(2D)*}(\alpha)} \tag{6.25}$$

In the following, the validity of the assumption given by Equation 6.25 is discussed for confinement ratios $2 \leq \alpha \leq 20$. For a discussion of the capillary radius for confinement ratios $1 < \alpha \leq 2$, see Appendix B.

A finite circular tube flow domain of packed monodisperse spheres is illustrated in Figure 6.13 at a confinement ratio of $\alpha = 2$.

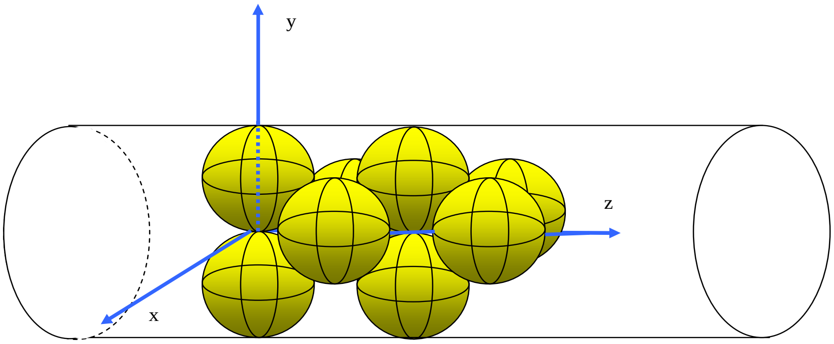

Figure 6.13 *Illustration of a packed bed of monodisperse spheres in a finite circular tube flow domain at a confinement ratio of* $\alpha = \frac{R}{r_p} = 2$.

The maximum particle volume fraction according to Equation 6.23 is $\phi_{p,w}^* = 0.472$ at $\alpha = 2$.

At $\alpha = 2$ it is possible to place the center of two particles in the same z position and the next pair of particles can be placed in a position of $Z_d = \mathrm{k}R$ as illustrated in Figure 6.14. This gives a value of $\mathrm{k} \approx 0.71$.

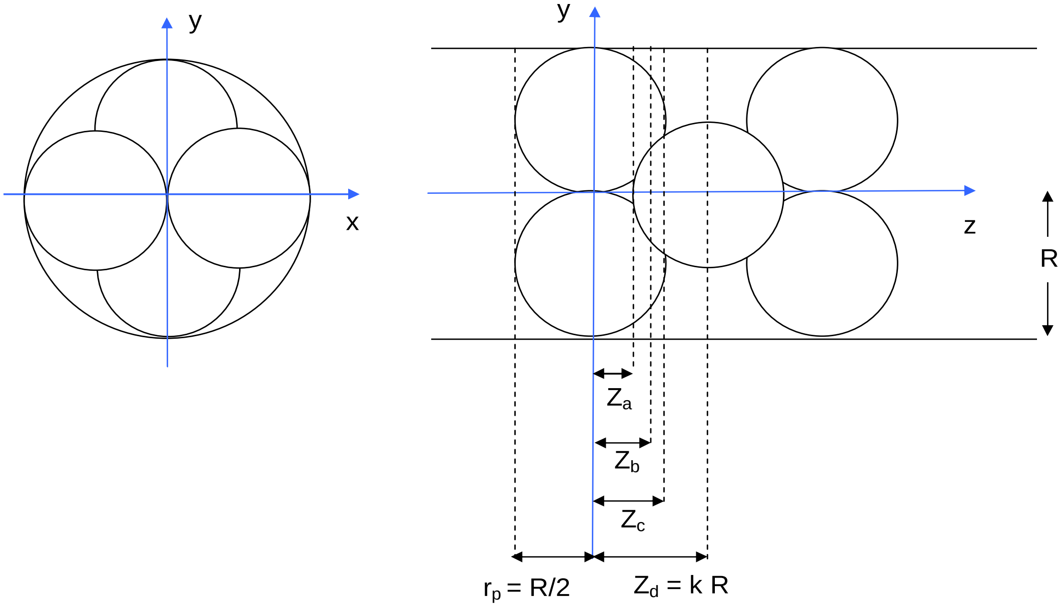

Figure 6.14 *Illustration of a packed bed of monodisperse spheres in a finite circular tube flow domain at a confinement ratio of* $\alpha = \frac{R}{r_p} = 2$ *and the meaning of* Z_a, Z_b, Z_c, *and* Z_d *[length dimension].*

The two-dimensional particle area fraction ($\phi_{p,w}^{(2D)*}$) as a function of z may be solved for the system shown in Figure 6.14. The particle volume fraction and the particle area fraction as a function of z are then shown in Figure 6.15. The results show that it seems reasonable to assume that the particle volume fraction applies in two-dimensions for confinement ratios $2 \leq \alpha \leq 20$. At $\alpha = 2$ the maximum and minimum particle area fraction is $\phi_{p,w}^{(2D)*} = 0.5$ and 0.41, respectively.

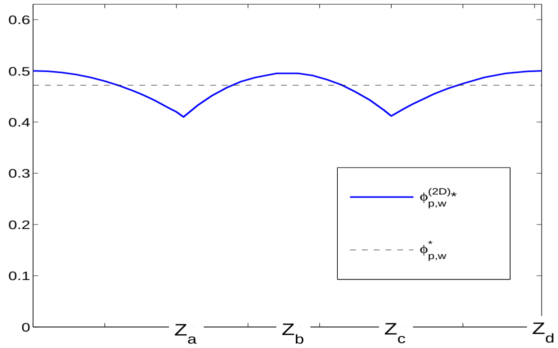

Figure 6.15 *The three-dimensional particle volume fraction* ($\phi_{p,w}^{*}$) *and the the two-dimensional particle area* ($\phi_{p,w}^{(2D)*}$) *fraction as a function of z* (Z_a, Z_b, Z_c, *and* Z_d *defined in Figure 6.14) for a packed bed of monodisperse spheres in a finite circular tube flow domain at a confinement ratio* $\alpha = \frac{R}{r_p} = 2$.

A view of the two-dimensional cross sections at positions $z = Z_a$, Z_b, Z_c, and Z_d are shown in Figure 6.16.

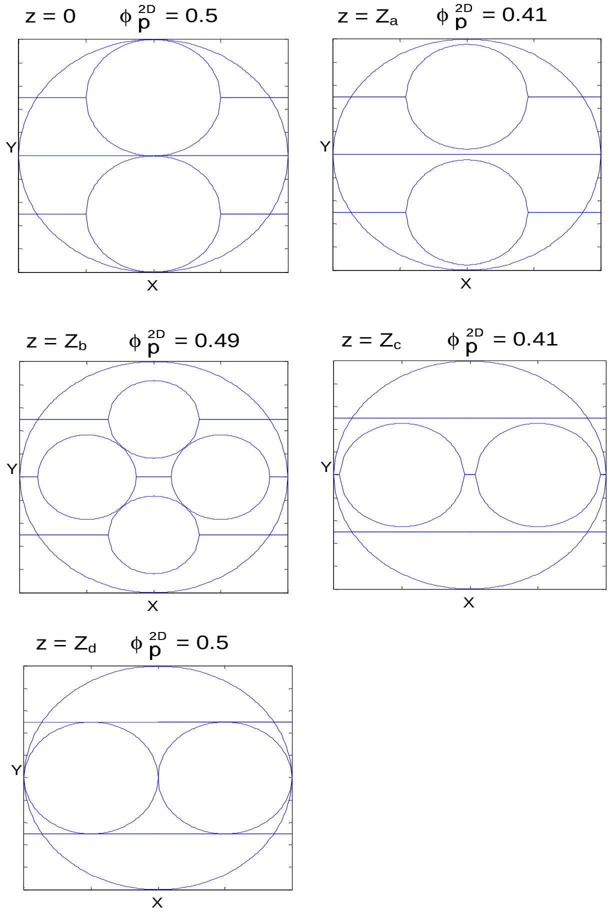

Figure 6.16 *The two-dimensional cross section of a packed bed of monodisperse spheres in a finite circular tube flow domain at a confinement ratio* $\alpha = \frac{R}{r_p} = 2$ *and at* $z = 0, z = Z_a, z = Z_b, z = Z_c, z = Z_d$ *(defined in Figure 6.14).*

The geometry of the interparticular space varies according to whether the cross section is dominated by two or four particles. However, it is assumed that the average capillary radius does not vary significantly and that Equation 6.24 applies for $2 \leq \alpha \leq 20$. According to Equation 6.24 the capillary radius at $\alpha = 2$ will then be:

$$r^{(2)*}_{cap,w} = 1.33 \cdot r_p \quad \text{at} \quad \alpha = 2 \tag{6.26}$$

The capillary radius $(r^{(2)*}_{cap,w}(\alpha))$ given by Equation 6.24 is compared to the capillary radius $(r^{(1)*}_{cap}(\alpha))$ given by Equation 6.18. In Equation 6.18, the maximum particle volume fraction $\phi^*_p = \phi^*_{p,w}(\alpha)$ given by Equation 6.23 is applied instead of $\phi^*_p = 0.64$.

The ratio $\frac{r^{(2)*}_{cap,w}(\alpha)}{r^{(1)*}_{cap}(\alpha)}$ is shown in Figure 6.17 as a function of the confinement ratio α. The ratio only applies for $2 \leq \alpha \leq 20$ and for a discussion of the region $1 \leq \alpha \leq 2$, see Appendix B.

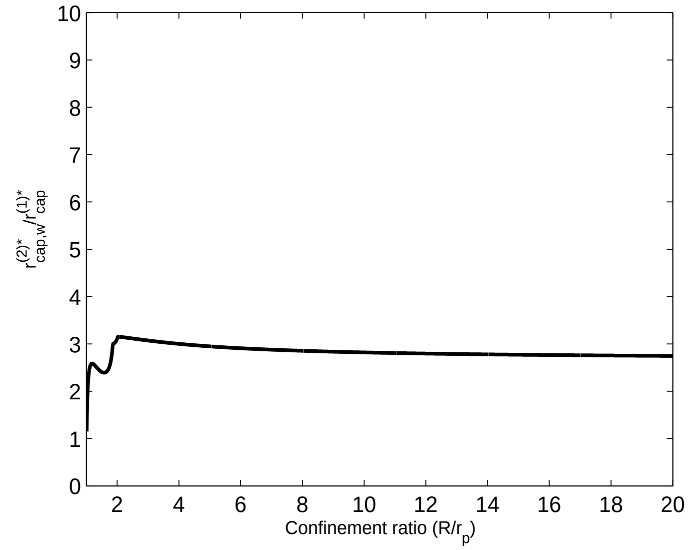

Figure 6.17 *The ratio* $\frac{r^{(2)*}_{cap,w}(\alpha)}{r^{(1)*}_{cap}(\alpha)}$ *as a function of the confinement ratio* $0 \leq \alpha \leq 20$.

As in the bulk region the ratio $\frac{r^{(2)*}_{cap,w}(\alpha)}{r^{(1)*}_{cap}(\alpha)}$ may be extended to include particle volume fractions below $\phi^*_{p,w}(\alpha)$ which gives:

$$r^{(2)}_{cap,w}(\alpha) = \left(\left(\frac{r^{(2)*}_{cap,w}(\alpha)}{r^{(1)*}_{cap}(\alpha)} - 1\right)\frac{\phi_p}{\phi^*_{p,w}(\alpha)} + 1 \right) r^{(1)}_{cap}(\alpha) \quad \phi_p \leq \phi^*_{p,w}(\alpha) \text{ and } \alpha \leq 20 \quad (6.27)$$

When $\phi^*_{p,w}(\alpha) = \phi^*_p$, approximately for $\alpha \geq 20$, Equation 6.27 becomes Equation 6.22.

6.4 Flow Rate Criterion

In Section 6.3, the assumption of blocking being initiated if heterogeneous flow can take place at a pressure drop lower than that required for homogeneous flow was outlined.

The heterogeneous flow is assumed to consist of a suspension and a capillary part. In Section 6.3.3, a modified capillary theory was proposed for calculation of the capillary radius which is used in calculation of the number of capillaries and in the pressure drop - flow rate relation for a single capillary. The pressure drop - flow rate relation for the capillary part is given by Equation 6.17 in which r_{cap} is replaced by $r^{(2)}_{cap,w}(\alpha)$ given by Equation 6.27 for $\alpha \leq 20$. The number of capillaries is given by:

$$n_{cap} = \frac{(1-\phi_p)R^2}{r^{(2)}_{cap,w}(\alpha)} \qquad \phi_p \leq \phi^*_{p,w}(\alpha) \text{ and } \alpha \leq 20 \tag{6.28}$$

Under a given macroscopic flow rate Q_0 blocking will be initiated if:

$$\Delta P_{sus} \geq \Delta P_{sep,sus} + \Delta P_{sep,cap} \tag{6.29}$$

Figure 6.18 illustrates the pressure drop - flow rate relation for homogeneous suspension flow at the particle volume fraction ϕ_p and heterogeneous flow at $\phi_p + d\phi_p$ divided into a suspension part and a capillary part.

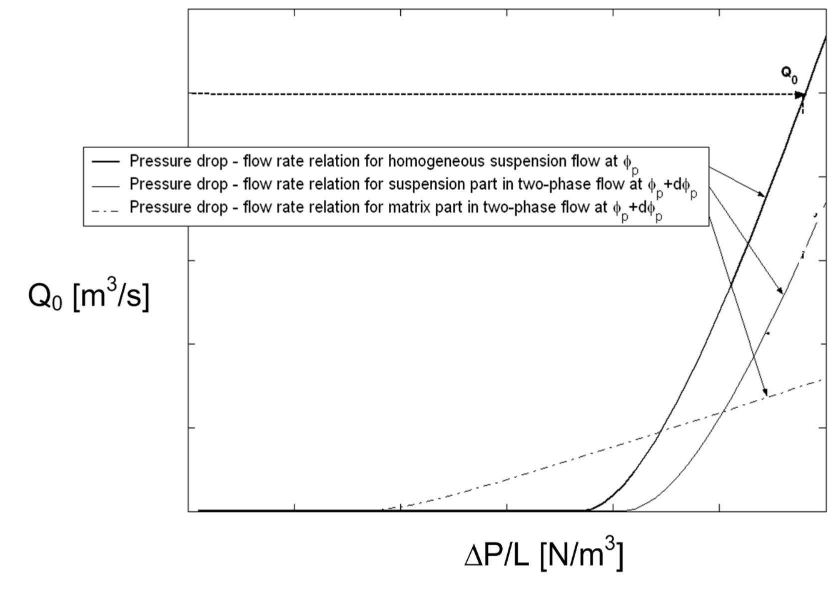

Figure 6.18 *Illustrations of the pressure drop - flow rate relation for homogeneous suspension flow at the particle volume fraction* ϕ_p *and heterogeneous flow at* $\phi_p + \Delta\phi_p$ *divided into a suspension part and a capillary part.*

The pressure drop - flow rate relation for homogeneous suspension flow is considered. This is shown as the solid black line and is calculated using $\tau_{s,0}(\phi_p)$ and $\eta_{s,pl}(\phi_p)$ where ϕ_p is the initial particle volume fraction. At a constant macroscopic flow rate Q_0, the responding pressure drop is denoted ΔP_{sus}.

Introducing a particle velocity gradient in the x-direction ($\Delta v_p/\Delta x$), this results in heterogeneous flow in which the particle volume fraction increases to $\phi_p(t=t_1) = \phi_p + \Delta\phi_p$ at time $t_1 = t_0 + \Delta t$. The pressure drop - flow rate relation for the suspension part in heterogeneous flow is calculated using the rheological parameters $\tau_{s,0}(\phi_p + \Delta\phi_p)$ and $\eta_{s,pl}(\phi_p + \Delta\phi_p)$. This is shown as the solid grey line. The pressure drop - flow rate relation for the capillary part in heterogeneous flow is calculated according to Equation 6.17 using $\phi_p(t=t_1) = \phi_p + \Delta\phi_p$ and the rheological parameters $\tau_{m,0}$ and $\eta_{m,pl}$. This is shown as the dotted line.

A parameter study shows that for $\Delta\phi_p \rightarrow 0$, Equation 6.29 is only fulfilled at the intersection point between the flow curve of homogenous flow and the capillary part in heterogeneous flow. At higher flow rates, the combined pressure drop (suspension part and matrix part) will be higher than that of the homogenous suspension flow to keep a constant flow rate Q_0. This result indicates that either complete homogeneous or capillary matrix flow will occur depending on the flow rate. Below a critical flow rate, the matrix and particle velocities will be given by

$$\begin{aligned} v_{p,1}(t) &= \frac{Q_0\phi_p(t_0)}{\phi_p(t)\Delta y\Delta z} \\ v_{m,1}(t) &= \frac{Q_0(1-\phi_p(t_0))}{(1-\phi_p(t))\Delta y\Delta z} \\ v_{p,2}(t) &= 0 \\ v_{m,2}(t) &= \frac{Q_0}{(1-\phi_p(t))\Delta y\Delta z} \end{aligned} \tag{6.30}$$

and the particle volume fraction is given by Equation 6.4.

Once blocking is initiated, particles continues to accumulate because the resistance to homogeneous flow increases more rapidly for increasing particle volume fractions than the resistance to matrix flow. This is a result of the suspension rheology being more dependent on the particle volume fraction than the dimension and numbers of capillaries used to calculate the capillary matrix flow.

6.5 Parameter Study

A parameter study is carried out to investigate the phenomenological behaviour of the model, i.e. assess the effect of the particle volume fraction, the rheological properties, the confinement ratio, and the tube radius on the critical flow rate. The relation between the flow rate (Q_0) and the average velocity flow velocity (U_m) is given by $U_m = \frac{Q_0}{\pi R^2}$.

The Figures 6.19, 6.20, and 6.21 show the average velocity (U_m) as a function of the pressure gradient ($\Delta P/L$) and the particle volume fraction (ϕ_p) whenever

$$Q_{m,0} - Q_{s,0} > 0 \tag{6.31}$$

where $Q_{m,0}$ is the matrix flow rate calculated according to Equation 6.17 and $Q_{s,0}$ is the homogeneous suspension flow rate calculated according to Equation 6.6. This corresponds to matrix flow dominating over homogeneous suspension flow and the initiation of blocking. If $Q_m - Q_s \leq 0$, it corresponds to homogeneous suspension flow dominating over matrix flow for which reason blocking is not initiated. This is indicated by average velocities $U_m = 0$.

Figure 6.19 shows the average velocity U_m for confinement ratios of 3, 4, 6 and 10. Calculations are carried out with $\eta_{m,pl} = \eta_{m,pl}^{ref} = 0.1$ Pa·s and $\tau_{m,0} = \tau_{m,0}^{ref} = 0.2$ Pa at a tube radius $R = R_a = 0.0125$ m. The reference tube radius is equal to the tube radius applied in the test setup (see Section 6.6.1).

Comparing the results at a given particle volume fraction (ϕ_p), it is seen that the critical velocity increases when the confinement ratio (α) decreases. Also, at low confinement ratios, the existence of a critical velocity occurs at lower particle volume fractions.

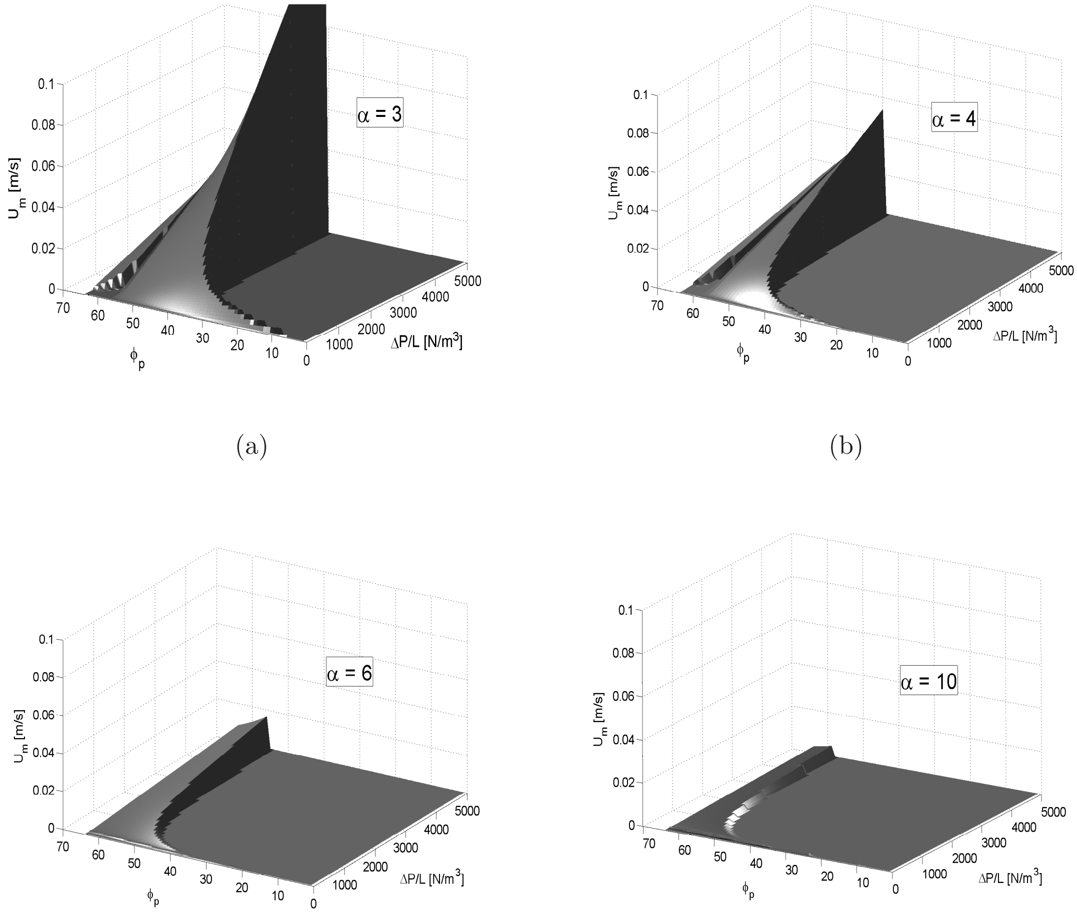

(a)

(b)

(c)

(d)

Figure 6.19 *Illustration of the average velocity U_m in a finite circular tube flow domain given by $U_m = \frac{Q_0}{\pi R_a^2}$ where Q_0 is the macroscopic flow rate and R_a is the tube radius. Average velocities $U_m > 0$ corresponds to $Q_{m,0} - Q_{s,0} > 0$ which is matrix flow dominating over homogeneous suspension (blocking). Average velocities $U_m = 0$ corresponds to $Q_{m,0} - Q_{s,0} \leq 0$ which is homogeneous suspension flow dominating over matrix flow (no blocking). It is shown as a function of the confinement ratio ($\alpha = R_a/r_p$), particle volume fraction (ϕ_p), and pressure gradient ($\Delta P/L$). The confinement ratios applied are 3 (upper left), 4 (upper right), 6 (lower left), and 10 (lower right). A reference plastic viscosity $\eta_{m,pl}^{ref} = 0.1$ Pa·s and a reference yield stress $\tau_{m,0}^{ref} = 0.2$ Pa have been applied.*

Figure 6.20 shows the effect of tube radius, R, as it appears as an absolute value in Equation 6.18. The average velocity U_m is studied for a tube radius $R_b = 2R_a$ and confinement ratios $\alpha = 4$ and 10.

Comparing the results in Figure 6.20 with the results in Figure 6.19, it shows that for a fixed confinement ratio, the critical velocity increases when the tube radius increases.

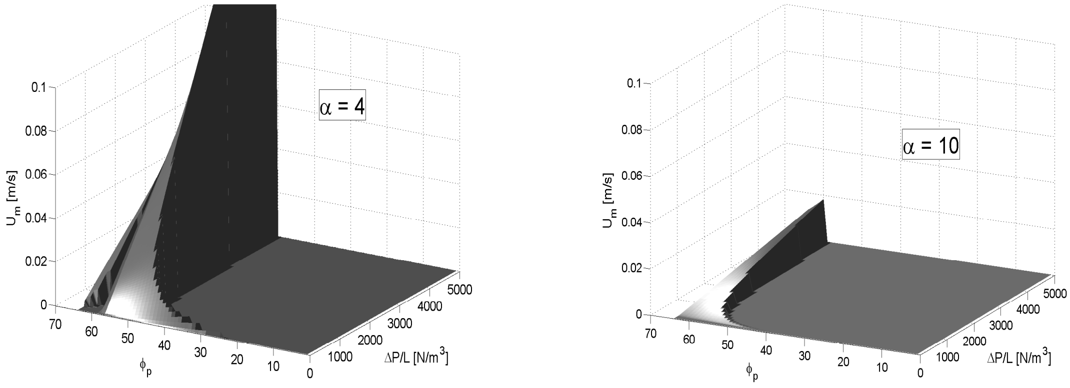

(a) (b)

Figure 6.20 *Illustration of the average velocity U_m in a finite circular tube flow domain given by $U_m = \frac{Q_0}{\pi R_b^2}$ where Q_0 is the macroscopic flow rate and $R_b = 2R_a$ is the tube radius (R_a was applied in Figure 6.19). Average velocities $U_m > 0$ corresponds to $Q_{m,0} - Q_{s,0} > 0$ which is matrix flow dominating over homogeneous suspension (blocking). Average velocities $U_m = 0$ corresponds to $Q_{m,0} - Q_{s,0} \leq 0$ which is homogeneous suspension flow dominating over matrix flow (no blocking). It is shown as a function of the confinement ratio ($\alpha = \frac{R_b}{r_p}$), particle volume fraction (ϕ_p), and pressure gradient ($\Delta P/L$). The confinement ratios applied are 4 (left) and 10 (right). A reference plastic viscosity $\eta_{m,pl}^{ref} = 0.1$ Pa·s and a reference yield stress $\tau_{m,0}^{ref} = 0.2$ Pa have been applied.*

Figure 6.21 illustrates the effect of the rheological properties of the matrix. Situation (b) in Figure 6.19 is reproduced using the rheological parameters 1) $\eta_{m,pl}^{ref}$ and $\tau_{m,0}^{ref}$, 2) $4\eta_{m,pl}^{ref}$ and $\tau_{m,0}^{ref}$, 3) $\eta_{m,pl}^{ref}$ and $4\tau_{m,0}^{ref}$, and 4) $4\eta_{m,pl}^{ref}$ and $4\tau_{m,0}^{ref}$.

The results show that by increasing the plastic viscosity the critical velocity decreases, which may be explained by an increase in the drag force. Increasing the yield stress has the opposite effect, i.e. the critical velocity increases. This may be explained by considering the intersection point in Figure 6.18. For $\tau_{0,m} \rightarrow 0$, both the matrix phase and suspension become Newtonian fluids and the intersection point diminishes. The flow rate criterion is then replaced by a critical particle volume fraction.

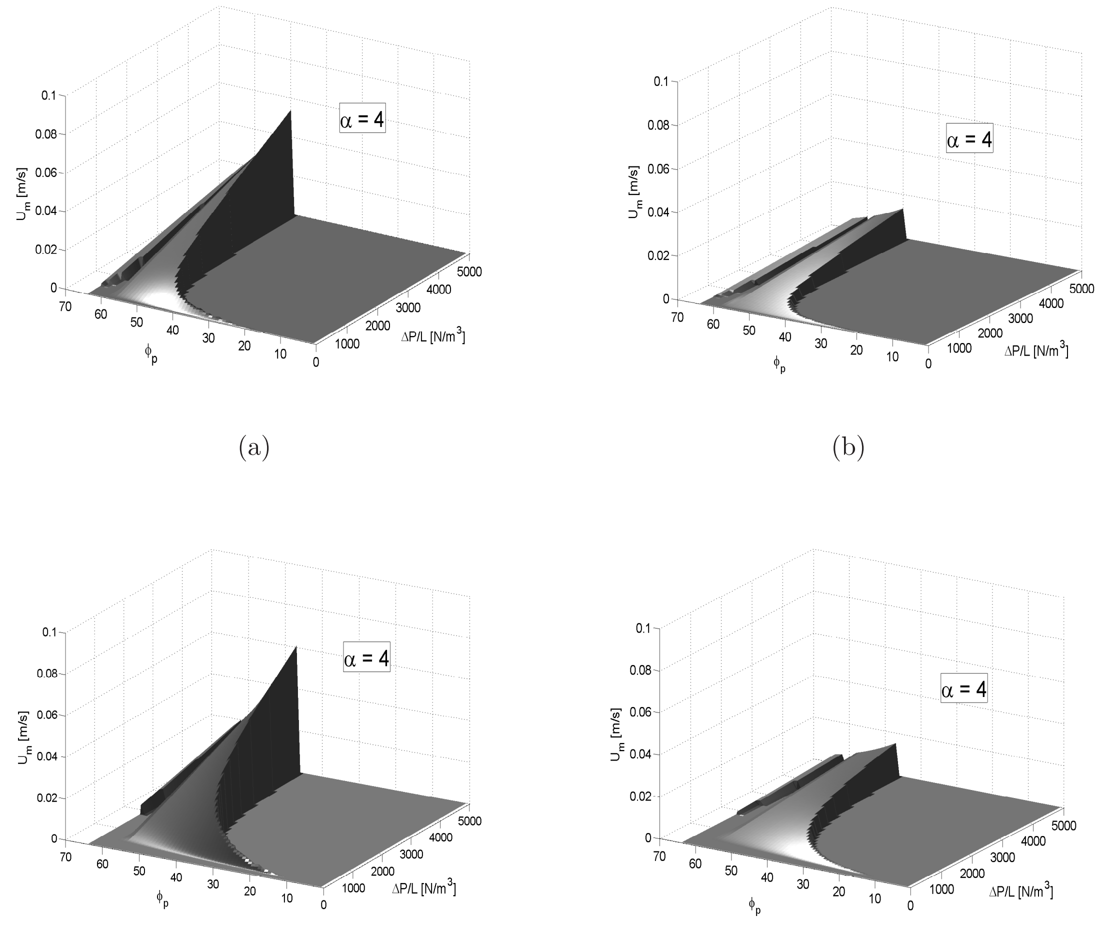

(a) (b)

(c) (d)

Figure 6.21 *Illustration of the average velocity U_m in finite circular tube flow domain given by $U_m = \frac{Q_0}{\pi R_a^2}$ where Q_0 is the macroscopic flow rate and R_a is the tube radius. Average velocities $U_m > 0$ corresponds to $Q_{m,0} - Q_{s,0} > 0$ which is matrix flow dominating over homogeneous suspension (blocking). Average velocities $U_m = 0$ corresponds to $Q_{m,0} - Q_{s,0} \leq 0$ which is homogeneous suspension flow dominating over matrix flow (no blocking). It is shown as a function of the particle volume fraction (ϕ_p) and pressure gradient ($\Delta P/L$). The rheological properties applied are $\eta_{m,pl}^{ref} = 0.1$ Pa·s and $\tau_{m,0}^{ref} = 0.2$ Pa (upper left), $4\eta_{m,pl}^{ref}$ and $\tau_{m,0}^{ref}$ (upper right), $\eta_{m,pl}^{ref}$, $4\tau_{m,0}^{ref}$ (lower left), $4\eta_{m,pl}^{ref}$ and $4\tau_{m,0}^{ref}$ (lower right). The confinement ratio applied is $\alpha = R_a/r_p = 4$.*

6.6 Testing

A phenomenological model for assessment of blocking of monodisperse suspensions was presented in the previous Sections.

The subsequent sections describe the results from testing of flow of monodisperse suspensions in a circular tube. The results are compared to the behaviour of the model.

The tests were partly carried out by Wolf & Jensen (2006) in their Diploma Engineer work.

The testing procedure, material properties, and mix compositions are described in Sections 6.6.1, 6.6.2, 6.6.3, 6.6.4, and 6.6.5. The experimental results are described in Sections 6.6.6 and 6.6.7, and in Section 6.6.8 the experimental results are compared with the model behaviour.

6.6.1 Test Setup

A test setup of piston driven flow in a circular tube has been applied. The setup was developed as part of an earlier project (BriteEuram 1997). The test setup is shown in Figure 6.22. It consists of a

- linear tube.
- tapered tube placed in continuation of the linear tube.
- moving piston.

The linear part of the tube has a diameter $D_L = 25$ mm and a length $L_L = 230$ mm.

The radius of the inlet to the tapered tube is $R_L = 12.5$ mm and R_T at the outlet. The outlet radius (R_T) and length of the tapered tube (L_T) applied in the experiments are shown in Table 6.1.

Table 6.1 *The geometry of the tapered tubes applied in tests.*

Name	R_T [mm]	L_T [mm]
B	6.0	14.0
C	3.0	6.0
D	4.5	6.0

The phenomenological model considered flow in a straight circular tube of radius R. For estimation of a critical flow rate in the test setup, it is assumed that $R = R_T$. Initially, it is assumed that the inclination of the tapered tube is negligible, but tests should look into the effect of the inclination for the same outlet radius (R_T).

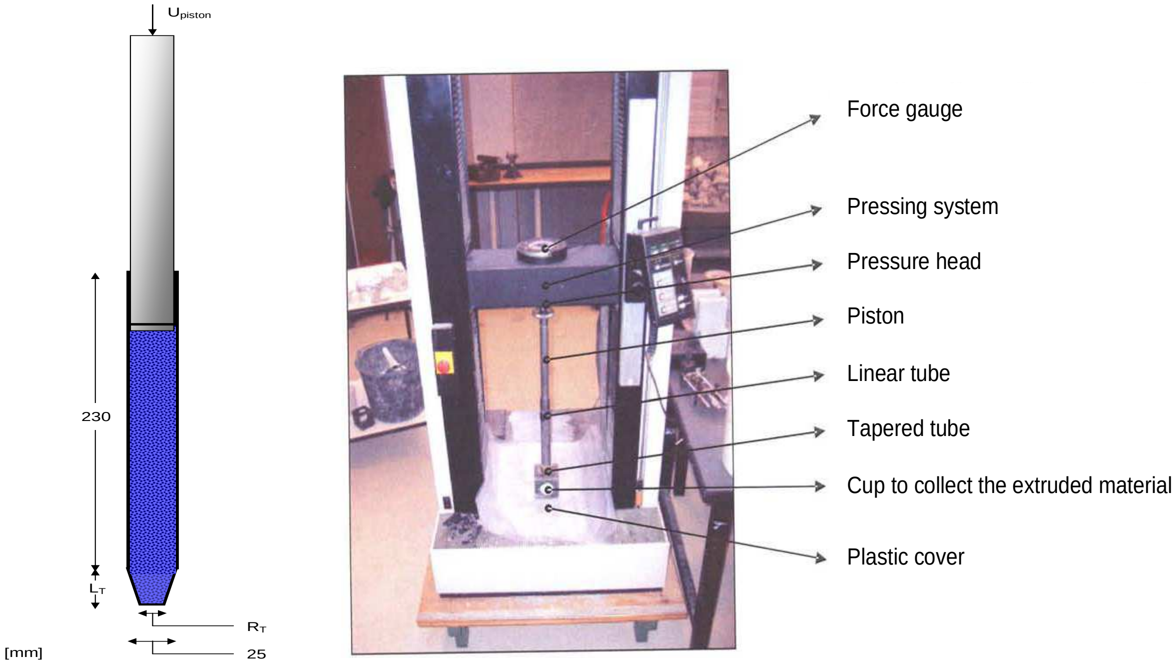

(a) (b)

Figure 6.22 *To the left, the test setup for piston driven flow of suspensions in a circular tube is illustrated. To the right, the actual test setup in the Instron 10 kN Pressure Machine (Wolf & Jensen 2006).*

The tube is filled with material without destroying the homogeneity of the suspension. The test setup is then placed in a 10 kN Instron Pressure machine.

Flow of the suspension is initiated by imposing a constant piston velocity (U_{piston}). The maximum piston velocity in the Instron Pressure Machine is 1000 mm/min = 16.67 mm/s.

The gap between the piston and the tube is tightened by a rubber ring around the piston. The tube and the piston are lubricated with a silicone grease before each test to avoid friction between the piston and the tube.

The piston is placed 15 mm down the tube before each test to ensure a stable vertical movement and to avoid entrapped air between the suspension and piston. Entrapped air can escape through small holes in the upper part of the linear tube. Therefore, the sample length in the linear part is approximately 215 mm.

During a test, the force required to retain a constant velocity is monitored. Complete blocking (or consolidation of the sample) is obtained when a force of 2 kN is reached.

The phenomenological model assumes that the matrix flow relative to particles is laminar and governed by viscous forces. As mentioned in Section 6.3.2, Fand & Thinakaran (1990) have studied the flow of a Newtonian fluid through a packed bed of monodisperse spheres and found that the upper bound for Darcy flow, where the viscous forces dominate, was $Re = 2.3$ where $Re = \frac{d_p U \rho_m}{\mu_m(1-\phi_m)}$. The so-called Forchheimer flow regime including both the viscous and inertial term was found for approximately $5 \leq Re \leq 80$ and turbulent flow was found for $Re > 120$.

An estimate of the Reynolds number for the tests carried out in this project may be based on the following values; particle diameter d_p=0.0022 m, plastic viscosity of the matrix phase $\eta_{m,pl} = 0.2$ Pa·s, matrix density $\rho_m = 1700$ kg/m^3, and particle volume fraction $\phi_p = 0.50$. At a piston velocity of $U_{piston} = 0.016$ m/s this gives a Reynolds number of 0.59 for matrix flow. Therefore, the assumption of laminar viscous flow seems reasonable.

The Reynolds number for the suspension is estimated at the same piston velocity ($U_{piston} =$ 0.016 m/s) when the Reynolds number is calculated as $Re = \frac{D_L U \rho_s}{\eta_{s,pl}}$ where $D_L = 0.025$ m. The plastic viscosity of the suspension ($\eta_{s,pl}$) is estimated using Equation 6.7 applying $\phi_p = 0.50$, $\phi_p^* = 0.64$, $\eta_{m,pl} = 0.2$ Pa·s, and $[\eta] = 2.5$. This gives $\eta_{s,pl} = 2.27$ Pa·s, and for a density of $\rho_s = 2300$ kg/m^3 this gives $Re = 0.40$ for which reason laminar viscous flow also seems reasonable to assume for the flow of the suspensions.

6.6.2 Materials and Properties

The materials applied consisted of a particle and matrix phase respectively.

The matrix phase is characterized by the rheological properties and the particle phase by the particle volume fraction, maximum particle volume fraction, and shape.

Initially, attempts were made to apply glucose as a model material for the matrix phase. However, it proved difficult to work with the glucose as a model material due to the stickiness. Instead it was decided to apply a semi-real matrix phase as a model material. The semi-real notification refers to the use of constituent materials which are normally applied in pastes, i.e. lime stone filler, fly ash and micro silica. The advantage of this approach is that it reminds of a real type paste and that the rheological properties do not change significantly over time as the reactiveness of the fly ash and micro silica is not activated unless cement hydration is present.

Superplasticiser is added to obtain a dispersed matrix phase. A 3rd generation type co-polymer has been applied (Viscocrete34 from SIKA). This is adapted for the ready mix industry as it has a longer opening time and it is possible to retain a flowable mix for approximately 2 hours without a visual change in the flow properties. It has a density of 1010 kg/m^3 and a water concentration of 70 %.

The rheological properties of the matrix phase are discussed in Section 6.6.5.

The phenomenological model was outlined for a particle phase consisting of dispersed monodisperse spherical particles. Glass beads have been applied to simulate spherical shaped particles. The glass beads have a diameter of $d_p = 2.2$ mm, so that surfaces forces between the glass beads can be neglected and the particle flow is only governed by hydrodynamics.

To test the effect of particle shape, it was decided to apply cube shaped particles. This particle shape was obtained from perforation of a 2.0 mm thick aluminium plate from RM Rich Muller A/S (Wolf & Jensen 2006). According to a pourbaix diagram for aluminium, these are stable at a pH value between 4 and 8.3 (engnet.anu.edu.au 2006)(Pade 2006). The exact pH of the combination of lime stone filler, fly ash and micro silica was not measured. However, to avoid any reaction, the aluminium particles were treated with a thin layer of lacquer and no signs of reaction were observed during mixing and testing.

Both the glass beads and the aluminium particles have a non porous surface and a smooth texture.

The maximum particle volume fraction in the bulk region was determined for both particle types. The particles were placed in a cylinder with a diameter of 80 mm placed on a manual operated drop table. The confinement ratio (α) in this test was approximately 35 so that the wall effect could be neglected. The maximum particle volume fraction was calculated after dropping the table 200 times. For each particle shape, the test was repeated three times (Wolf & Jensen 2006).

In the model a value of the intrinsic viscosity of 2.5 have been applied to both the glass beads and the aluminium particles. According to the discussion in Section 3.1.3 this value should be probably be higher for the aluminium particles. Therefore, the critical velocities shown for the aluminium particles are likely to be higher.

The properties of the glass beads and aluminium particles are summarized in Table 6.2.

For estimation of a critical flow rate when using the aluminium particles, a characteristic diameter d_c has to be determined. The characteristic diameter (d_c) may de determined using the circumscribe or inscribed sphere of the cube shape, which denotes the maximum and minimum characteristic diameters, respectively. This is referred to as model 1 and 2 in Table 6.3.

Table 6.2 *Properties of glass beads and aluminium particles applied in tests.*

	Glass beads	Aluminium boxes
Density [kg/m^3]	2525	2646
Diameter [mm]	2.2	
Height [mm]		2.0
Width [mm]		2.3
Length [mm]		2.3
Maximum Packing Density (ϕ_p^*)	0.619	0.698

Table 6.3 *Characteristic diameter and confinement ratios for glass beads and the cube shaped aluminium particles.*

	Glass beads	Alu. part. model 1	Alu. part. model 2	Alu. part. Average
Characteristic Diameter (d_c) [mm]	2.2	3.85	2.72	3.28
Confinement ratio (setup B)	5.45	3.11	4.41	3.76
Confinement ratio (setup C)	2.72	1.56	2.21	1.88
Confinement ratio (setup D)	4.09	2.33	3.31	2.82

Table 6.3 also shows the confinement ratios given as the ratio of the outlet tube radius (R_T) over the characteristic radius ($0.5 \cdot d_c$) for setup B, C, and D in Table 6.1, respectively.

6.6.3 Mix Compositions

The mix compositions applied in the tests are presented. The matrix phase composition, the particle volume fraction, and the particle shape vary. A total of 27 mix compositions have been tested and these are shown in Table 6.4.

Three different matrix phases have been applied and these are referred to as Mix-1, Mix-2, and Mix-3. These are shown in Table 6.5, 6.6, and 6.7. Most of the suspensions apply Mix-3 (21 out of 27 suspensions).

For the flow properties of the matrix phase, the aim was to obtain a dispersed and stable matrix phase. For each batch, the superplasticicer dosage was adjusted during mixing to obtain the desired flowability based on visual observations, however, not more than the particles would remain stable, and the only possible cause of phase separation would be blocking. The superplasticizer dosages (SP) (% weight of powder), applied in each of the suspensions, are shown in Table 6.4 under SP.

Table 6.4 *Mix composition of suspensions.*

Name	Matrix	Shape	SP (% weight of powder)	ϕ_p (%)
A-1	Mix 1	Sphere	0.90	52,6
A-2	Mix 1	Sphere	0.90	29.6
B-1	Mix 2	Sphere	0.90	31.5
B-2	Mix 2	Sphere	0.90	38.2
B-3	Mix 2	Sphere	0.90	39.2
B-4	Mix 2	Sphere	0.90	44.3
C-1	Mix 3	Sphere	0.90	39
C-2	Mix 3	Sphere	0.90	39
C-3	Mix 3	Sphere	0.90	37-38
C-4	Mix 3	Sphere	1.07	41
D-1	Mix 3	Sphere	1.07	45
D-2	Mix 3	Sphere	1.24	45
D-3	Mix 3	Sphere	0.98	40.3
D-4	Mix 3	Sphere	1.21	40.3
D-5	Mix 3	Sphere	0.98	40.3
D-6a	Mix 3	Sphere	0.94	35
D-6b	Mix 3	Sphere	1.06	37.5
D-8	Mix 3	Sphere	0.98	38, 39, 40, 41, 42
D-9	Mix 3	Sphere	0.99	40, 40.2, 41.25, 41.5
D-10	Mix 3	Box	0.99	34, 36
D-11	Mix 3	Box	0.83	20
D-12	Mx 3	Sphere	0.98	45, 47.5, 50, 50.75
D-13	Mix 3	Box	0.92	32, 35, 40
D-13*	Mix 3	Box	0.98	35, 40
D-14	Mix 3	Box	0.98	38, 38.25, 38.50, 38.75
D-15	Mix 3	Box	0.99	38, 38.75, 39, 39.25

Table 6.5 *Matrix composition - Mix-1*

Material	Density (kg/m3)	Volume (l)	Mass (kg/m^3)
Fly ash	2300	204	469
Micro silica	2290	59	135
Lime stone filler	2700	145	392
Water	1000	591	591
Total		1000	1588
Water/Binder			0.59

Table 6.6 *Matrix composition - Mix-2*

Material	Density (kg/m3)	Volume (l)	Mass (kg/m^3)
Fly ash	2300	200	460
Micro silica	2290	58	134
Lime stone filler	2700	143	386
Water	1000	598	598
Total		1000	1579
Water/Binder			0.61

Table 6.7 *Matrix composition - Mix-3*

Material	Density (kg/m3)	Volume (l)	Mass (kg/m^3)
Fly ash	2300	268	617
Micro silica	2290	79	180
Lime stone filler	2700	192	519
Water	1000	461	461
Total		1000	1777
Water/Binder			0.35

6.6.4 Mixing Procedure

The suspensions were mixed in a food processer and the mixing procedure was as follows:

- The dry materials were put into the mixer and dry mixing was carried out for 1 min.
- Half of the water was added and mixing continued for 30 s. A scraper was used on the sides and in the bottom of the mixer to remix agglomerates.
- The rest of the water was added over the next 20 s and the mix started to look like wet clay and agglomerates were now dispersed. Mixing continued for 1 min.
- Particles were added over a period of 1.5 min. Again the scraper was used to make sure no agglomerates were formed at the bottom and sides of the mixer.
- Superplasticiser was added over a period of 3 min. The mix was continuously supervised for a visual assessment of the consistency and stability. Mixing continued for 1 min after adding the last dosage of superplasticiser.

6.6.5 Rheological Properties of the Matrix Phase

The final input parameters to the phenomenological model are the rheological properties of the matrix phase. The particle volume fraction, maximum particle volume fraction, particle shape, confinement ratio, and tube radius were discussed in the previous sections.

Unfortunately, a paste rheometer was not available at the time of testing. Instead reasonable estimates for the yield stress and plastic viscosity are discussed below.

Qualitatively, the suspensions were all very easy to stir, and when moving a device through a suspension it would return to its original shape. This indicated both a low plastic viscosity and yield stress.

Within the framework of the Danish SCC Consortium, the rheological properties of a wide number of pastes have been measured by Dunschede (2004) in his Master project at the research institute EMPA. The Paar Physica MCR 300 viscometer was applied (plate-plate system). Dunschede (2004) tested different types of superplasticizers (Sika Viscocrete 3082, Degussa Glenium C151, and Fosroc Structuro A1510) and paste compositions.

A total of 125 tests were carried out and some of the results of yield stress and plastic viscosity are reproduced in Figure 6.23. The yield stress and plastic viscosity are shown as a function of the superplasticizer dosage (SP^*) which is given as the solid content of the superplasticer in % weight of the powder. The measurements were carried out 10 min after adding water during mixing.

Results are shown for pure cement pastes and for pastes with a powder combination consisting of cement and fillers. The water cement ratio of the pure cement pastes was 0.35 (by weight). Substitution of cement with filler was done so that the powder volume remained constant. The cements in the pure cement pastes consisted of white Portland cement (CEM I 52.5 N, white), rapide hardening cement (CEM I 52.5 N), and low alkali sulphate resistant cement (CEM I 42.5 N). Powder combinations consisted of 1) white cement and limestone filler (70:30 by volume), 2) rapid hardening cement, fly ash, and micro silica (65:30:5 by volume), and 3) low alkali sulphate resistant cement, fly ash, and micro silica (65:30:5 by volume). In Figure 6.23, the terms HOC, ROC, SAC, LM, FA, and MS refer to the white cement, rapide cement, low alkali cement, lime stone, fly ash, and micro silica, respectively.

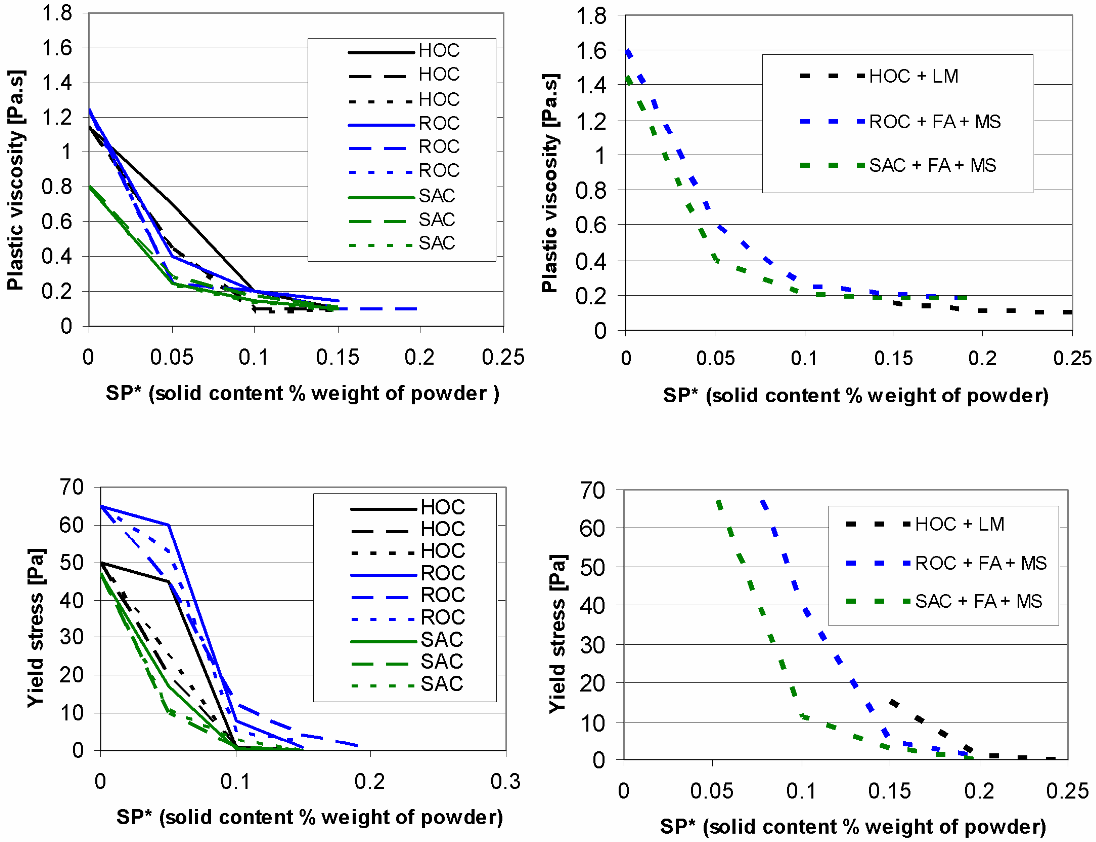

Figure 6.23 *Results by Dunschede (2004) on the yield stress and plastic viscosity of different paste systems. Three different types of superplasticizers were applied. Solid lines refer to Fosroc Structuro A1510. Dashed lines refer to Sika Viscocrete 3082. Dotted lines refer to Degussa Glenium C151. The terms HOC, ROC, SAC, LM, FA, and MS refer to the white cement, rapide cement, low alkali sulphate resistant cement, lime stone filler, fly ash, and micro silica, respectively.*

In general, for superplasticizer dosages above approximately 0.15 % there seems to be no significant difference between the results for yield stress and plastic viscosity for the different superplastizers. For the values of yield stress and plastic viscosity, relatively low values are obtained at dosages from approximately 0.2 %. For the yield stress, it seems that at superplasticizer dosages of 0.2 %, the yield stress is very low in the range of 0 to 1.0 Pa. In the same range of superplaticizer dosages, the plastic viscosity is approximately 0.2 Pa·s.

The superplasticizer dosages applied for the blocking tests were shown in Table 6.4. The superplasticizer dosages were given as the solid content + water in % weight of powder and the dosages applied were approximately 0.90 to 1.00 %. In terms of the solid content of the superplasticizer, this gives 0.27 to 0.30 % weight of powder.

The qualitative assessment of the matrix phase compared with the quantitative results of Dunschede (2004) indicates relatively low values for the yield stress and plastic viscosity.

Though the suspensions had a low yield stress, visual observations of the suspensions after mixing showed that these did not exhibit static segregation. In Section 3.2.2 an equation for estimating the critical particle diameter of a single particle in a yield stress matrix phase was presented (Bethmont et al. 2003). Knowing the diameter of the particles, it may be written in terms of a critical yield stress

$$\tau_{m,0} \geq \frac{d_p \Delta\rho_{pm} g}{20.97} \tag{6.32}$$

where d_p is the particle diameter, $\Delta\rho_{pm}$ is the difference between the particle density and matrix density, $\tau_{m,0}$ is the matrix yield stress, and g is gravity.

When using $d_p = 0.0022$ m, $\Delta\rho_{pm} =$ 2525-1777=748 kg/m^3 (glass beads - matrix Mix-3), and $g = 9.81$ m/s^2, it results in an estimate of the critical matrix yield stress of $\tau_{m,0} =$ 0.76 Pa if only one particle is placed in the matrix.

In summery, it is expected that the yield stress and plastic viscosity of the matrix phase are low, approximately 0.5 to 1.5 Pa for the yield stress and 0.2 to 0.6 Pa·s for the plastic viscosity. However, to show the effect of yield stress and plastic viscosity, the results of the model will be compared to the experimental results for a wider range of yield stresses and plastic viscosities, i.e. $0.5 \leq \tau_{m,o} \leq 6.0$ Pa and $0.2 \leq \eta_{m,pl} \leq 2.0$ Pa·s.

6.6.6 Experimental Results

A total of 120 tests have been carried out and the previous sections have presented the different tube setups and mix compositions.

The test have been carried out for various piston velocities (U_{piston}), and the results are shown as piston velocity versus particle volume fraction (ϕ_p). The blue markers represent that blocking has occurred and the black markers represent homogeneous flow. In Appendix C, the piston load versus the piston travelling length are shown for each test.

In Section 6.6.8, the experimental results are compared to the model behaviour. The model shows the critical piston velocity as a function of the particle volume fraction.

Figure 6.24 shows U_{piston} versus ϕ_p applying tube setup B when using glass beads corresponding to an confinement ratio $\alpha = 5.45$. The results show that the risk of blocking increases as a function of the particle volume fraction. In a very narrow range of particle volume fractions at approximately $\phi_p = 0.50$, the results show that it is possible to avoid blocking by increasing the piston velocity. The critical velocity increases when going from $\phi_p = 0.50$ to 0.5075 at which point blocking was not observed for piston velocities of 500 and 1000 mm/min, respectively. Above $\phi_p = 0.5075$, it was not possible to obtain homogenous flow within the limits of the test setup.

In general, these results indicate that blocking is significantly dependent on the particle volume fraction which seem to be critical at approximately $\phi_p = 0.50$. A critical velocity is only obtained in narrow range of particle volume fractions. However, if it had been possible to apply higher velocities it may have been possible to avoid blocking at particle volume fractions higher than $\phi_p = 0.5075$.

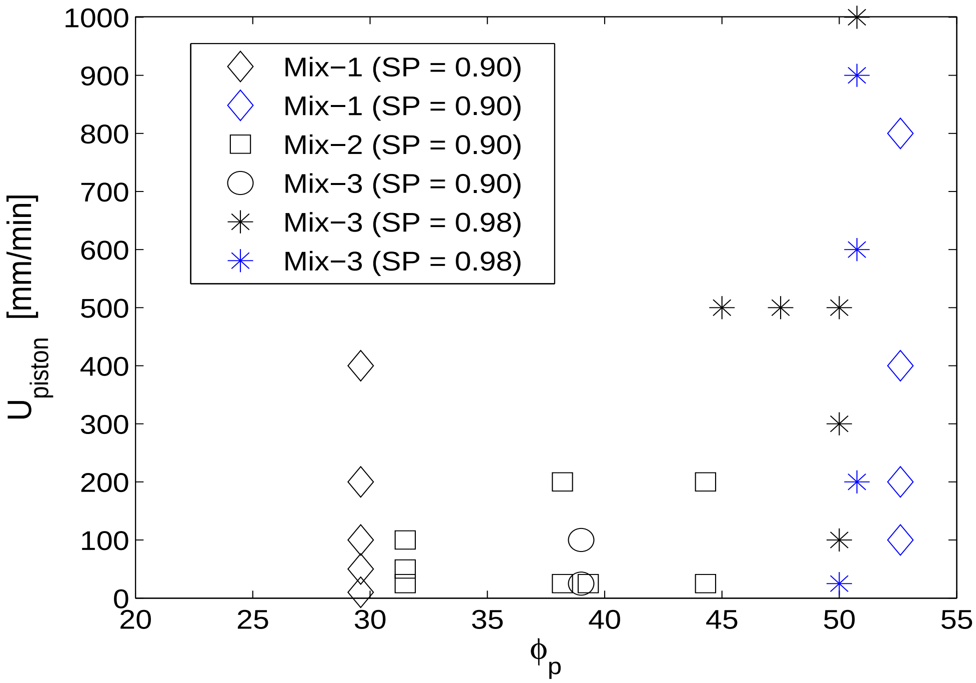

Figure 6.24 *Results from testing suspensions with glass beads when using tube B corresponding to an confinement ratio of $\alpha = 5.45$ (ϕ_p is in [%]). Blue markers = blocking and black markers = no blocking. Mix-1, Mix-2, and Mix-3 refer to the matrix composition.*

Figure 6.25 shows U_{piston} versus ϕ_p applying tube setup B when using the aluminium particles. This corresponds to a confinement ratio of $\alpha = 3.11$ or 4.41 according to model 1 and 2 in Table 6.3, respectively (in average 3.76).

Again, blocking is clearly dependent on the particle volume fraction and compared to the glass bead suspensions in Figure 6.24, blocking is obtained at lower particle volume fractions. As for the glass bead suspension, blocking seems to be flow rate dependent in a very narrow range of particle volume fractions at approximately $\phi_p = 0.37$ to 0.39. At $\phi_p = 0.39$ blocking could be avoided at 200 mm/min, but not at lower piston velocities. The particle volume fraction where blocking cannot be overcome by increasing the velocity occurs at approximately $\phi_p = 0.40$ compared to approximately $\phi_p = 0.51$ for the glass bead suspensions. This may be explained by the confinement ratio which was 5.45 for the glass bead suspensions, and 3.76 in average for the aluminium particles.

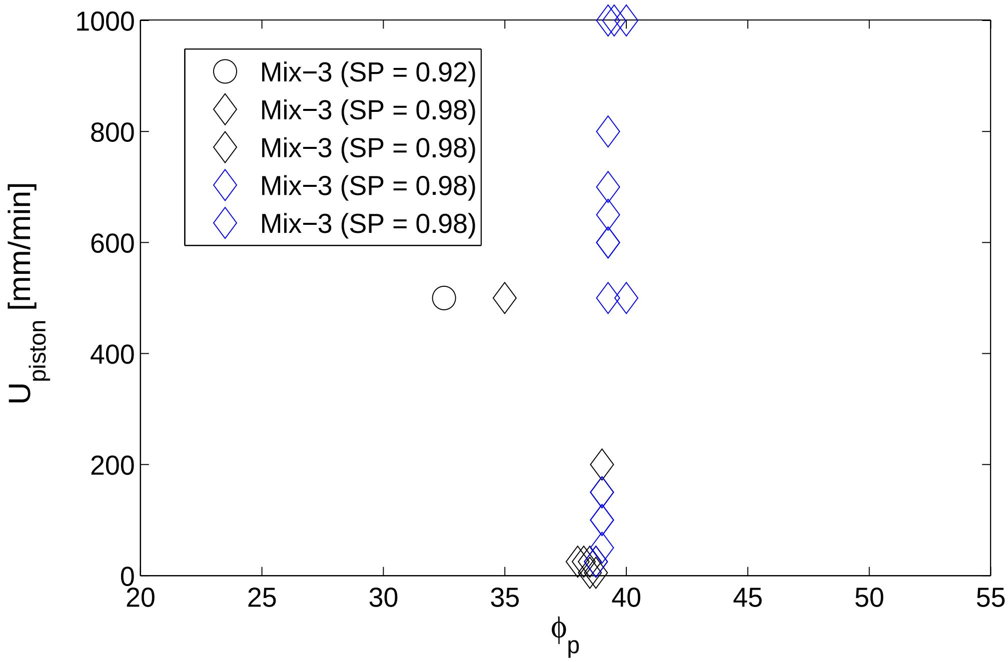

Figure 6.25 *Results from testing suspensions with aluminium boxes when using tube B corresponding to an confinement ratio of* $\alpha = 3.11$ *or* 4.41 *according to model 1 and 2 in Table 6.3 (*ϕ_p *is in [%]). Blue markers = blocking and black markers = no blocking. Mix-3 refers to the matrix composition.*

Figure 6.26 shows U_{piston} versus ϕ_p for the glass bead suspensions when applying tube setup C corresponding to a confinement ratio of $\alpha = 2.72$.

It is observed that blocking occurs at a lower particle volume fractions compared to applying tube B ($\alpha = 5.45$). Blocking occurred in each of the tests so it was not possible to assess the effect of flow rate and the range of particle volume fractions where blocking would not be initiated.

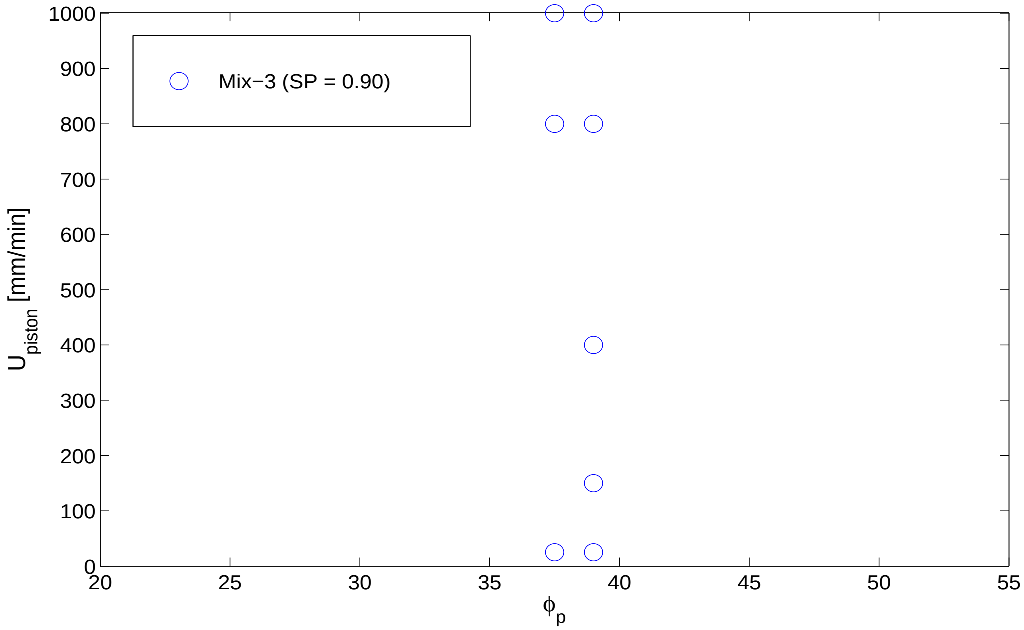

Figure 6.26 *Results from testing suspensions with glass beads when using tube C corresponding to a confinement ratio of $\alpha = 2.72$ (ϕ_p is in [%]). Blue markers = blocking and black markers = no blocking. Mix-3 refers to the matrix composition.*

Figure 6.27 shows U_p versus ϕ_p for glass bead suspensions applying tube D corresponding to a confinement ratio of 4.09.

The risk of blocking is clearly dependent on the particle volume fraction (ϕ_p) and it observed that the critical particle volume fraction is approximately $\phi_p = 0.40$, which is lower than when using a confinement ratio α =5.45 and higher than when using a confinement ratio $\alpha = 2.72$. Over a narrow range of particle volume fractions at approximately $\phi_p = 0.40$ flow rate dependency is observed. Reaching $\phi_p \approx 0.42$ it is not possible to avoid blocking within the limits of the test setup.

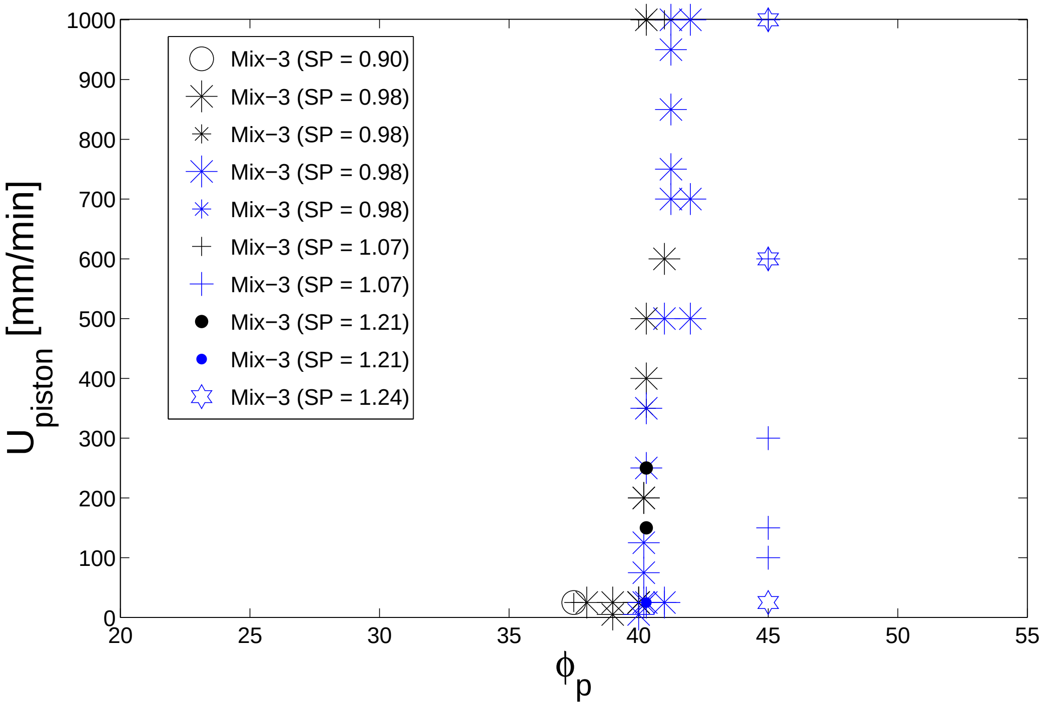

Figure 6.27 *Results from testing suspensions with glass beads when using tube D corresponding to a confinement ratio of* $\alpha = 4.09$ *(*ϕ_p *is in [%]). Blue markers = blocking and black markers = no blocking. Mix-3 refers to the matrix composition.*

Figure 6.28 shows U_{piston} versus ϕ_p applying tube D when using the aluminium particles. This corresponds to a confinement ratio of $\alpha = 2.33$ or 3.31 according to model 1 and 2 in Table 6.3, respectively (in average 2.82).

Compared to the results in Figure 6.25 (average confinement ratio of 3.76) it is observed that blocking occurs at lower particle volume fractions due to a lower confinement ratio.

Flow rate dependency has been shown at $\phi_p = 0.20$ where blocking is observed at $U_{piston} =$ 500 mm/min and not at 1000 mm/min. The other results showed that flow rate dependency occurred over a narrow range of particle volume fractions, which indicate that the critical particle volume fraction is in the range of $\phi_p = 0.20$.

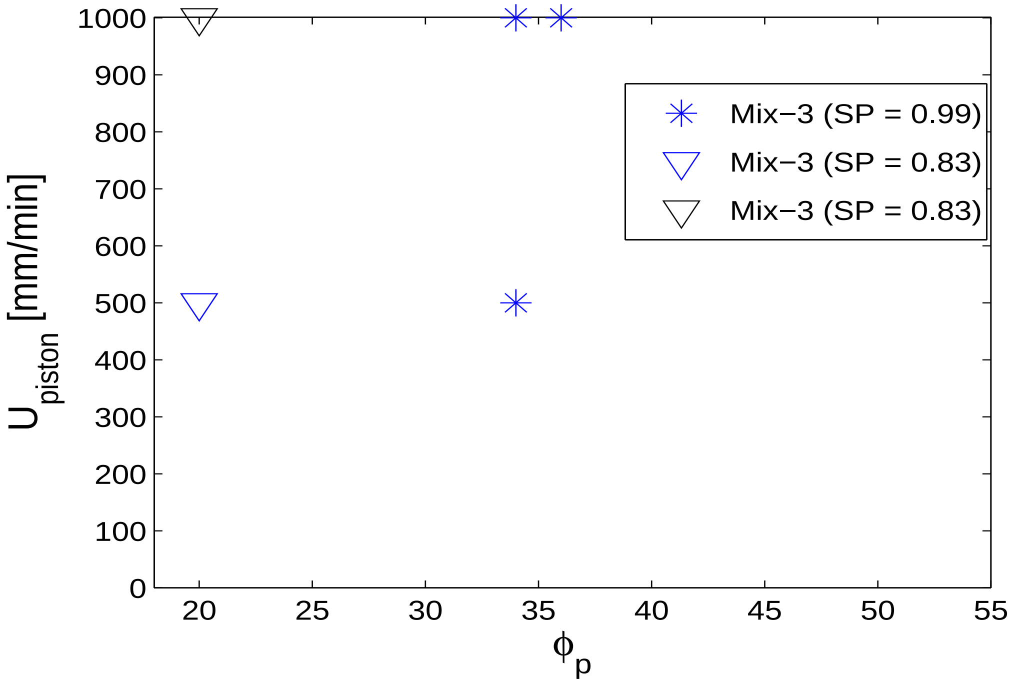

Figure 6.28 *Results from testing suspensions with aluminium boxes when using tube D corresponding to a confinement ratio of* $\alpha = 2.33$ *or* 3.31 *according to model 1 and 2 in Table 6.3 (*ϕ_p *is in [%]). Blue markers = blocking and black markers = no blocking. Mix-3 refers to the matrix composition.*

6.6.7 Sample Accuracy

The sampling accuracy was investigated by Wolf & Jensen (2006) by comparing the particle volume fraction of the sample in the tube with the bulk particle volume fraction. In ten tests a sample was collected after the test to determine the actual particle volume fraction applied in the test. The results are shown in Table 6.8.

For the seven suspensions with a particle volume fraction of 0.40 the sample mean and standard deviation are 0.419 and 0.012, respectively.

For the three suspensions with a particle volume fraction of 0.45 the sample mean and standard deviation are 0.431 and 0.033, respectively. However, these values are strongly affected by a very low value of 0.399 for one of the samples.

Given the small number of samples at particle volume fraction of 0.45, it seems reasonable to assume that the standard deviation is in the range of the value found for the particle volume fraction of 0.40.

Table 6.8 *Particle volume fraction in the mix composition and the tested sample.*

ϕ_p in mix	ϕ_p in sample
0.45	0.431
0.45	0.464
0.45	0.399
0.40	0.424
0.40	0.429
0.40	0.420
0.40	0.418
0.40	0.433
0.40	0.415
0.40	0.397

The standard deviation is relatively low compared to the difference between the critical particle volume fractions found for different confinement ratios and particle shape. However, the flow rate dependency was found over a narrow range of particle volume fractions (approximately 0.01), which are in the range of the standard deviation.

6.6.8 Comparison of Experimental Results and Model Estimates

The experimental results are compared to the model behaviour.

The results are shown for the glass bead suspensions followed by the results for the aluminium suspensions.

The initial values of the maximum particle volume fraction, characteristic diameter, confinement ratio, and tube radius applied in the model were presented in the previous sections.

The model behaviour is shown for different values of the yield stress and plastic viscosity of the matrix phase.

Figures 6.29, 6.30, and 6.31 show the results for suspensions with glass beads when using tube B corresponding to a confinement ratio of $\alpha = 5.45$. The model has been shown for a yield stress of $\tau_{0,m} = 0.5$, 2.0, and 6.0 Pa and a plastic viscosity of $\eta_{pl} = 0.2$, 0.8, and 2.0 Pa·s. Figure 6.29 shows the results for the lowest value of yield stress (0.5 Pa) and the three values of plastic viscosity. In the same way Figures 6.30 and 6.31 show the results for yield stress 2.0 and 6.0 Pa, respectively.

It seems a reasonable estimate is obtained for the critical particle volume fraction when taking into account the sample accuracy. The model estimates a critical particle volume fraction of approximately 0.52 compared to approximately 0.50 in the experiments.

As it was discussed in the previous section, flow rate dependency is only observed over a narrow range of particle volume fractions (ϕ_p) and blocking is more dependent on the particle volume fraction. In section 6.5 the importance of the rheological properties on the critical velocity was discussed. It was shown that for yield stresses approaching zero the blocking criterion would reduce to a critical particle volume fraction. The actual yield stress of the matrix phase in these test is relatively low and likely in the range from 0.5 to 2.0 Pa (Figure 6.29 and 6.30). Depending on the value of the plastic viscosity more or less flow rate dependency is estimated. As discussed in Section 6.6.5 the plastic viscosity may be in the range of 0.2 Pa·s for which reason it seems the best correlation between the model estimate and the experimental results is obtained when using a yield stress of 0.5 Pa.

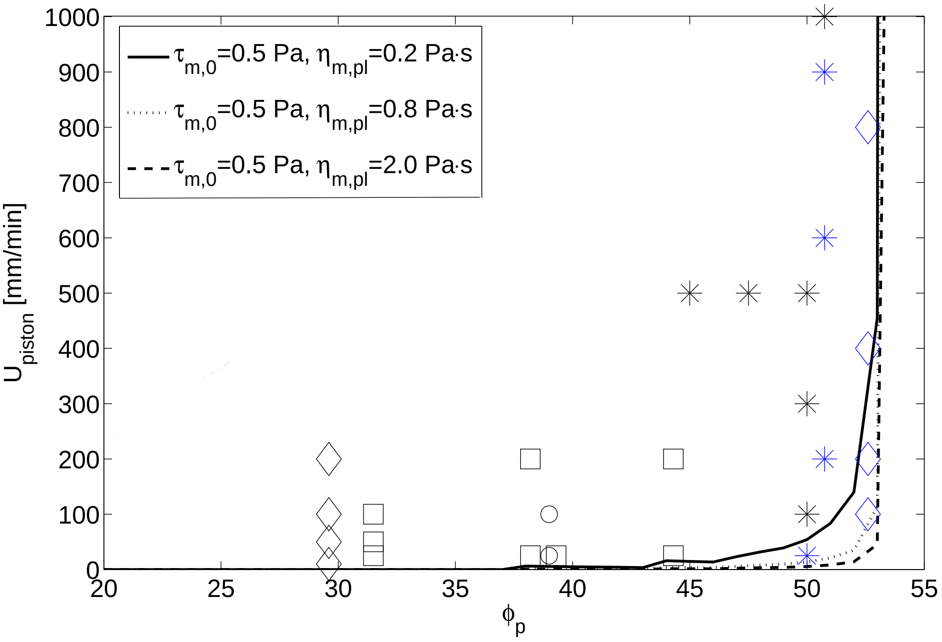

Figure 6.29 *Experimental results and model prediction of the critical piston velocity for glass bead suspensions when using tube B corresponding to a confinement ratio α = 5.45 (ϕ_p is in [%]). Blue markers = blocking and black markers = no blocking.*

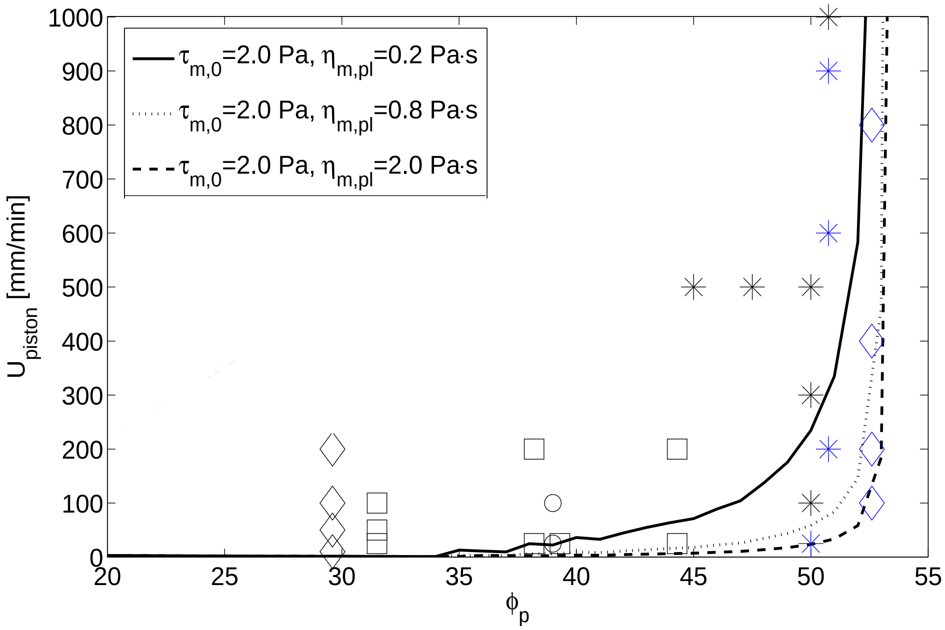

Figure 6.30 *Experimental results and model prediction of the critical piston velocity for glass bead suspensions when using tube B corresponding to a confinement ratio $\alpha = 5.45$ (ϕ_p is in [%]). Blue markers = blocking and black markers = no blocking.*

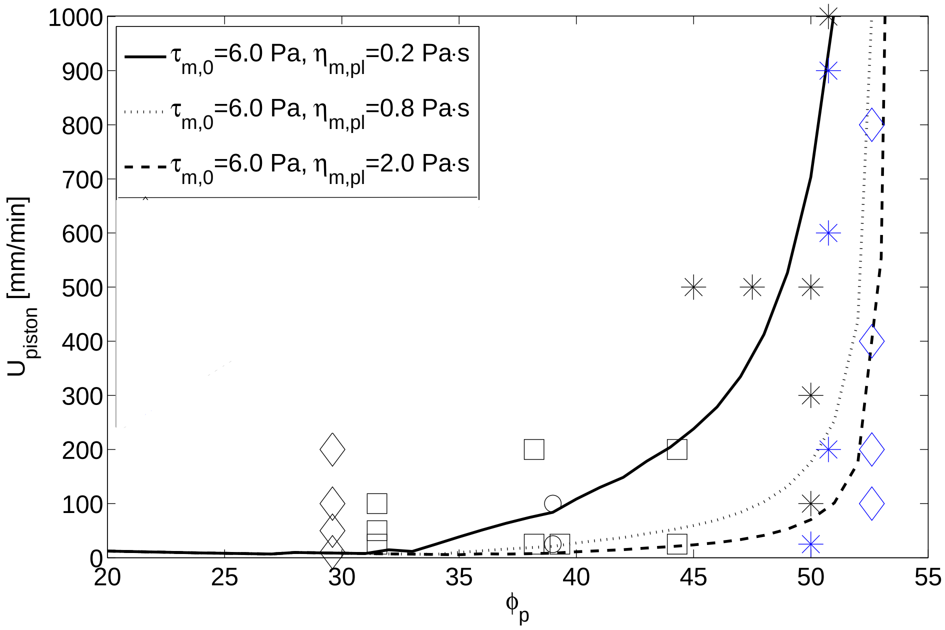

Figure 6.31 *Experimental results and model prediction of the critical piston velocity for glass bead suspensions when using tube B corresponding to a confinement ratio $\alpha = 5.45$ (ϕ_p is in [%]). Blue markers = blocking and black markers = no blocking.*

Figure 6.32 shows the results for suspensions with glass beads when using tube C corresponding to a confinement ratio $\alpha = 2.72$. The model is just shown for the lowest value of yield stress (0.5 Pa) and the three values of plastic viscosity because blocking was obtained in each of the tests so only the critical particle volume fraction may be compared. The model estimates a critical particle volume fraction of approximately 0.35 which corresponds to the experimental results which were tested at volume fractions of 0.37 to 0.39 and blocking was obtained in each of the tests. Tests need to be carried out at $\phi_p \leq 0.35$ to further assess the accuracy of the model estimate for the critical particle volume fraction, and to assess the effect of flow rate.

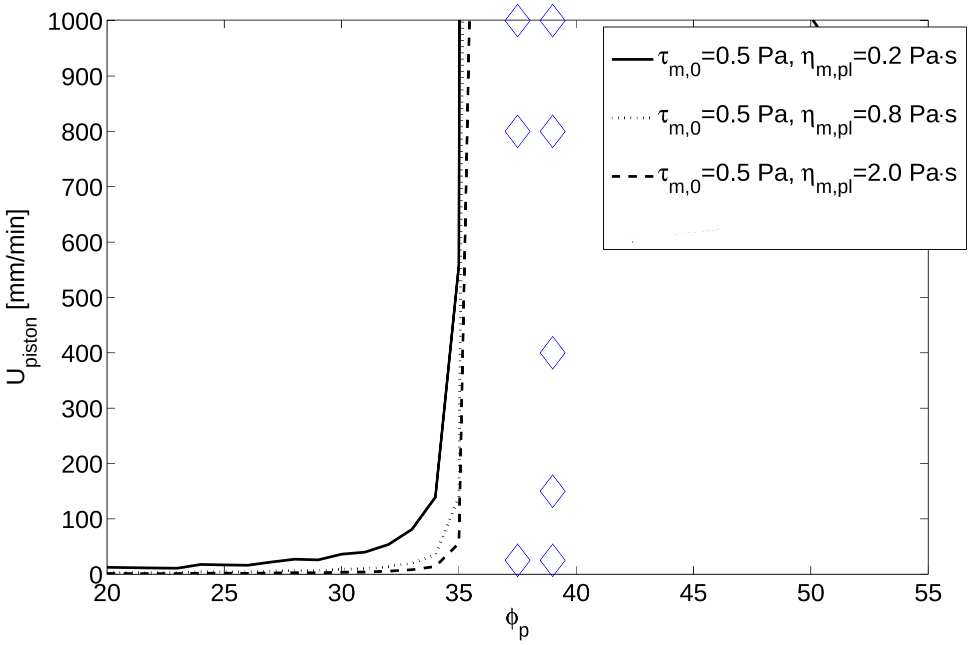

Figure 6.32 *Experimental results and model prediction of critical piston velocity for glass bead suspensions when using tube C corresponding to a confinement ratio α = 2.72 (ϕ_p is in [%]). Blue markers = blocking and black markers = no blocking.*

Figure 6.33 shows the results for suspensions with glass beads when using tube D corresponding to a confinement ratio $\alpha = 4.09$. Again the model is just shown for the lowest value of yield stress (0.5 Pa) and the three values of plastic viscosity. Initially, the measured maximum particle volume fraction of $\phi_p^* = 0.62$ was applied in the model. However, this results in an underestimation of the risk of blocking, e.g. the model estimates a critical particle volume fraction of approximately 0.48 compared to a lower value of approximately 0.40 in the experiments.

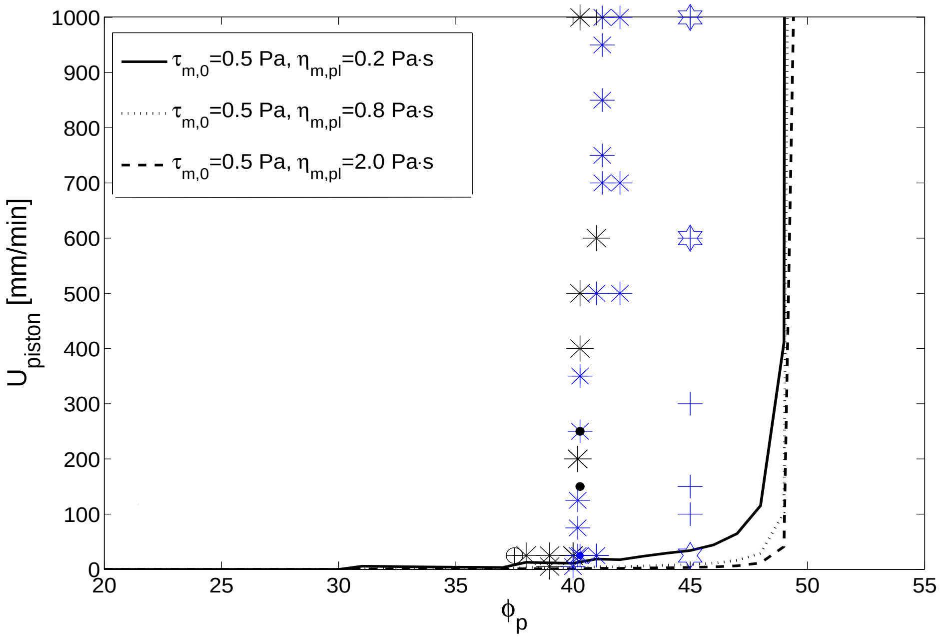

Figure 6.33 *Experimental results and model prediction for the critical piston velocity for glass bead suspensions when using tube D corresponding to a confinement ratio α = 4.09 (ϕ_p is in [%]). Blue markers = blocking and black markers = no blocking.*

When using the initial value $\phi_p^* = 0.62$ this results in a maximum particle volume fraction within a circular tube of $\phi_{p,w}^* = 0.58$ at a confinement ratio of 4.09 (according to Equation 6.23). Two experiments were carried out to determine the maximum particle volume fraction at $\alpha = 4.0$. Glass beads with a diameter of 4 mm were placed in a glass tube with a diameter of 16 mm. In the first test the glass beads were placed one at a time and in the second test the particles were added all at once. A maximum particle volume fraction of 0.57 and 0.50 was obtained in test 1 and 2, respectively. The result of the first test correlates with the results of (Fand & Thinakaran 1990) whereas the second value is lower. As expected, the maximum particle volume fraction depends on the process of packing the particles. If $\phi_{p,w}^* = 0.50$ is applied instead of 0.58 at $\alpha = 4.09$ the experimental results and model estimates correlate reasonable well when taking into account the sample accuracy. This is shown in Figure 6.34.

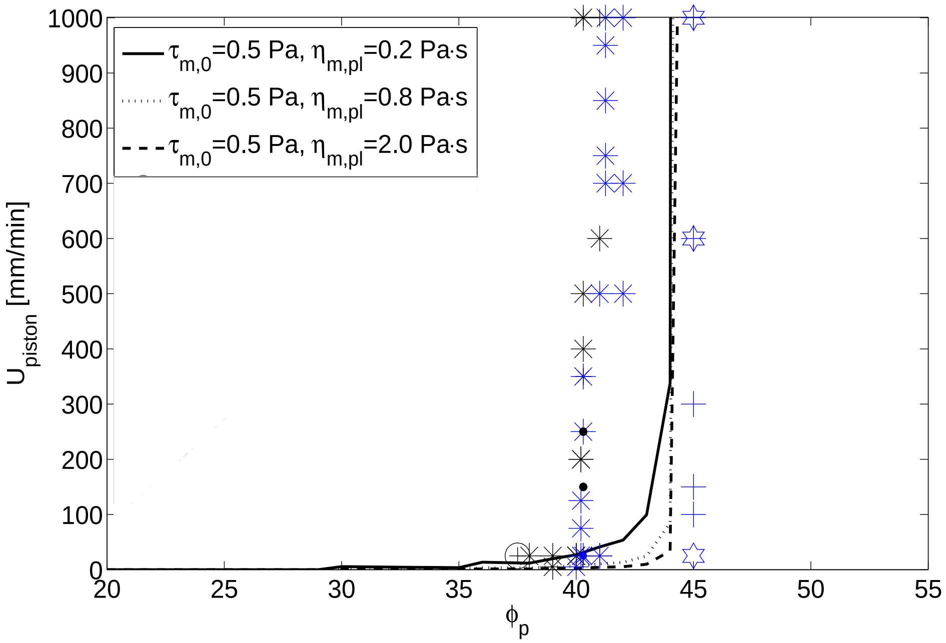

Figure 6.34 *Experimental results and model prediction for the critical piston velocity for glass bead suspensions when using tube D corresponding to a confinement ratio* α *= 4.09 (*ϕ_p *is in [%]). Blue markers = blocking and black markers = no blocking.*

Figure 6.35 shows the results for suspensions with aluminium particles when tube B is applied corresponding to a confinement ratio $\alpha = 3.11$ and 4.41 according to model 1 and 2 in Table 6.3 (in average 3.76). Here the model is shown when using $\alpha = 3.11$ which come closest to estimating the critical particle volume fraction of approximately $\phi_p = 0.38$ obtained in the experiments. The two tests carried out at particle volume fractions of $\phi_p \approx 0.32$ and 0.35 did not show blocking. These were carried out at piston velocities above the estimated critical velocities, however it seems likely that blocking would not have occurred at lower velocities as blocking was not observed in some of the tests at $\phi_p \approx 0.37$ at low velocity. Therefore, as for the other results, it seems the critical velocity increases rapidly when approaching the critical particle volume fraction. Again, the model is just shown for the lowest value of yield stress (0.5 Pa) and the three values of plastic viscosity. The rapid increase in the critical velocity may be obtained for $\eta_{m,pl} = 0.8$ and 2.0 Pa·s.

As mentioned in 6.6.2 the value of the intrinsic viscosity for the aluminium particles is likely higher than 2.5. This means that the rheological parameters of the suspension would be higher at a given particle volume fraction and subsequently it would result in higher critical velocities. Further testing are needed to assess the most appropriate way to include irregular shaped particles i.e. the value of the characteristic diameter and the value of the intrinsic viscosity.

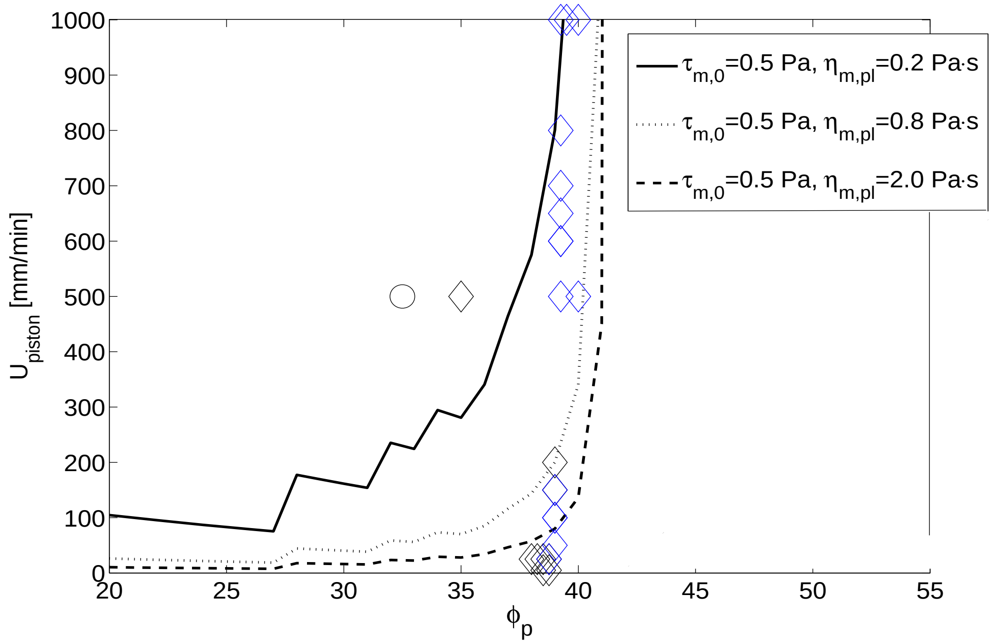

Figure 6.35 *Experimental results and model prediction for aluminium suspensions when using tube B corresponding to a confinement ratio* $\alpha = 3.11$ *and* 4.41 *according to model 1 and 2 in Table 6.3 (*ϕ_p *is in [%]). Here is shown for* $\alpha = 3.11$. *Blue markers = blocking and black markers = no blocking.*

Figure 6.36 and 6.37 shows the results for suspensions with aluminium boxes when tube D is applied corresponding to a confinement ratio $\alpha = 2.33$ and 3.31 according to model 1 and 2 in Table 6.3. Figure 6.36 shows the model estimate when using the low yield stress (0.5 Pa) and the three values of the plastic viscosity. The model is shown for the average value of $\alpha = 2.82$. This gives a critical particle volume fraction of approximately 0.35 which is an overestimation compared to the experimental results, which show that it is more likely in the range of 0.20. This indicate that the lowest value of the confinement ratio should be applied, which was also shown in Figure 6.35. However, also the rheological properties may be important. Figure 6.37 shows the model estimate for a yield stress of 2.0 Pa and the three values of the plastic viscosity. Though, it not possible to justify the exact effect of the superplasticizer dosage, the tests carried out at $\phi_p = 0.20$ contained the lowest amount of superplasticizer (0.83 %) which indicate that the yield stress may have been higher than in all of the other tests. However, as for the previous results, further assessment of the value of the intrinsic viscosity are also needed.

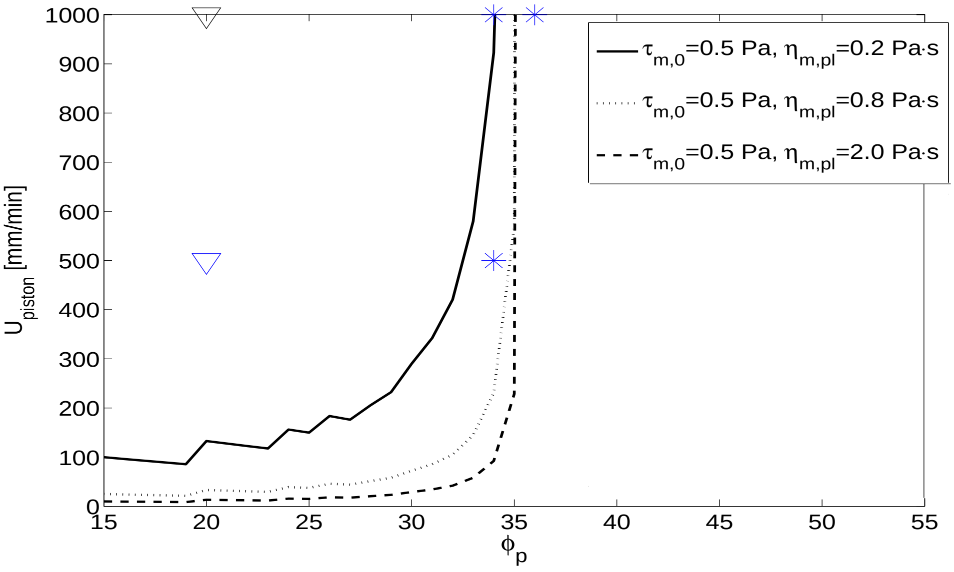

Figure 6.36 *Experimental results and model prediction for aluminium suspensions when using tube D corresponding to a confinement ratio* α = 2.33 *and* 3.31 *according to model 1 and 2 in Table 6.3. Here the model is shown with an average value of* α = *2.82 (*ϕ_p *is in [%]). Blue markers = blocking and black markers = no blocking.*

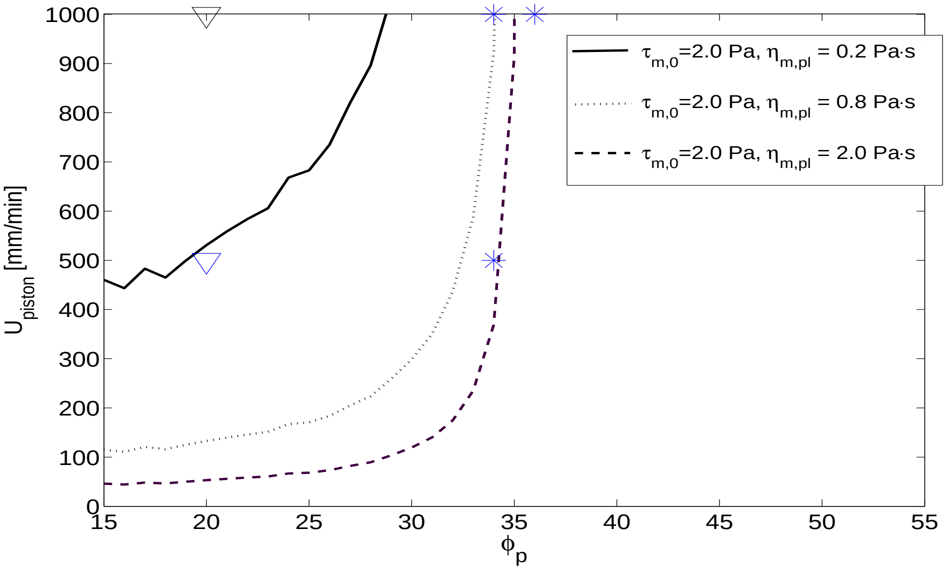

Figure 6.37 *Experimental results and model prediction for aluminium suspensions when using tube D corresponding to a confinement ratio* α = 2.33 *and* 3.31 *according to model 1 and 2 in Table 6.3. Here the model is shown with an average value of* α = *2.82 (*ϕ_p *is in [%]). Blue markers = blocking and black markers = no blocking.*

6.7 Flow Between Reinforcement

The phenomenological model has been derived for a circular tube flow domain which is different from flow between reinforcement. For an initial assessment of the critical velocity for flow between reinforcement it is proposed that the reinforcement geometry may be replaced by a corresponding tube radius.

The confinement ratio for flow between reinforcement is determined as the ratio of clear spacing between the reinforcement (c) over particle size (d_p). It was shown that the critical velocity depends on the absolute value of the tube radius. For a constant confinement ratio the highest critical velocity is obtained for the largest tube radius. Figure 6.38 shows two different assumptions for estimating the corresponding tube radius when the confinement ratio is held constant. These are referred to as $R_{c,1}$ and $R_{c,2}$.

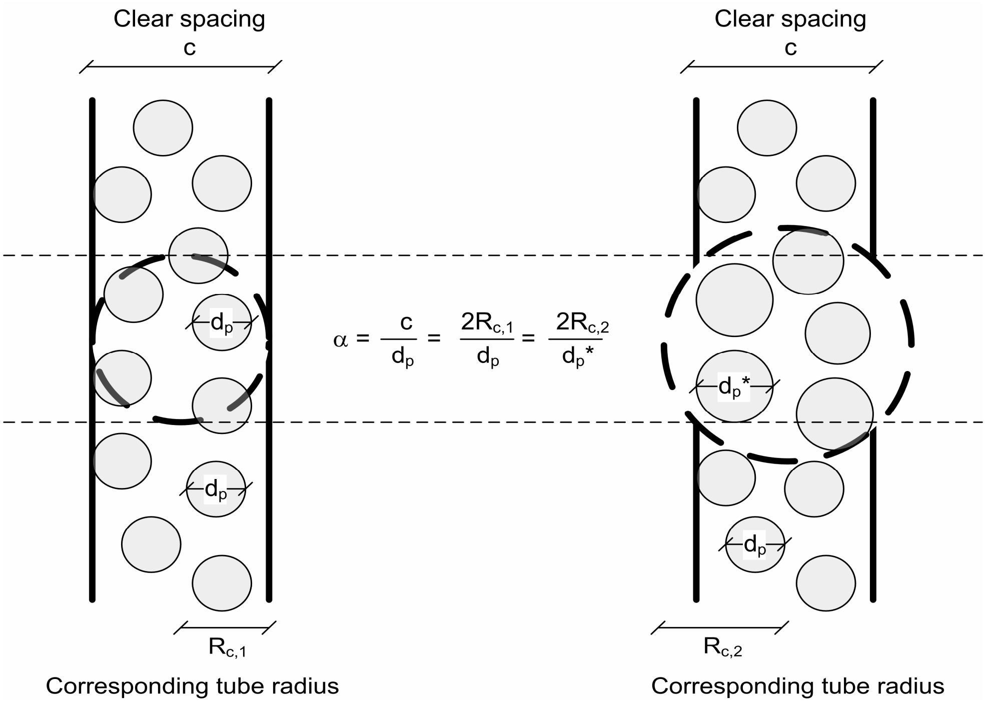

Figure 6.38 *Illustrations of two ways to estimate a corresponding tube radius for flow between reinforcement bars when the confinement ratio is held constant. These are referred to as* $R_{c,1}$ *and* $R_{c,2}$*.*

To the left the corresponding radius is equal to the clear spacing ($R_{c,1}$). To the right, the corresponding radius is equal to the radius of the circumscribed circle around a quadrant with side lengths equal to the clear spacing ($R_{c,2}$). The confinement ratio is held constant so a corresponding diameter (d_p^*) is applied in the situation to the right instead of d_p.

The corresponding radii $R_{c,1}$ and $R_{c,2}$ will be applied for estimation of the critical flow rate in the L-box test and the form filling applications including reinforcement presented in Chapter 7.

6.8 Conclusion

This Chapter has presented an initial step toward developing a phenomenological model for assessment of blocking based on physical principles. The model introduces a flow rate criterion where blocking occurs below a critical flow rate.

The model has been derived by comparing the pressure gradient needed to retain a constant flow rate in the two situations; homogeneous flow and heterogeneous flow in a circular tube. In the latter the matrix phase flows at an average velocity which is higher than the average particle velocity.

The monodisperse suspension and matrix phase are both considered to follow a Bingham plastic law. For the homogeneous flow the well-known Buckingham-Reiner equation for tube flow has been applied. A Krieger-Dougherty type relation has been applied for estimation of both the yield stress and the plastic viscosity of the suspension as a function of the Bingham parameters of the matrix phase, the particle volume fraction, the maximum particle volume fraction, and the intrinsic viscosity.

It has been assumed that the matrix flow takes place in straight circular capillaries, which are of the same length as the sample length. Calculation of the pressure drop-flow rate relation for matrix flow is based on existing theories for estimation of the hydraulic radius and correspondingly the capillary radius (twice the hydraulic radius) when also taking into account the wall effect. An important aspect of the proposed model is the assumption made on the capillary radius in a packed bed of monodisperse spherical particles. It is assumed that the capillary radius is equal to the particle radius for a random packed bed which is approximately 2.6 times the value estimated using the existing theories. This results in a lower pressure drop at a given flow rate of the matrix phase. The modified radius has been extended to include also the channeling effect of the wall.

The proposed model estimates a critical flow rate as a function of the Bingham parameters of the matrix phase, the particle diameter, the tube radius, the particle volume fraction, and the maximum particle volume fraction.

Results show that for a given confinement ratio and absolute tube ratio there is a critical particle volume fraction above which blocking will always occur. Below the critical particle volume fraction the critical flow rate is introduced. The critical flow rate depends on the rheological parameters of the matrix phase. When decreasing the plastic viscosity the critical velocity increases due to the generation of a lower viscous drag. When decreasing the yield stress the critical velocity decreases, and for a zero yield stress the blocking criterion reduces to a critical particle volume fraction.

An experimental program was carried out and the results of piston driven flow of monodisperse suspensions were compared with the model behaviour. The matrix phase had relatively low values of the yield stress and the plastic viscosity for which reason blocking was most dependent on the particle volume fraction.

When testing the monodisperse suspension with spherical glass beads the model shows a reasonable correlation with the experimental results, however, in one test (confinement ratio of approximately 4.09) the use of the theoretical value of the maximum particle volume fraction (0.57) overestimated the critical particle volume fraction. This corresponds to a process of packing where the particles are placed one at the time. A better estimate of the critical particle volume fraction was obtained when using a maximum particle volume fraction of 0.50 which corresponds to a process of packing where all the particles are placed at the same time.

For the cube shaped particles a corresponding particle diameter was introduced in terms of the circumscribe or inscribed sphere, respectively. The test results indicate that the circumscribe sphere assumption should be applied. Initially, the effect of the shape has only been studied in relation to the matrix flow in terms of this corresponding particle diameter. However, the irregular shape may also affect the intrinsic viscosity applied in calculation of the rheological parameters of the suspension and thus the pressure drop of the suspension. A higher value of the intrinsic viscosity will result in higher critical velocities.

For flow between reinforcement a corresponding tube radius have been proposed to simulate the clear spacing between the reinforcement.

Further development and verification of the phenomenological model may include:

- The use of the modified capillary radius in the model seems to give a reasonable estimate of the risk of blocking. However, tests should be carried out to verify it by measuring the pressure gradient - flow rate for a packed bed of monodisperse spheres at a low bed length to particle diameter.
- The outline of the model indicates that either pure blocking or homogeneous flow occurs. A possible intermediate stage is presently not captured by the model. Further modelling of the matrix flow may look into the combined effect of a pressure gradient and the shearing of the matrix phase in the tube flow of a suspension.
- The model was derived for circular tube flow domain and a similar procedure may be applied to other flow domains e.g. between parallel plates.
- The test setup included a tapered tube and further modelling and testing of the effect of the inclination may be carried out.
- The effect of the rheological properties of the matrix phase should be further assessed especially testing should apply higher values of the yield stress and plastic viscosity.
- Measurements of the maximum particle volume fraction in a circular tube should be carried out to assess the effect of flow rate and confinement ratio.
- Experimental studies should look into the most appropriate way of describing irregular shaped particles i.e. the characteristic diameter and the intrinsic viscosity.

Chapter 7

Simulation and Testing of Form Filling with Self-Compacting Concrete

This Chapter presents the results from the simulation and testing of the slump flow test, the L-box test, and the form filling applications.

The models applied for simulation of the homogeneous flow were presented in Chapter 3, 4 and 5, respectively. The model for assessment of a critical flow rate for assessment of blocking was presented in Chapter 6.

The aim is to investigate if

- it is possible to simulate the observed behavior in different flow domains.
- the rheological properties used to simulate one type of flow domain also applies to other flow domains.
- the rheological properties used to simulate the flow behavior in the flow domains are consistent with measured values.
- blocking can be simulated using the proposed flow rate criterion.

Initially, a parameter study of the slump flow test is carried out to illustrate the effect of the cone lifting velocity, the cone orientation, the rheological properties, the density, and the slippage behaviour. The aim is not to make complete generalizations but rather to outline what to be aware of when comparing experimental results with simulations. Therefore, some of the effects are only illustrated for one set of realistic rheological properties. The results of the slump flow test are compared to the expressions presented in Chapter 3 for estimation of the yield stress and plastic viscosity.

For the L-box, two-dimensional and three-dimensional simulations are compared to assess the assumption of channel flow in a two-dimensional simulation. The effect of the gate lifting velocity and the rheological properties are illustrated in the subsequent cases.

Then, simulations of the slump flow test and L-box are compared to the experimental results in terms of the flow propagation versus time, and for the L-box, also the risk of blocking.

Finally, the form filling experiments are compared to simulations with respect to the form filling ability, flow patterns, and risk of blocking. Observations of dynamic segregation and surface quality are discussed in relation to the simulated flow patterns.

For the L-box tests and the form filling application with reinforcement, the risk of blocking is assessed by comparing the critical velocity with the simulated average velocity between the reinforcement. When the simulated flow rate is below the critical value, blocking is estimated. The theoretical estimate of the risk of blocking is compared with the experimental observations.

7.1 Parameter Study of the Slump Flow Test and L-box Test

This Section shows a parameter study of the slump flow test and some considerations of the flow in the L-box.

As mentioned in Chapter 3, much work have been carried out on the slump test and the slump flow test, and relations have been proposed for estimation of the yield stress and the plastic viscosity.

It was assumed that inertia had no effect on the final slump flow and thereby the yield stress, however, numerical simulations are needed to study the effect of inertia on both the final slump and the transient flow behaviour. The effect of inertia depends on the Reynolds number and a simple estimate is given below based on the geometrical characteristic shown in Figure 7.1. The Reynolds number is given by Equation 4.1.1.

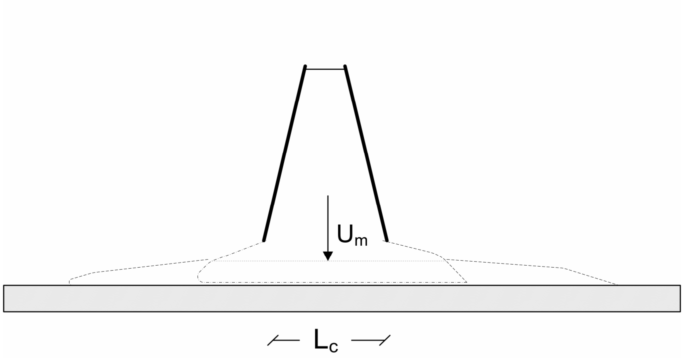

Figure 7.1 *The geometrical characteristics of the slump flow test used to estimate the Reynolds number. The characteristic length L_c = 200 mm.*

Assuming that it takes 1 s to empty the slump cone and applying a characteristic dimension $L_c = 200$ mm, this results in a velocity $U_m = 500$ mm/s. Assuming a Newtonian viscosity of $\mu = 10$ Pa·s and a density $\rho = 2300$ kg/m^3, this results in a Reynolds number of approximately 25. Two simulations of the slump flow test when using a Newtonian viscosity of $\mu = 10$ Pa·s and a density $\rho = 2300$ kg/m^3 are shown in Figure 7.2. In one of the simulations, the convective term has been excluded in the momentum equation. A numerical model with the cone placed at a fixed height of 5 cm above the base plate and the large diameter turning downwards has been applied.

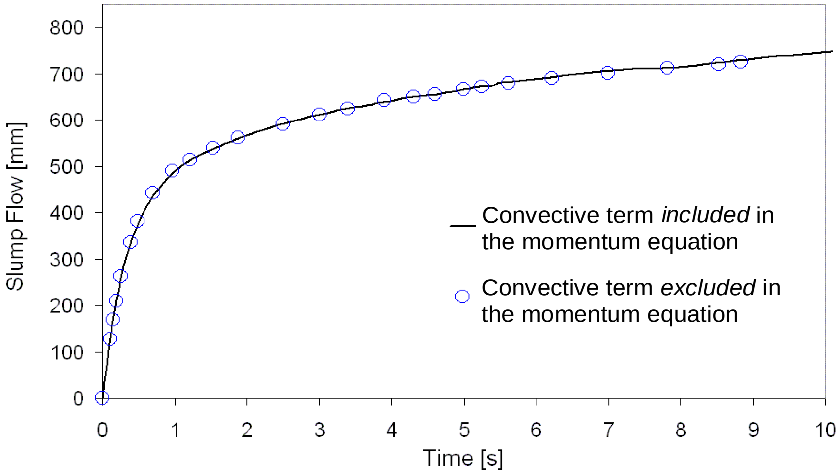

Figure 7.2 *Simulation of the slump flow test showing flow versus time for the cone placed at a fixed height of 5 cm above the base plate and the large diameter turning downwards. A Newtonian viscosity of μ = 10 Pa·s and a density of ρ = 2300 kg/m^3 have been applied.*

The results indicate that the convective term may be neglected in the momentum equation thereby avoiding non-linear algebraic equations due to inertia. Ongoing simulations of the slump flow test for Bingham fluids will include the convective term when a plastic viscosity lower than 10 Pa·s is applied.

An estimate of the Reynolds number in the L-Box is approximately 50 when using $U_m =$ 1500 mm/s (see cases), $L_c =$ 150 mm, $\rho =$ 2300 kg/m^3 and $\mu =$ 10 Pa·s. Ongoing simulations of the L-box will include the convective term as the effect of it has not been verified.

The effect of density (ρ) is shown in Figure 7.3. Simulations are carried out for densities within the range of concrete densities, i.e. $\rho =$ 2200, 2300, 2400, and 2600 kg/m^3. Simulations have been carried out at two different yield stresses of $\tau_0 =$ 45 and 15 Pa corresponding to final slump flows of approximately $SF \approx$ 550 and 700 mm. A constant plastic viscosity of $\eta_{pl} =$ 25 Pa·s has been applied. The large diameter faces the plate and a constant cone lifting velocity has been applied.

Comparing the transient spread within the typical range of concrete densities between 2200 and 2400 kg/m^3, it is found that the maximum, minimum and average difference is approximately 15, 0.1, and 10 mm, respectively. The importance of the density is relatively small compared to the effect of the rheological properties shown in Figures 7.6 and 7.7.

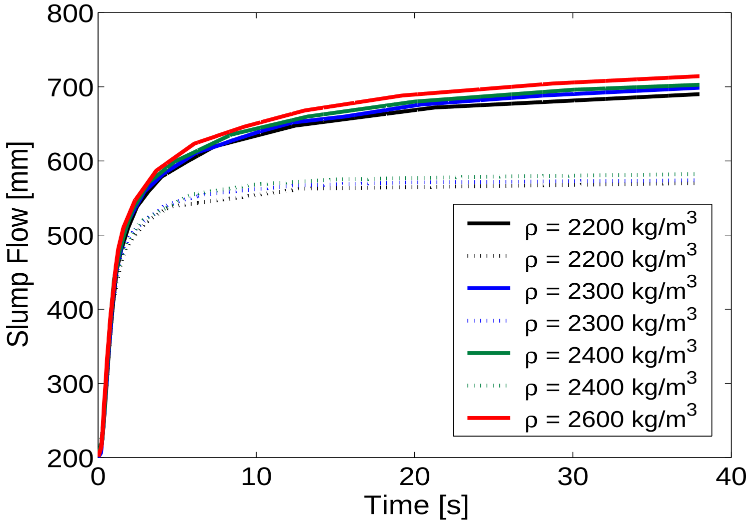

Figure 7.3 *Simulation of the slump flow test showing slump flow versus time. The solid and dotted lines show results using τ_0 = 15 Pa and τ_0 = 45 Pa at a constant plastic viscosity η_{pl} = 25 Pa·s.*

Two examples of the effect of cone orientation are shown in Figure 7.4. It shows slump flow versus time for the cone placed at a fixed height of 5 cm above the plate. Newtonian viscosities of $\mu = 10$ and 50 Pa·s have been applied.

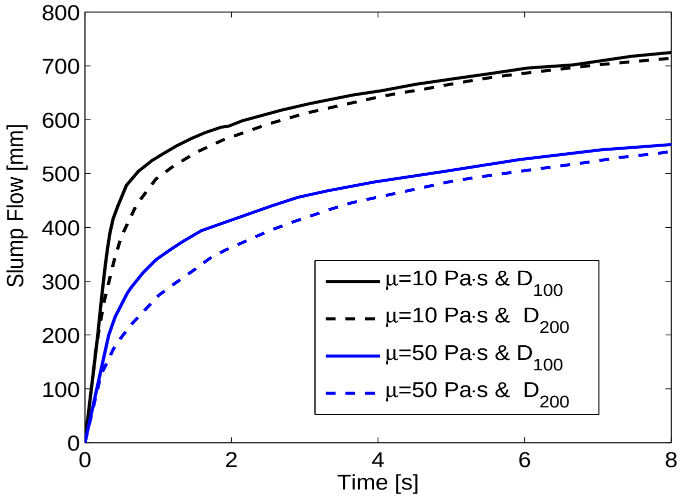

Figure 7.4 *Simulation of the slump flow test showing slump flow versus time. The solid lines show results for the large diameter turning downwards (D_{200}). The dotted lines show results for the small diameter turning downwards (D_{100}). Newtonian viscosities of μ = 10 and 50 Pa·s have been applied.*

The results show that the cone orientation does influence the flow and especially the initial flow is influenced by the cone orientation. The effect of the cone orientation increases when increasing the viscosity. Furthermore, the effect of increasing the viscosity may be enhanced depending on the lifting procedure applied when the cone is turned upside down. When the cone is turned upside down it is possible to induce potential energy into the concrete when lifting the cone.

The effect of cone lifting velocity (U_{lift}) is illustrated in Figure 7.5 where the slump flow versus time is shown for three different cone lifting velocities of U_{lift} = 10, 70, and 700 mm/s. A constant yield stress of $\tau_0 = 45$ Pa has been applied. A plastic viscosity of $\eta_{pl} =$ 35 Pa·s has been applied at $U_{lift} = 70$ and 700 mm/s, but a lower value of $\eta_{pl} = 12$ Pa·s has been applied at $U_{lift} = 10$ mm/s.

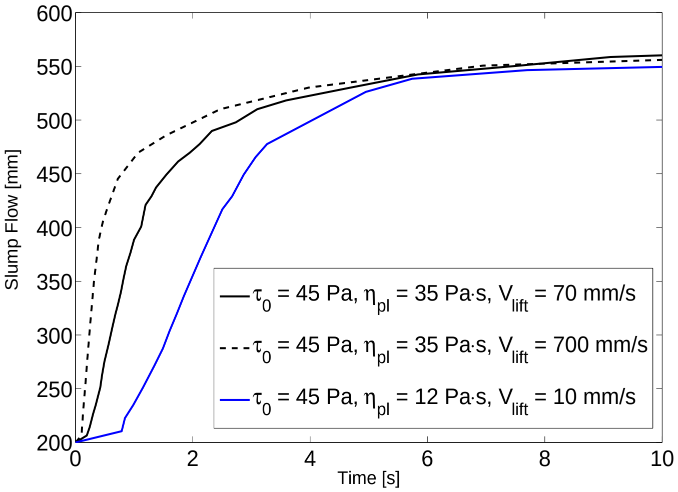

Figure 7.5 *Simulation of the slump flow test for different cone lifting velocities and Bingham rheological parameters.*

The results show that the lifting velocity influences on the deformation rate, and if not accounted for, it may lead to incorrect interpretation of the rheological properties. For instance, the blue line with the lowest plastic viscosity ($\eta_{pl} = 12$ Pa·s) would falsely be designated the highest plastic velocity compared to the black lines applying higher plastic viscosities ($\eta_{pl} = 35$ Pa·s) without taking the lifting velocity into considerations.

The effect of the rheological properties is illustrated in Figures 7.6 and 7.7. The simulations carried out in this project show that the slump flow (SF) is independent on the plastic viscosity, cone orientation and lifting velocity which corresponds to previous results. The slump flow - yield stress relation found in this project, is shown in Figure 7.6 together with the relation given by Equation 3.18 presented in Section 3.1.5.

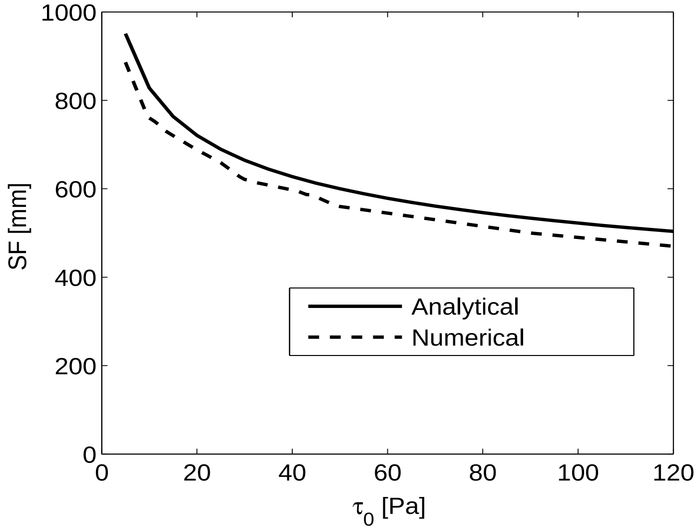

Figure 7.6 *The relation between the yield stress τ_0 and the final slump flow SF from the numerical simulations of this project and the analytical relation by Roussel & Coussot (2005) (Equation 3.18), respectively. A density of ρ = 2300 kg/m^3 has been applied.*

The results seem to correlate well, however, a vertical displacement of approximately $\Delta SF = SF^1 - SF^2 =$ -30 mm is obtained where SF^1 and SF^2 refer to the results of Roussel & Coussot (2005) and of this project, respectively.

The combined effect of the yield stress and the plastic viscosity on the transient flow behavior is shown in Figure 7.7. It shows that the time to reach 300, 400, 500, and 600 mm as a function of yield stress ($10 \leq \tau_0 \leq 90$ Pa) and plastic viscosity ($10 \leq \eta_{pl} \leq 100$ Pa·s). Simulations have been carried out at a constant cone lifting velocity of 70 mm/s and a density of $\rho = 2300$ kg/m^3. It shows that the time to reach a slump flow of 300 mm is mostly dependent on the plastic viscosity. At increasing slump flows, the yield stress becomes more significant. For instance, it shows that the yield stress has a significant influence on the time to reach 500 mm, the so-called $T50$ value. This may be one of the reasons why it has not been possible to establish good relations between the plastic viscosity and the T50 value (Nielsson & Wallevik 2003). However, also the effect of lifting and monitoring accuracy are important to consider.

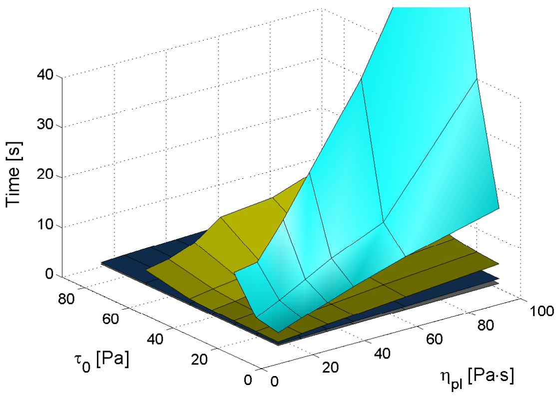

(a) SF = 300, 400, 500 and 600 mm

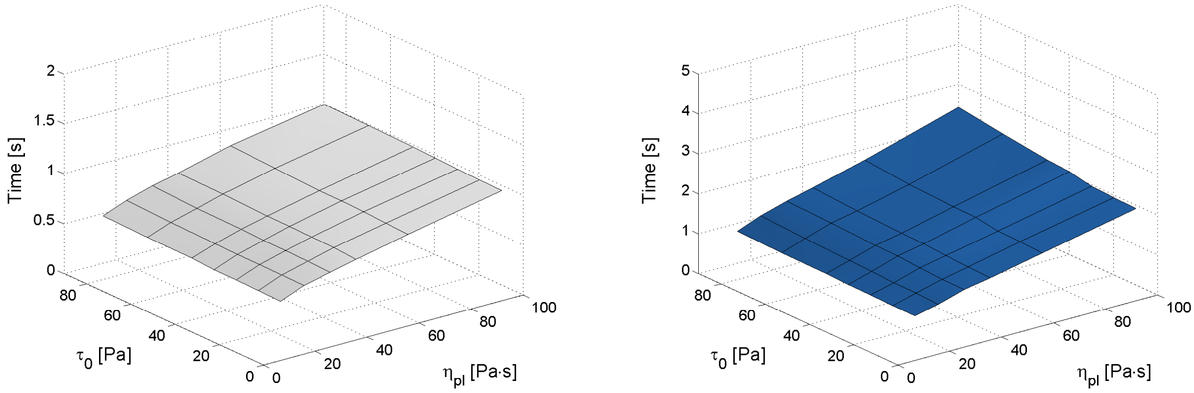

(b) SF = 300 mm

(c) SF = 400 mm

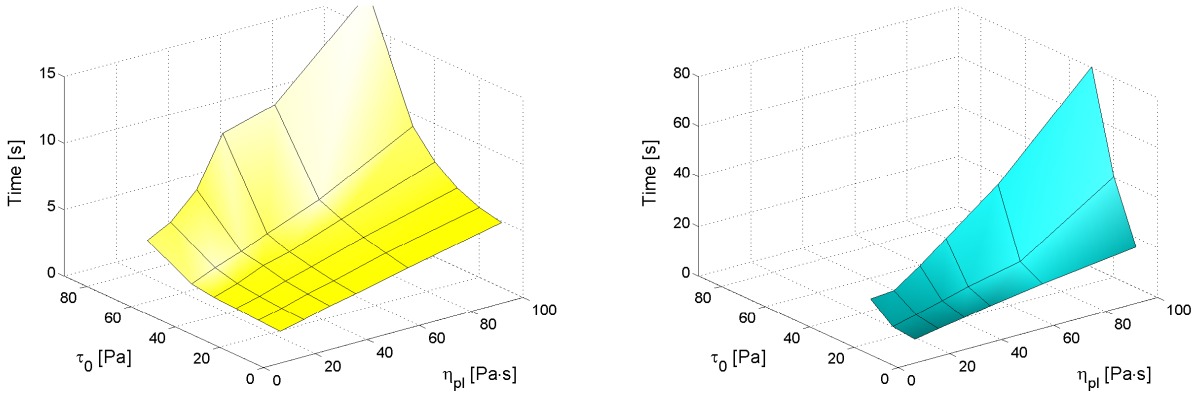

(d) SF = 500 mm

(e) SF = 600 mm

Figure 7.7 *The time to reach a slump flow (SF) of 300, 400, 500, and 600 mm as a function of yield stress ($10 \leq \tau_0 \leq 90$ Pa) and plastic viscosity ($10 \leq \eta_{pl} \leq 100$ Pa·s). A constant cone lifting velocity of $U_{lift} = 70$ mm/s and a density of $\rho = 2300$ kg/m^3 have been applied. Notice the variation between the time scales applied.*

In Section 3.1.5, relations were proposed between the value of $T50$, the plastic viscosity (η_{pl}), and the final slump flow (SF) by Kurokawa et al. (1994) (Eq. 3.20) and Sedran (2000) (Eq. 3.21).

Figure 7.8 shows Equations 3.20 and 3.21 for final slump flows of $SF = 525$ and 700 mm compared with the numerical simulations of this project. For the latter, the yield stress - slump flow relation shown in Figure 7.6 is applied for estimation of the yield stress. At $SF = 525$ and 700 mm, the yield stress $\tau_0 \sim 70$ and 17 Pa, respectively.

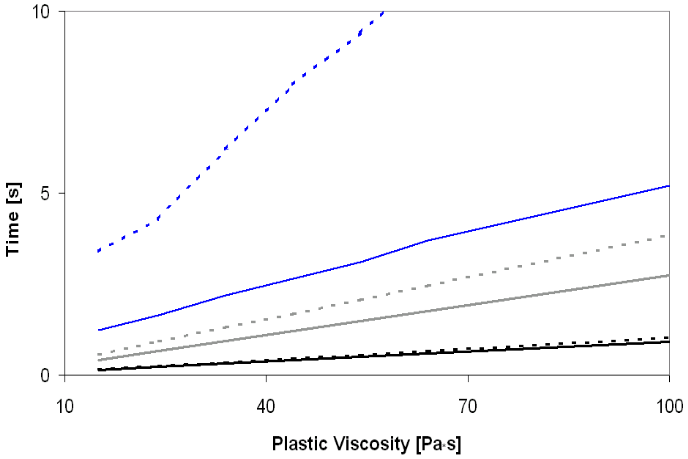

Figure 7.8 *The time to reach a slump flow of 500 mm (T50) as a function of the plastic viscosity and final spread given by Equation 3.20 (black), Equation 3.21 (grey), and the numerical simulations of this project (blue). The dotted and solid lines correspond to a final slump flow SF of 525 and 700 mm, respectively. A density of 2300 kg/m^3 is applied.*

Equation 3.20 shows very little dependency on the final slump flow and it underestimated the experimental results found in Sedran (2000), who proposed Equation 3.21 based on experimental results. 3.21 shows more dependency on the final slump flow (SF), but compared to the numerical simulations of this project, it underestimates the ($T50$) value, especially at $SF = 525$ mm ($\tau_0 \sim 70$ Pa).

Concerning estimation of the rheological parameters, the results show that each curve of the slump flow versus time only assigns one set of Bingham parameters. Under controlled boundary conditions and accurate monitoring of the transient flow, this may be used to estimate both the yield stress and plastic viscosity without having to use the final slump flow for estimation of the yield stress. This may be an advantage at high slump flows where the particle size and particle volume fraction may affect the slump flow behaviour as discussed in Section 3.1.5.

An example of a simulation using the slip model given by Equation 5.20 is shown in Figure 7.9. Equation 5.20 described the relation between the slip coefficient β and the height of the slippage layer h_1, the matrix viscosity μ_m, and the suspension viscosity μ_s. For a yield stress of $\tau_0 = 45$ Pa and a plastic viscosity $\eta_{pl} = 25$ Pa·s, results are shown for a slip coefficient $\beta = 3 \cdot 10^{-4}$. This could correspond to, e.g. $\mu_m = 1$ Pa·s, $\mu_s = 20$ Pa·s, and h_1= 0.3 mm.

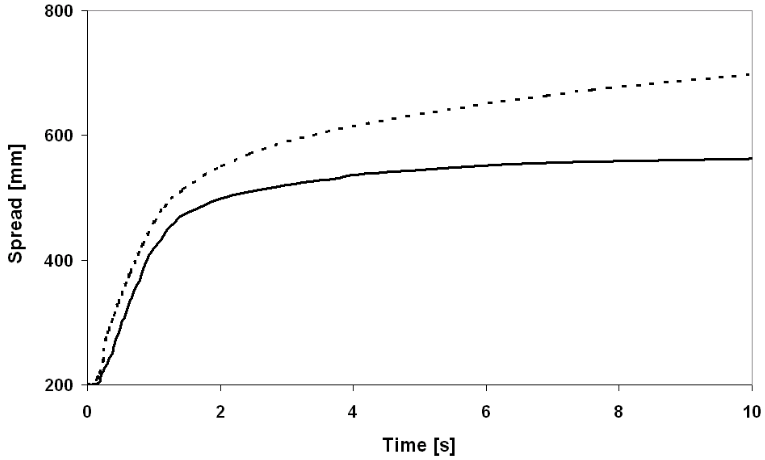

Figure 7.9 *The slump flow versus time for $\tau_0 = 45$ Pa and $\eta_{pl} = 25$ Pa·s without slip coefficient (solid line) and with a slip coefficient $\beta = 3 \cdot 10^{-4}$ (dotted line) applied to the base plate.*

The results show that it is possible to simulate a slip behavior resulting in an increased slump flow. Further investigations may look into the height of a possible slippage layer, the rheological properties of the lubrication matrix layer, and whether the slip coefficient is constant. In the ongoing simulations, a no-slip condition will be applied.

For the L-box test, it is initially investigated whether it is reasonable to assume two-dimensional flow (channel flow) in the L-box to limit the requirements to computational capacity.

Figure 7.10 shows two-dimensional and three-dimensional simulations of the L-box without reinforcement for a particular choice of viscosity, in this case a Newtonian viscosity of $\mu = 20$ Pa·s. An instant lifting of the gate is assumed corresponding to $U_{lift} = \infty$. The results indicate that the viscous contribution due to the shear introduced by the boundaries (xy-plane at z = 0 and z =-200 mm) influences on the flow into the horizontal section of the L-box. For instance, the time to reach the end wall (x = 700 mm) is 0.70 s and 1.20 s for "2d/-bars" and "3d-sym/-bars", respectively.

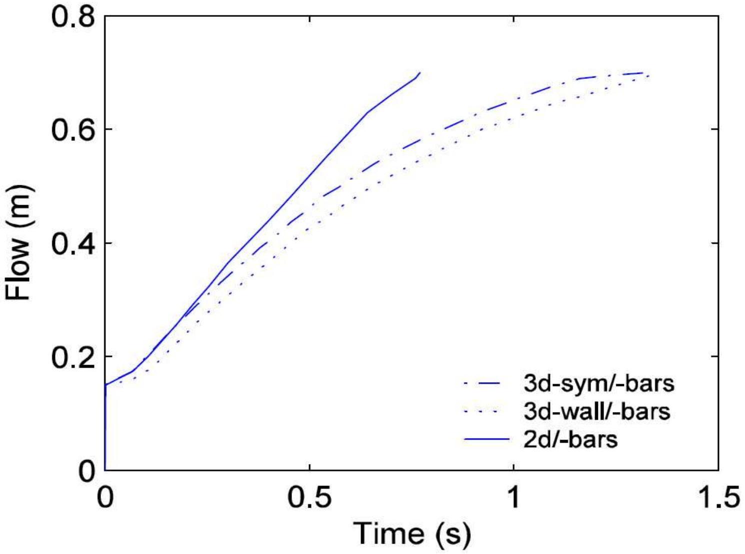

Figure 7.10 *Two and three-dimensional flow of a Newtonian fluid into the horizontal section of the L-box without reinforcement. The viscosity μ = 20 Pa·s. Sym = plane of symmetry. Wall = flow at the boundary (z = 0 and z = -200 mm). /-bars = no reinforcement.*

Therefore, it does not seem reasonable to assume channel flow in the L-box, though, it is expected that this effect will decrease for lower viscosities. However, bars would also have to be placed horizontally in a two-dimensional setup. As flow stops, the free surface has levelled due to the properties of a Newtonian fluid.

7.2 Test Setup

7.2.1 Slump Flow Test

The results presented in the previous section showed the effect of various parameters on the slump flow behaviour. The results showed that it is important to control the boundary conditions, such as lifting velocity and ensure a accurate monitoring of the transient flow behavior for comparison of the experimental results with simulations.

In the ongoing, results from the slump flow test are reported for two different setups.

The first setup referred to as "setup 1" has a steel cone placed on a plywood base plate. The cone is attached to a hydraulic lifting device placed in a steel frame work. The transient flow behavior (flow versus time) has been measured from video shootings with a frame rate of 30 s^{-1}. The spread in three directions from the center axis has been used to calculate an average slump flow (0, π, and $\frac{3}{2}\pi$). The surface of the plate has been dried before each test to simulate the no-slip condition. The lifting velocity used as input in the simulation has been detected from the video shootings.

Later, a second setup was developed referred to as "setup 2" which has an upright steel cone placed on a sand blast glass plate. Electric controlled lifting device with a constant lifting velocity of 7 cm/s and an automatic camera shootings combined with image analysis are used to measure the slump flow versus time (Thrane 2004).

7.2.2 L-Box

Experimental results are presented for two different setups of the reinforcement in the L-box. The cross-sections through the center of the reinforcement bars are shown in Figure 7.11. In the situation shown to the left, three sections are identified and these are referred to as A_1, A_2, and A_3 (setup A_{lbox}). In the situation to the right, two sections are identified and these are referred to as B_1 and B_2 (setup B_{lbox}).

Simulations of the L-box have been carried for the setup A_{lbox} (see Section 5.3.2). However, the critical flow rate is estimated for both the test setups. As the flow rate is not simulated for the setup to the right, a reasonable estimate is given based on the simulations for the other setup.

The gate was lifted manually and the lifting velocity was detected from video shootings by analyzing the position of markers on the gate. Markers were placed at an interval of 20 mm.

The flow into the horizontal section versus time has been measured from video shootings. Markers were placed at an interval of 50 mm.

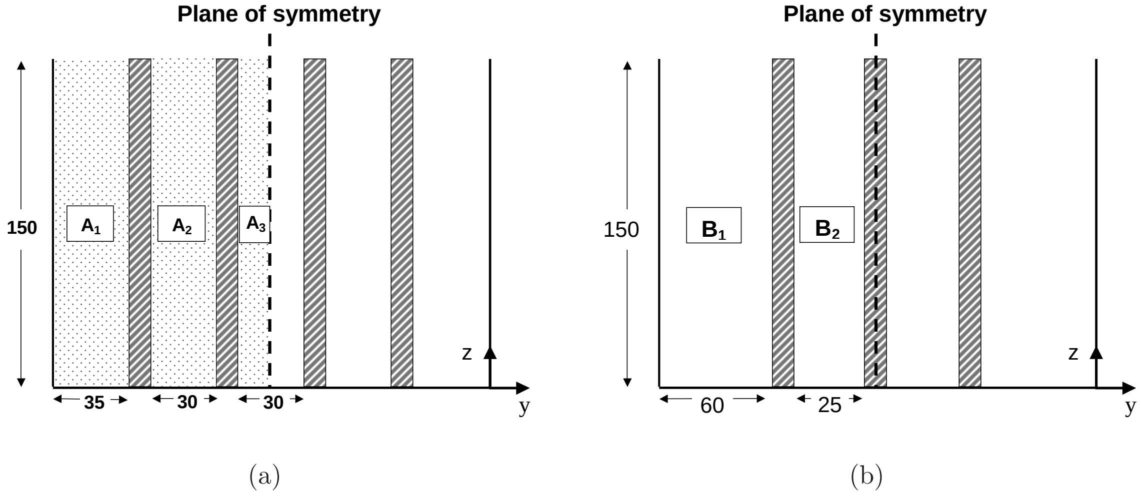

(a) (b)

Figure 7.11 *Cross section through the center axis of the reinforcement bars in the two L-box setups applied (setup A_{lbox} and B_{lbox})(units in mm). Areas A_1, A_2 and A_3 represents the computational domain of the model presented in Section 5.3.2.*

7.2.3 Form Filling Applications

The form filling applications comprise laboratory and full-scale tests, respectively.

On a laboratory scale, the two form filling experiments presented are referred to as $FF1$ and $FF2$ (see Section 5.3.3). Experiment $FF1$ was carried out in the laboratory at the Danish Technological Institute, and experiment $FF2$ was carried out at a 4k-Beton A/S ready mix plant.

The form work is shown in Figure 7.12. It has a length of 3.00 m, a width of 0.30 m and a height of 1.20 m. An inlet is placed at the bottom lower corner and one side of the form consists of a transparent acrylic plate to allow visual observations of the flow during casting.

In $FF2$, different monitoring equipment were applied. It consisted of 80 thermal detectors evenly distributed to monitor the free surface movement (see Appendix D) and load cells placed at the bottom and top of the central frame to measure the form pressure. Electromagnetic tags were placed in the concrete for particle tracing (tag density is approximately the same as the aggregate).

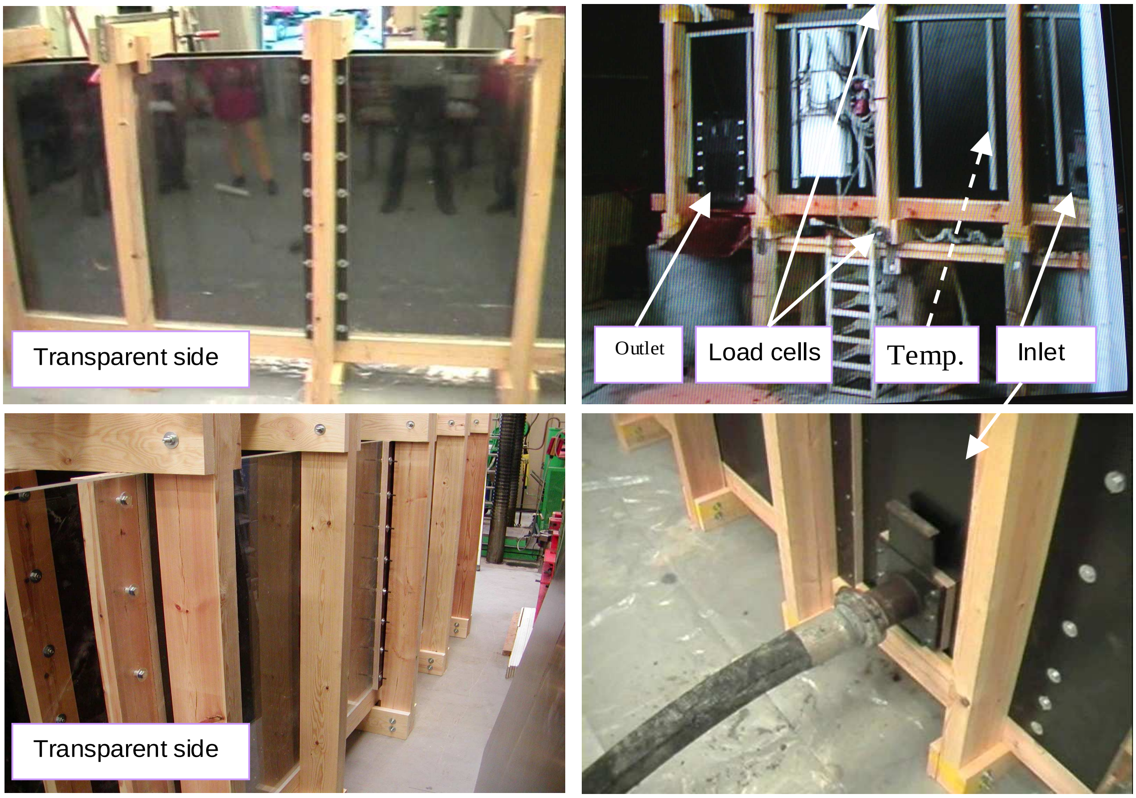

Figure 7.12 *The vertical laboratory form work applied for form filling test $FF1$ and $FF2$, respectively.*

In test $FF2$, reinforcement has been included and the configuration was presented in Section 5.3.3. Before casting, the concrete was tested in the L-box applying the reinforcement setup shown in Figure 7.11 to the right. The minimum gap between the reinforcement bars is 25 mm in both the L-box test and the form filling test.

To improve the visual observations of the flow patterns, the first and second half of each form have been casted with normal grey and red-pigmented SCC, respectively. The batch of red and grey concrete was produced, and from two rotary trucks the grey and red concrete were poured into the pump. Casting was performed by pumping from the bottom corner at a filling rate of approximately 10 m^3/h.

On a full-scale, five form filling tests have been carried out and the dimensions and casting technique applied were presented in Section 5.3.4.

7.2.4 Viscometric Measurements

In some of the experiments, the rheological properties were measured in a concentric viscometer (BML viscometer) and the Bingham parameters obtained were applied as initial input in the simulations. The measuring procedure is shown in Table 7.1 and corresponds to the one found in Geiker, Brandl, Thrane, Bager & Wallevik (2002). The measuring procedure applied includes 8 different rotation velocities with a maximum and minimum value of 0.57 s^{-1} and 0.05 s^{-1}, respectively. To obtain steady state flow and limit segregation, testing have been undertaken for 15 s at each rotational velocity.

Table 7.1 *The geometrical setup and testing procedure in the BML viscometer.*

Parameter	Value
Inner cylinder radius	0.100 m
Outer cylinder radius	0.145 m
Maximum Rotation Velocity	0.57 s^{-1}
Minimum Rotation Velocity	0.05 s^{-1}
Number of Velocities	8
Transient Interval	0 s
Sampling Interval	15 s

The Bingham parameters are calculated by linear regression of the flow curve at steady state based on the Reiner-Riwlin equation (Bird et al. 1987).

7.3 Mix Compositions

The mix compositions applied in the slump flow test, L-box test, and laboratory form filling applications are given in Appendix A.

For the concrete mixes C_1 to C_6 and the mortar mix M_1, the rheological properties have been measured in the BML viscometer.

The concrete mixes C_1 to C_6 have been tested in the slump flow test using setup 1.

The mortar M_1 has been tested in the slump flow test, however, with the cone turned upside down to avoid the mortar from lifting the cone before testing, as it has a low plastic viscosity (see Section 7.4.1), and in the L-box test using setup A_{lbox}.

Concrete mixes E_1, E_2, E_3, and E_4 have been tested in the slump flow test using setup 1 for E_1 and setup 2 for E_2, E_3, and E_4. The same mixes have been tested in the L-box using setup A_{lbox}.

Concrete mixes F_1 and F_2 were applied in the laboratory form filling experiments $FF1$ and $FF2$ presented in section 7.2.3. The rheological properties of mix composition F_2 were measured with the BML viscometer. The rheological parameters of the mix composition F_1 were estimated based on the slump flow test. At this point of time, the slump flow setups presented in Section 7.2.1 were not ready, and estimates of the rheological parameters have been made based on the final slump flow SF and the $T50$ value measured during testing. The L-box test for mix composition F_2 was carried out using setup B_{lbox}.

Concrete mixes for the full-scale tests comprised two commercial SCC mixes classified for moderate and aggressive environments, respectively. These are referred to as FuM and FuA. The rheological properties have been estimated based on the slump flow test results using setup 1.

For estimation of the critical flow rate for assessment of the risk of blocking, the particle volume fraction (ϕ_p) and the maximum particle volume fraction (ϕ_p^*) of particles larger than 4 mm are given in Appendix A. The maximum particle volume fraction (ϕ_p^*) of the combination of the fractions 4-8 mm and 8-16 mm is estimated using the 4C Packing software.

7.4 Results of Testing and Simulation

7.4.1 Rheological Properties

Figure 7.13 shows the rheological measurements of concrete mixes C_1 to C_6 and the mortar M_1. It shows torque over height at the inner cylinder versus time and the interpreted torque values versus rotational velocity.

Figure 7.14 shows the results for the grey and red batch of concrete mix F_2, respectively.

Leaving out the points where equilibrium is not reached and where plug flow occurs, the results indicate a linear behavior according to a Bingham model. The Bingham parameters are shown in Table 7.2.

Table 7.2 *Yield stress $\tau_{s,0}$ and plastic viscosity η_{pl} of concretes C_1 to C_6, mortar M_1, and grey/red concrete F_2 obtained from measurements in the BML viscometer.*

Name	$\tau_{s,0}$ [Pa]	$\eta_{s,pl}$ [Pa·s]
C_1	131	30
C_2	45	32
C_3	77	27
C_4	85	15
C_5	105	18
C_6	28	15
M_1	39	5
F_2 (grey)	44	21
F_2 (red)	57	29

The yield stresses range from 28 to 131 Pa and the plastic viscosity range from 5 to 32 Pa·s.

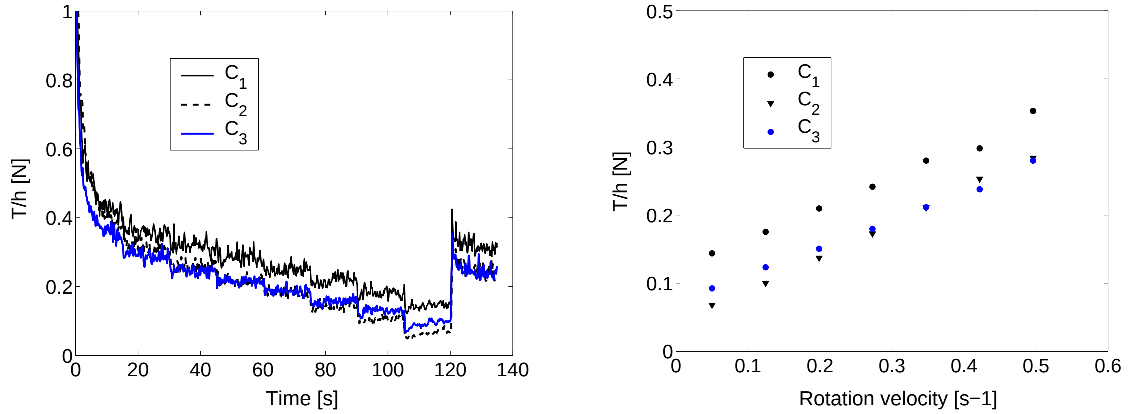

(a) C_1 to C_3 (b) C_1 to C_3

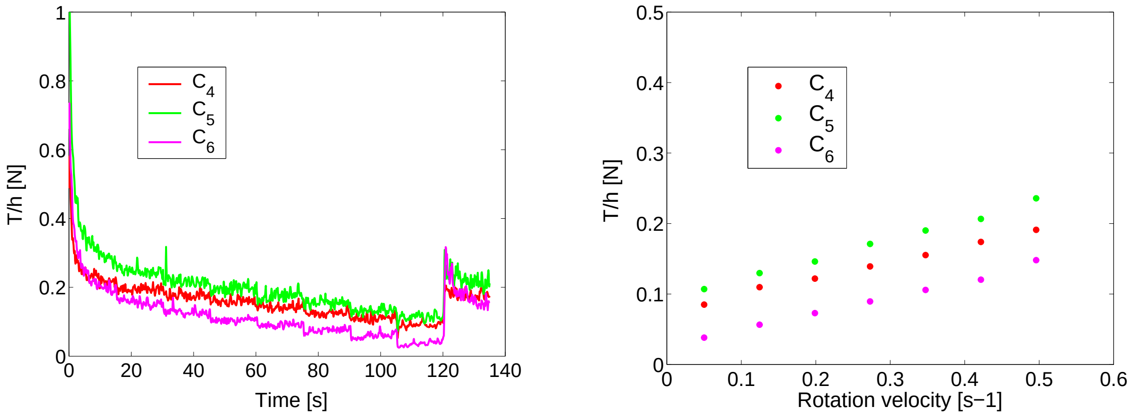

(c) C_4 to C_6 (d) C_4 to C_6

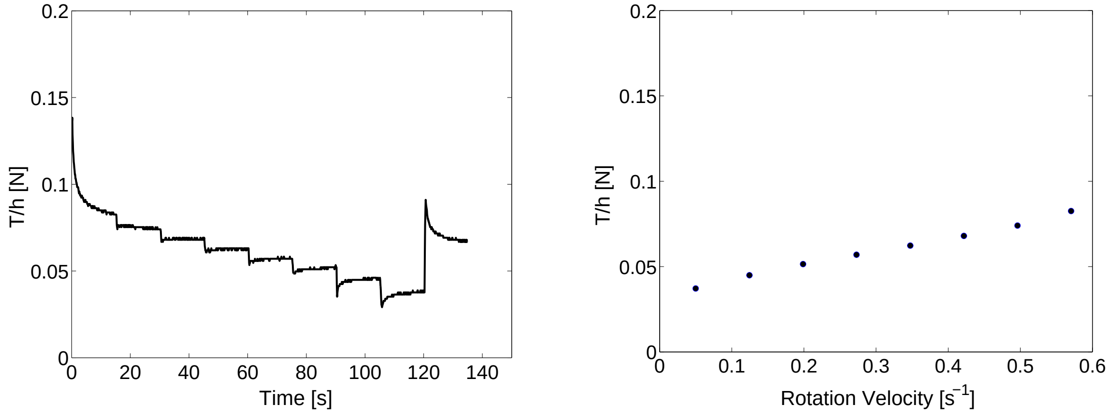

(e) M_1 (note axis) (f) M_1 (note axis)

Figure 7.13 *Results from measurements of the rheological properties of concretes* C_1 *to* C_6 *and the mortar* M_1*. It shows torque over height at the inner cylinder versus time (left column) and the interpreted torque versus rotational velocity (right column). Note variations in axes between tests on concrete and on the mortar.*

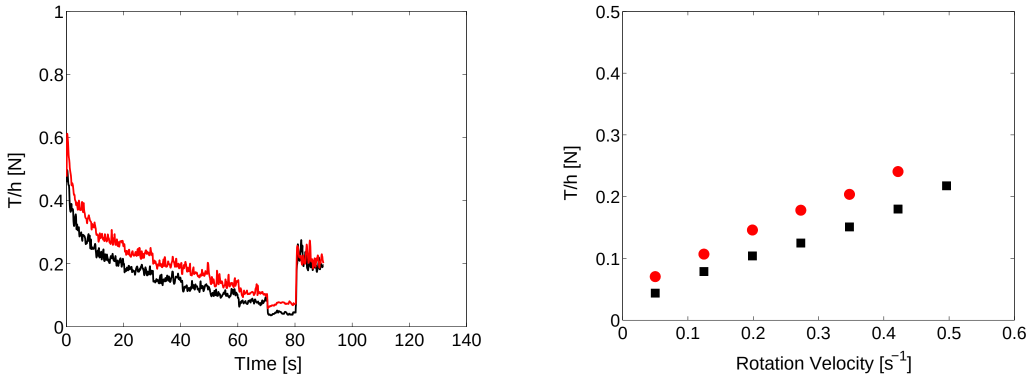

(a) F_2 (grey and red concrete) (b) F_2 (grey and red concrete)

Figure 7.14 *Results from measurements of the rheological properties of the grey and red batch of concrete mix F_2, respectively. It shows torque over height at the inner cylinder versus time and the interpreted torque values versus rotational velocity.*

7.4.2 Slump Flow Test and L-Box Test

Mix C_1 to C_6

Figure 7.15 shows the test results and simulations of the slump flow test for concrete mixes C_1 to C_6. The transient slump flow as a function of time is compared. Initially the measured values of the yield stress, plastic viscosity, and lifting velocity have been applied. Simulations carried out with other values of the yield stress, plastic viscosity, and lifting velocity are discussed in each case.

For mix C_1 and C_2, simulations are shown for the measured values of the yield stress, plastic viscosity, and lifting velocity. It seems a good correlation is obtained. To illustrate the effect of lifting, a simulation with a lifting velocity of $U_{lift} = 5.6$ cm/s has been carried out for mix C_1. It is four times higher than the actual lifting velocity of 1.4 cm/s and results in a significant overestimation of the initial slump flow and would lead to false interpretation of the plastic viscosity if not accounted for.

For mix C_3 and C_4, the simulations are shown for the measured values of the plastic viscosity ($\eta_{pl} = \eta_{s,pl}$ =27 Pa·s) and the lifting velocity ($U_{lift} = 1.8$ cm/s and 1.4 cm/s). However, to fit the final slump behavior for mix C_3, a yield stress of $\tau_0 = 90$ Pa has to be applied instead of $\tau_{s,0}$ =77 Pa. According to the relation between the yield stress and final slump flow shown in Figure 7.6, this corresponds to a relatively low final slump flow difference of approximately 15 mm (SF at $\tau_0 = 77$ Pa minus SF at $\tau_0 = 90$ Pa). For mix C_4, a yield stress of τ_0 =48 Pa has to be applied instead of $\tau_{s,0}$ =85 Pa which corresponds to a final spread difference of approximately -50 mm (SF at $\tau_0 = 85$ Pa minus SF at $\tau_0 =$

48 Pa). It is difficult to assess the validity of the homogeneous fluid assumption because the particle compositions applied in mix C_1, C_2, C_3, and C_4 are the same and mix C_1, C_2 and C_3 showed a reasonable correlation between the measured yield stress and the one applied to simulate the slump flow.

In mix C_5 simulations are shown for the measured values of the yield stress ($\tau_0 = \tau_{s,0} =$ 105 Pa), plastic viscosity ($\eta_{pl} = \eta_{s,pl} =$ 18 Pa·s), and lifting velocity ($U_{lift} =$ 1.5 cm/s). Good correlation is obtained for the initial spread, but the final spread is overestimated by approximately 50 mm. The yield stress determined in the viscometer ($\tau_{s,0} =$ 105 Pa) is lower than the yield stress determined for mix C_1 ($\tau_{s,0} =$ 131 Pa) though the final slump flow is higher. This may be an effect of accuracy in the viscometric measurement associated with the linear regression. Again, the effect of the particle phase is difficult to assess as the coarse aggregate fraction of C_1 to C_5 is almost the same.

In mix C_6, simulations are shown for the measured value of the plastic viscosity ($\eta_{pl} = \eta_{s,pl} =$ 15 Pa·s), and a lifting velocity ($U_{lift} =$ 1.0 cm/s). However, assuming a homogeneous approach, a yield stress of $\tau_0 =$ 18 Pa has to be applied instead of $\tau_{s,0} =$ 28 Pa, which corresponds to a final slump flow difference of approximately -50 mm (SF at $\tau_0 =$ 28 Pa minus SF at $\tau_0 =$ 18 Pa). To assess the effect of plastic viscosity, another simulation applying a plastic viscosity of 90 Pa·s corresponding to six times the actual plastic viscosity has been carried out at two times the lifting velocity, i.e. 2.0 cm/s. It shows that the transient slump flow is significantly underestimated.

In general, it seems that there is a good correlation between the plastic viscosity determined in the viscometer and the one applied to simulate the initial slump flow behavior when the correct lifting velocity is applied. Assuming a homogeneous suspension approach, results have shown a reasonable good correlation between the final slump flow and the yield stress for mixes C_1, C_2, and C_3. In mixes C_4, C_5, and C_6, some fitting of the yield stress were needed to obtain the final slump flow behavior. Applying the yield stress measured in the viscometer resulted in a difference between the final slump of the experiment and the simulation of approximately 50 mm. In mixes C_4 and C_6, the simulation underestimated the final slump flow and in C_5, it was overestimated. It has not been possible from these tests to assess the effect of the particle size distribution and particle volume fraction on the final slump flow as these were almost the same. Also, taking into account the accuracy of the viscometric measurements, it is difficult to conclude to which extent the yield stress - slump flow relation of a homogeneous flow approach applies, and more testing are needed in order to investigate limits to the final slump flow as a function of the particle size distribution and volume fraction, respectively. As mentioned in Section 7.1, each slump flow curve will only assign one set of parameters given controlled testing conditions. This could be one way to estimate both the yield stress and plastic viscosity without having to apply a slump flow - yield stress relation at high slump flows.

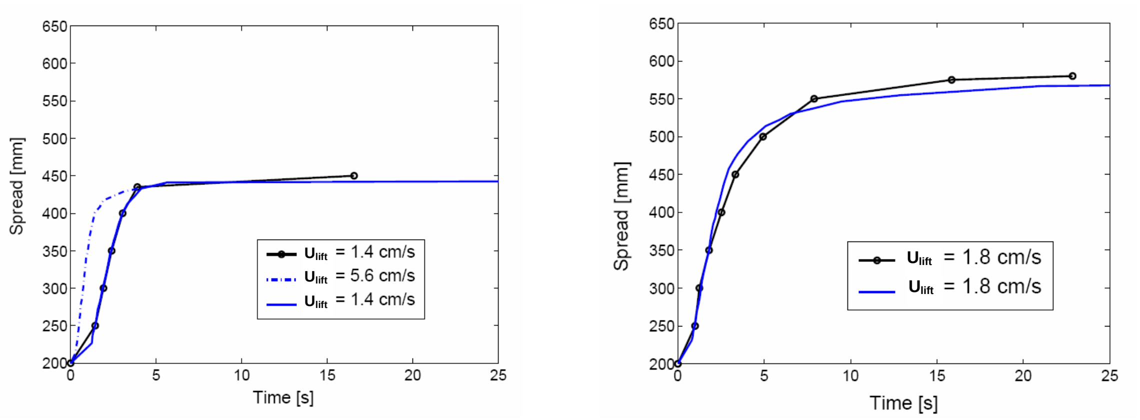

(a) C_1: $\tau_0 = \tau_{s,0}$ =131 Pa, $\eta_{pl} = \eta_{s,pl}$ =30 Pa·s

(b) C_2: $\tau_0 = \tau_{s,0}$ =45 Pa, $\eta_{pl} = \eta_{s,pl}$ =32 Pa·s

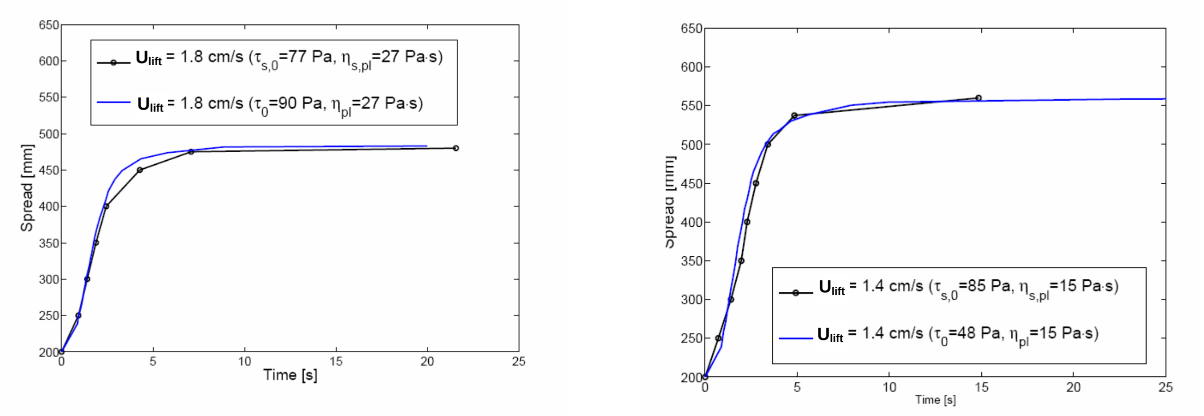

(c) C_3

(d) C_4

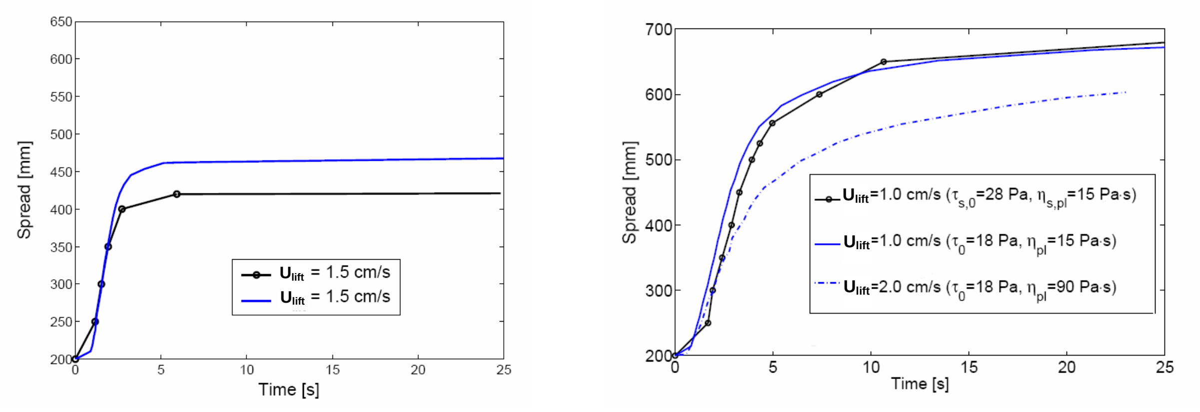

(e) C_5: $\tau_0 = \tau_{s,0}$ =105 Pa, $\eta_{pl} = \eta_{s,pl}$ =18 Pa·s

(f) C_6

Figure 7.15 *Results from testing (black) and simulation (blue) of the slump flow test for concrete mixes C_1 to C_6.*

Mix M_1

The results of simulating and testing the mortar (M_1) in the slump flow test and L-box are presented. The slump cone was turned upside down ($D100$). Reinforcement was included in the L-box test using setup A_{lbox}. To assess the effect of reinforcement and the assumption of channel flow, simulations have also been carried out without reinforcement in both two and three dimensions.

The rheological properties of the mortar, $\eta_{s,pl} = 5$ Pa·s and yield stress $\tau_{s,0} = 39$ Pa, were used as initial values in the simulations.

The lifting velocity of the slump cone was determined to U_{lift}= 7 cm/s.

The lifting velocity in the L-box was found to be nonlinear due to lifting resistance caused by friction and a slight twisting of the gate when it was lifted. The experimental lifting velocity is shown in Figure 7.16. To assess the effect of lifting, three different lifting models have been applied. Models 1 and 2 are also shown in Figure 7.16, and model 3 corresponds to an instant removal of the gate of ($U_{lift} = \infty$).

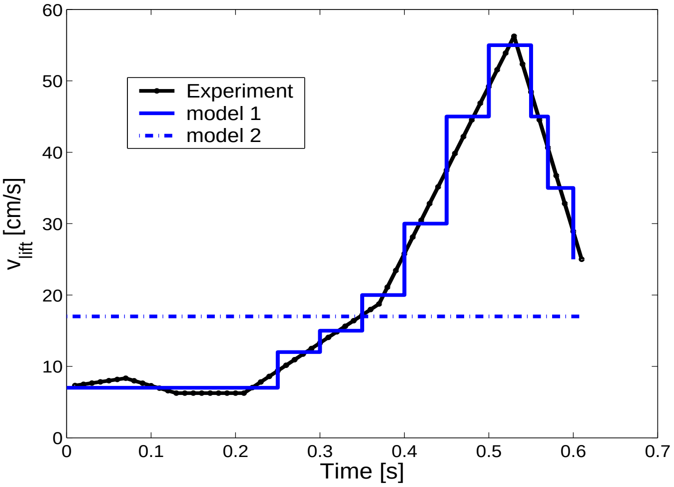

Figure 7.16 *Gate lifting velocity as a function of time for mortar M_1. It shows the experimental lifting velocity and the three different models applied to assess the effect of lifting velocity (model 3: $U_{lift} = \infty$).*

Initially, the effect of reinforcement and the assumption of channel flow in the L-box is assessed. Figure 7.17 shows the flow into the horisontal section as a function of time in the experiment and simulations when using lifting model 3 corresponding to an instantaneous removal of the gate. The results of the experiment and the three-dimensional simulations are shown for both the plane of symmetry and at the wall. However, there is only a little difference so the subsequent results from the L-box are only reported for the plane of symmetry.

For the effect of reinforcement, the simulations show that the reinforcement bars retain the flow into the horizontal section, e.g. compare "3d-sym/+bars" to the left with "3d-sym/-bars" to the right. However, this may be even more evident at higher plastic viscosities.

For the channel flow assumption, it is seen that though a yield stress is included, the flow in the plane of symmetry (no reinforcement) is more similar to that of the two-dimensional model due to a low plastic viscosity compared to Figure 7.10 where a Newtonian viscosity $\mu = 20$ Pa·s was applied.

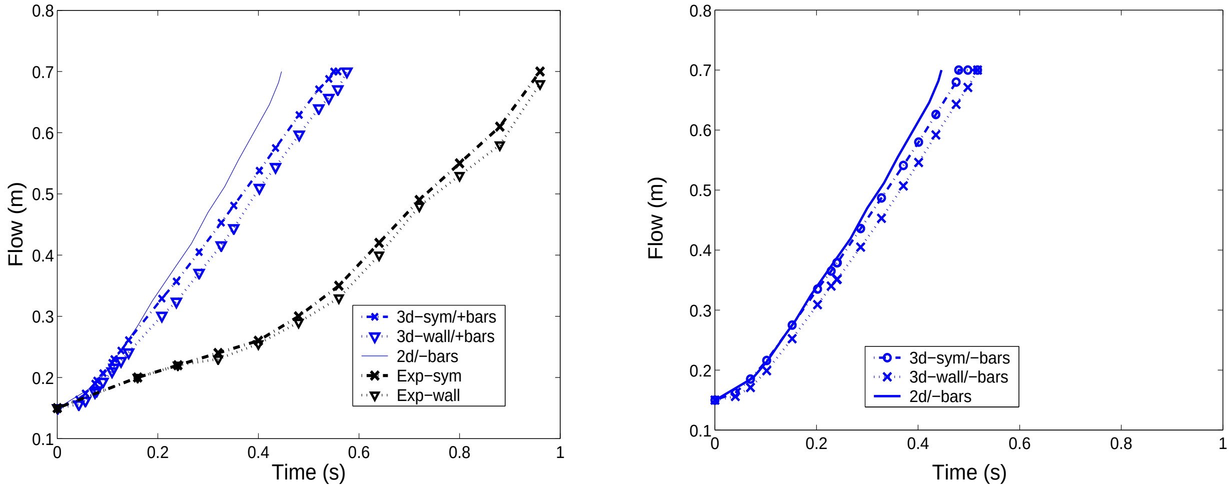

(a) (b)

Figure 7.17 *Flow into the horisontal section of the L-box as a function of time for simulations and testing of mortar M_1. The yield stress $\tau_0 = \tau_{s,0} = 39$ Pa, $\eta_{pl} = \eta_{s,pl} = 5$ Pa·s. Sym = plane of symmetry ($z = 0$) Wall = flow at the boundary ($z = -200$ mm). /-bars = no reinforcement. /+bars = reinforcement. Exp = experiment. Lifting model 3 has been applied in the simulations ($U_{lift} = \infty$)*

The experimental result compared with the three-dimensional simulation shows a poor correlation. The effect of lifting and the rheological properties are discussed below.

Figure 7.18 shows the results from testing and simulation of the slump flow test and L-box when using the three different lifting models in the L-box.

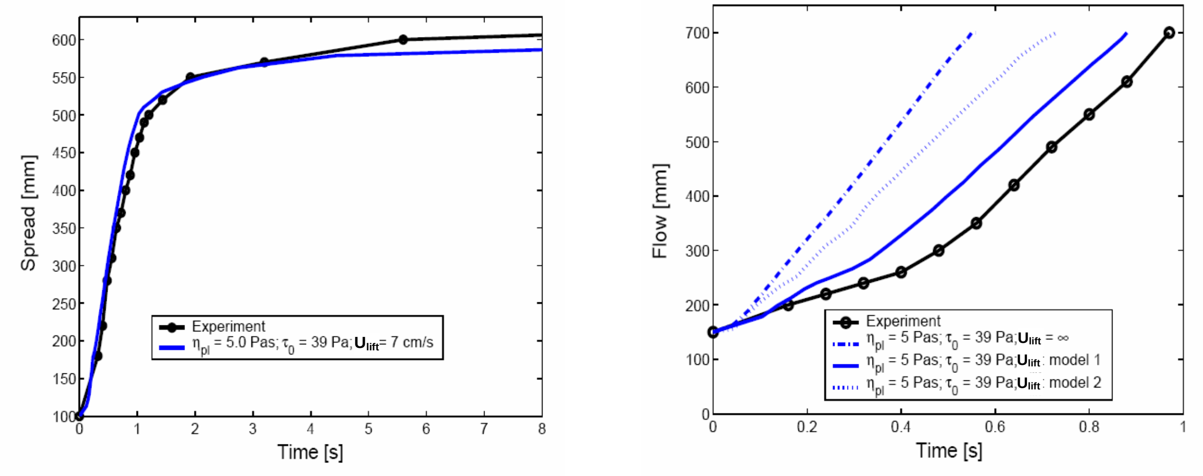

(a) Slump flow test

(b) L-box test

Figure 7.18 *Simulations and testing of the slump flow test and L-box test for mortar M_1 The slump cone is turned upside down ($D100$). Measured values of yield stress and plastic viscosity have been applied. Three different lifting models have been applied in the simulations of the L-box test.*

The slump flow is overestimated with up to approximately 2 s, which indicates that the plastic viscosity applied in the simulations is too low. The final slump flow is underestimated by approximately 40 mm compared to the experimental result of $SF = 630$ mm, which indicates a too high yield stress. Based on the relation given in Figure 7.6, a value of $\tau_0 = 28$ Pa is proposed.

Simulations of the L-box show the importance of including the lifting velocity. However, though lifting model 1 is applied, the simulation still overestimates the flow. Furthermore, the L-box simulation shows a slight overflow at the end of the L-box ($x = 700$ mm), which is inconsistent with the experiment. In the experiment a maximum height of approximately 11 cm is reached at the end of the L-box, which is only 2 cm above the final horizontal level. The simulation of the overflow is shown in Figure 7.19 to the left and indicates that the plastic viscosity applied in the simulations is too low.

Simulations have been repeated with $\eta_{pl} = 7.5$ Pa·s and $\tau_0 = 28$ and 39 Pa. The spread versus time for the slump flow test and L-box with the revised Bingham parameters are shown in Figure 7.20.

Using these fitted rheological parameter, it seems that the experimental data for both the L-box and the slump flow test can be simulated satisfactorily. It is observed that the flow response at the end of the L-box is consistent with that of the experiment (see Figure 7.19 to the right), and the effect of yield stress is limited compared to the plastic viscosity. Though a yield stress is included, the H_2/H_1 reach a value of 1, which show the importance of inertia when the plastic viscosity is low and the lifting velocity is high.

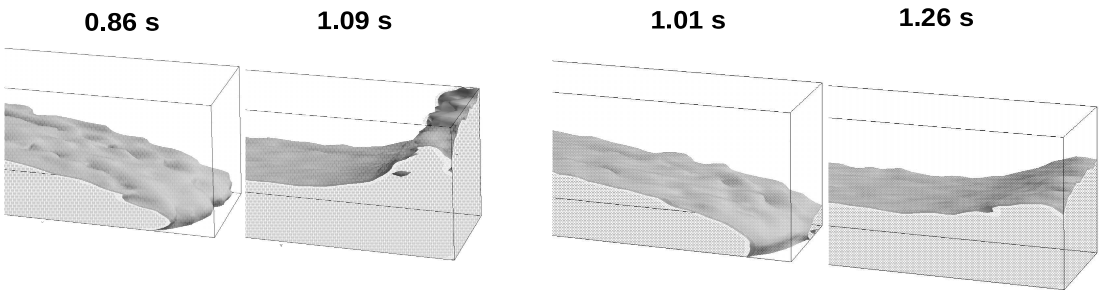

Figure 7.19 *Simulated response for mortar* M_1 *at x = 700 mm in the L-box test for 1)* η_{pl}= *5 Pa·s;* τ_0 = = *39 Pa (left) and 2)* η_{pl} = *7.5 Pa·s;* τ_0 = *28 Pa (right).*

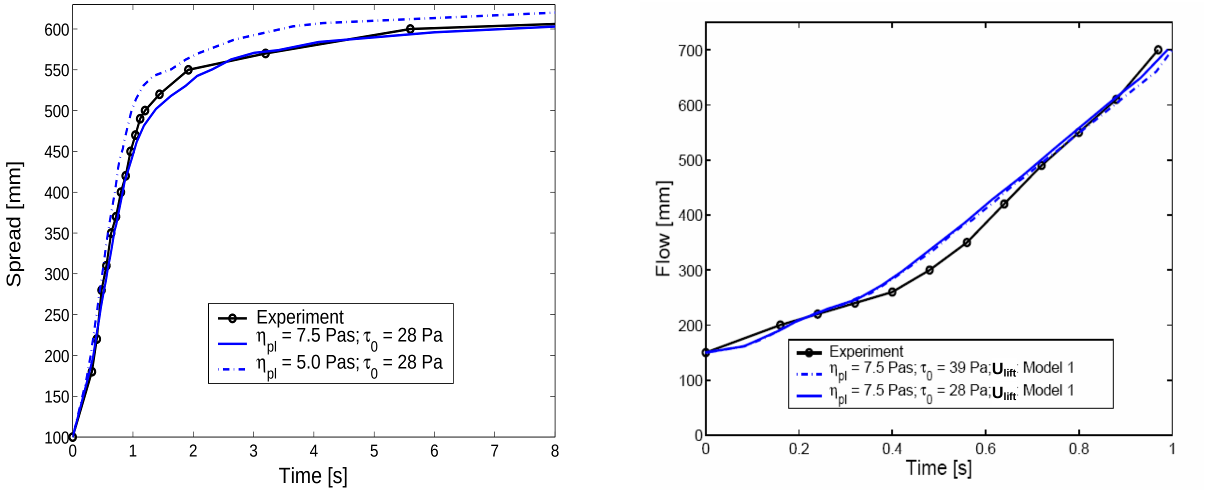

(a) Slump flow test

(b) L-box test

Figure 7.20 *Simulations and testing of the slump flow test and L-box test for mortar* M_1 *when using revised Bingham parameters compared to those applied in Figure 7.18.*

Figure 7.21 shows the free surface of the simulation and in the experiment at different flow propagations. The results show that a good correlation is obtained between the simulated and observed behavior in the experiment.

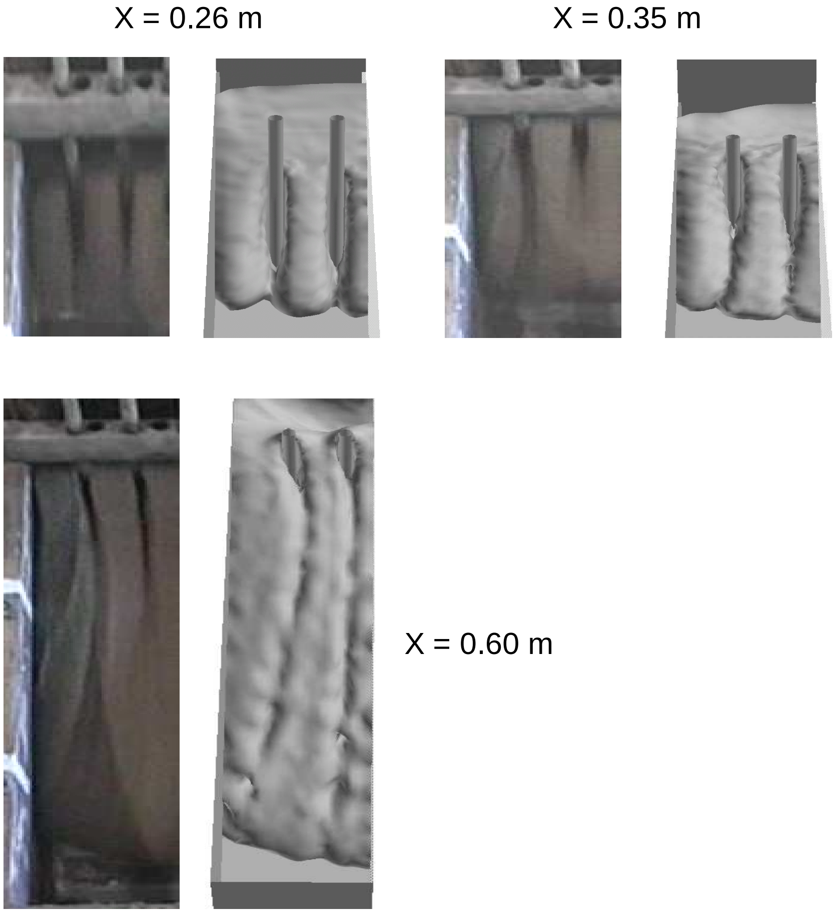

Figure 7.21 *Examples of the free surface shape of mortar M_1 at different flow propagations in the L-box. The experimental observations are shown to the left and the simulations are shown to the right.*

Based on these results, it seems that a reasonable agreement between measured rheological parameters and those used to simulate flow can be obtained when taking into account the accuracy at which it is possible to measure and calculate the rheological properties by linear regression.

A homogeneous approach seems applicable for simulation of flow domains including reinforcement when blocking does not occur.

Finally, the effect of lifting is especially important in both the slump flow test and the L-box, especially at low plastic viscosities.

Mix E_1

The results of simulating and testing concrete mix E_1 in the slump flow test and the L-box are presented. The slump cone was turned upright $D200$ and the lifting velocity was determined to $U_{lift} = 4$ cm/s. The lifting velocity in the L-box was determined to $U_{lift} = 29$ cm/s and the reinforcement setup A_{lbox} was applied.

In the L-box, the methodology for assessment of blocking is outlined and will also be used for the subsequent mixes when aggregates sizes $d_p > 4$ mm are applied. The estimate of the risk of blocking is compared to the visual observation.

The initial rheological parameters applied in simulation of the L-box are estimated based on the slump flow test. Figure 7.22 shows the results of the slump flow test and the L-box test.

For the yield stress, the relation in Figure 7.6 is used to deduce a value of $\tau_0 = 18$ Pa.

To estimate the plastic velocity, the experimental curve was initially compared to the results of the parameter study on the effect of yield stress and plastic viscosity at a lifting velocity of 7 cm/s. With considerations of the effect of lifting, a proposed value of $\eta_{pl} =$ 30 Pa·s is applied. Simulation of the slump flow is repeated with $U_{lift} = 4$ cm/s when using $\tau_0 = 18$ Pa and $\eta_{pl} = 30$ Pa·s. It seems that the simulation correlates well with the experimental result. If the lifting was not taken into account this would result in an estimate of the plastic viscosity higher than 30 Pa·s, approximately 35 Pa·s.

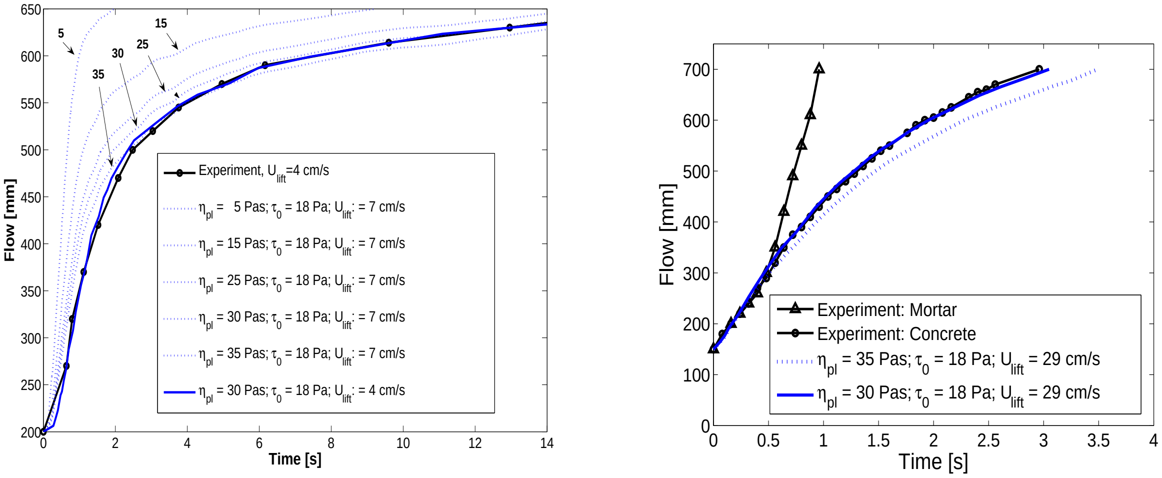

(a) Slump flow test

(b) L-box test

Figure 7.22 *Simulations and testing of the slump flow test and L-box test for concrete mix E_1. In the slump flow test, the numbers 5, 15, 25, 30, and 35 refer to values of the plastic viscosity η_{pl}. The L-box results for the mortar M_1 has been included for comparison.*

Therefore, simulations of the L-box have been carried out for a yield stress of τ_0= 18 Pa and a plastic viscosity of both η_{pl} = 30 and 35 Pa·s. The best correlation is obtained at 30 Pa·s which is consistent with the result of the slump flow test.

The results show a good correlation between the behavior in the slump flow test and the L-box when applying the same rheological parameters and when taking into account the boundary conditions.

The procedure to assess the risk of blocking is discussed in the following.

In Chapter 6, a critical flow rate or correspondingly a critical velocity in a circular tube flow domain was proposed as a criterium for assessment of blocking. Flow rates are only comparable if the material occupies the same cross-sectional area. Otherwise, the critical velocity determined for the circular tube flow must be compared to an average velocity determined for the cross-section of the reinforcement bars. The average velocity between reinforcement bars is deduced from the homogeneous flow simulation.

Examples of the free surface flow near the reinforcement is shown in Figure 7.23. The mesh shows the lifting of the gate and the transition from white to black corresponds to the height of the gate.

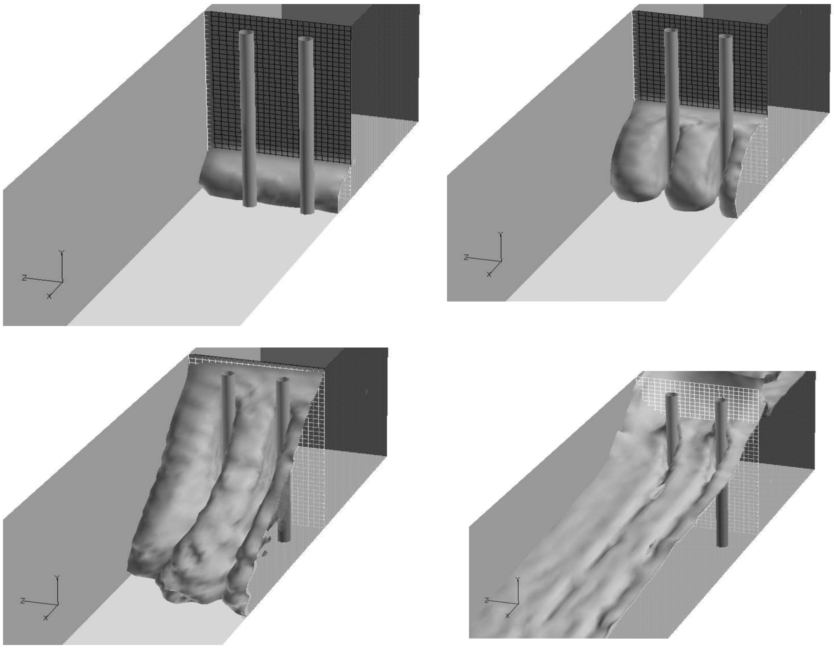

Figure 7.23 *Simulation of flow near the reinforcement in the L-box of concrete mix* E_1 *at time 0.10, 0.22, 0.51, and 3.06 seconds. The mesh shows the gate and the transition from black to white which corresponds to the height of the gate at the specific time.*

The average velocity is derived for the sections A_1, A_2 and A_3.

The cross-sectional area occupied by material ($A_{f,i}$) is obtained from numerical integration of the concentration $g_i(y,z)$ over the cross sectional area A_i which is given by:

$$A_{f,i} = \int_{A_i} g_i(y,z)dydz \quad i = 1,2,3 \tag{7.1}$$

The concentrations of the three sections for the situations shown in Figure 7.23 are shown in Figure 7.25. Black and white correspond to a concentration of 1 and 0, respectively.

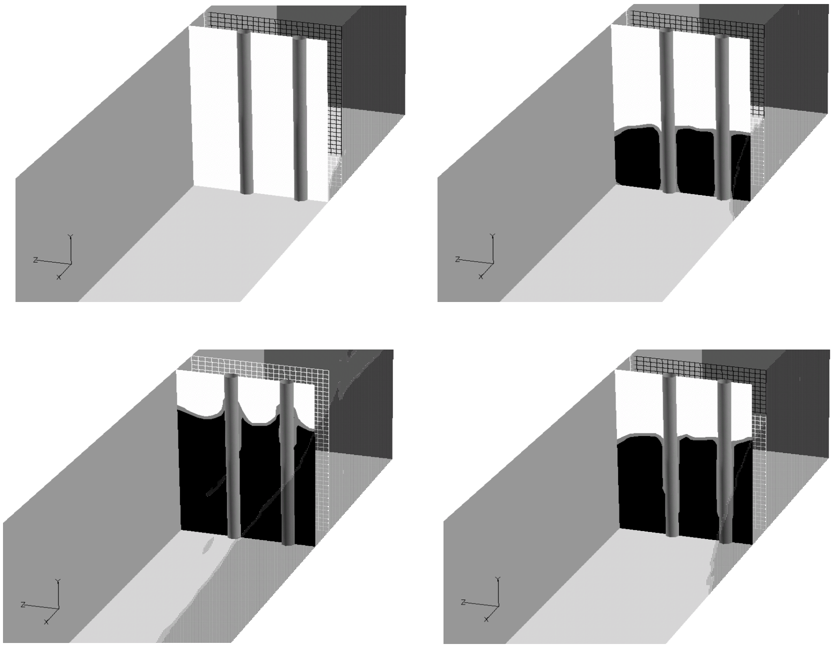

Figure 7.24 *Concentrations $g(y,z)$ near the reinforcement in L-box for concrete mix E_1 at time 0.10, 0.22, 0.51, and 3.06 seconds. Black and white correspond to g = 1 and 0, respectively.*

The flow rate in the x-direction is deduced from numerical integration of the velocity field in the x-direction over the cross-sectional area A_i and is given by:

$$Q_{x,i} = \int_{A_i} U_{x,i}(x,y)dydz \quad i = 1,2,3 \tag{7.2}$$

The velocity field in the x-direction of the three sections for the situations shown in Figure 7.23 are shown in Figure 7.25.

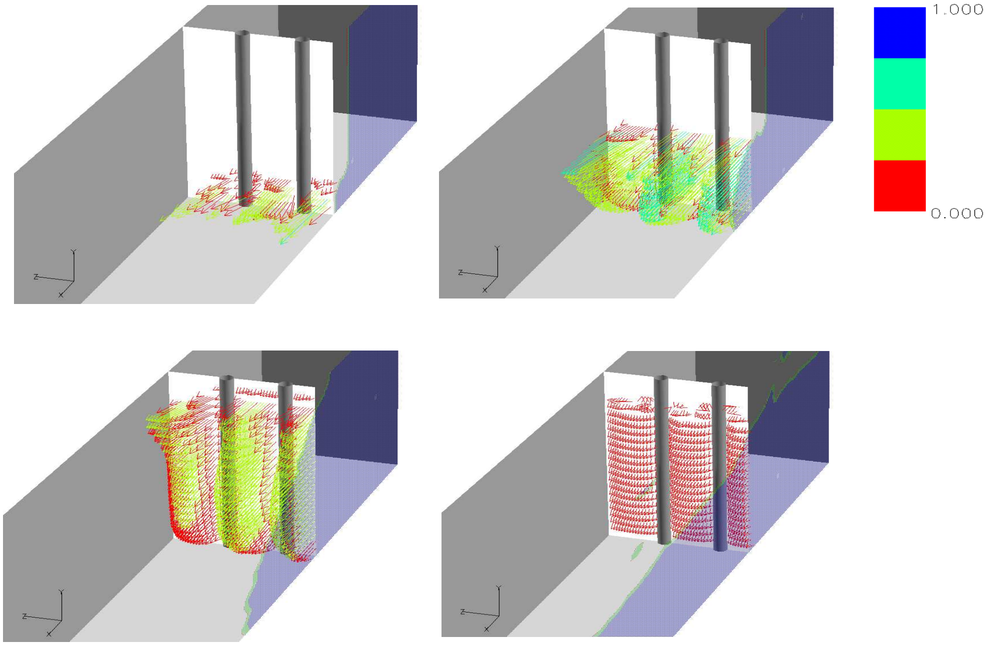

Figure 7.25 *Velocity field in the x-directions near the reinforcement in the L-box for concrete mix E_1 at time 0.10, 0.22, 0.51, and 3.06 seconds.*

The average velocity, $U^{av}_{x,i}$ is then given by:

$$U^{av}_{x,i} \quad = \quad \frac{Q_{x,i}}{A_{f,i}} \qquad i = 1, 2, 3 \tag{7.3}$$

Figure 7.26 shows the results of calculating the material cross-sectional area, flow rate and average velocity given by Equations 7.1, 7.2, and 7.3, respectively.

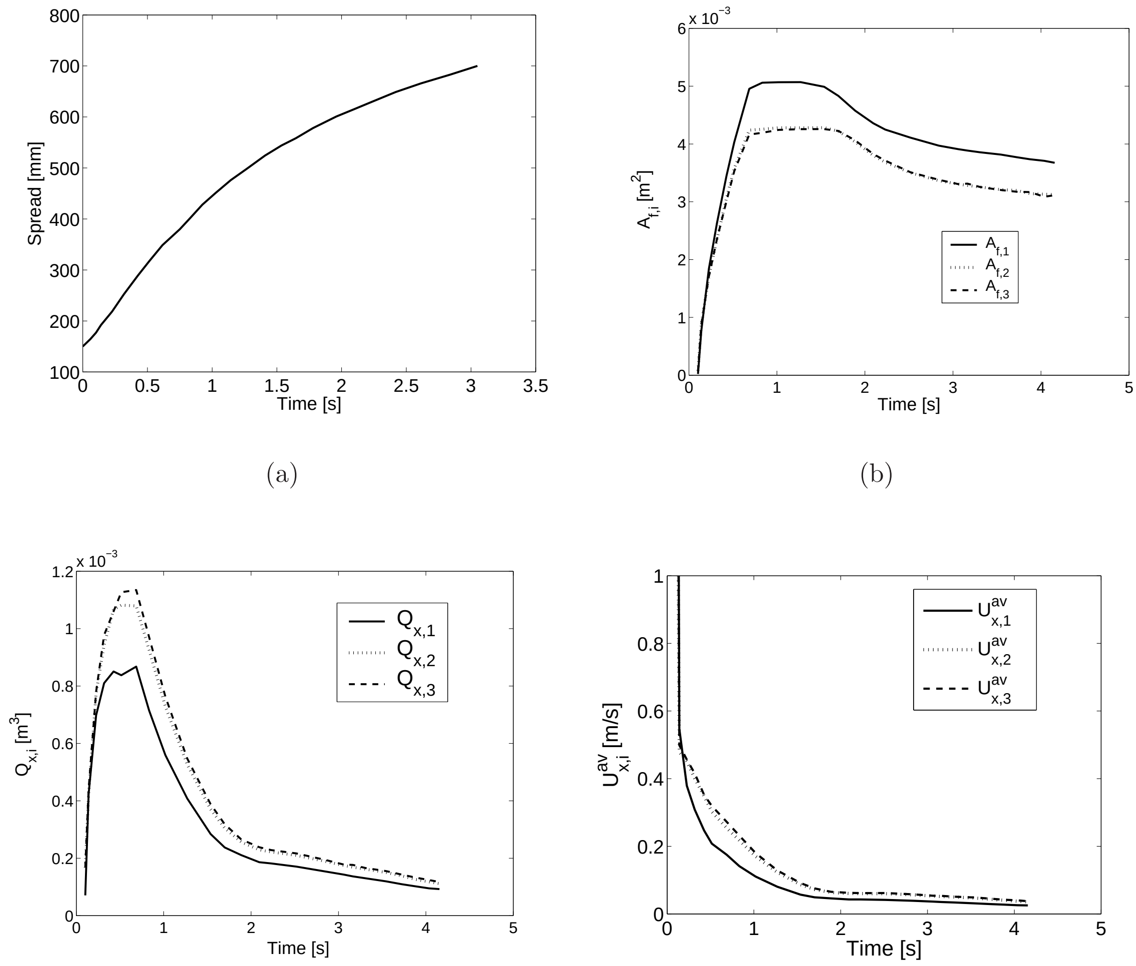

(a) (b)

(c) (d)

Figure 7.26 *Results from simulation of concrete mix E_1 in the L-box. Upper left: Flow into the horisontal section versus time. Upper right: The cross-sectional area occupied by material in reinforcement sections A_1, A_2, and A_3 (Eq. 7.1). Lower left: Flow rate in sections A_1, A_2, and A_3 (Eq. 7.2). Lower right: Average velocity in sections A_1, A_2, and A_3 (Eq. 7.3).*

The critical average velocity is estimated based on the particle volume fraction, maximum particle volume fraction, rheological parameters of the matrix phase, confinement ratio, and clear spacing between the reinforcement bars.

The rheological properties of the matrix phase is estimated using Equation 6.7 for the yield stress and plastic viscosity of the suspension. The aggregates are natural rounded (seashore) for which reason it is assumed that the intrinsic viscosity for spheres applies ($[\eta] = 2.5$). Using the estimate of the rheological properties from the slump flow test and L-box, the particle volume fraction $\phi_p = 0.38$, and the maximum particle volume fraction $\phi_p^* = 0.636$, this gives an estimate of the rheological parameters of the matrix phase (see Table 7.3).

Table 7.3 *Parameters used to estimate $\eta_{m,pl}$ and $\tau_{m,0}$ of the matrix in concrete mix E_1.*

ϕ_p	ϕ_p^*	$[\eta]$	$\eta_{s,pl}$ [Pa·s]	$\tau_{s,0}$ [Pa]	$\eta_{m,pl}$ [Pa·s]	$\tau_{m,0}$ [Pa]
0.380	0.636	2.5	30	18	7	4.5

For the confinement ratio, it is necessary to estimate a weighted confinement ratio because a polydisperse aggregate fraction has been applied. The particle size distribution of fraction 4-8 mm, 8-16 mm, and the combined one is shown in Figure 7.27.

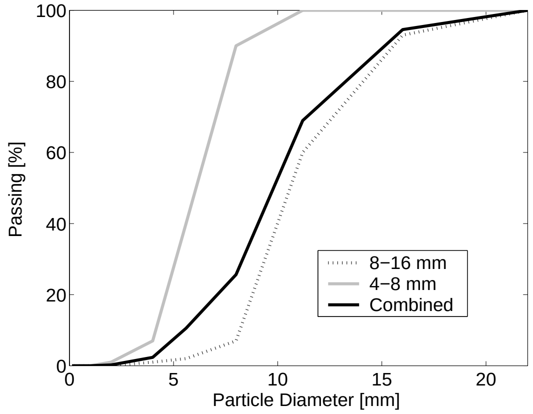

Figure 7.27 *The particle size distribution of fraction 4-8 mm, 8-16 mm, and the combined one used in concrete mix E_1.*

To estimate a weighted confinement ratio, the combined particle size distribution is divided into $i = 1, 2, ...N$ fractions of average particle size $d_{p,i}$ given by

$$d_{p,i} = (d_{u,i} - d_{L,i}) \cdot W + d_{L,i} \quad i = 1, 2, ...N \tag{7.4}$$

where $d_{u,i}$ and $d_{L,i}$ denote the upper and lower particle diameter of fraction i and W is weighing constant.

In this case, the combined particle size distribution shown in Figure 7.27 is divided into 5 fractions between 4 and 22 mm and W values of $\frac{1}{2}$ and $\frac{2}{3}$ has been applied as shown in Table 7.4.

Table 7.4 *Average particle diameter of five fractions of the combined particle size distribution in concrete mix E_1.*

i	1	2	3	4	5
$d_{u,i}$ [mm]	22.0	16.0	11.2	8.0	5.6
$d_{L,i}$ [mm]	16.0	11.2	8.0	5.6	4.0
$d_{p,i}$ [mm] (w=$\frac{1}{2}$)	19.0	13.6	9.6	6.8	4.8
$d_{p,i}$ [mm] (w=$\frac{2}{3}$)	20.0	14.4	10.1	7.2	5.1

The weighed confinement ratio, α^*, is determined by

$$\alpha^* = \sum_{i}^{N} \left(\frac{\phi_{p,i}}{\Sigma\phi_{p,i}} \frac{c}{d_{p,i}} \right) \qquad i = 1, 2, ...N \tag{7.5}$$

where c is the clear spacing between reinforcement bars and $\phi_{p,i}$ is the particle volume of fraction i.

For area A_1 the clear spacing is 35 mm, and for A_2 and A_3 the clear spacing is 30 mm, respectively. For a weighing constant W of $\frac{1}{2}$ and $\frac{2}{3}$, this gives weighted confinement ratios as shown in Table 7.5.

Table 7.5 *Weighted confinement ratio α^* of mix E_1.*

	A_1	A_2 and A_3
c [mm]	35	30
α^* (w=$\frac{1}{2}$)	3.80	3.25
α^* (w=$\frac{2}{3}$)	3.60	3.08

Finally, the corresponding tube radius is determined, which was introduced in Section 6.7.

For sections A_1, A_2, and A_3, the corresponding radius according to the two procedures shown in Figure 6.38 is given in Table 7.6.

Table 7.6 *Corresponding radius of sections A_1, A_2, and A_3 in the L-box test.*

	A_1	A_2 and A_3
c [mm]	35	30
$R_{c,1}$ [mm]	17.5	15.0
$R_{c,2}$ [mm]	24.8	21.2

Using these input parameters, the critical velocity is estimated. Figure 7.28 shows to the left the critical velocity as a function of particle volume fraction for sections A_2 and A_3. To the right, the critical velocity at $\phi_p = 0.38$ has been shown for all three sections.

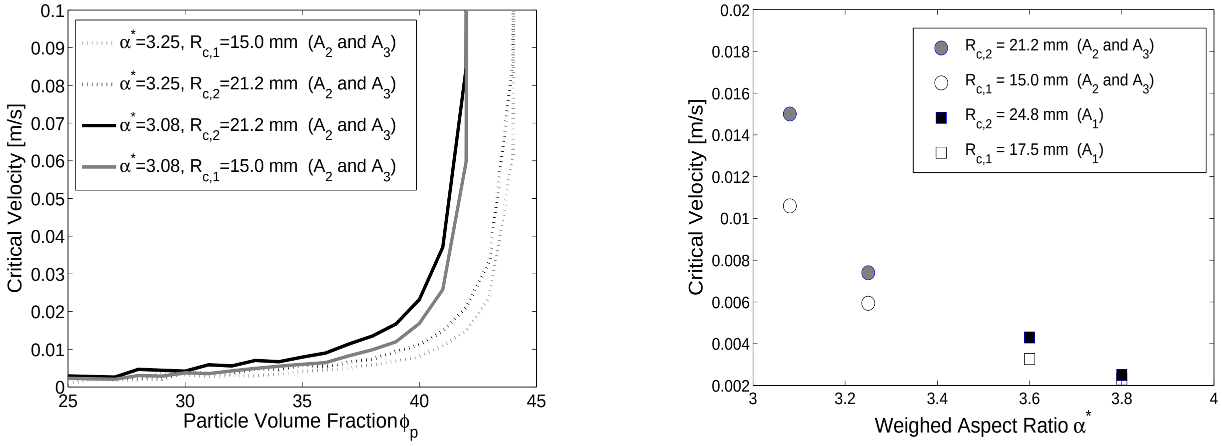

Figure 7.28 *To the left, the critical velocity as a function of particle volume fraction (in [%]) for sections A_2 and A_3 applying different confinement ratios and corresponding tube radii. To the right, the critical velocity at $\phi_p = 0.38$ for sections A_1, A_2 and A_3.*

The critical velocity may now be compared to the average velocity for the three sections found using the homogeneous simulation (Figure 7.26). Figure 7.29 shows the average velocity in the L-box as a function of time and the highest value of the critical velocity U_{crit}= 0.015 m/s which was found for section A_2 and A_3 when using the weighted confinement ratio $\alpha^* = 3.08$ and the corresponding tube radius $R_{c,2} = 21.2$ mm. The results indicate that blocking will not occur.

For comparison with the experiment, some pictures from testing concrete mix E_1 are shown in Figure 7.30. Observations of the flow showed that blocking did not occur. However, watching a video of the experiment seems to show that the risk of blocking increases at the end of the test which may relate to the decrease in average velocity.

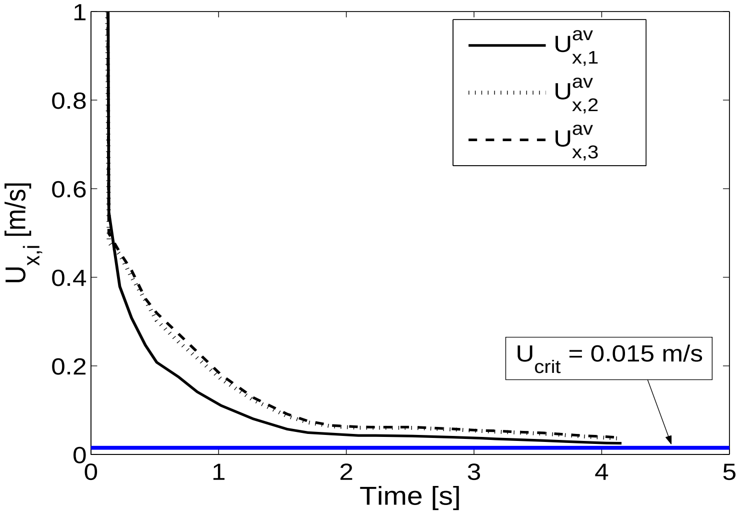

Figure 7.29 *The average velocity in the three sections A_1, A_2, and A_3 in the L-box as a function of time according to the homogeneous simulation. The blue line shows the estimate of the critical velocity for the weighed confinement ratio $\alpha^* = 3.08$ and the corresponding tube radius $R_{c,2} = 21.2$ mm.*

Figure 7.30 *Photos from testing mix E_1 in the L-box test with reinforcement setup A_{lbox}.*

Mix E_3 and F_2

The slump flow and L-box results for concrete mix E_3 and F_2 are presented.

The L-box configuration for E_3 and F_2 correspond to setup A_{lbox} and B_{lbox}, respectively.

For mix E_3, the rheological properties used to simulate the L-box are based on the slump flow test using setup 2.

For mix F_2, the measured values of the yield stress and plastic viscosity are shown in Table 7.2.

The slump flow test result for E_3 is shown in Figure 7.34. Simulations are shown for a yield stress of $\tau_0 = 40$ and 30 Pa and a plastic viscosity of $\eta_{pl} = 10$ and 15 Pa·s.

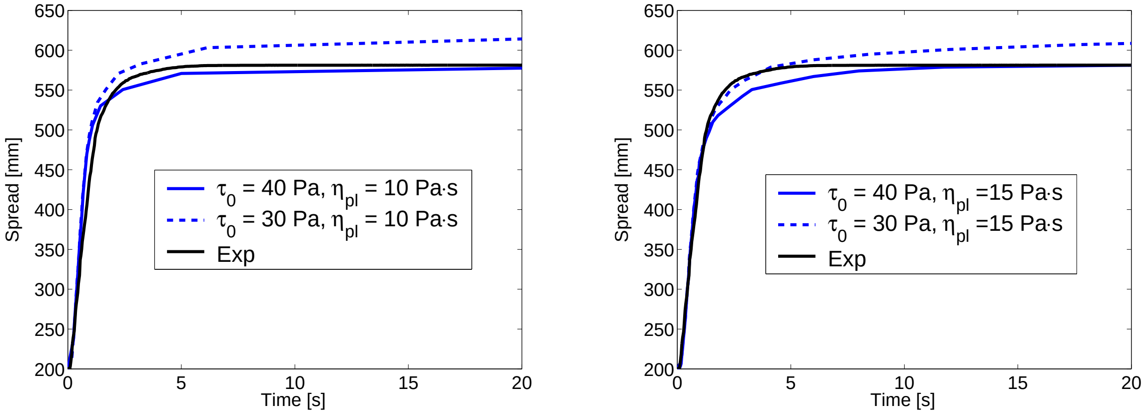

(a) (b)

Figure 7.31 *Slump flow test results for concrete mix E_3 and results from simulation when using yield stresses and plastic viscosities as shown.*

When comparing the simulations with the test results, it is estimated that the yield stress $\tau_0 \approx 40$ Pa and the plastic viscosity $\eta_{pl} \approx 12$ Pa·s.

In the following, the critical velocity for concrete mix F_2 and E_3 is estimated following the procedure outlined in the previous section for concrete mix E_1.

The combined particle size distributions are shown in Appendix A. Natural rounded and crushed aggregates were applied in mix E_3 and F_2, respectively. Initially it is assumed that the characteristic diameter is equal to the particle size. However, as discussed in Chapter 6, the irregular shape of the aggregates may lead to a higher characteristic diameter.

Tables 7.7, 7.8, and 7.9 show the input parameters applied in the model. Table 7.7 shows the material characteristics. Table 7.8 shows the weighed confinement ratios and Table 7.9 shows the corresponding radius.

Table 7.7 *Material characteristics of concrete mixes E_3 and F_2.*

Mix	ϕ_p	ϕ_p^*	$[\eta]$	$\eta_{s,pl}$ [Pa·s]	$\tau_{s,0}$ [Pa]	$\eta_{m,pl}$ [Pa·s]	$\tau_{m,0}$ [Pa]
E_3	0.417	0.638	2.5	12	40	2.2	7.5
F_2	0.364	0.628	2.5	25	50	6.5	13

Table 7.8 *Weighted confinement ratio α^* of concrete mixes E_3 and F_2.*

	A_1	A_2 and A_3	B_1	B_2
c [mm]	35	30	60	25
α^* (w=$\frac{1}{2}$)	3.90	3.35	6.67	2.78
α^* (w=$\frac{2}{3}$)	3.70	3.17	6.33	2.63

Table 7.9 *Corresponding radius of concrete mixes E_3 and F_2.*

	A_1	A_2 and A_3	B_1	B_2
c [mm]	35	30	60	25
$R_{c,1}$ [mm]	17.5	15.0	30	12.5
$R_{c,2}$ [mm]	24.8	21.2	42.4	17.6

Figure 7.32 shows to the left the critical velocity as a function of the particle volume fraction for mix F_2 in section B_2 (with the lowest confinement ratio). It is shown for the combinations of the confinement ratio and corresponding tube radius, which lead to the highest and lowest estimate of the critical velocity. At a particle volume fraction of $\phi_p = 0.364$, this results in estimates of $U_{crit} = 6$ m/s and ∞. As previous mentioned, the L-box setup B_{lbox} have not been simulated using the homogeneous approach. However, for comparison, the average velocity simulated for concrete mix E_1 (sections A_2 and A_3) are shown to the right. The results show that the average velocity is much smaller than the critical velocity indicating that blocking will occur.

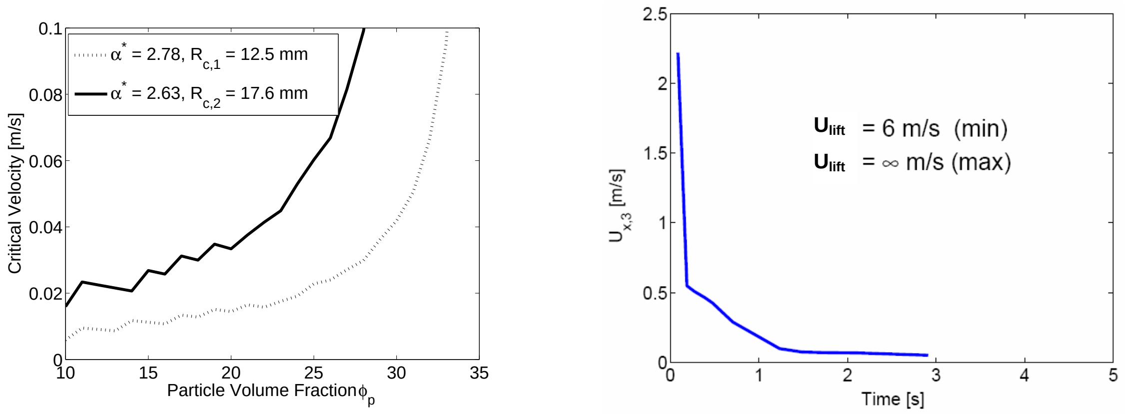

(a) (b)

Figure 7.32 *To the left, the critical velocity as a function of the particle volume fraction (in [%]) for concrete mix F_2 in L-box section B_2. To the right, both the critical velocity and an estimate of the average velocity in the section B_2 when using the average velocity from simulation of concrete mix E_1 in L-box section A_2 and A_3.*

For section B_1, a critical velocity close to zero is estimated indicating that blocking will not occur. Figure 7.33 shows some pictures from the L-box test, which show that blocking occurs in section B_2 but not in B_1 corresponding to the estimate of the model.

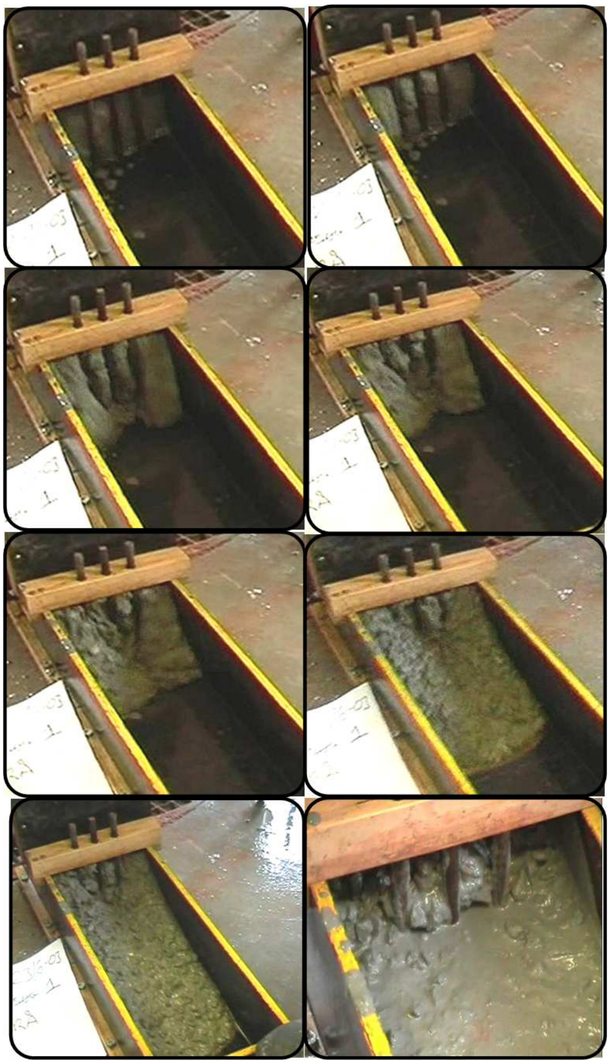

Figure 7.33 *Photos from testing mix F_2 in the L-box using setup B_{lbox}. Blocking is clearly observed in section B_2 (between bars). In section B_1 (between wall and bar) blocking does not occur.*

Figure 7.34 shows the results from testing and simulation of concrete mix E_3 in the L-box. A plastic viscosity and yield stress of approximately $\eta_{pl} = 12$ Pa·s and $\tau_0 = 40$ Pa were estimated from the slump flow test. Simulations of the L-box have been carried out for a plastic viscosity of $\eta_{pl} = 10$ and 20 Pa·s and yield stresses of $\tau_0 = 40$ and 45 Pa.

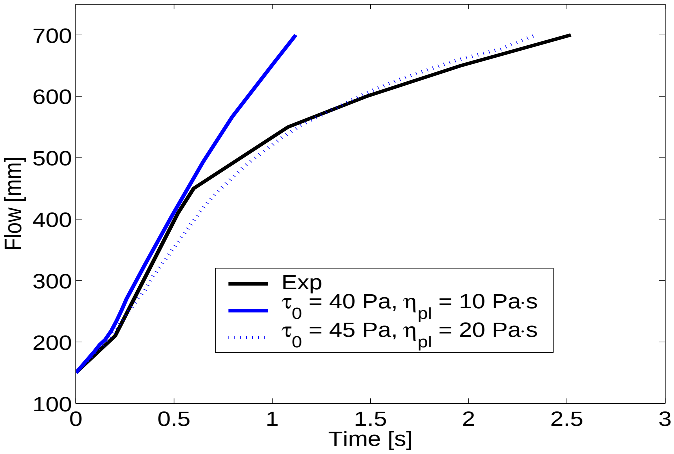

Figure 7.34 *The results from testing and simulation of mix E_3 in the L-box.*

It is observed that the experimental flow curve initially follows the simulation using $\eta_{pl} = 10$ Pa·s. At $t = 0.5$ s, it starts to deviate from this flow curve and comes closer to the flow curve which is simulated using $\eta_{pl} = 20$ Pa·s. The observations during the test dos not indicate a higher plastic viscosity. Instead, it seems to be a result of blocking, enforcing more resistance to flow (see Figure 7.36). The estimate of the critical velocity and the average velocity from the homogeneous simulation are shown in Figure 7.35.

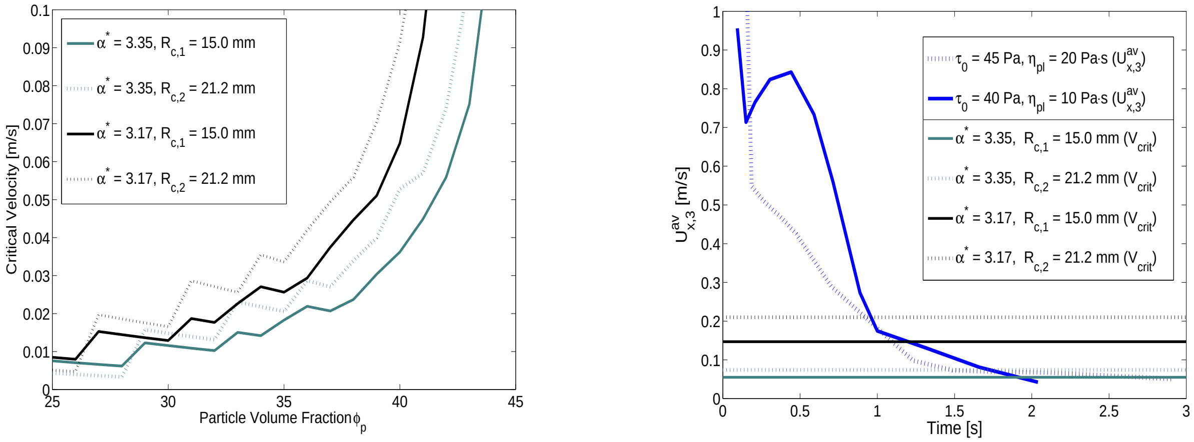

Figure 7.35 *To the left, the critical velocity as a function of particle volume fraction (in [%]) for concrete mix E_3 in the L-box sections A_2 and A_3. To the right, the critical velocity at $\phi_p = 0.417$ and the simulated average velocities using the homogeneous flow approach.*

The highest and lowest values of the critical velocity are approximately $U_{crit} = 0.2$ m/s and 0.05 m/s, respectively. These two values indicate that blocking may be initiated during testing approximately between $t = 1$ and 2 s, respectively. Comparing the critical velocity as a function particle volume fraction of mix E_3 and E_1, it is observed that the critical velocity is higher for mix E_3 even though the confinement ratio is higher (3.17 in E_3 and 3.08 E_1). This is mainly due to a lower plastic viscosity of the matrix phase for mix E_3 ($\eta_{m,pl} = 2.2$ Pa·s for mix E_3 and $\eta_{m,pl} = 7.0$ Pa·s for mix E_1).

Figure 7.36 shows some pictures from the L-box test of mix E_3. Observations of the flow indicate that the concrete remain homogeneous in the initial period of the test. At approximately $t = 0.5$ s, the slope of the free surface across the reinforcement increases, which could indicate that blocking is initiated. At the end, blocking is observed in the L-box sections A_2 and A_3.

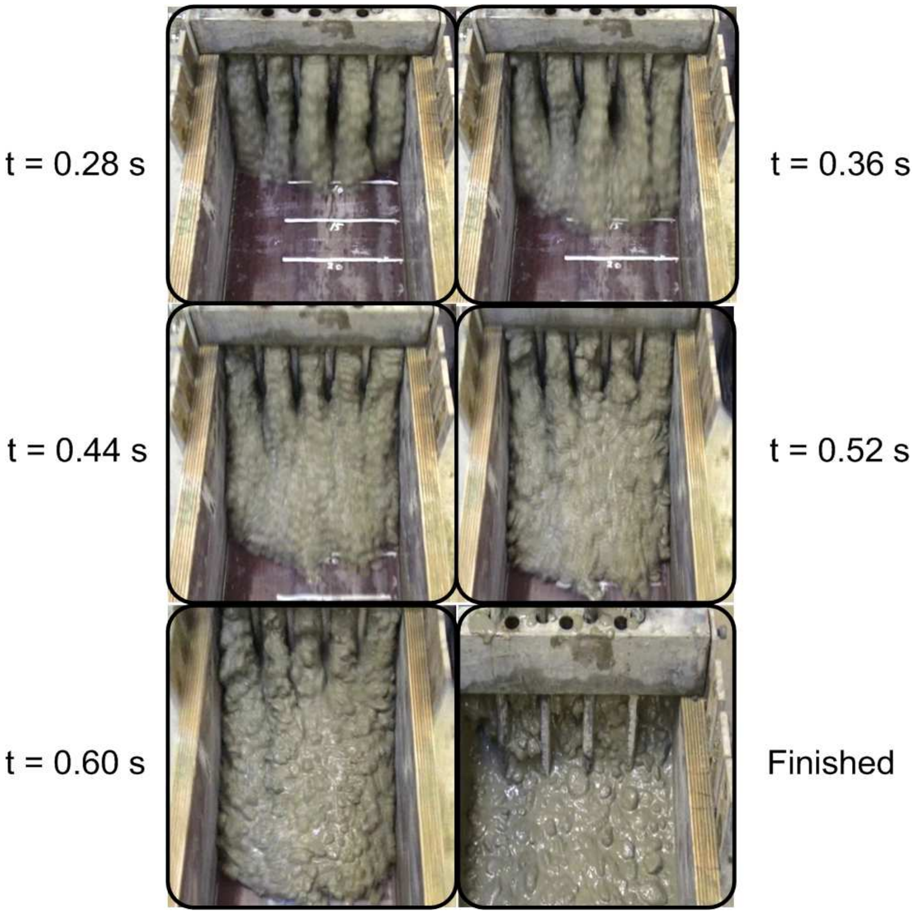

Figure 7.36 *Photos from testing mix E_3 in the L-box using setup A_{lbox}. Blocking is observed at the end of the test in the section A_2 and A_3.*

Mix E_2 and E_4

The results of the slump flow test (setup 2) and the L-box test (setup A_{lbox}) for concrete mixes E_2 and E_4 are presented. Different simulations have been carried out to show the correlation between those applied to simulate the slump flow test and the L-box, respectively.

Situation (a) in Figure 7.37 shows the slump flow test results of concrete mix E_4 (black). Assuming a homogeneous flow approach, a yield stress of $\tau_0 = 45$ Pa is estimated. The blue lines show simulations for $\tau_0 = 45$ Pa and plastic viscosities of $\eta_{pl} = 15$, 20, 30, 35 and 45 Pa·s. The results indicate a plastic viscosity in the range of 30 Pa·s. Situation (b) shows a simulation of the L-box for $\tau_0 = 45$ Pa and plastic viscosities of $\eta_{pl} = 20$ and 35 Pa·s. As for the slump flow test, the results indicate that the plastic viscosity is in the range of 30 Pa·s.

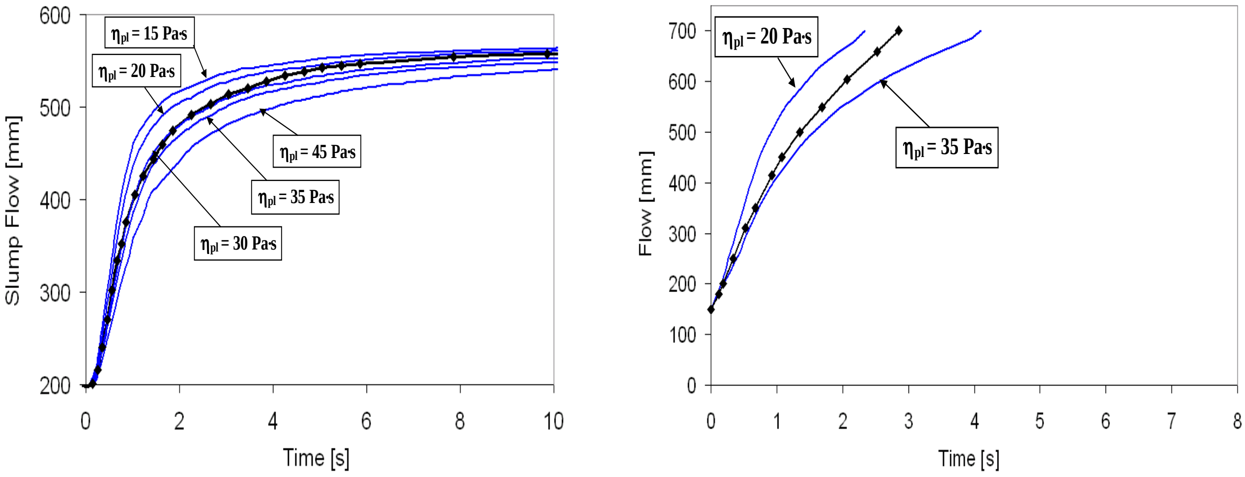

(a) E_4 : Slump Flow

(b) E_4 : L-Box

Figure 7.37 *The results of testing and simulation of concrete mix E_4 in the slump flow test (setup 2) and L-box test (setup A_{lbox}). Black and blue lines correspond to the experimental results and simulations, respectively. Simulations have been carried out using a yield stress $\tau_0 = 45$ Pa and plastic viscosities as shown.*

Situation (a) and (b) in Figure 7.38 shows the results for concrete mix E_2. Based on the slump flow test, the yield stress was estimated to $\tau_0 = 55$ Pa. Simulations are shown for plastic viscosities of $\eta_{pl} = 55$, 65 and 120 Pa·s. Based on the slump flow test, the plastic viscosity seems to be in the range of $\eta_{pl} = 65$ Pa·s. For the L-box, only a single simulation have been carried out for $\tau_0 = 55$ Pa and $\eta_{pl} = 50$ Pa·s. The simulation overestimates the flow which correspond to the slump flow test showing that the plastic viscosity is higher than 50 Pa·s.

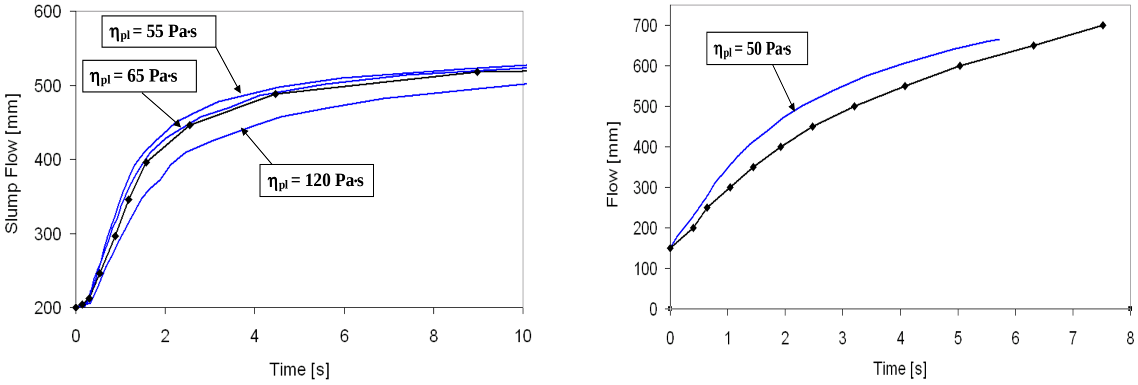

(a) E_2 : Slump Flow (b) E_2 : L-Box

Figure 7.38 *The results of testing and simulation of concrete mix E_2 in the slump flow test and L-box. Black and blue lines correspond to the experimental results and simulations, respectively. Simulations in (a) and (b) have been carried out using a yield stress of τ_0 = 55 Pa and plastic viscosities as shown.*

For comparison of the final free surface location in the L-box, the simulation of mix E_2 have been continued until complete stop after $t = 12$ s. Good correlation between the free surfaces of the simulation and the experiment has been obtained and is shown in Figure 7.39.

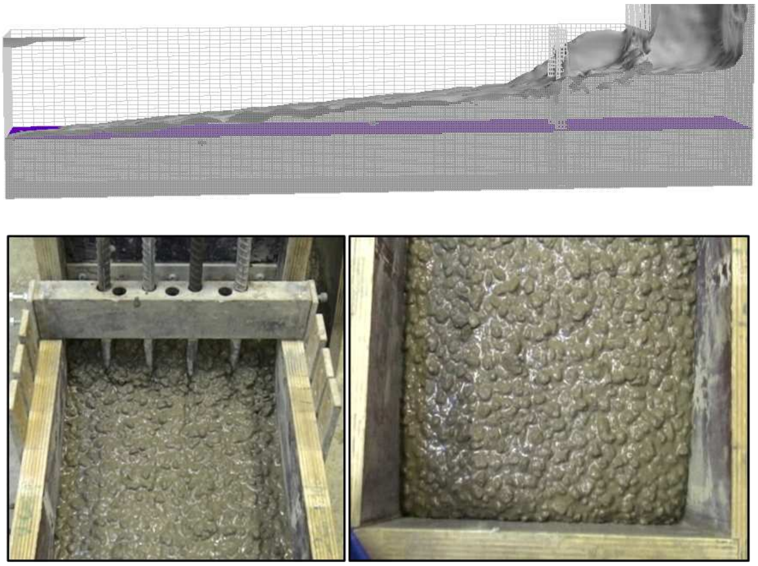

Figure 7.39 *The final free surface location of concrete mix E_2 in the L-box test (setup A_{lbox}) in the simulation and experiment, respectively.*

The simulation and experiment shows a final height at $x = 0$ and 700 mm of approximately $H_2 \approx 55$ mm and $H_1 \approx 100$ mm, respectively. This gives a ratio of $H_2/H_1 \approx 0.55$.

The sloping behavior is a result of the yield stress when inertia can be neglected as discussed in Section 3.1.5. It may be assumed that the effect of inertia is limited due to a relatively high value of the plastic viscosity compared to mix M_1 ($\eta_{pl} = 7.5$ Pa·s) where inertia could not be neglected. The good correlation between the yield stress applied to simulate the slump flow (≈ 510 mm) and the H_2/H_1 ratio in the L-box (≈ 0.55) indicate that the homogeneity assumption is valid in this case. The concrete had a maximum aggregate fraction of 4-8 mm at a particle volume fraction of 0.43. Further research should compare the results of the slump flow and the L-box test for a wider range of particles sizes and particle volume fractions in order to set limits for the slump flow as a valid estimate of the yield stress.

In Section 3.1.5 an analytical relation between the yield stress and the H_2/H_1 ratio derived by Nguyen et al. (2006) was presented. The relation when including reinforcement may be written in terms of the yield stress given by:

$$\tau_0 \cong \frac{\rho_s g(1 - \frac{H_2}{H_1})}{100(\frac{H_2}{H_1} + 1)} \qquad \text{with bars} \tag{7.6}$$

For a density of $\rho_s = 2369$ kg/m^3, this gives a yield stress of $\tau_0 = 67$ Pa. Without the reinforcement bars, a yield stress of 80 Pa is found. Thus, a reasonable agreement is obtained between the analytical expression when including reinforcement and the numerical simulation where a yield stress of $\tau_0 = 55$ Pa was applied.

In general, there is a good correlation between the Bingham parameters used to simulate the transient flow in the slump flow test and the L-box test.

For both mixes, the maximum aggregate fraction applied was 4-8 mm for which reason blocking did not occur. This is consistent with the estimate of the critical velocity $U_{crit} = 0$.

7.4.3 Form Filling Applications

Test $FF1$

The results from testing and simulation of form filling experiment $FF1$ are presented. The numerical model was outlined in Chapter 5.

As mentioned in Section 7.2.3, it was not possible to measure the rheological properties of concrete mix F_1. Instead, the rheological properties have been estimated based on the slump flow test, however, not as shown in the above cases where the transient behavior was compared. In this case only the final slump flow $SF = 570$ mm and $T50 \approx 2$ s were recorded. The yield stress and plastic viscosity have been estimated from the parameter study on the effect of the rheological parameters presented in Section 7.1. A simulation using a yield stress $\tau_0 = 40$ Pa and a plastic viscosity $\eta_{pl} = 20$ Pa·s seems to correspond to the values of SF and $T50$, see Figure 7.40.

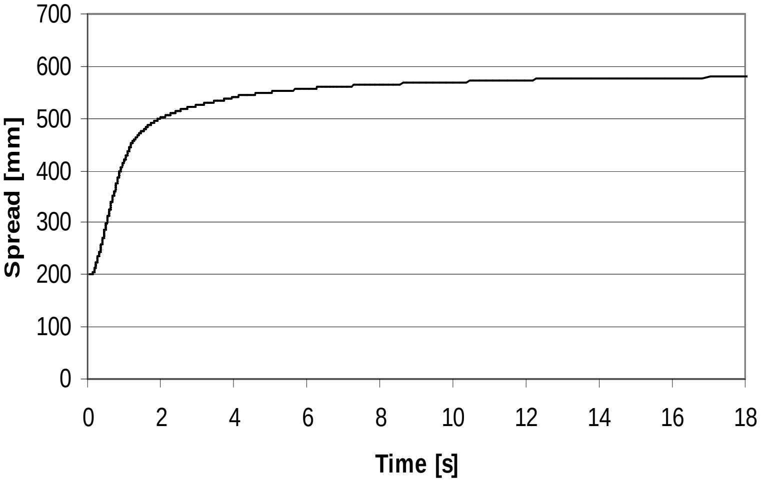

Figure 7.40 *Simulation of the slump flow test for a yield stress* $\tau_0 = 40$ *Pa and a plastic viscosity* $\eta_{pl} = 20$ *Pa·s.*

To assess the effect of a yield stress, the simulation is repeated for a Newtonian fluid with a viscosity $\mu = 20$ Pa·s.

Figure 7.41, 7.42, 7.43, and 7.44 show results for the free surface (corresponding to the filling ability) at $t = 6$ s, 36 s, 60 s, 250 s, and 360 s for the experiment and the two simulations.

The filling rate applied in the test is approximately 10 m/hour corresponding to filling velocity $U_{fill} = 0.35$ m/s (see Figure 5.11).

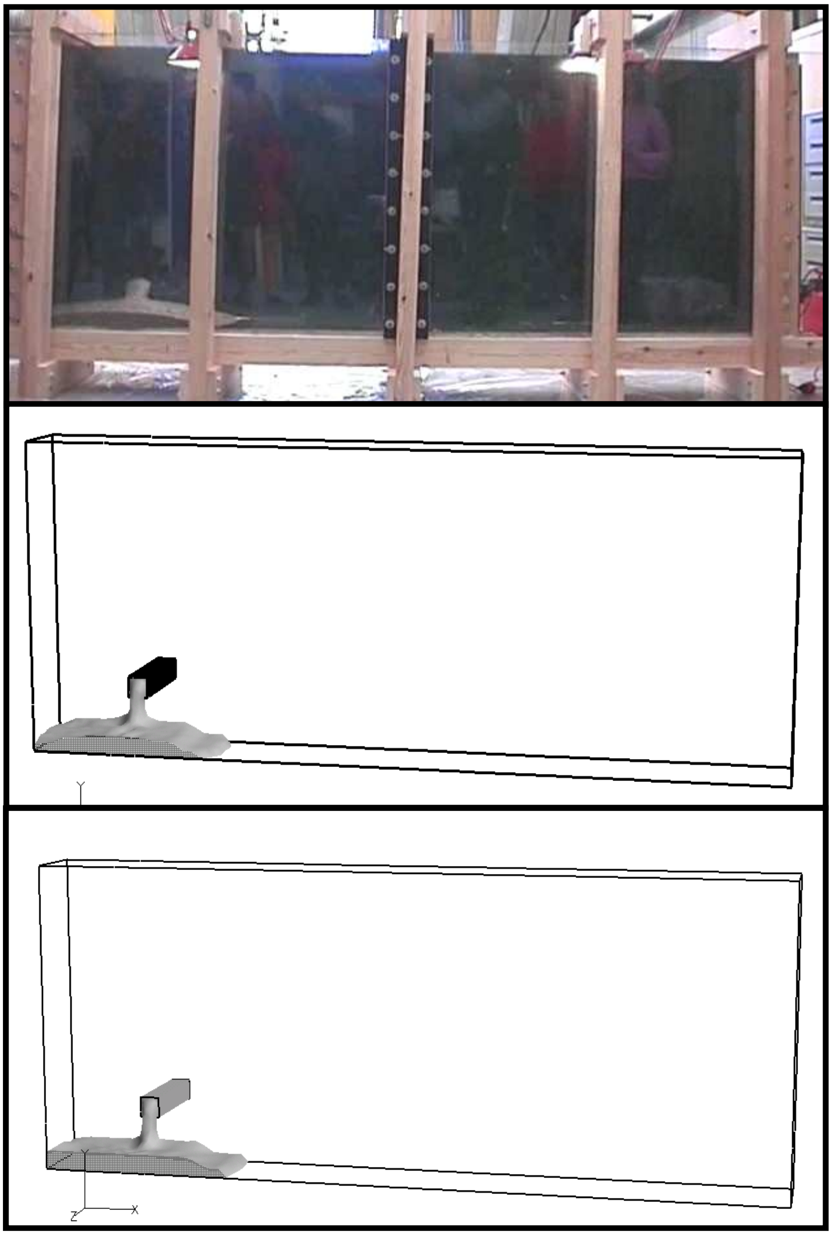

Figure 7.41 *The free surface of the test (top) and simulations of a Bingham (middle) and Newtonian (bottom) fluid at* $t = 6$ *s. A yield stress of* $\tau_0 = 40$ *Pa and plastic viscosity* $\eta_{pl} = 20$ *Pa·s have been applied for the Bingham fluid and* $\mu = 20$ *Pa·s for the Newton fluid.*

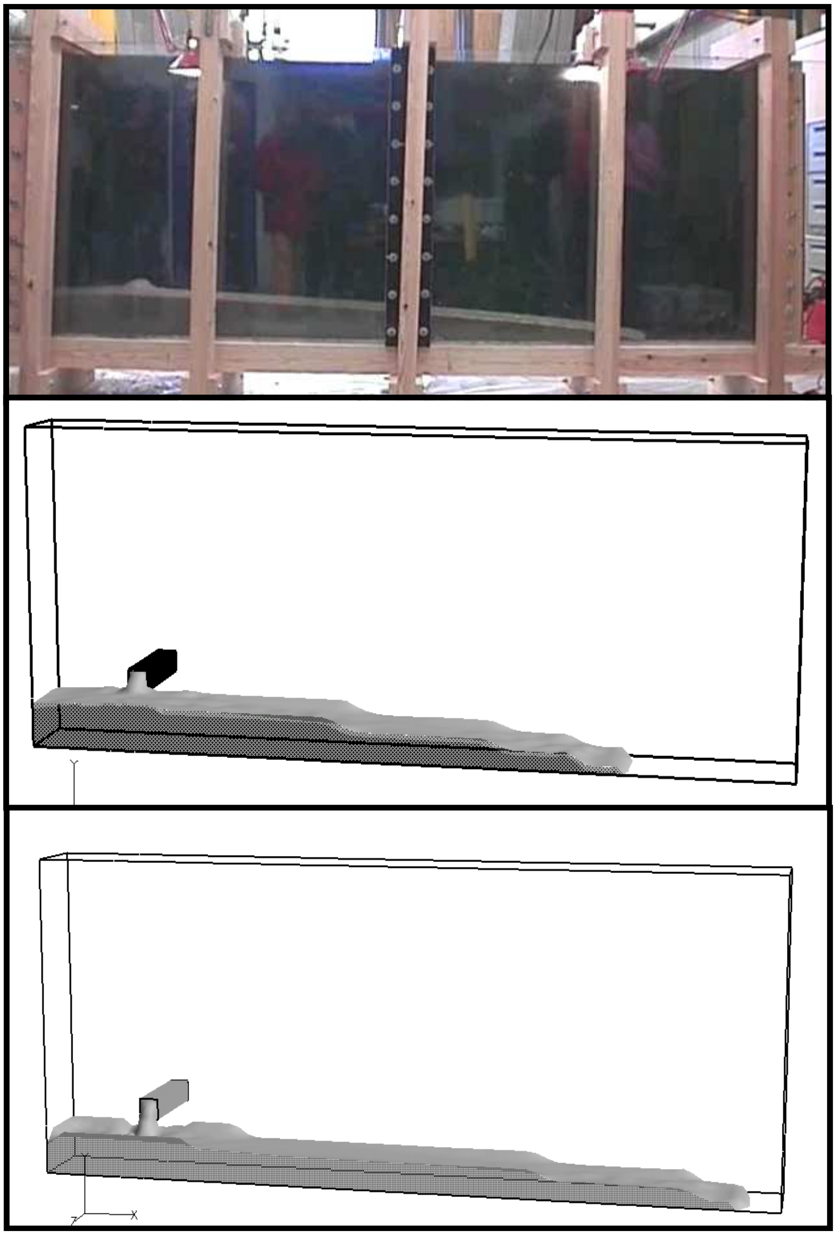

Figure 7.42 *The free surface of the test (top) and simulations of a Bingham (middle) and Newtonian (bottom) fluid at* $t = 36$ *s. A yield stress of* $\tau_0 = 40$ *Pa and plastic viscosity* $\eta_{pl} = 20$ *Pa·s have been applied for the Bingham fluid and* $\mu = 20$ *Pa·s for the Newton fluid.*

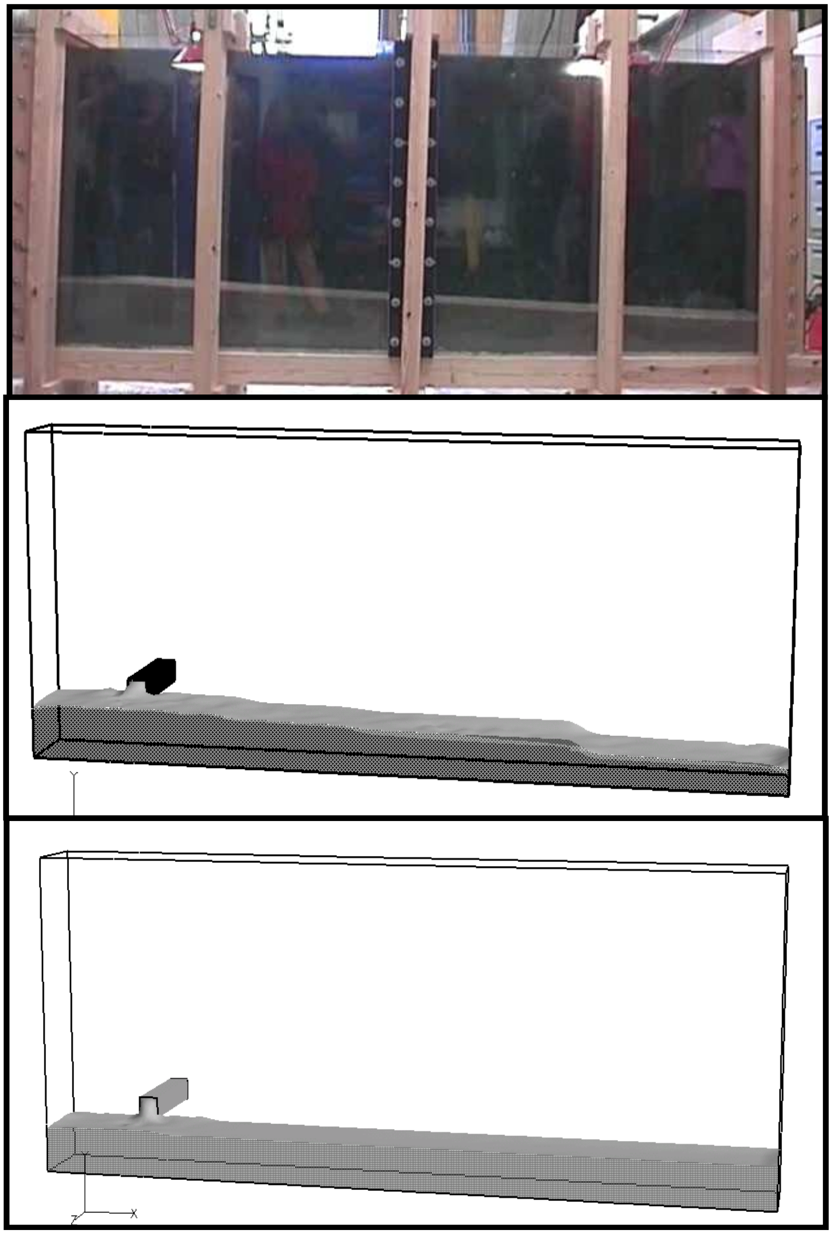

Figure 7.43 *The free surface of the test (top) and simulations of a Bingham (middle) and Newtonian (bottom) fluid at* $t = 60$ *s. A yield stress of* $\tau_0 = 40$ *Pa and plastic viscosity* $\eta_{pl} = 20$ *Pa·s have been applied for the Bingham fluid and* $\mu = 20$ *Pa·s for the Newton fluid.*

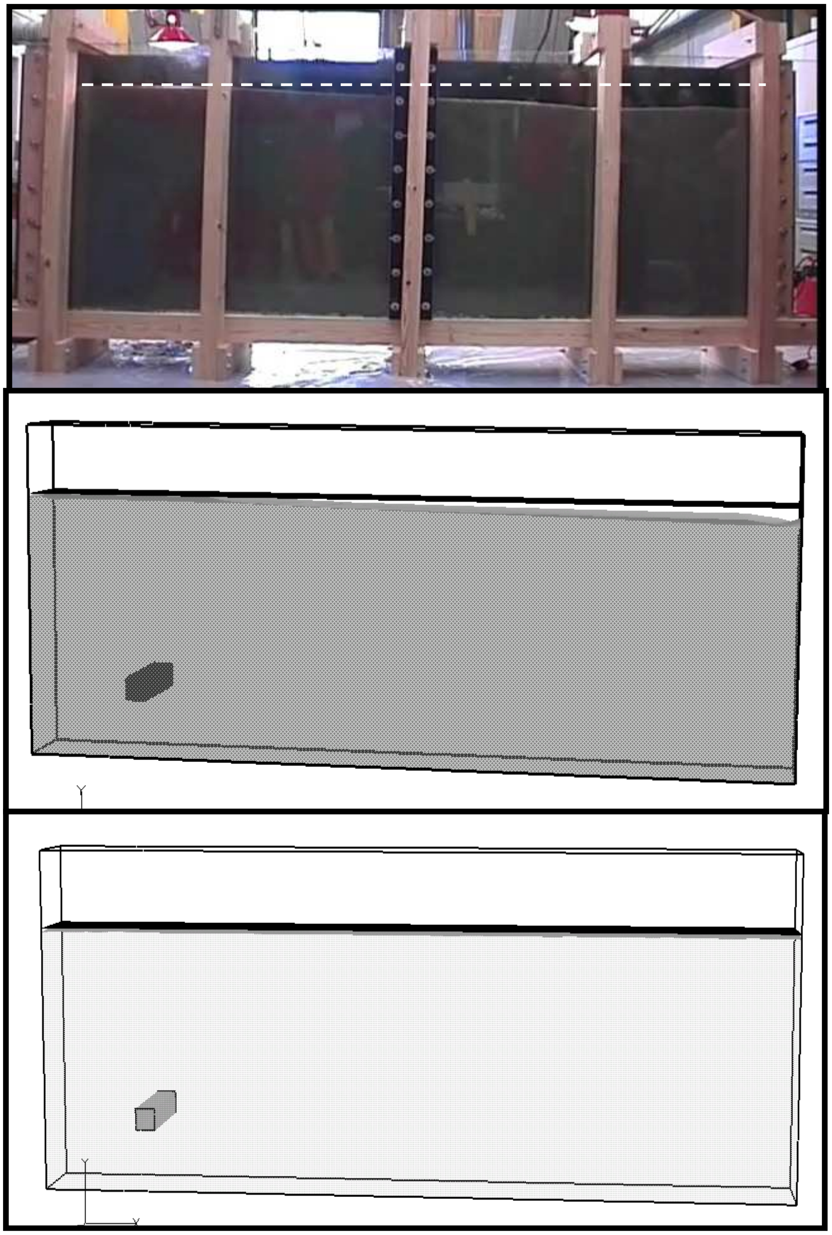

Figure 7.44 *The free surface of the test (top) and simulations of a Bingham (middle) and Newtonian (bottom) fluid at t = 360 s. A yield stress of τ_0 = 40 Pa and plastic viscosity η_{pl} = 20 Pa·s have been applied for the Bingham fluid and μ = 20 Pa·s for the Newton fluid.*

The results show good correlation between the free surface of the concrete and the simulated Bingham fluid with regard to curvature and flow propagation. For instance, at $t = 6$ and 36 s, the Bingham fluid simulation captures the slope and propagation better than the simulation of a Newtonian fluid which shows a lower slope and overestimates the propagation in the x-direction. As the concrete reaches the end wall at $x = 3.0$ m, the filling continues with a slightly inclined free surface. This is captured by the Bingham fluid but not by the Newtonian fluid. The latter is completely levelled during the filling process.

At $t = 360$ s, the filling stops and the inclination is illustrated in the simulations by plotting a surface plane at a constant height of 1 m. Correspondingly, a dotted line has been plotted in the result of the experiment. The Newtonian fluid coincides with the surface plane, however, the height difference of the Bingham fluid at $x = 0$ and 3.0 m (~ 60 mm) correlates well with the height difference found in the experiment (~ 50 mm).

Figures 7.45, 7.46, 7.47, 7.48, and 7.49 show the flow patterns observed in the experiment and the results from simulations.

The applied amount of red pigmentation did not allow observations of the flow behavior during casting. However, in the hardened concrete the red color is more easily identified and does provide a qualitative estimate of the flow behavior during form filling. Figure 7.45 shows the interpretation of the experimental results. It shows the side of the inlet ("backside"), the side of the acrylic plate ("transparent side"), and the top surface.

Dead zones seem to appear near the end wall at $x = 3.0$ m and at the bottom corner at $x = 0$ mm. When the concrete flows into the form it flows in a combined upwards and cross diagonal direction forcing the existing concrete toward the end wall as indicated by the arrows. The red color is clearly observed on the backside indicating this flow behavior.

At the transparent side, red concrete is observed in a circular area directly across the inlet and at the top. A break of grey concrete is observed between these two areas of red concrete. This indicates that the momentum of the concrete flowing into the form forces it to the transparent side just across the inlet and that the concrete at the backside flows more upwards than at the transparent side.

At the top surface, the location of the red concrete and the folds created indicate the above mentioned flow behavior. The folds are created when the existing concrete is forced in the direction towards the end wall.

After the test, the top showed a paste layer with a thickness of approximately 2 to 4 cm. This indicates that dynamic segregation has occurred during the test. It seems to be initiated when the concrete is forced upwards from the inlet to the top surface.

Regarding the surface finish, the best surfaces are obtained in the mid area sections where only very few blowholes are observed. In the dead zones and at the top at $x \sim 3.0$ m blowholes are clearly observed.

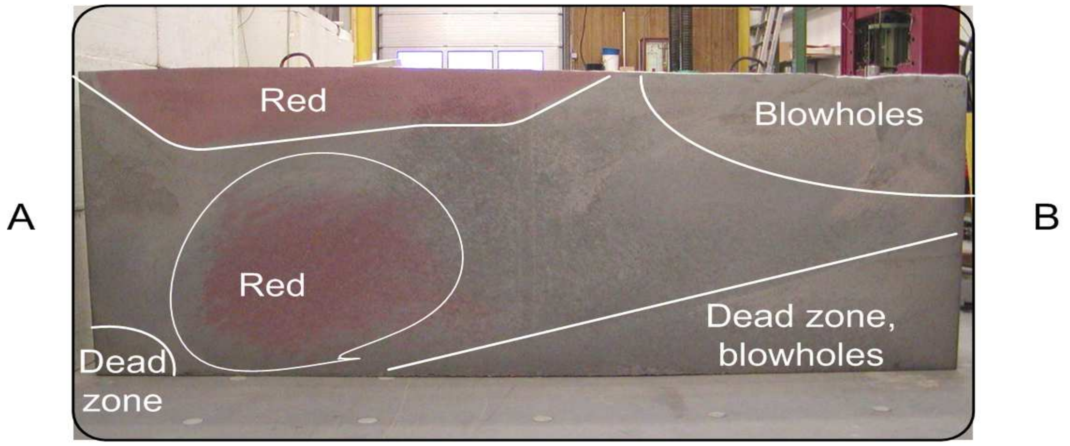

Transparent side

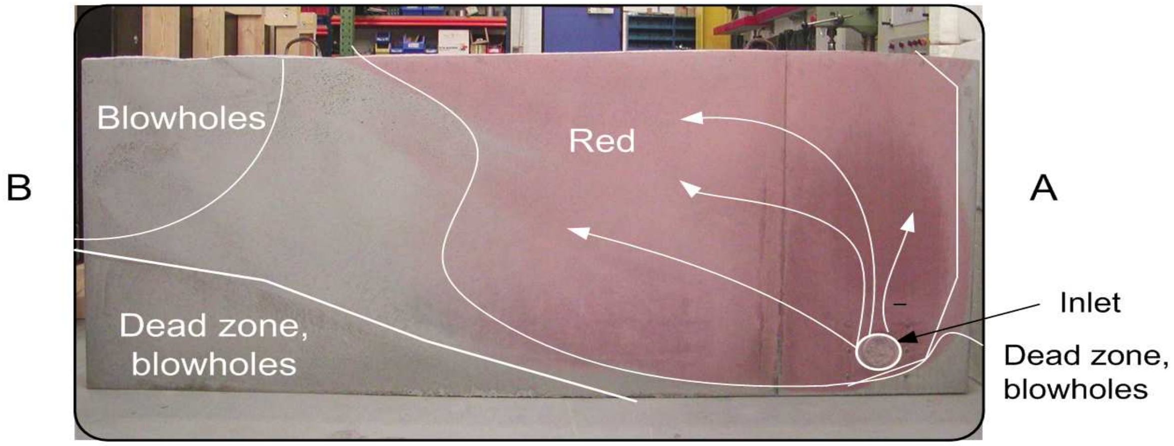

Backside

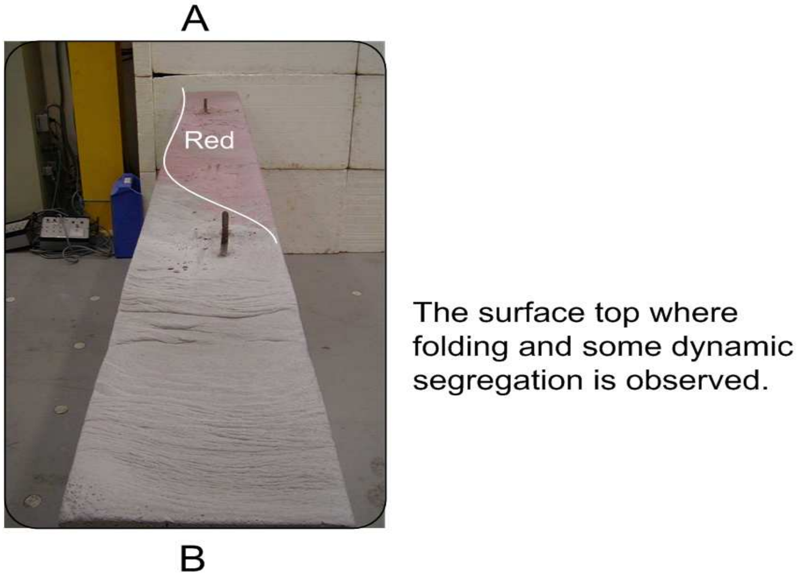

Figure 7.45 *Observed flow behavior in the experiment (dead zones, particle path of the red SCC, surface quality, folds, and dynamic segregation).*

Figure 7.46 shows the simulated particle paths for the Bingham fluid calculated from integration of the velocity field in the time interval from 120 to 250 s. The initial particle locations x-y plane are shown at the top. The initial z-positions are $z = 2$, 15, and 28 cm corresponding to the side of the inlet, the middle section, and the transparent side. The particle path is calculated for a number of particles released in the given time interval.

The results show a good correlation between the flow behavior observed in the experiment and the simulation with respect to detection of dead zones and particle paths. It is observed that particles released in the middle sections travel the longest distance in the x-direction and particles released near the transparent side travel the shortest distance. Only particles from the middle section and side of the inlet travel to the top surface. This seem to correspond with the red zone observed in the experiment near the top when viewed from the transparent side. The circular zone of red concrete at the transparent side across the inlet is also captured well by the simulation, which is shown in Figure 7.48. Particles are released below the inlet, the center of the inlet, and above the inlet. The particles released from the center of the inlet travel to the other side and creates the red zone observed in the experiment.

The simulation of the Bingham fluid indicates dead zones as observed in the experiment. For comparison, the particle paths obtained from simulation of a Newtonian fluid are shown in Figure 7.47. The dead zones are not obtained and vertical flow over the whole length of the form work is observed.

Comparing the observations on dynamic segregation and the flow patterns indicates that dynamic segregation is initiated when the concrete is forced in an upwards direction against gravity. Possible causes for dynamic segregation was discussed in Section 3.2.2. It is expected that dynamic segregation may be back-traced to the combined effect of shear induced particle migration and gravity induced segregation due to differences in density.

Figure 7.49 shows plots of the shear rates calculated according to Equation 3.4 at 120 s and 250 s. The shear rates are shown for planes at $z = 2$, 15, and 28 cm. In the z-direction, the highest shear rates are obtained near the surfaces and are decreasing towards the middle plane. In the x-y plane the highest shear rates are obtain in the parts where flow takes place (see figures with particle paths) and decrease towards the boundaries. The results indicate that shear rate gradients may affect the risk of dynamic segregation. The particles will tend to move from regions of high shear rates to regions of low shear rates. Through more detailed studies of the combined effect of shear rate gradients and gravity induced migration, it may be possible to establish a analytical criterion for dynamic segregation in the same way as for blocking and static segregation.

Regarding the surface finish, the surface areas with the lowest number of blowholes are obtained in the parts of the form where continuous shearing across the surface walls have occurred. This may also be a result of particle migration as the particles will have a tendency to move from the sides toward the middle plane in the z-direction. The generation of paste to the surface combined with the continuous shearing may have a positive effect on the surface finish.

Besides the zone inside the inlet, the shear rates are approximately in the range of 0 to 1.5 s^{-1}. This correlates, for instance, with a simple estimate of the horizontal (x-y) shear rate assuming zero velocity at the bottom, a concrete height of 0.20 m, and a time of 40 s to reach the end wall, which results in a shear rate of approximately 0.4 s^{-1}. Inside the inlet, a maximum shear rate of $\dot{\gamma} = 36\ s^{-1}$ is obtained.

The shear rate range during the form filling gives an indication of the range of shear rates which should be applied in viscometers for assessment of the rheological properties. For instance, in the BML-viscometer, it is possible to vary the shear rate between 0.20 and 14 s^{-1}.

As discussed in Chapter 3, the effect of thixotropy depends on the material characteristic and the shear rate history. It was assumed that thixotropy could be neglected in continuous castings and only flocculation at rest would be of importance. This assumption may be assessed by looking at results of form pressure measurements in vertical SCC castings by Billberg (2003). Here it was found that for thixotropy to have an effect on the form pressure during filling it was necessary to apply filling rates below 2 m/hour. This would result in lateral form pressures lower than the hydrostatic form pressure. The filling rate applied in this test is approximately 10 m/hour indicating that the assumption of thixotropy being negligible in continuous castings seems reasonable.

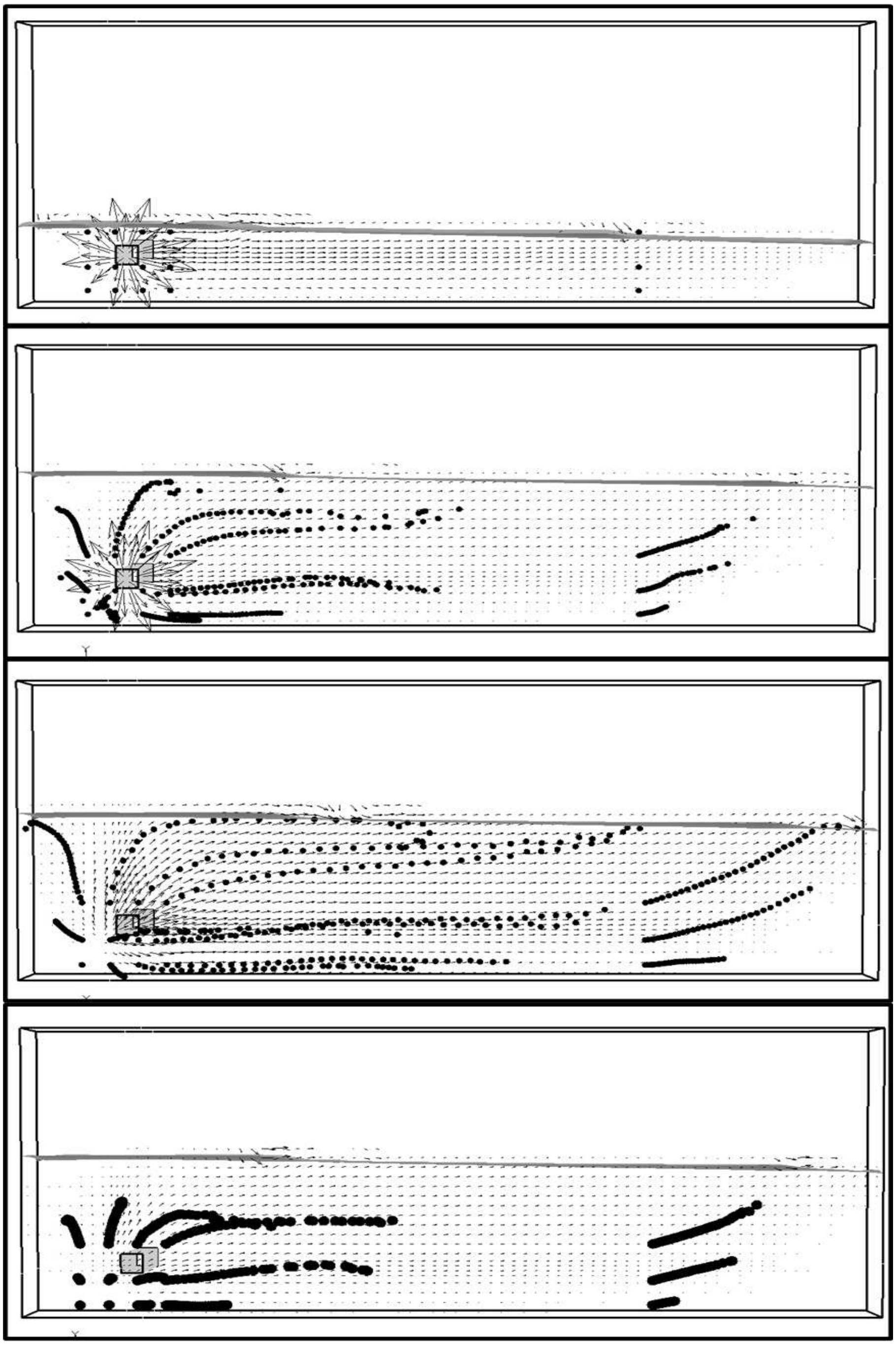

Figure 7.46 *Simulated particle paths in the time interval from 120 to 250 s for the Bingham fluid with $\tau_0 = 40$ Pa and $\eta_{pl} = 20$ Pa·s. Initial x-y location is shown at the top. The plots below represents particle paths for the initial z coordinates of z = 2, 15, and 28 cm corresponding to the side of the inlet, middle section and the transparent side.*

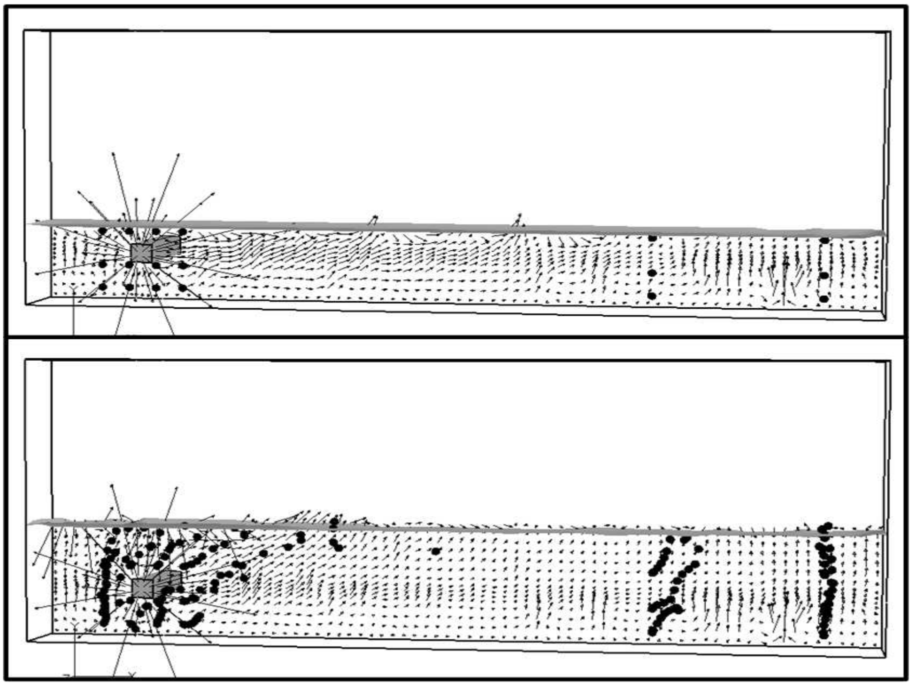

Figure 7.47 *Simulated particle paths in the time interval 130 to 200 s for a Newton fluid with $\mu=$ Pa·s. Initial x-y location is shown at the top. The plot below represents particle paths for an initial z coordinate of $z = 2$ cm corresponding to the side of the inlet.*

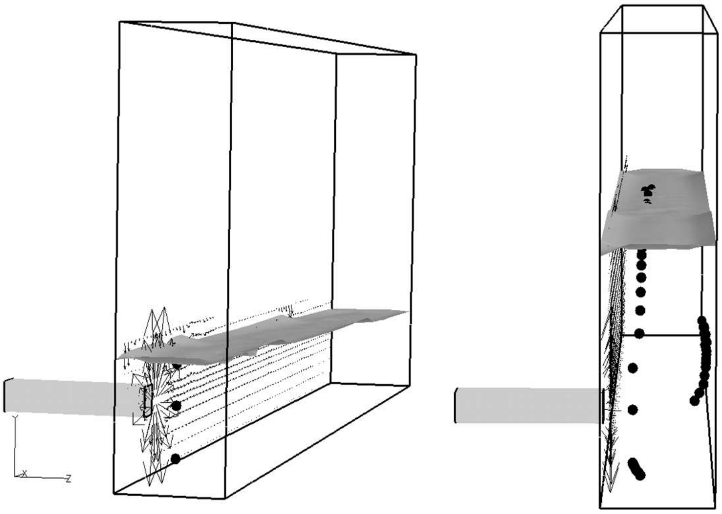

Figure 7.48 *Simulated particle paths for Bingham fluid with $\tau_0 = 40$ Pa and $\eta_{pl} = 20$ Pa·s with initial positions near the inlet as shown to the left and final positions shown to the right.*

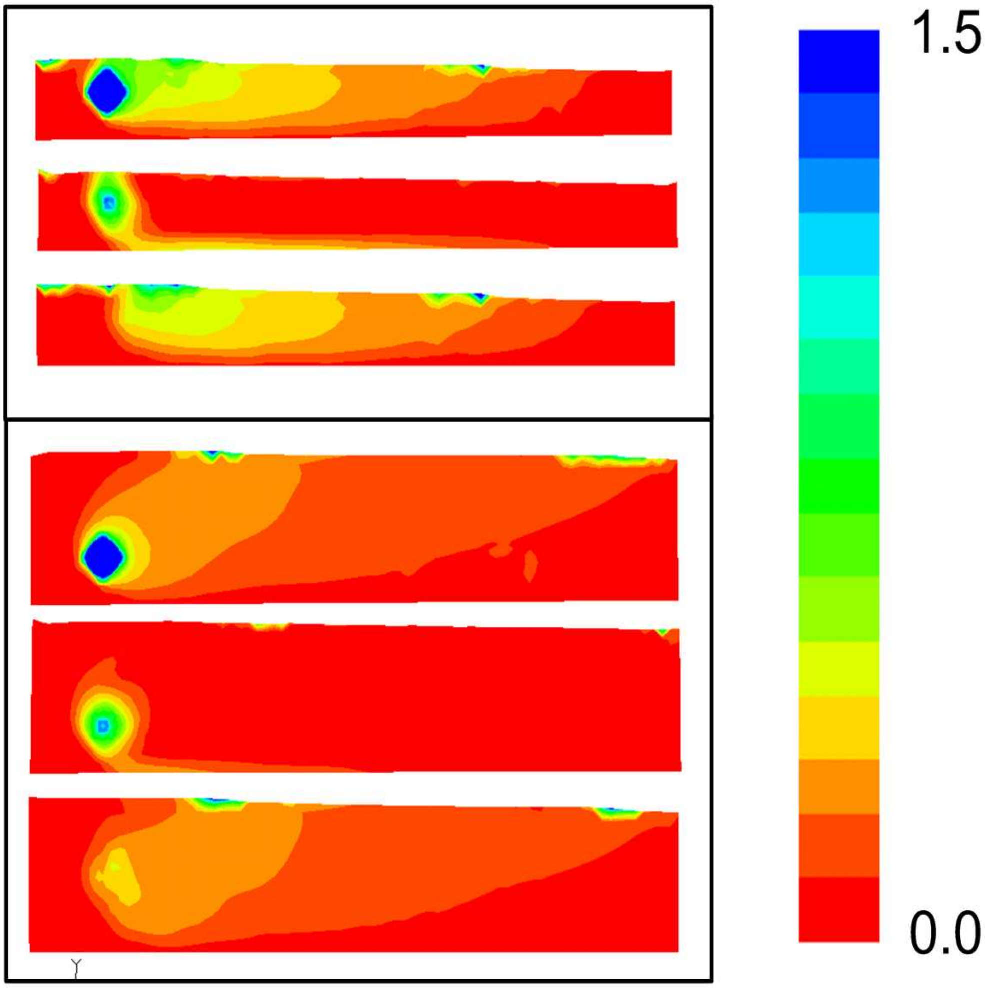

Figure 7.49 *Calculated shear rates $\dot{\gamma}$ [s^{-1}] for a Bingham fluid with τ_0 = 40 Pa and η_{pl} = 20 Pa·s at t = 120 (top) and 250 s (bottom). The three plots at each time represents x-y planes at z = 2, 15, and 28 cm corresponding to the side of the inlet, the middle section, and the transparent side.*

The next section shows results from the laboratory formwork including reinforcement.

Test $FF2$

The results of form filling test $FF2$ with concrete mix F_2 are presented.

Observations of the free surface and flow patterns are shown in Figure 7.50.

It is observed that the free surface starts to build-up in front of the reinforcement. The slope of the free surface throughout the filling process is different from the one observed in experiment $FF1$. When the concrete meets the reinforcement, the cross-sectional area is decreased, which in terms of a homogeneous approach will reduce the horizontal movement. However, the main reason for the build-up seems to be that blocking occurs in the narrow parts of the reinforcement configuration. When testing the concrete in the L-box (see Figure 7.33), complete blocking was obtained in section B_2 (clear spacing of 25 mm) in accordance with the model estimate. The narrow part of the reinforcement setup in the form filling test applies the same clear spacing of 25 mm (see Figure 5.13 for reinforcement configuration).

The combined effect of the flow resistance due to the narrow gaps and the complete blocking in the narrow parts of the reinforcement configuration results in a free surface location before passing the reinforcement that is approximately 15 cm higher than in experiment $FF1$.

In the other parts of the reinforcement (clear spacing of ≈ 50 mm) blocking is not observed.

It is observed that the build-up in front of the reinforcement is reduced when the concrete height is above the narrow parts of the reinforcement.

Due to the above mentioned reasons, the red concrete is observed to be located in a more upwards direction compared to test $FF1$.

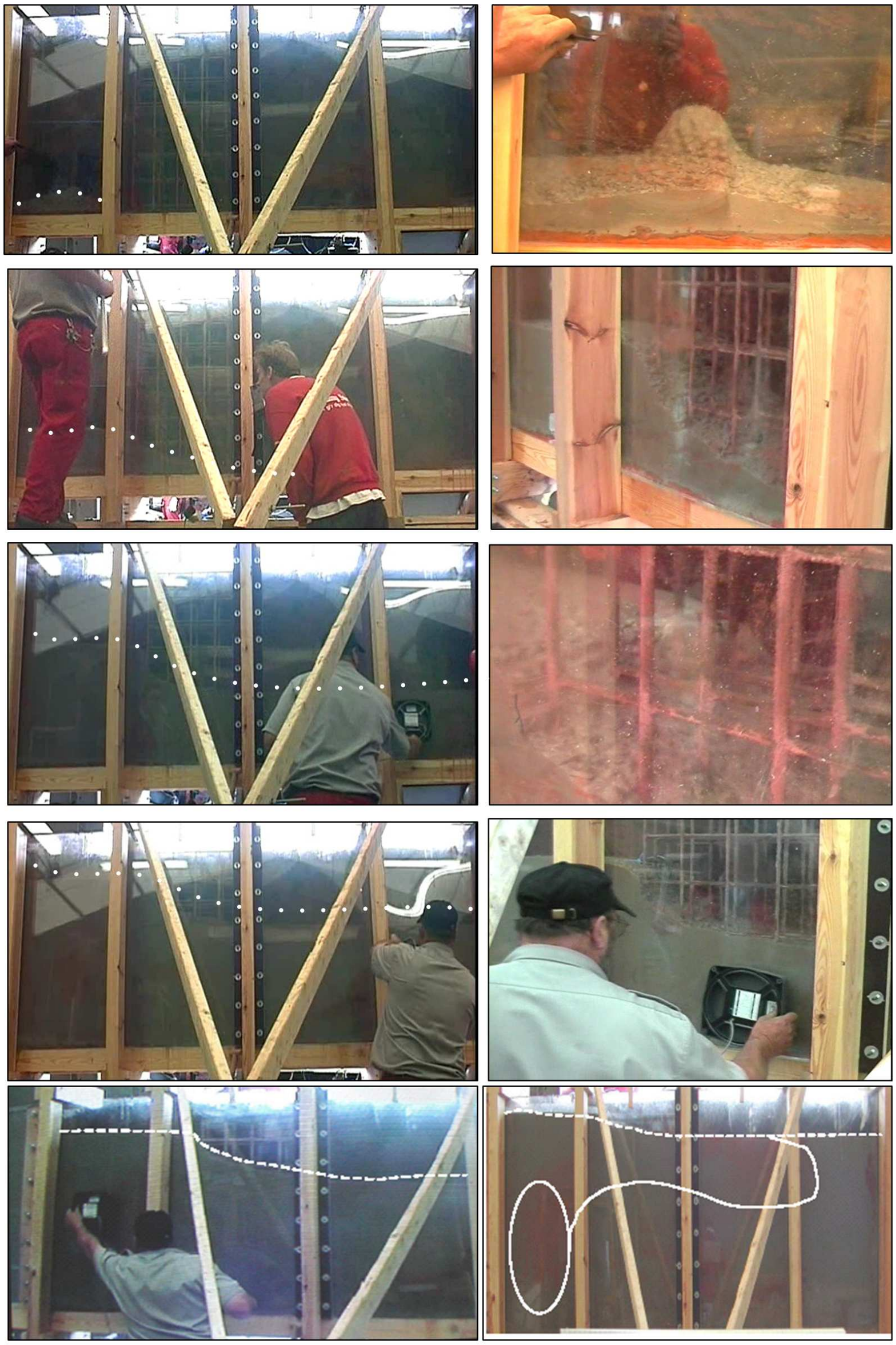

Figure 7.50 *Experimental results of form filling test $FF2$. The location of the free surface during filling and the red concrete after filling is shown.*

The simulation of the free surface is shown in Figure 7.51 and 7.52. The same filling rate have been applied in tests $FF1$ and $FF2$. It is observed that the time it takes for the fluid to reach the end wall is about 40 s in test $FF1$ and 60 s in test $FF2$. Even though the rheological properties are slightly different ($FF1$: τ_0=40 Pa, η_{pl}=20 Pa·s and

$FF2$: $\tau_0 = \tau_{s,0}$=50 Pa and $\eta_{pl} = \eta_{s,pl}$=25 Pa·s) the main reason for this is the increased resistance to flow from the reinforcement in $FF2$.

The simulation of the free surface seems to correlate with the experimental observations when taking into account that blocking occurs in the narrow parts of the experiment. For instance, at 56 s the simulation show a similar build-up in front of the reinforcement bars, however, less than in the experiment due to the occurrence of blocking.

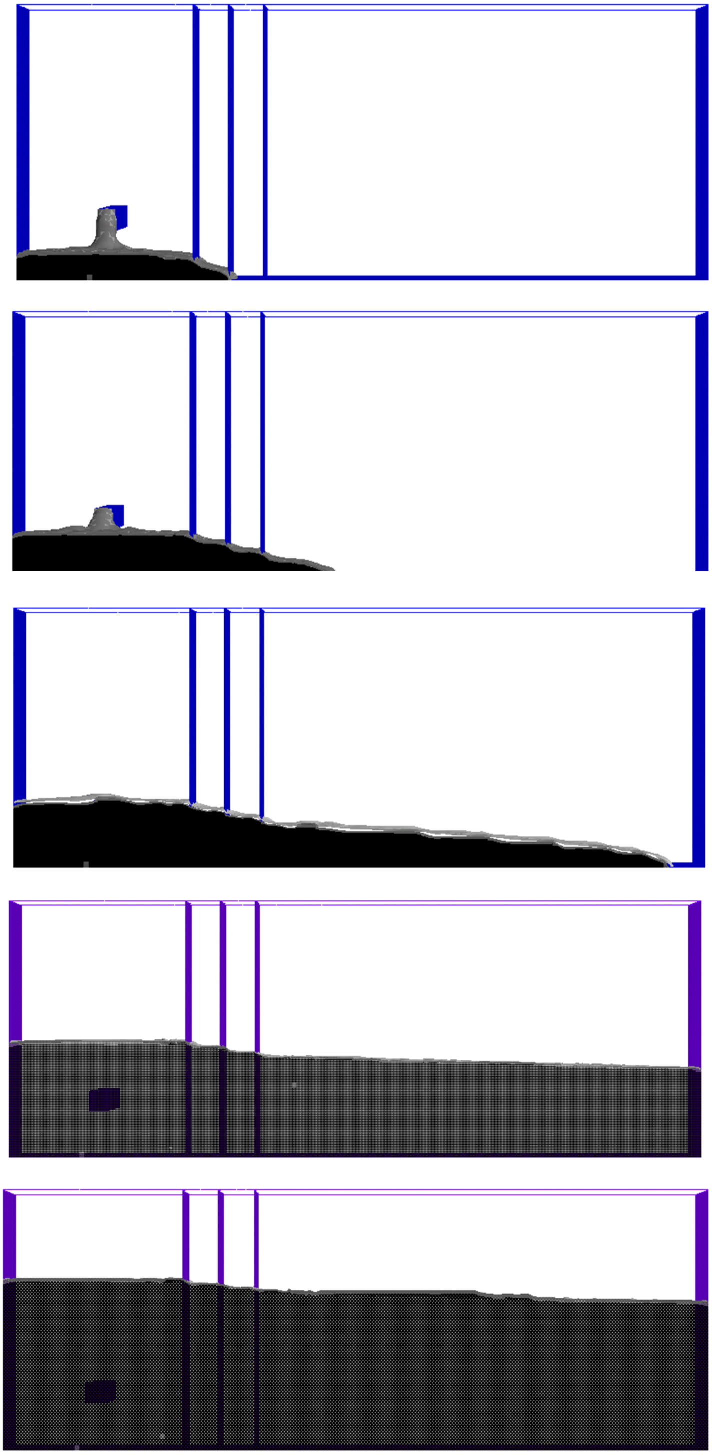

Figure 7.51 *Simulation of form filling test $FF2$ showing the free surface at times 9, 20, 56, 147, and 230 s.*

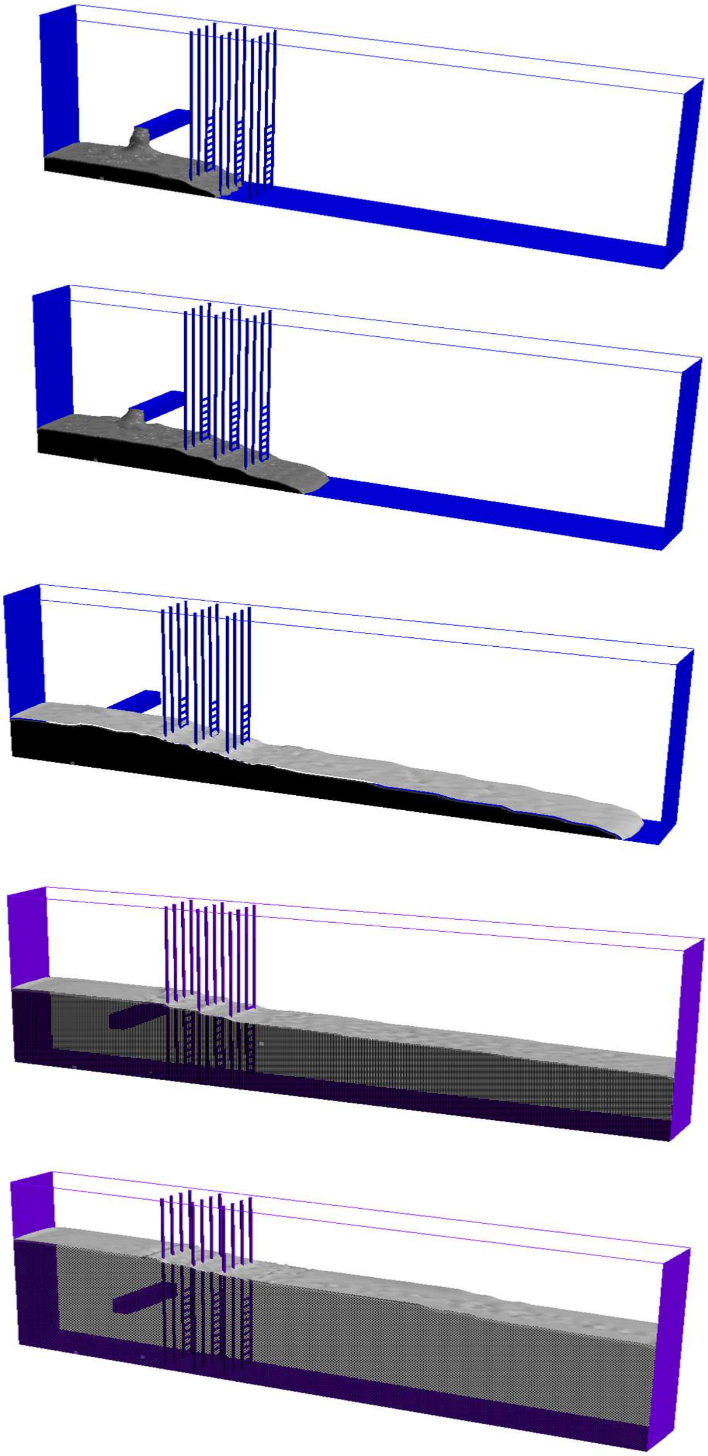

Figure 7.52 *Simulation of form filling test $FF2$ showing the free surface at times 9, 20, 56, 147, and 230 s.*

The procedure for simulating blocking follows the procedures presented earlier for the L-box tests. In the L-box test of concrete mix F_2, the critical velocity was approximately zero for section B_1 (clear spacing of 60 mm) and ∞ for section B_2 (clear spacing of 25 mm). Section B_2 corresponds to the narrow part of the reinforcement configuration in the form filling test. The other part of the reinforcement have a clear spacing of 50 mm. Applying a corresponding radius of $R_{c,2} = 35$ mm and a weighted confinement ratio of $\alpha^* = 4.8$, this gives a critical velocity as a function of the particle volume fraction as shown in Figure 7.53. At a particle volume fraction $\phi_p \approx 0.37$, the critical velocity is approximately U_{crit} =0.005 m/s.

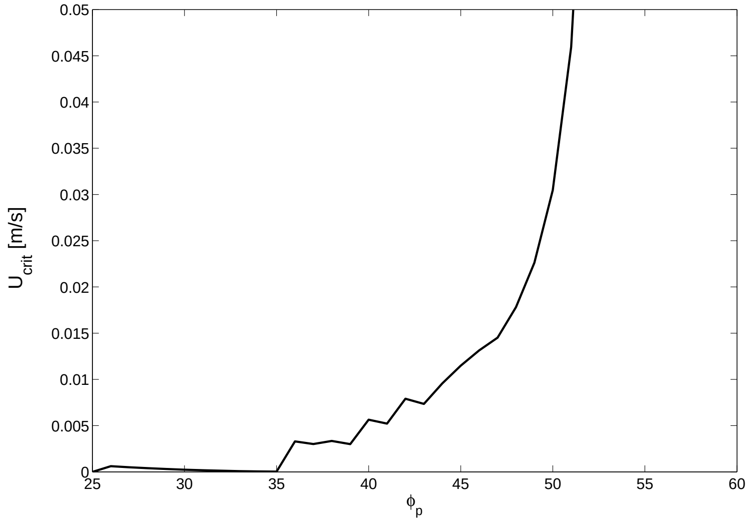

Figure 7.53 *The critical average velocity for the parts of the reinforcement in form filling test $FF2$ with a clear spacing of 50 mm.*

As for the L-box, the average velocity near the reinforcement may be estimated from the homogeneous form filling simulation.

Figure 7.54 shows the velocity field at $t = 9$ s when the concrete has just reached the reinforcement bars. By integration of the velocity field, the flow rate is calculated. Dividing this with the fluid cross-sectional area, this results in an average velocity of 0.050 m/s or approximately 10 times the critical velocity, which corresponds to the experimental observations that did show blocking in this part of the reinforcement configuration.

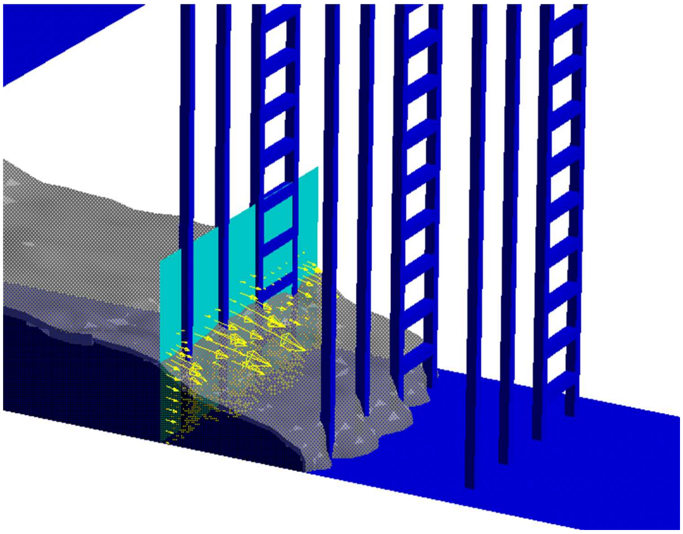

Figure 7.54 *Simulation of form filling test $FF2$ showing the free surface and velocity field in the x-direction near the reinforcement.*

The results have shown a good correlation between the simulation and experiment with regard to the free surface and the theoretical estimate of the risk of blocking. The deviation between the free surface of the simulation and experiment is explained by the occurrence of blocking in the narrow parts of the reinforcement configuration.

The form pressure was measured and the results showed hydrostatic pressure. The filling rate is 10 m/s which corresponds to the results discussed under form filling test $FF1$.

Finally, the use of thermal detectors proved useful for detection of the free surface in the experiment. The results are shown in Appendix D.

Full Scale

The results of five full scale form filling tests are presented. These are referred to as Fu_1, Fu_2, Fu_3, Fu_4, and Fu_5. The casting technique applied for each of these tests is found in Chapter 5.

Two different types of SCC mixes were applied referred to as FuA and FuM. FuA was applied in test Fu_1, Fu_2, and Fu_3. FuM was applied in tests Fu_4 and Fu_5.

The rheological parameters have been estimated based on the slump flow test using setup 1. For the batches tested, the estimates are given in Table 7.10.

Table 7.10 *Estimates of Bingham parameters in full scale tests.*

Test	τ_0 [Pa]	η_{pl} [Pa·s]
Fu_1, Fu_2, Fu_3	20	60
Fu_4	60	35
Fu_5	45	35

The experimental observations on the form filling ability, blocking, dynamic segregation and surface finish are discussed below.

The form geometry and reinforcement configuration did not impose difficulties with respect to obtaining a complete form filling. However, it was observed that when a height of 4 m was reached at the end of the inlet, the surface was inclined towards the other end. This was similar to the observations in the laboratory form filling tests $FF1$ and $FF2$. For tests Fu_1 and Fu_2, the height difference was approximately 2 to 5 cm, and for Fu_4 and Fu_5, it was approximately 10 cm. This is due to a higher yield stress of mixes used for tests Fu_4 and Fu_5.

The form filling applications included a light reinforcement near the formwork sides. Following a procedure similar to the ones presented for the L-box tests, a low critical velocity is estimated at a particle volume fraction of $\phi_p \approx 0.39$ indicating no blocking (weighed confinement ratio of $\alpha^* \approx 4.8$). A picture of the flow near the reinforcement in test Fu_4 is shown in Figure 7.55. Blocking was not observed in any of the form filling tests.

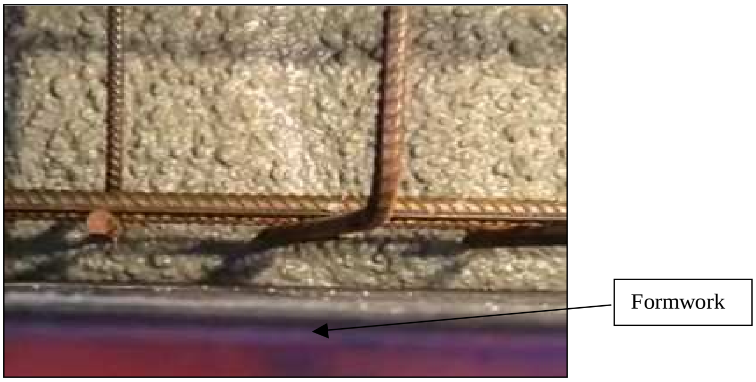

Figure 7.55 *A photo from the casting of form filling test Fu_4 showing flow near the reinforcement. Blocking was not observed in any of the form filling tests.*

Regarding dynamic segregation, it was observed that the casting technique and rheological properties had a significant influence on the risk of dynamic segregation. Figure 7.56 shows pictures of the top surface of test Fu_1 to Fu_3, and Figure 7.57 shows the top surface for Fu_4 and Fu_5. A folding rule was applied to measure the distance from the free surface to the coarse aggregates. The observations on the degree of segregation were later confirmed in drilled core samples from the top of each wall.

For casting of Fu_1 to Fu_3, the results show clear segregation when casting was carried out from the bottom (Fu_3), no segregation when casting was carried out with the inlet placed 0.5 m above the free surface (Fu_2), and some segregation when casting is carried out with the inlet 0.5 m below the free surface (Fu_1). For casting of Fu_4 and Fu_5 segregation was not observed.

The results indicate that the flow patterns have an influence on the risk of dynamic segregation. For instance, casting from the bottom (Fu_3) introduces a flow pattern similar to the one presented for the laboratory form filling test $FF1$ where dynamic segregation was also observed. The flow pattern of test Fu_3 is shown in Figure 7.58 to the left. The upwards flow is reduced when the inlet is placed above the free surface of the concrete which is shown to the right in a simulation of test Fu_5. Here the flow patterns indicate flow in layers.

The effect of the rheological properties may be assessed by comparing tests Fu_1 and Fu_4, which were both cast with the inlet placed 0.5 m below the free surface. Dynamic segregation was not observed in Fu_4, which is likely due to a higher yield stress of $\tau_0 =$ 60 Pa compared to $\tau_0 = 20$ Pa in test Fu_1.

Fu$_1$: Folding rule submerged approximately 5 cm

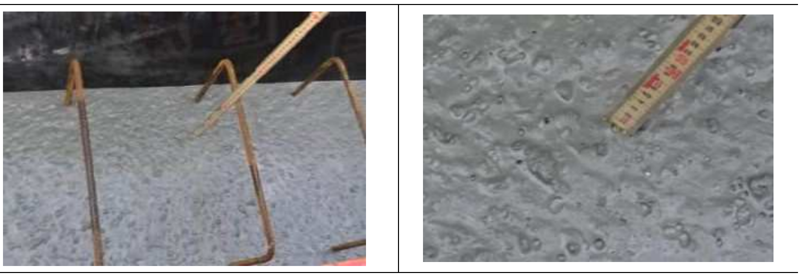

Fu$_2$: Folding rule cannot be submerged. No segregation (aggregates seen at the top)

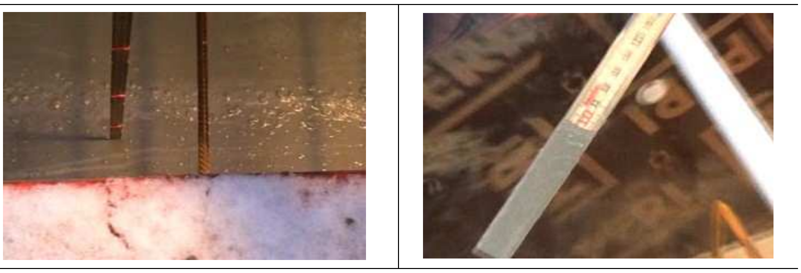

Fu$_3$: Folding rule submerged 10 cm

Figure 7.56 *Photos of the top surface after casting in form filling test Fu_1, Fu_2, Fu_3. A folding rule has been used to indicate the distance between the top surface and the coarse aggregate.*

Fu$_4$: Folding rule cannot be submerged. No segregation (aggregates seen at the top)

Fu$_5$: Folding rule cannot be submerged. No segregation (aggregates seen at the top)

Figure 7.57 *Photos of the top surface after casting in form filling applications Fu_4 and Fu_5. A folding rule has been used to indicate the distance between the top surface and the coarse aggregate.*

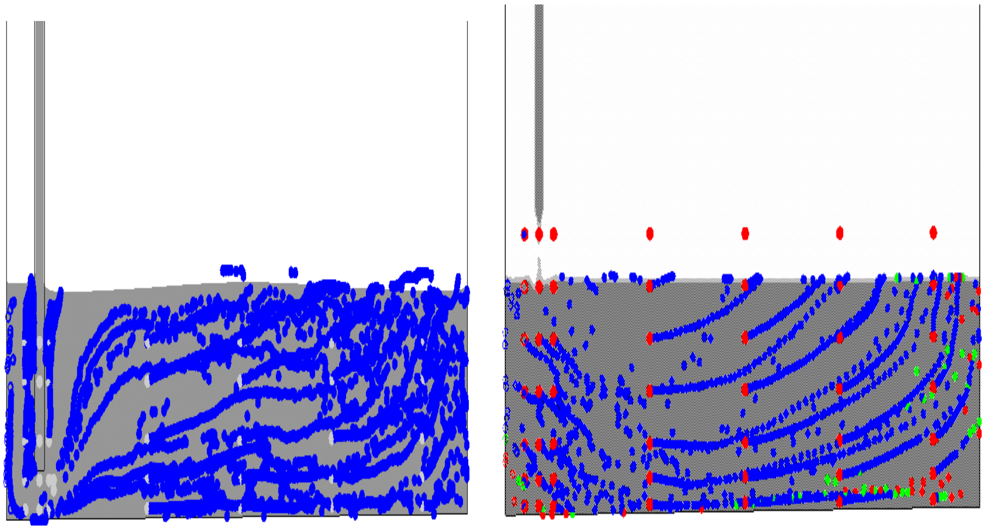

Figure 7.58 *The simulated flow patterns of form filling test* Fu_3 *(left) and* Fu_5 *(right).*

It was also observed that the combined effect of the casting technique and the rheological properties has an influence on the surface finish. The number of air voids was counted in four different sections each of 1 m^2. These were placed approximately 0.7 m from each of the ends. Two were placed 0.5 m above the bottom and two 0.5 m below the top surface. Figure 7.59 shows the total number of air voids categorized according to the pore size.

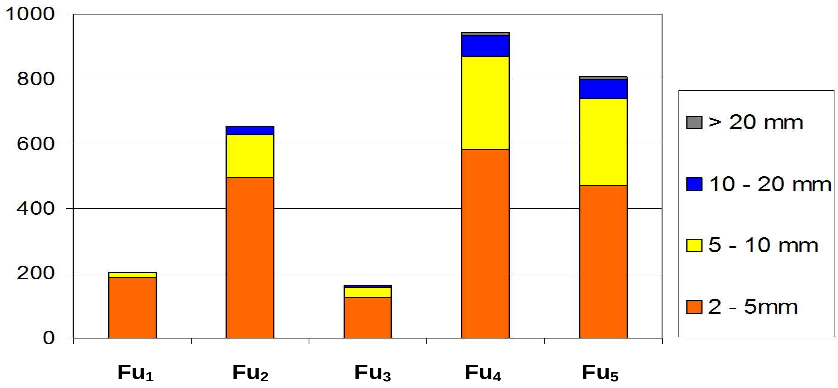

Figure 7.59 *The total number of air voids counted in four sections each of 1* m^2.

The results show that it is positive to cast from the bottom, whereas the highest amount of air voids is obtained when the inlet is placed 0.5 m above the free surface. As it was discussed in form filling test $FF1$, the casting from the bottom imposes a continuous shearing across the formwork, which may generate paste to the surface. When cast with the inlet above the free surface, the flow patterns indicated flow in layers. The extent to which paste is generated to the formwork may depend on the rheological properties. Comparing the results of Fu_1 and Fu_2 with Fu_4 and Fu_5 shows that the highest amount of air voids are obtained in Fu_4 and Fu_5, which had the highest yield stresses.

7.5 Conclusions on Simulation and Testing of SCC Flow

The main conclusions on SCC flow in the slump flow test, the L-box test and the form filling applications are summarized below.

- Consistency between the experimental and simulated flow behavior has been obtained in both the slump flow test setup, L-box and form filling test applying the same set of rheological parameters.
- A reasonable agreement between rheological parameters determined in a viscometer and those applied to simulate the flow has been obtained.
- For assessment of the rheological properties based on the slump flow test or L-box test, complete control of the lifting velocity and a detailed and accurate monitoring of the transient flow behavior are required. Further research are needed to assess the effect of the particle size and the particle volume fraction on the slump flow value and thus the homogeneity assumption. Comparative studies of the slump flow test and the L-box test for various particle sizes and particle volume fractions may be applied to assess the homogeneity assumption.
- Consistency between the experimental and simulated flow patterns in a form filling test without reinforcement has been obtained.
- The theoretical estimate of blocking correlates with the observed behavior in both the L-box and the form filling applications including reinforcement. As expected the macroscopic flow behavior of the experiment and simulations deviate when blocking occurs.
- Results indicate that the risk of dynamic segregation depends on the combined effect of flow patterns and the rheological properties of the mix. The risk is increased when the concrete is forced to flow in a upwards direction against gravity. This may be due to the combined effect of shear induced particle migration and gravity induced segregation due to differences in density. Especially in full-scale applications this tendency was shown.
- Results indicate that the surface quality depends on the combined effect of flow patterns and rheological properties. The best surfaces (no blowholes) are obtained where continuous shearing across the formwork have occurred which may be explained by the the generation of paste to the surface due to particle migration away from the surfaces.

Chapter 8

Conclusions and Future Perspectives

The overall aim of this project has been to simulate form filling with Self-Compacting Concrete. The important form filling characteristics comprise the form filling ability, the flow patterns, and the heterogeneous flow phenomena blocking and dynamic segregation. The focus of this project has been on simulating the form filling ability, the flow patterns and blocking.

A modelling approach has been proposed within the framework of Computational Fluid Dynamics (CFD). The form filling ability and flow patterns describe homogeneous flow characteristics, which has been simulated based on the Bingham rheological parameters and the casting technique.

A phenomenological model have been developed for assessment of blocking introducing a flow rate criterion. Introducing a flow rate criterion in the homogeneous flow simulation provides a tool to assess the risk of blocking near the reinforcement in the formwork. This is done by comparing the average velocity found in the homogeneous simulation with the critical velocity estimated from the blocking model. The blocking model has been derived for flow of a monodisperse suspension in a circular tube and takes into account the rheological properties of the matrix phase, the particle volume fraction, the maximum particle volume fraction, the particle diameter, the particle shape, and the tube radius. When the yield stress of the matrix phase reduces to zero, the flow rate criterion is replaced by a critical particle volume fraction. A reasonable agreement was obtained between the results obtained in a tube flow test and the model behaviour. For assessment of a critical average velocity between reinforcement a so-called corresponding tube radius was introduced and it was applied in the simulations of the flow in the L-box and the form filling applications with reinforcement.

The results of testing and simulating the slump flow test, the L-box test, and the form filling applications have shown:

- Slump flow test and the L-box
    - It is possible to simulate the transient flow, i.e. the spread and the shape of the

free surface when applying correct boundary condition, especially the lifting velocity is important to consider. A reasonable agreement between rheological parameters determined in a viscometer and those applied to simulate the flow has been obtained.

In both tests the validity of the homogeneity assumption depends on the particle size and particle volume fraction. In the slump flow test the particles may affect the slump flow and in the L-box the particles may cause blocking.

Assuming blocking and inertia does not influence the flow in the L-box, the homogeneity assumption of the slump flow test may be assessed by comparing the slump flow SF with the H_2/H_1 ratio in the L-box. For a concrete mixture with a maximum aggregate fraction of 4-8 mm at a particle volume fraction of 0.43 it was found that the same yield stress applied for simulation of the slump flow ($SF \approx 510$ mm) and the H_2/H_1 ratio in the L-box ($H_2/H_1 \approx 0.55$). Further research should include a wider range of particles sizes and particle volume fractions in order to assess limits for the slump flow as a valid estimate of the yield stress. Assessment of the plastic viscosity based on the slump flow test must consider the transient slump flow curve. Especially, the initial part of the slump flow curve is dominated by the plastic viscosity, however, for at slump flows above approximately 300 mm, the yield stress also start to be of importance. Estimating the plastic viscosity based on the slump flow curve requires accurate handling of the boundary conditions in the simulation and an accurate and detailed monitoring of the slump curve during testing. Further research are looking into the most proper way of estimating the plastic viscosity based on the slump flow test.

For the risk of blocking in the L-box, the use of the homogenous flow simulation to derive an average velocity and compare it to the critical average velocity seems to be an applicable approach for assessment of blocking. Reasonable agreement was obtained between the simulations and the experimental observations on blocking.

- Form filling applications
  - It is possible to simulate the form filling ability (the free surface location during filling). Good correlation was obtained between the experimental observations and the simulations with regard to the curvature and flow propagation during filling. For instance, the final sloping behaviour due to the yield stress was obtained. When including reinforcement, the homogenous simulation shows a change in the free surface due to the increased viscous resistance. However, not to the extent which was observed in the experiment which was explained by the occurrence of blocking in the narrow parts of the reinforcement configuration. The estimates of the risk of blocking correlated well with the experimental observations in the two different sections of the reinforcement configuration.

    A good correlation was also obtained between the simulation and experimental observations of the flow patterns. The simulation can be used to assess particle paths and detect possible dead zones.

> Comparing the observations on dynamic segregation and the flow patterns indicates that dynamic segregation is strongly dependent on the flow patterns. Especially the results show that the risk of dynamic segregation increased when forcing the concrete in an upwards direction against gravity. It is expected that dynamic segregation may be back-traced to the combined effect of shear induced particle migration and gravity induced segregation due to differences in density. Through more detailed studies it may be possible to establish a analytical criterion for dynamic segregation in the same way as for blocking.
>
> Comparing the observations on the surface finish and the flow patterns shows that the surface quality is also dependent on the flow patterns. The lowest number of blowholes were obtained where continuous shearing across the surfaces had occurred. It is likely that this may also be back-traced to particle migration. As a results of this, it is interesting to see that the flow patterns preferred to avoid dynamic segregation are those which result in the lowest number of blowholes and vice versa. This was particulary evident in the full-scale castings.

The proposed modelling approach provides a tool to assess the most proper rheological properties, particle configuration and casting technique for a given form filling application e.g. for a future construction like the one showed in Figure 8.1. Especially in vertical structures with a complicated form geometry and reinforcement configuration theoretical models to predict form filling are important. It is often not possible to observe the flow behaviour during casting for which reason the structural quality rely solely on the initial choice of the rheological properties, particle configuration and casting technique.

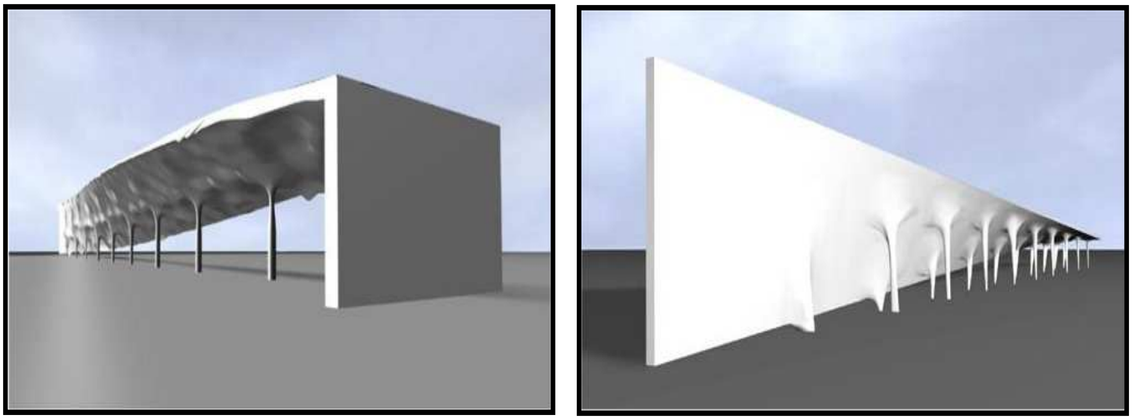

Figure 8.1 *Example of a possible future concrete structure (Christiansen & Dombernowsky 2003).*

The modelling approach may also bring further understanding into the effect of the yield stress and plastic viscosity on the form filling characteristics. This may help to broaden the use of rheology for characterization of the flow properties of SCC and bring it from research and development into the field of practical applications.

Bibliography

2, E. (2002), Eurocode 2: Design of concrete structures. general rules and rules for buildings, Report.

Abbott, J., Tetlow, N., Graham, A., Altobelli, S., Fukushima, E., Mondy, L. & Stephens, T. (1991), 'Experimental observations of particle migration in concentrated suspensions: Couette flow', *Journal of Rheology* **35**(5), 773–795.

Altobelli, S., Fukushima, E. & Mondy, L. (1997), 'Nuclear magnetic resonance imaging of particle migration in suspensions undergoing extrusion', *Journal of Rheology* **41**(5), 1105–1115.

Anderson, J. D., Degrez, D., Dick, E. & Grundmann, R., eds (1995), *Computational Fluid Dynamics - An Introduction*, Springer.

Assaad, J., Khayat, K. & Mesbah, H. (2003), 'Variation of formwork pressure with thixotropy of self-consolidating concrete', *ACI Materials Journal* **100**(1), 29–37.

Banfill, P. (2003), The rheology of fresh cement and concrete - a review, *in* 'Proceedings of 11th International Cement Chemistry Congress, Durban, South Africa, Vol. 1', ed. G. Grieve and G. Owens, pp. 50–62.

Barentin, C., Azanza, E. & Pouligny, B. (2004), 'Flow and segregation in sheared granular slurries', *Europhysics Letters* **66**(1), 139–145.

Barnes, H. (1995), 'A review of the slip (wall depletion) of polymer solutions, emulsions and particle suspensions in viscometers: its cause, character, and cure', *Journal of Non-Newtonian Fluid Mechanics* **56**(3), 221–251.

Barnes, H. A. (1997), 'Thixotropy–a review', *Journal of Non-Newtonian Fluid Mechanics* **70**(1-2), 1–33.

Barnes, H., Hutton, J. & Walters, K., eds (1989), *An Introduction to Rheology*, Elsevier: New York, pp. 212.

Basu, S. (2001), 'Wall effect in laminar flow of non-newtonian fluid through a packed bed', *Chemical Engineering Journal* **81**(1-3), 323–329.

Beaupre, D., Chapdelaine, F., Domone, P., Koehler, E., Shen, L., Sonebi, M., Struble, L., Tenke, D., Wallevik, O. & Wallevik, J. E. (2003), Comparison of concrete rheometers:

International tests at mb (cleveland oh, usa) in may, 2003, Technical report, NISTIR 7154, 47p, National Institute of Standards and Technology, NIST.

Bennenk, I. H. W. (2005), Self-compacting concrete - five years of experience with scc in the netherlands, *in* 'Proceedings of the 18th BIBM International Congress, Amsterdam'.

Beris, A. N., Tsamopoulos, J. A., Armstrong, R. C. & Brown, R. A. (1985), 'Creeping motion of a sphere through a bingham plastic', *Journal of Fluid Mechanics* **158**, 219–244.

Bethmont, S. (2005), Self-compacting concretes (SCC) segregation mechanisms Experimental study of granular interactions, PhD thesis, Laboratorie Central des Ponts et Chaussees, Nantes site of the LCPC, Route de Bouaye BP 4129, France.

Bethmont, S., Schwarzentruber, L., Stefani, C. & Leroy, R. (2003), Defining the stability criterion of sphere suspended in a cement paste: A way to study the segregation risk in self-compacting concrete (scc), *in* 'Proceedings of the 3rd International RILEM Symposium on Self-Compacting Concrete', ed. Ó. Wallevik and I. Nielsson, RILEM Publications S.A.R.L, pp. 94–105.

Billberg, P. (1999), Self-compacting concrete for civil engineering structures - the swedish experience, Report, Swedish Cement and Concrete Research Institute.

Billberg, P. (2003), Form pressure generated by self-compacting concrete, *in* '3rd International Symposium on Self-Compacting Concrete, 17-20 August 2003, Reykjavik, Iceland', ed. Ó. Wallevik and I. Nielsson, RILEM Publications S.A.R.L, pp. 271–280.

Billberg, P. (2005), Development of scc static yield stress at rest and its effect on the lateral form pressure, *in* 'Proceedings of The Second North American Conference on The Design and Use of Self-Consolidating Concrete (SCC) and the Fourth International RILEM Symposium on Self-Compacting Concrete', ed. S.P. Shah, A Hanley Wood Publication, pp. 583–589.

Billberg, P. (2006), Form Pressure Generated by Self-Compacting Concrete - Influence of Thixotropy and Structural Behavior at Rest, PhD thesis, KTH Architecture and the Built Environment, School of Architecture and the Built Environment, Division of Concrete structures, Royal Institute of Technology SE-100 44 Stockholm, Sweden.

Billberg, P. & Osterberg, T., eds (2002), *Självkompakterende betong - Rekommendationer för användning (english: Self-Compacting Concrete - recommendations for using SCC)*, Svenska Betongfrening.

Bird, R. B., Armstrong, R. C. & Hassager, O., eds (1987), *Dynamics of Polymeric Liquids - Volume 1, Fluid Dynamics*, John Wiley and Sons.

Bird, R. B., Stewart, W. E. & Lightfoot, E. N., eds (1960), *Transport Phenomena*, John Wiley and Sons.

Blake, F. (1922), The resistance of packing to fluid flow, *in* 'Transactions, American Institute of Chemical Engineering', Vol. 14, pp. 415–421.

BriteEuram (1997), Improved quality assurance and methods of grouting post-tensioned tendons, Sub-task report, Department of Structural Engineering and Materials, Coordinaters Gifford and Partners LTD.

BriteEuram (2000), Rational production and improved working environment through using self compacting concrete, report, Brite EuRam Project, Final report of Subtask 8.5.

Buckingham, E. (1921), *in* 'Proceedings of ASTM', Vol. 117, pp. 1154–1161.

Bui, V. K. (1994), A method for the optimum proportioning of the aggregate phase of highly durable vibration-free concrete, Master's thesis, Asian Institute of Technology, Bangkok, Thailand.

Buscall, R., Mills, P. D. A., Stewart, R. F., Sutton, D., White, L. R. & Yates, G. E. (1987), 'The rheology of strongly-flocculated suspensions', *Journal of Non-Newtonian Fluid Mechanics* **24**(2), 183–202.

Candau, F., Buchert, P. & Krieger, I. (1990), 'Rheological studies on inverse microlatices', *Journal of Colloid and Interface Science* **140**(2), 466–473.

Carlsward, J. (2003), Use of scc for housing applications - experience from case studies in stockholm, *in* 'Nordic Mini-Seminar on the Form Filling Ability of Self-Compacting Concrete, Taastrup, Denmark', Vol. 1, ed. L.N. Thrane, Danish Technological Institute, pp. 16–20.

Carman, P. C. (1937), Fluid flow through granular beds, *in* 'Transactions of the Institute of Chemical Engineers, London', Vol. 15a, pp. 150–166.

Chase, G. & Dachavijit, P. (2005), 'A correlation for yield stress fluid flow through packed beds', *Rheologica Acta* **44**(5), 495–501.

Cheng, D. (1987), 'Thixotropy', *International Journal of Cosmetic Science* **9**, 151–191.

Cheng, D. & Evans, F. (1965), 'Phenomenological characterization of the rheological behaviour of inelastic reversible thixotropic and antithixotropic fluids', *British Journal of Applied Physics* **16**(11).

Chow, A., Sinton, S., Iwamiya, J. & Stephens, T. (1994), 'Shear-induced particle migration in couette and parallel-plate viscometers: Nmr imaging and stress measurements', *Physics of Fluids* **6**(8), 2561–2576.

Christensen, G. (1991), Modelling the Flow of Fresh Concrete: The slump test, PhD thesis, Princeton University.

Christiansen, K. & Dombernowsky, P. (2003), presented by S. Rottig at the Nordic Mini-Seminar on the Form Filling Ability of Self-Compacting Concrete under the subject "Self-Compacting Concrete - A Major Breakthrough", November 3-4, ed. L.N. Thrane, Danish Technological Institute, Taastrup, Denmark.

Chu, H., Machida, A. & Suzuki, N. (1996), 'Experimental investigation and dem simulation of filling capacity of fresh concrete', *Transactions of the Japan Concrete Institute* **18**, 9–14.

Chung, T. J., ed. (1978), *Finite Element Analysis in Fluid Dynamics*, 1 edn, McGraw-Hill, Inc.

Clayton, S., Grice, T. & Boger, D. (2003), 'Analysis of the slump test for on-site yield stress measurement of mineral suspensions', *International Journal of Mineral Processing* **70**(1-4), 3–21.

Cleary, P. (1998), 'Discrete element modelling of industrial granular flow applications', *TASK Quarterly* **2**(3), 385–415.

Cohen, Y. & Metzner, A. (1981), 'Wall effects in laminar flow of fluids through packed beds', *AIChE Journal* **27**(5), 705–715.

Collepardi, M. (1998), *Cement & Concrete Composites* **20**(2), 103–112.

Coussot, P. & Ancey, C. (1999), 'Rheophysical classification of concentrated suspensions and granular pastes', *Physical Review E (Statistical Physics, Plasmas, Fluids, and Related Interdisciplinary Topics)* **59**(4), 4445–4457.

Coussot, P., Nguyen, Q., Huynh, H. & Bonn, D. (2002), 'Viscosity bifurcation in thixotropic, yielding fluids', *Journal of Rheology* **46**(3), 573–589.

Coussot, P., Proust, S. & Ancey, C. (1996), 'Rheological interpretation of deposits of yield stress fluids', *Journal of Non-Newtonian Fluid Mechanics* **66**(1), 55–70.

Cundall, P. A. & Strack, O. D. L. (1979), 'A discrete numerical model for granular asemblies', *Geotechnique* **29**(1), 47–64.

Darcy, H. P. G., ed. (1856), *Les Fontaines Publiques de La Ville de Dijon*, Victor Dalamont, Paris.

Delhaye, N., Poitou, A. & Chaouche, M. (2000), 'Squeeze flow of highly concentrated suspensions of spheres', *Journal of Non-Newtonian Fluid Mechanics* **94**, 67–74.

Dunschede, S. (2004), Untersuchungen zum einfluss von zement, fullern und fliessmitteln auf die rheologie von zementleimen, Master's thesis, Laboratory for Concrete and Construction Chemistry, EMPA.

Efnarc (2002), Specification and guidelines for scc, www.efnarc.org, Efnarc publications.

engnet.anu.edu.au (2006), Pourbaix diagrams, homepage, http://engnet.anu.edu.au /DEcourses/engn4520/Pourbaix.pdf, assessed december 2006.

Epstein, B., Peigin, S. & Tsach, S. (2006), 'A new efficient technology of aerodynamic design based on cfd driven optimization', *Aerospace Science and Technology* **10**(2), 100–110.

Ergun, S. (1952), 'Fluid flow through packed columns', *Chemical Engineering Progress* **48**(2), 89–94.

ermco.org (2005), 'European ready-mixed concrete industry statistics, assessed in 2005', www.ermco.org.

E.S.Boek, Coveney, P., Lekkerkerker, H. & Schoot, P. (1997), 'Simulating the rheology of dense colloidal suspensions using dissipative particle dynamics', *Physical Review E (Statistical Physics, Plasmas, Fluids, and Related Interdisciplinary Topics)* **55**(3), 3124–3133.

Fand, R. M. & Thinakaran, R. (1990), 'The influence of the wall on flow through pipes packed with spheres', *Journal of Fluids Engineering* **112**, 84–88.

Fernandez-Altable, V. & Casanova, I. (2006), 'Influence of mixing sequence and superplasticiser dosage on the rheological response of cement pastes at different temperatures', *Cement and Concrete Research* **36**(7), 1222–1230.

Ferraris, C. F., Brower, L. E., Banfill, P., Beaupre, D., Chapdelaine, F., de Larrard, F., Domone, P., Nachbaur, L., Sedran, T., Wallevik, O. & Wallevik, J. E. (2000), Comparison of concrete rheometers: International tests at lcpc (nantes, france) in october, 2000, Technical report, NISTIR 6819, 156p, National Institute of Standards and Technology, NIST.

Ferraris, C. F., Larrard, F. & Martys, N. (2001), Fresh concrete rheology: Recent developments, *in* 'Materials Science of Concrete VI. Proceedings. American Ceramic Society', ed. S. Mindess and J. Skalny, American Ceramic Society, Westerville, OH, pp. 215–241.

Ferraris, C. F. & Martys, N. (2003), 'Relating fresh concrete viscosity measurement from different rheometers', *Journal of Research of the National Institute of Standards and Technology* **108**(3), 229–234.

FIDAP (2000), *Fidap Manual*, 7.0 edn, Fluent, 416 64 Goteborg, Sweden.

Fieldview, M. (2002), *Fieldview, Users Guide*, 8.1 edn, Intelligent Light, Intelligent Light, 1290 Wall Street West, Lyndhurst, NJ 07071.

Flatt, R. J. (2004*a*), 'Dispersion forces in cement suspensions', *Cement and Concrete Research* **34**(3), 399–408.

Flatt, R. J. (2004*b*), 'Towards prediction of superplasticized concrete rheology', *Materials and Structures/Materiaux et Constructions* **37**(239), 289–300.

Fortin, J., Millet, O. & d. Saxce, G. (2005), 'Numerical simulation of granular materials by an improved discrete element method', *International Journal for Numerical Methods in Engineering* **62**(5), 639–663.

Frandsen, J. & Schultz, K.-I. (1997), Investigation of poker vibration, Report no. 89, Danish Road Directorate, Ministry of Transport.

Frankel, N. & Acrivos, A. (1967), 'On the viscosity of a concentrated suspension of solid spheres', *Chemical Engineering Science* **22**(6).

Gadala-Maria, F. & Acrivos, A. (1980), 'Shear-induced structure in a concentrated suspension of solid spheres.', *Journal of Rheology* **24**(6), 799–814.

Gardner, M., ed. (1966), *New Mathematical Diversions from Scientific American*, 1 edn, New York, Simon and Schuster.

Geiker, M., Brandl, M., Thrane, L. N., Bager, D. H. & Wallevik, O. (2002), 'The effect of measuring procedure on the apparent rheological properties of self-compacting concrete', *Cement and Concrete Research* **22**(11), 1791–1795.

Geiker, M., Brandl, M., Thrane, L. N. & Nielsen, L. F. (2002), 'On the effect of coarse aggregate fraction and shape on the rheological properties of self-compacting concrete', *Cement, Concrete and Aggregates* **24**(1), 3–6.

Glavind, M. & Frederiksen, J. O. (2001), 'Formtryk og selvkompakterende beton (in english: form pressure and self-compacting concrete)', *Dansk Beton* **4**.

Goldsmith, H. & Mason, S. (1962), 'The flow of suspensions through tubes. i. single spheres, rods, and discs', *Journal of Colloid Science* **17**(5), 448–476.

Graham, A., Altobelli, S., Fukushima, E., Mondy, L. & Stephens, T. (1991), 'Nmr imaging of shear-induced diffusion and structure in concentrated suspensions undergoing couette flow', *Journal of Rheology* **35**(1), 191–201.

Gregory, J. (1981), 'Flocculation in laminar tube flow', *Chemical Engineering Science* **36**(11), 1789–1794.

Gresho, P. M. & Sani, R. L., eds (2000), *Incompressible Flow and the Finite Element Method, Volume 2, Isothermal Laminar Flow*, John Wiley and Sons Ltd.

Hackley, V. A. & Ferraris, C. F. (2001), Guide to rheological nomenclature: Measurements in ceramic particulate systems, Special publication 946, National Institute of Standards and Technology, NIST.

Hampton, R., Mammoli, A., Graham, A., Tetlow, N. & Altobelli, S. (1997), 'Migration of particles undergoing pressure-driven flow in a circular conduit', *Journal of Rheology* **41**(3), 621–640.

Han, M., Kim, C., Kim, M. & Lee, S. (1999), 'Particle migration in tube flow of suspensions', *Journal of Rheology* **43**(5), 1157–1174.

Hasholt, M. T., Pade, C. & Winnefeld, F. (2005), A conceptual and mathematical model for the flowability of scc, *in* 'Proceedings SCC 2005, the second North American Conference on the Design and Use of Self-Consolidating Concrete (SCC) and the Fourth International RILEM Symbosium on Self-Compacting Concrete', ed. S. P. Shah, A Hanley Wood Production, pp. 641–647.

Hattori, K. & Izumi, K. (1990), A new viscosity equation for non-newtonian suspensions and its application, *in* 'Rheology of Fresh Cement and Concrete, Proceedings of the Int. Conference organized by the British Society of Rheology, University of Liverpool, UK, March 1990', ed. P. F. G. Banfill, E.F.N. Spon, pp. 83–92.

Hayes, R., Afacan, A., Boulanger, B. & Shenoy, A. (1996), 'Modelling the flow of power law fluids in a packed bed using a volume-averaged equation of motion', *Transport in Porous Media* **23**(2), 175–196.

Helmuth, R., Mills, L. M., Whiting, D. A. & Bhattacharja, S. (1995), Abnormal concrete performance in the presence of admixtures, Technical report, Research and Development Information, Portland Cement Associtation.

Herholdt, A., Justesen, C., Christensen, P. & Nielsen, A., eds (1985), *Beton Bogen*, Aalborg Portland CTO.

Hinch, E. & Leal, L. (1972), 'The effect of brownian motion on the rheological properties of a suspension of non-spherical particles', *Journal of Fluid Mechanics* **52**, 683–712.

Hirt, C. & Nichols, B. (1981), 'Volume of fluid (vof) method for the dynamics of free boundaries', *Journal of Computational Physics* **39**(1), 201–225.

Hohenemser, K. & Prager, W. (1932), 'On the construction of mechanics of isotropic continua', *ZAMM* **12**, 216–226.

Hong, D. & McLennan, J. (1992), 'Molecular dynamics simulations of hard sphere granular particles', *Physica A* **187**(1-2), 159–171.

Hu, C. & Larrard, F. (1996), 'The rheology of fresh high-performance concrete', *Cement and Concrete Research* **26**(2), 283–294.

Jacobsen, T. B. (2004), *Private communication*, Danish Technological Institute.

Jaeger, H. M. & Nagel, S. R. (1992), 'Physics of the granular state', *Science* **255**(5051), 1523–1531.

Jalali, P. & Li, M. (2004), 'An estimate of random close packing density in monodisperse hard spheres', *Journal of Chemical Physics* **120**(2), 1138–1139.

Jie, P. & Zhu, K. Q. (2006), 'Drag force of interacting coaxial spheres in viscoplastic fluids', *Journal of Non-Newtonian Fluid Mechanics* **135**(2-3), 83–91.

Kapur, P. C., Scales, P. J., Boger, D. V. & Healy, T. W. (1997), 'Yield stress of suspensions loaded with size distributed particles', *AIChE Journal* **43**(5), 1171–1179.

Karnis, A., Goldsmith, H. & Mason, S. (1966), 'The kinetics of flowing dispersions. i. concentrated suspensions of rigid particles', *Journal of Colloid and Interface Science* **22**(6).

Kemblowski, Z. & Michniewicz, M. (1979), 'A new look at the laminar flow of power law fluids through granular beds', *Rheologica Acta* **18**(6), 730–739.

Kieffer, W., Moujaes, S. & Armbya, N. (2006), 'Cfd study of section characteristics of formula mazda race car wings', *Mathematical and Computer Modelling* **43**(11-12), 1275–1287.

Kitaoji, H., Tanigawa, Y., Mori, H., Kurokawa, Y. & Urano, S. (1996), 'Flow simulation of fresh concrete cast in wall structure by viscoplastic divided element method', *Transactions of the Japan Concrete Institute* **18**, 45–52.

Ko, F. & Mei, C. (1989), 'Slow spreading of a sheet of bingham fluid on an inclined plane', *Journal of Fluid Mechanics* **207**, 505–529.

Koelman, J. M. V. A. & Hoogerbrugge, P. J. (1993), 'Dynamic simulation of hard-sphere suspension under steady shear', *Europhysics* **363**(21).

Koh, C., Hookham, P. & Leal, L. (1994), 'An experimental investigation of concentrated suspension flows in a rectangular channel', *Journal of Fluid Mechanics* **266**, 1–32.

Kozeny, J. (1927), 'Uber die kapillare leitung des wassers in boden', *Sitzungsberichte Akademie der Wissenschaft Wien Math-naturw* **139**, 271–306.

Kozicki, W., Hsu, C. & Tiu, C. (1967), 'Non-newtonian flow through packed beds and porous media', *Chemical Engineering Science* **22**(4).

Krieger, I. (1972), 'Rheology of monodisperse latices', *Advances in Colloid and Interface Science* **3**(2), 111–136.

Kruif, C., van Iersel, E., Vrij, A. & Russel, W. (1985), 'Hard sphere colloidal dispersions: viscosity as a function of shear rate and volume fraction', *Journal of Chemical Physics* **83**(9), 4717–4725.

Kruse, D. & Lemmon, R. (2005), 'Using the discrete element method as an everyday design tool', *Bulk Solids Handling* **25**(6), 358–367.

Kurokawa, Y., Tanigawa, Y., Mori, H. & Nishinosono, Y. (1996), 'Analytical study on effect of volume fraction of coarse agregate on binghams constants of fresh concrete', *Transactions of the Japan Concrete Institute* **18**, 37–44.

Kurokawa, Y., Taniwawa, Y., Kim, W. & Teranishi, K. (1995), 'Evaluation method of passability of high-fluidity concrete', *Transactions of the Japan Concrete Institute* **17**, 9–16.

Kurokawa, Y., Taniwawa, Y., Mori, H. & Komura, R. (1994), 'A study on the slump test and slump-flow test of fresh concrete', *Transactions of the Japan Concrete Institute* **16**, 25–32.

Lafarge.com (2005), www.lafarge.com, assessed oktober 2006.

Lai, W., Rubin, D. & Krempl, E., eds (1996), *Introduction to Continuum Mechanics, third edition*, 1 edn, Butterworth Heinemann.

Langston, P., Al-Awamleh, M., Fraige, F. & Asmar, B. (2004), 'Distinct element modelling of non-spherical frictionless particle flow', *Chemical Engineering Science* **59**(2), 425–435.

Larrard, F., ed. (1999), *Concrete Mixture Proportioning: a Scientific Approach*, 1 edn, Modern Concrete Technology Series, E FN SPON, London.

Larrard, F., Ferraris, C. F. & Sedran, T. (1998), 'Fresh concrete: A herschel-bulkley material', *Materials and Structures* **31**, 494–498.

Larson, R. G., ed. (1999), *The Structure and Rheology of Complex Fluids*, 1 edn, Oxford University Press, New York.

Lauritsen, I. & Thrane, L. (2003), Use of scc in prefabricated concrete elements - examples and observations, *in* 'Nordic Mini-Seminar on the Form Filling Ability of Self-Compacting Concrete, Taastrup, Denmark', Vol. 1, ed. L.N. Thrane, Danish Technological Institute, pp. 50–57.

Leemann, A., Hoffmann, C. & Winnefeld, F. (2006), 'Formwork - pressure of self-consolidating concrete on formwork - high pressures justify caution in formwork design', *Concrete International - the Magazine of the American Concrete Institute* **28**(2), 27–32.

Leighton, D. & Acrivos, A. (1987), 'The shear-induced migration of particles in concentrated suspensions', *Journal of Fluid Mechanics* **181**, 415–439.

Lewis, R., C., S. N. & Taylor (1997), 'A mixed lagrangian-eulerian approach to modelling fluid flow during mould filling', *International Journal for Numerical Methods in Fluids* **25**(8), 931–952.

Lewis, R. W., Postek, E. W., Han, Z. & Gethin, D. T. (2006), 'A finite element model of the squeeze casting process', *International Journal of Numerical Methods for Heat and Fluid Flow* **16**(5), 539–572.

Lin, C. & Miller, J. (1999), 'Network analysis of filter cake pore structure by high resolution x-ray microtomography', *Chemical Engineering Journal* **77**(1-2), 79–86.

Lin, X. & Ng, T. (1995), 'Contact detection algorithms for three dimensional ellipsoids in discrete element modelling', *International Journal for Numerical and Analytical Methods in Geomechanics* **19**(9), 653–660.

Liu, B., Muller, S. & Denn, M. (2003), 'Interactions of two rigid spheres translating collinearly in creeping flow in a bingham material', *Journal of Non-Newtonian Fluid Mechanics* **113**(1), 49–67.

Luoma, J. & Voller, V. (2000), 'An explicit scheme for tracking the filling front during polymer mold filling', *Applied Mathematical Modelling* **24**(8-9), 575–590.

Martys, N. & Farraris, C. F. (2002), Simulation of scc flow, *in* 'Proceedings of 1st North American Conference On the Design and Use of Self-Consolidating Concrete', Centre for Advanced Cement Based Materials, North Western University, Chicago IL., Washington: Hanley-Wood, pp. 27–30.

Martys, N. S. & Mountain, R. D. (1999), 'Velocity verlet algoritm for dissipative-particle-dynamics-based model of suspensions', *Physical Review E* **59**(3), 3733–3736.

Matveev, A., Barysheva, L., Koptyug, I., Khanaev, V. & Noskov, A. (2006), 'Investigation of fine granular material flow through a packed bed', *Chemical Engineering Science* **61**(8), 2394–2405.

McMahon, T. & Parker, R. (1975), 'Particles in tube flow at moderate reynolds number', *Transactions of the Society of Rheology* **19**(3), 445–456.

Mehta, D. & Hawley, M. (1969), 'Wall effect in packed columns', *Industrial and Engineering Chemistry, Process Design and Development* **8**(2), 280–282.

Mehta, P. (2002), 'Sustainability - greening of the concrete industry for sustainable development - concrete's environmental impact and implications for the future', *Concrete International - Design and Construction* **24**(7), 23–29.

Mirbagheri, S., Shrinparvar, M., Ashory, H. & Davami, P. (2004), 'Simulation of surface roughness on the flow pattern in the casting process', *Materials and Design* **25**(8), 655–661.

Montillet, A. (2004), 'Flow through a finite packed bed of spheres: A note on the limit of applicability of the forchheimer-type equation', *Journal of Fluids Engineering, Transactions of the ASME* **126**(1), 139–143.

Moore, F. (1959), 'Rheology of ceramic slips and bodies', *British Ceramic Society – Transactions* **58**(7), 470–492.

Moraczewski, T., Tang, H. & Shapley, N. C. (2005), *Journal of Rheology* **49**(6), 1409–1428.

Mori, H. & Tanigawa, Y. (1992), 'Simulation methods for fluidity of fresh concrete', *Memoirs of the School of Engineering, Nagoya University* **44**(1), 71–134.

Mujumdar, A., Beris, A. N. & Metzner, A. B. (2002), 'Transient phenomena in thixotropic systems', *Journal of Non-Newtonian Fluid Mechanics* **102**(2), 157–178.

Murata, J. (1984), 'Flow and deformation of fresh concrete', *Materials and Structures* **98**(3), 117–129.

Neville, A. & Brooks, J., eds (1990), *Concrete Technology, Revised*, Longman Scientific & Technical.

Nguyen, T., Roussel, N. & Coussot, P. (2006), 'Correlation between l-box test and rheological parameters of a homogeneous yield stress fluid', *Cement and Concrete Research* **36**(10), 1789–1796.

Nielsen, C. V. (2006), Arbejdsmiljø og scc (in english: Working environment and scc), report, Danish SCC Consortium, Danish Technological Institute.

Nielsen, L. F. (2003), Composite materials - mechanical and physical behavior as influenced by phase geometry, Report series r, Department of Civil Engineering Technical University of Denmark.

Nielsson, I. & Wallevik, O. H. (2003), Rheological evaluation of some empirical test methods - preliminary results, *in* 'Proceedings of the 3rd International Symposium on SCC, Reykjavik', ed. Ó. Wallevik and I. Nielsson, RILEM Publications S.A.R.L, pp. 59–69.

Noguchi, T., Oh, S. G. & Tomosawa, F. (1999), Rheological approach to passing ability between reinforcing bars of self-compacting concrete, *in* 'Proceedings of the First International RILEM Symposium on Self-Compacting Concrete', ed. Ä. Skarendahl and Ö.Petersson, Rilem Publications, pp. 59–70.

Noor, M. A. & Uomoto, T. (1999), Three-dimensional discrete element simulation of rheology tests of self-compacting concrete, *in* 'Proceedings of the first International RILEM Symposium on Self-Compacting Concrete', ed. Ä. Skarendahl and Ö.Petersson, Rilem Publications, pp. 35–46.

Oh, S. G., Noguchi, T. & Tomosawa, F. (1999), Toward mix design for rheology of self-compacting concrete, *in* 'Proceedings of the First International RILEM Symposium on Self-Compacting Concrete', ed. Ä. Skarendahl and Ö.Petersson, Rilem Publications, pp. 361–372.

Okamura, H. & Ouchi, M. (2003), 'Self compacting concrete development, applications, and investigations', *Journal of Advanced Concrete Technology, Japan Concrete Institute* **1**(1), 5–15.

Oldroyd, J. G. (1947), A rational formulation of the equations of plastic flow for a bingham solid, *in* 'Proceedings of Camb. Phil. Soc.', Vol. 43, pp. 100–105.

Olsen, M. K., Thrane, L. N., Nielsen, J. B. & Brandl, M. (2001), 'Model for selvkompakterende beton (in english: Model for self-compacting concrete)', *Dansk Beton* **5**(4), 10–11.

Österberg, T. (2002), The use of scc in the södra länken project, *in* 'Proceedings of the First North American Conference on the Design and Use of Self Consolidating Concrete', Centre for Advanced Cement Based Materials, North Western University, Chicago IL., Washington: Hanley-Wood.

Ouchi, M. (1999), 'Self compacting concrete development, applications, and investigations', *Proceedings of the 17th Nordic Concrete Research Symposium, Reykjavik* pp. 29–34.

Ouchi, M., Nakamura, S. A., Österberg, T., Hallberg, S. & Lwin, M. (2003), 'Applications of self compacting concrete in japan, europe and the united states', *US Department of Transportation, Federal Highway Administration, assessed http://www.fhwa.dot.gov/BRIDGE/scc.htm in 2006* (ISHPC).

Ovarlez, G., Bertrand, F. & Rodts, S. (2006), 'Local determination of the constitutive law of a dense suspension of noncolloidal particles through magnetic resonance imaging', *Journal of Rheology* **50**(3), 259–292.

Ovarlez, G. & Roussel, N. (2006), 'A physical model for the prediction of lateral stress exerted by self-compacting concrete on formwork', *Materials and Structures/Materiaux et Constructions* **39**(286), 269–279.

Pade, C. (2006), private communication.

Pandya, V., Bhuniya, S. & Khilar, K. C. (1998), 'Existence of a critical particle concentration in plugging of a packed bed', *AIChE Journal* **44**(4), 978–981.

Papir, Y. & Krieger, I. (1970), 'Rheological studies on dispersions of uniform colloidal spheres - ii. dispersions in nonaqueous media', *Journal of Colloid and Interface Science* **34**(1), 126–130.

Papo, A. (1988), 'Thixotropic behavior of white portland cement pastes', *Cement and Concrete Research* **18**(4), 595–603.

Pashias, N., Boger, D. V., Summers, J. & Glenister, D. J. (1996), 'A fifty cent rheometer for yield stress measurement', *Journal of Rheology* **40**(6), 1179–1189.

Petersson, O. (2003), Simulation of self-compacting concrete laboratory experiments and numerical modeling of testing methods, j-ring and l-box tests, *in* 'Proceedings of the third International RILEM Symposium on Self-Compacting Concrete', ed. Ó. Wallevik and I. Nielsson, RILEM Publications S.A.R.L, pp. 202–207.

Petersson, O. & Hakami, H. (2001), Simulation of scc laboratory experiments and numerical modeling of slump flow and l-box tests, *in* 'Proceedings of the Second International Symposium on Self-Compacting Concrete, Tokyo', ed. K. Ozawa and M. Ouchi, Coms Engineering Corporation, pp. 79–88.

Phan, T. & Chaouche, M. (2005), 'Rheology and stability of self-compacting concrete cement', *Applied Rheology* **15**(5), 336–343.

Phillips, R., Armstrong, R., Brown, R., Graham, A. & Abbott, J. (1992), 'A constitutive equation for concentrated suspensions that accounts for shear-induced particle migration', *Physics of Fluids A (Fluid Dynamics)* **4**(1), 30–40.

Piau, J.-M. (2005), 'Axisymmetric slump and spreading of cohesive plastic soft materials: A yield stress measurement by consisto-rheometry', *Journal of Rheology* **49**(6), 1253–1276.

Poitou, A. & Racineux, G. (2001), 'A squeezing experiment showing binder migration in concentrated suspensions', *Journal of Rheology* **45**(3), 609–625.

Quoc, L., Zhang, X. & Walton, O. (2000), 'A 3-d discrete-element method for dry granular flows of ellipsoidal particles', *Computer Methods in Applied Mechanics and Engineering* **187**(3-4), 483–528.

Ramachandran, V., Venkatesan, R., Tryggvason, G. & Fogler, H. S. (2000), 'Low reynolds number interactions between colloidal particles near the entrance to a cylindrical pore', *Journal of Colloid and Interface Science* **229**, 311–322.

Reiner, M. & Riwlin, R. (1927), 'Uber die stromung einer elastische flussigkeit im couette apparat', *Kolloid-Z* **43**, 1–5.

Rottig, S. (2003), Self-compacting concrete - a major breakthrough, *in* 'Nordic Mini-Seminar on the Form Filling Ability of Self-Compacting Concrete, Taastrup, Denmark', Vol. 1, ed. L.N. Thrane, Danish Technological Institute, pp. 1–8.

Rough, S. L., Wilson, D. I. & Bridgwater, J. (2002), 'A model describing liquid phase migration within an extruding microcrystalline cellulose paste', *Chemical Engineering Research and Design* **80**(Part A), 701–714.

Roussel, N. (2004), 'Three dimensional numerical simulations of slump tests', *Annual Transactions of the Nordic Rheology Society* **12**, 55–62.

Roussel, N. (2005), 'Steady and transient flow behavior of fresh cement paste', *Cement and Concrete Research* **35**, 1656–1664.

Roussel, N. (2006*a*), 'A theoretical frame to study stability of fresh concrete', *Materials and Structures* **39**(285), 75–84.

Roussel, N. (2006*b*), 'A thixotropy model for fresh fluid concretes: Theory, validation and applications', *Cement and Concrete Research* **36**(10), 1797–1806.

Roussel, N. & Coussot, P. (2005), '"fifty-cent rheometer" for yield stress measurements: From slump to spreading flow', *Journal of Rheology* **49**(3), 705–718.

Roussel, N., Roy, R. L. & Coussot, P. (2004), 'Thixotropy modelling at local and macroscopic scales', *Journal of Non-Newtonian Fluid Mechanics* **117**(2-3), 85–95.

Roussel, N., Stefani, C. & Leroy, R. (2005), 'From mini-cone test to abrams cone test: measurement of cement-based materials yield stress using slump tests', *Cement and Concrete Research* **35**(5), 817–822.

Saak, A., Jennings, H. & Shah, S. (2001), 'New methodology for designing self-compacting concrete', *ACI Materials Journal* **98**(6), 429–439.

Saak, A., Jennings, H. & Shah, S. (2004), 'A generalized approach for the determination of yield stress by slump and slump flow', *Cement and Concrete Research* **34**, 363–371.

Sakai, E. & Daimon, M. (1995), Mechanism of superplastification, *in* 'Material Science of Concrete IV', The American Ceramic Society, pp. 91–111.

Scales, P., Johnson, S., Healy, T. & Kapur, P. (1998), 'Shear yield stress of partially flocculated colloidal suspensions', *AIChE Journal* **44**(3), 538–544.

Scheidegger, A. E., ed. (1974), *The Physics of Flow Through Porous Media*, MacMillan, New York.

Schowalter, W. R. & Christensen, G. (1998), 'Toward a rationalization of the slump test for fresh concrete: Comparisons of calculations and experiments', *Journal of Rheology* **42**(4), 865–870.

Sedran, T. (2000), Mix design methods, Technical report, Brite EuRam Proposal No. BE96-3801.

Sharp, K. V. & Adrian, R. J. (2005), 'On flow-blocking particle structures in microtubes', *Microfluidics and Nanofluidics* **1**(4), 376–380.

Shauly, A., Averbakh, A., Nir, A. & Semiat, R. (1997), 'Slow viscous flows of highly concentrated suspensions–part ii: particle migration, velocity and concentration profiles in rectangular ducts', *International Journal of Multiphase Flow* **23**(4), 613–629.

Sinton, S. & Chow, A. (1991), 'Nmr flow imaging of fluids and solid suspensions in poiseuille flow', *Journal of Rheology* **35**(5), 735–772.

Skarendahl, A. (2003), The present - the future, *in* 'Proceedings of the 3rd International RILEM Symposium on SCC, Reykjavik, Iceland', ed. Ó. Wallevik and I. Nielsson, RILEM Publications S.A.R.L, pp. 6–14.

Sodre, J. (1998), 'Fluid flow pressure drop through an annular bed of spheres with wall effects', *Experimental Thermal and Fluid Science* **17**(3), 265–275.

Souli, M. & Zolesio, J. (2001), 'Arbitrary lagrangian-eulerian and free surface methods in fluid mechanics', *Computer Methods in Applied Mechanics and Engineering* **191**(3-5), 451–466.

Steinhaus, H., ed. (1999), *Mathematical Snapshots*, 1 edn, New York, Dover.

Stovall, T., Larrard, F. & Buil, M. (1986), 'Linear packing density model of grain mixtures', *Powder Technology* **48**(1), 1–12.

Struble, L. & Sun, G. (1995), 'Viscosity of portland cement paste as a function of concentration', *Advanced Cement Based Materials* **2**(2), 62–69.

Suzuki, M., Michitaka, K., Yamada, M. & Iinoya, K. (1981), 'Study on the coordination number in a system of randomly packed, uniform-sized spherical particles.', *International Chemical Engineering* **21**(3), 482–488.

Tangtermsirikul, S. & Bui, V. K. (1995), Blocking criteria for aggregate phase of self-compacting high performance concrete, *in* 'Proceedings of the Regional Symposium on Infra-Structures Development in Civil Engineering, Bangkok, Thailand', pp. 58–65.

Tattersall, G. (1955), 'Rheology of portland cement pastes', *British Journal of Applied Physics* **6**(5), 165–167.

Tattersall, G. H. & Banfill, P. F. G. (1983), *The Rheology of Fresh Concrete*, Pitman, London.

Tetlow, N., Graham, A., Ingber, M., Subia, S., Mondy, L. & Altobelli, S. (1998), 'Particle migration in a couette apparatus: experiment and modeling', *Journal of Rheology* **42**(2), 307–327.

Thrane, L. N. (2004), 'Nordic mini-seminar on the form filling ability of self-compacting concrete', *Nordic Concrete Research* (32), 139–150.

Thrane, L. N. (2005), 'Manufacturing and handling of self-compacting concrete', *Working report, Danish Technological Institute* pp. 1–25.

Thrane, L., Szabo, P., Geiker, M., Glavind, M. & Stang, H. (2004), 'Simulation of the test method "l-box" for self-compacting concrete', *Annual Transactions of the Nordic Rheology Society* **12**, 47–54.

Tie, G., Dequn, L. & Huamin, Z. (2006), 'Three-dimensional finite element method for the filling simulation of injection molding', *Engineering with Computers* **21**(4), 289–295.

To, K., Lai, P. V. & Pak, H. (2002), 'Flow and jam of granular particles in a two-dimensional hopper', *Physica A: Statistical Mechanics and its Applications* **315**(1), 174–180.

Tome, M., McKee, S., Barratt, L., Jarvis, D. & Patrick, A. (1999), 'Experimental and numerical investigation of container filling with viscous liquids', *International Journal for Numerical Methods in Fluids* **31**(8), 1333–1353.

Tsai, J., Losert, W., Voth, G. & Gollub, J. (2002), 'Two-dimensional granular poiseuille flow on an incline: Multiple dynamical regimes', *Physical Review E. Statistical Physics, Plasmas, Fluids, and Related Interdisciplinary Topics* **65**(1), 113061–1130613.

Uzomaka, O. (1974), 'A concrete rheometer and its application to a rheological study of concrete mixes', *Rheologica Acta* **13**(1), 520–529.

voscc.dk (2006), Danish Technological Institute, assessed October 2006.

Wallevik, J. E. (1998*a*), Rheology of concrete and matrix systems, the single-phase approach and measuring technique, *in* 'Borregaard Symposium on Workability and Workability Retention, Sarpsborg, Norway'.

Wallevik, J. E. (2003*a*), Fresh Concrete, Mortar and Cement Paste with Various Types of Lignosulfonates, PhD thesis, Department of Structural Engineering, The Norwegian University of Science and Technology, ISBN 82-471-5566-4, ISSN 0809-103X.

Wallevik, O. (1998*b*), *The BML Viscometer, The Viscometer 4, Operating Manual*, Contec Ltd.

Wallevik, O. (2003*b*), Rheology - a scientific approach to develop self-compacting concrete, *in* 'Proceedings of the 3rd International RILEM Symposium on SCC, Reykjavik, Iceland', ed. Ó. Wallevik and I. Nielsson, RILEM Publications S.A.R.L, pp. 23–31.

Wallin, K. (2003), Pictures from excursion at the nordic mini seminar on the form filling ability, *in* 'Nordic Mini-Seminar on the Form Filling Ability of Self-Compacting Concrete, Taastrup, Denmark', ed. L.N. Thrane, Danish Technological Institute.

Walraven, J. (2003), Structural aspects of self compacting concrete, *in* 'Proceedings of the 3rd International RILEM Symposium on SCC, Reykjavik, Iceland', ed. Ó. Wallevik and I. Nielsson, RILEM Publications S.A.R.L, pp. 15–22.

Walton, O. (1982), Explicit particle dynamics model for granular materials, *in* 'Numerical Methods in Geomechanics Edmonton, Proceedings of the Fourth International Conference, Volume 3', A. A. Balkema, pp. 1261–1268.

Wendt, J. F. (1992), *Computational Fluid Dynamics, An Introduction*, Springer.

White, J. L. (1977), 'A plastic-viscoelastic constitutive equation to represent the rheological behavior of concentrated suspensions of small particles in polymers melts', *Journal of Non-Newtonian Fluid Mechanics* **45**, 177–190.

Wolf, C. & Jensen, M. G. (2006), Vurdering af risikoen for blokering af scc (in english: Assessment of the risk of blocking of scc), Master's thesis, Department of Civil Engineering, Technical University of Denmark.

Woods, M. & Krieger, I. (1970), 'Rheological studies on dispersions of uniform colloidal spheres i. aqueous dispersions in steady shear flow', *Journal of Colloid and Interface Science* **34**(1), 91–99.

Worrall, W. & Tuliani, S. (1964), 'Viscosity changes during ageing of clay-water suspensions', *British Ceramic Society – Transactions* **63**(4), 167–185.

Xu, Z. (2003), 'An experimental and simulation study on mould filling and solidification of castings', *Mechanics and Material Engineering for Science and Experiments* pp. 382–385.

Yamada, K., Takahashi, T., Hanehara, S. & Matsuhisa, M. (2000), 'Effects of the chemical structure on the properties of polycarboxylate-type superplasticizer', *Cement and Concrete Research* **30**(2), 197–207.

Zhao, D., Nezami, E., Hashash, Y. & Ghaboussi, J. (2006), ‘Three-dimensional discrete element simulation for granular materials’, *Engineering Computations* **23**(7), 749–770.

Zhou, Z., Solomon, M., Scales, P. & Boger, D. (1999), ‘The yield stress of concentrated flocculated suspensions of size distributed particles’, *Journal of Rheology* **43**(3), 651–671.

Appendix A

Mix Compositions

Tables A.1, A.2, A.3, and A.4 show mix compositions tested.

For mix compositions showing an air content of 6.5 %, an air entrainer has been applied. Otherwise 2 % is applied in the calculation of the mix composition.

Commercial co-polymer superplasticicers have been applied. These were added during mixing of the concretes until a preferable consistency was obtained.

Material	ρ [$\frac{kg}{m^3}$]	Mass [kg]						Volume [l]					
		C_1	C_2	C_3	C_4	C_5	C_6	C_1	C_2	C_3	C_4	C_5	C_6
Low alkali	3120						330						103
Rapide	3130	426	426	276		344		136	136	88		110	
White	3150				300						95		
Fly ash	2250			99		51	73			44		22	32
Silica Fume	2200			32			21			15			9
Limestone	2700				110						41		
Free Water	1000	149	149	138	149	145	146	149	149	138	149	145	146
0-0.25	2627					129						49	
0-2 (Halne)	2626	675	675	675	675			257	257	257	257		
0-4 (sea)	2615					633						242	
0-4 (sea)	2640						759						287
4-8 (Sea)	2585	323	323	323	323			125	125	125	125		
4-8 (Sea)	2623					309						118	
4-8 (Sea)	2704						225						83
8-16(Sea)	2616	818	818	818	818			313	313	313	313		
8-16(Sea)	2610					768						294	
8-16(Sea)	2704						725						268
Air								20	20	20	20	20	65
Total		2391	2391	2363	2376	2377	2285	1000	1000	1000	1000	1000	
$(v/c)_{eq}$ (w%)		0.33	0.33	0.35	0.47	0.40	0.36						

Table A.1 *Concrete mix compositions C_1 to C_6 tested in the BML viscometer and the slump flow test.*

Material	ρ $[\frac{kg}{m^3}]$	Mass $[kg]$	Volume [l]
		M_1	M_1
Low alkali	3200	506	158
Fly ash	2300	143	62
Silica fume	2290	16	7
Free Water	1000	226	226
0-4 (Sea)	2640	1273	482
Air			65
Total		2165	1000
$(v/c)_{eq}$	0.37 w%		

Table A.2 *Mortar mix composition M_1 tested in the BML viscometer, the slump flow test and the L-box.*

Material	ρ $[\frac{kg}{m^3}]$	Mass $[kg]$				Volume [l]			
		E_1	E_2	E_3	E_4	E_1	E_2	E_3	E_4
Rapide	3130	260	297		294	83	95		94
Low alkali				355				111	
Fly ash	2250	68	107		106	30	47		47
Silica fume	2200	10	35	27	34	4.5	16	12	16
Free Water	1000	154	135	154	146	154	135	154	146
0-2	2626		667	644	658		254	245	251
0-4	2600	722				277			
4-8	2585	223	1128	308	1103	86	436	119	427
8-16	2590	770		780		297		298	
Air						65	20	60	20
Total		2211	2369	2268	2341	1000	1000	1000	
ϕ_p^*		0.636	0.68	0638	0.68				
ϕ_p		0.38	0.436	0.417	0.427				
$\frac{\phi_p^*}{\phi_p}$		0.597	0.640	0.627	0.627				
$(v/c)_{eq}$ (w%)		0.49	0.32	0.375	0.35				

Table A.3 *Concrete mix compositions E_1 to E_4 tested in slump flow test and L-box.*

Material	ρ $[\frac{kg}{m^3}]$	Mass [kg]		Volume [l]	
		F_1	F_2	F_1	F_2
Low alkali	3200		319	100	100
Rapide	3130	319		101	
Fly ash	2250	73	73	32	32
Silica fume	2290	12	12	5	5
Free Water	1000	163	142	163	142
0-4	2645	775	790	293	299
4-8 (crush)	2734	262	285	96	104
8-16 (crush)	2732	694	710	254	260
Air				60	60
Total		2298	2331	1000	1000
SP					
ϕ_p^*			0.628		
ϕ_p			0.364		
$\frac{\phi_p^*}{\phi_p}$			0.579		
$(v/c)_{eq}$ (w%)		0.42	0.37		

Table A.4 *Concrete mix compositions F_1 and F_2 applied in form filling test $FF1$ and $FF2$. For the red concrete mixes, part of the cement and fly ash was replaced 1:1 (mass) with a red powder having a similar particle size distribution.*

Concrete mixes for the full-scale tests comprised two commercial SCC mixes classified for moderate and aggressive environments, respectively. These are referred to as FuM and FuA. The paste compositions consisted of rapide hardening cement, fly ash, and silica fume. In mix FuA, the aggregate fraction 0-4 mm consisted of a class E sand. In mix FuM, the aggregate fraction 0-4 mm consisted of a combination of the same class E sand and a class P sand. In mix FuA, the fractions 4-8 mm and 8-16 mm consisted of crushed aggregate (class E). In mix FuM, the fractions 4-8 mm and 8-16 mm consisted of natural rounded aggregate (class M).

Figure A.1 shows combined coarse aggregate size distribution of mix E_1.

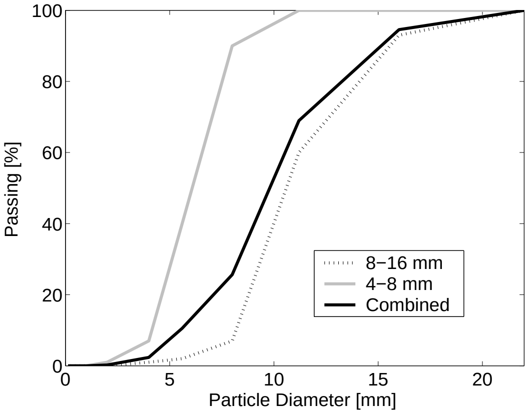

Figure A.1 *The particle size distribution of fraction 4-8 mm, 8-16 mm, and the combined one used in mix E_1.*

Figure A.2 shows combined coarse aggregate size distribution of mix E_3 and F_2.

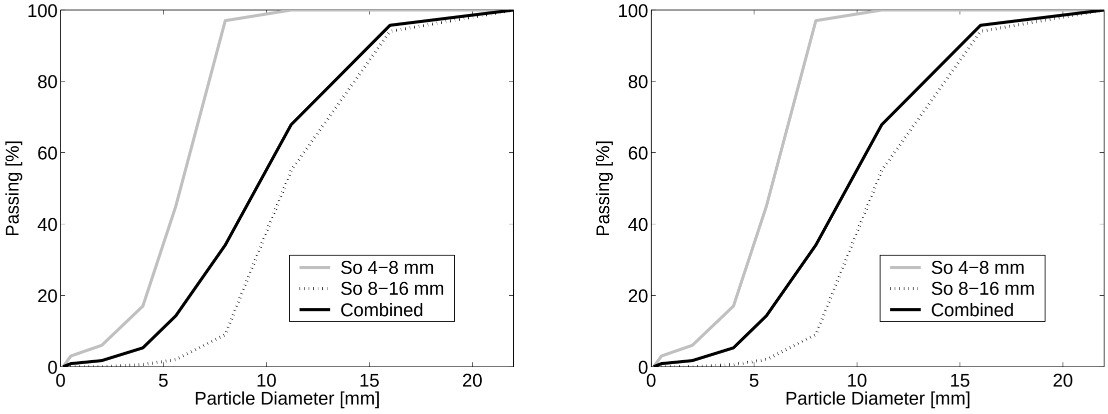

(a)

(b)

Figure A.2 *The particle size distribution of fraction 4-8 mm, 8-16 mm, and the combined one used in mix E_3 and F_2.*

Appendix B

Capillary Radius at Confinement Ratios from 1 to 2

For confinement ratios $\alpha < 2$, it is not possible to place the center of 2 particles at the same z position.

At a confinement ratio $1 \leq \alpha \leq 1.86$, one particle can only be in contact with two other particles. An example of the three-dimensional packing of monodisperse spheres at $1 < \alpha < 1.86$ is illustrated in Figure B.1. Figure B.2 illustrates the situation at $\alpha = 1$.

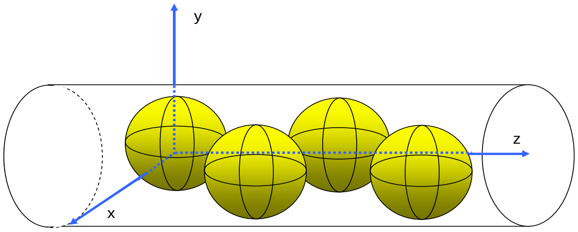

Figure B.1 *Illustration of a packed bed of monodisperse spheres in a cylindrical tube at a confinement ratio* $1 < \alpha < 1.86$.

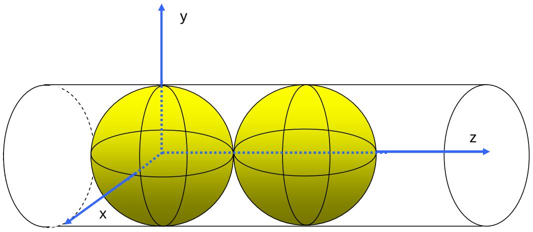

Figure B.2 *Illustration of a packed bed of monodisperse spheres in a cylindrical tube at a confinement ratio* $\alpha = 1$.

The particle area fractions ($\phi_{p,w}^{(2D)*}$) and the particle volume fractions ($\phi_{p,w}^{*}$) at confinement ratios of 1.8, 1.6, 1.4, 1.2 and 1.0 are shown in Figure B.3. It is observed that the particle area fraction deviates increasingly from the particle volume fraction when the confinement ratio decreases. For instance, at α =1.2 the particle volume fraction $\phi^*_{p,w}$ = 0.472, which was also obtained for α =2. However, the maximum and minimum particle area fractions are 0.70 and 0.05, respectively (0.5 and 0.41 for α =2).

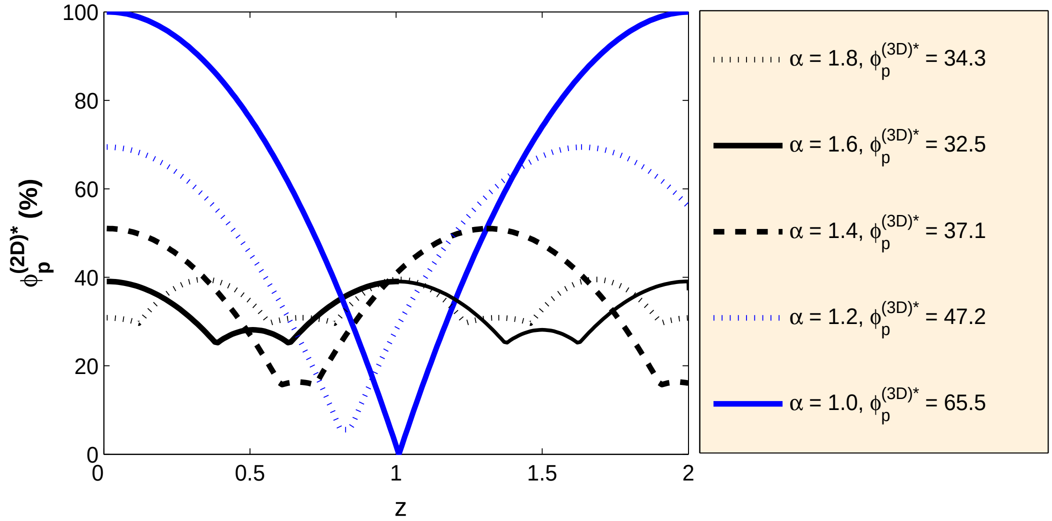

Figure B.3 *The particle area fraction* $\phi^{(2D)*}_{p,w}$ *for monodisperse spheres in a circular tube at confinement ratios,* $\alpha = \frac{R}{r_p}$ *of* 1.8, 1.6, 1.4, 1.2 *and* 1.0. *The maximum particle volume fractions* $\phi^*_{p,w}$ *are noted in the legend as* $\phi^{(3D)*}_p$.

It is now assumed that the capillary radius given by Equation 6.24 also applies for $\alpha = 1.86$ which gives:

$$r^{(2)*}_{cap,w} = 1.67 \cdot r_p \quad \text{at} \quad \alpha = 1.86 \tag{B.1}$$

To fulfil the requirements of $\frac{r^{(2)*}_{cap,w}}{r_p} < \alpha$ and $\frac{r^{(2)*}_{cap,w}}{r_p} = 1$ at $\alpha = 1$ a function has been proposed given by:

$$\frac{r^{(2)*}_{cap,w}}{r_p} = \sqrt{(a-1)^2 - (x-a)^2} \quad \text{for} \quad 1 < \alpha < 1.86 \quad (a = 3.05) \tag{B.2}$$

Figure B.4 shows $\frac{r^{(2)*}_{cap,w}}{r_p}$ according to Equation 6.24 for $\alpha \geq 1.86$ and Equation B.2 for 1$\leq \alpha \leq$ 1.86.

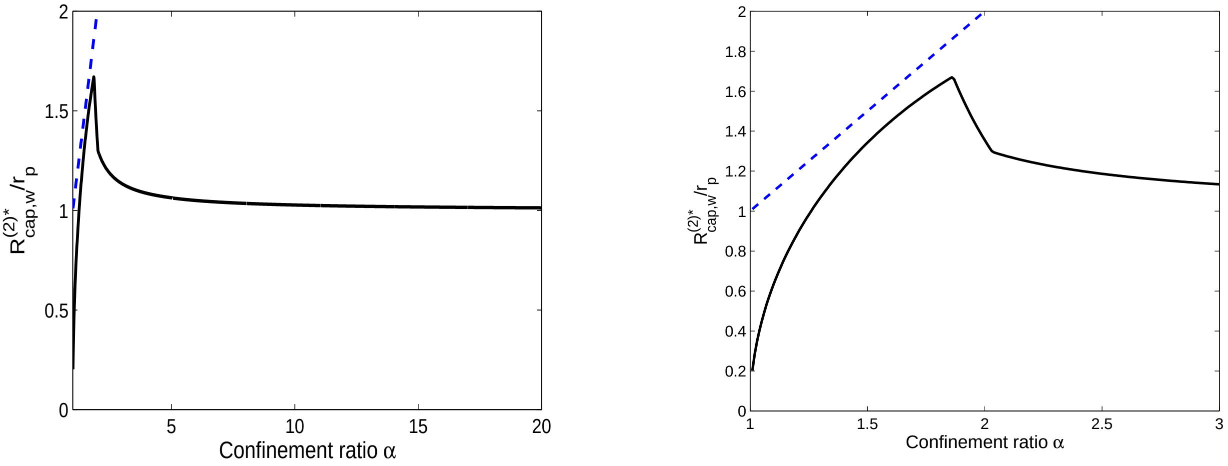

(a)

(b)

Figure B.4 *The ratio of capillary radius to particle radius,* $\frac{r^{(2)*}_{cap,w}}{r_p}$*, for monodisperse spheres in a circular tube as a function of the confinement ratio* α*. The ratio is given by Equation 6.24 for* $\alpha \geq 1.86$ *and by Equation B.2 for* $1 \leq \alpha \leq 1.86$*.*

Appendix C

Piston Load versus Travelling Length

The results of piston load versus travelling length from experimental tests on blocking are presented.

Figure C.1 shows piston load F_L versus piston travel length z for glass bead suspensions at $\phi_p = 0.45$ and 0.50. Tests are carried out with tube B corresponding to confinement ratio $\alpha = 5.45$. When complete blocking or consolidation of particles is obtained, the load increases rapidly and the test is stopped at $F_L = 2000$ N. The theory suggests that flow takes place either as homogeneous suspension flow or by pure matrix flow. A transition consisting of partly suspension flow and matrix superficial flow is not considered. According to this it is possible to calculate a theoretical travel length of the piston as

$$Z_L = L_t - \frac{\phi_p L_t}{\phi^*_{p,w}} \tag{C.1}$$

where $L_t = 215$ mm and $\phi^*_{p,w}$ is calculated according to Equation 6.23. At $\phi_p = 0.50$ and 0.5075, the maximum travel length is 35 mm and 31 mm, respectively.

It is observed that the experimental maximum travel length is higher than the theoretical value. This indicates that heterogeneous flow occurs where $0 < v_{p,2} < v_{m,2}$. Therefore the rate of change in particle volume fraction ϕ_p is lower than the theoretical value.

The load in each of the tests increases to approximately 100 N before it decreases depending on the piston velocity. At $\phi_p = 0.45$ and $U_{piston} = 500$ mm/min, the level reached is approximately constant throughout the test and complete homogeneous suspension flow seems to be obtained. Increasing the particle volume fraction to 0.50, the load level is a little higher until it increases rapidly at $z = 160$ mm to reach 400 N whereafter it starts to decrease and blocking is not obtained. This tendency increases when going from U_{piston} of 500 mm/min to 100 mm/min, and at 25 mm/min the load continues to increase to form complete consolidation. It is difficult to assess whether this tendency is a result of the test setup or it is actually possible for the suspension to overcome initial initiation of blocking and return to a homogeneous suspension flow. If blocking is initiated, it is possible that the maximum particle volume fraction is reached at the outflow, but the increased pressure may force it through in a non-viscous way. The results indicate that it may be avoided if it is possible to apply velocities higher than $U_{piston} = 1000$ mm/min. The effect of the outflow length has not been tested. In this setup it is approximately 3 mm.

The same tendencies are shown for F_L versus z at $\phi_p = 50.75$ (Figure C.2).

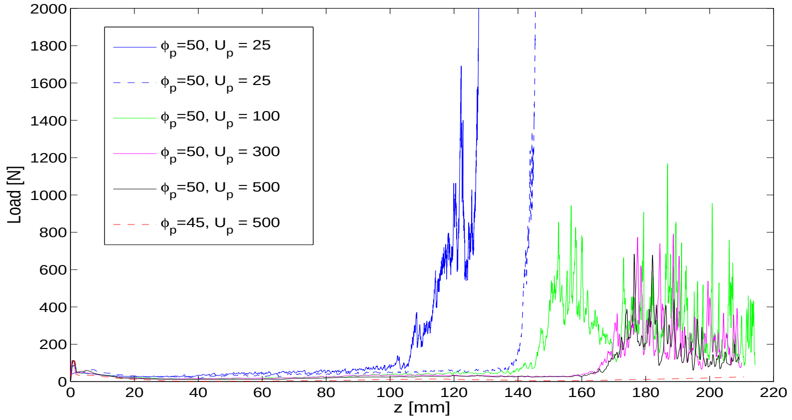

(a)

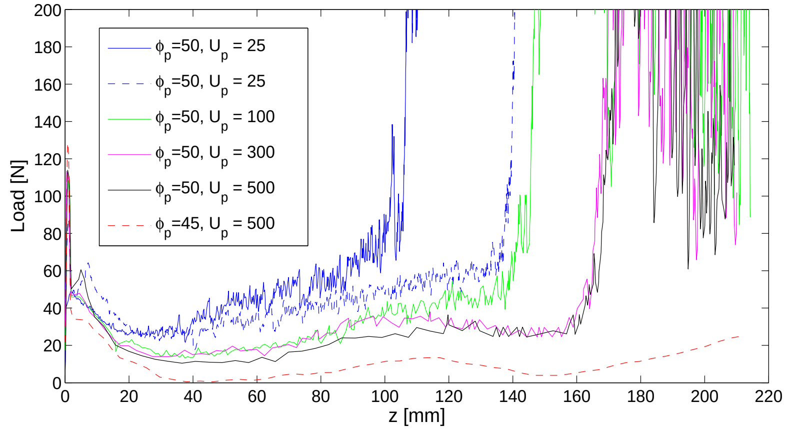

(b)

Figure C.1 *Blocking results showing piston load F_L versus piston travel length z for glass bead suspensions at $\phi_p = 0.45$ and 0.50. Tests are carried out with tube B corresponding to a confinement ratio of $\alpha = 5.45$. At $F_L = 2000$ N complete consolidation is obtained.*

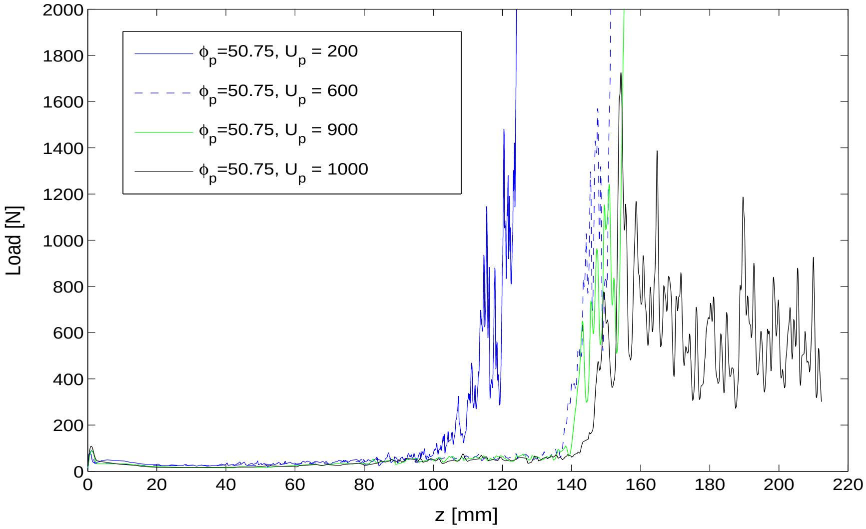

Figure C.2 *Blocking results showing piston load F_L versus piston travel length z for glass bead suspension at $\phi_p = 0.5075$. Tests are carried out with tube B corresponding to a confinement ratio of $\alpha = 5.45$. At $F_L = 2000$ N complete consolidation is obtained.*

Figure C.3 shows piston load F_L versus piston travel length z for some aluminium box suspensions at different particle volume fractions ϕ_p. Tests are carried out with tube B corresponding to a confinement ratio $\alpha = 3.11$ and 4.41 according to model 1 and 2 in Table 6.3. When complete blocking or consolidation of particles is obtained, the load increases rapidly and the test is stopped at $F_L = 2000$ N. The results are divided into blocking and non blocking curves.

It is observed that once the load curves starts to increase rapidly, this continues to form complete consolidation. For the blocking cases, it is observed that the maximum travel length is not as may be expected highest for the highest velocities. This may have something to do with the compaction of particles once blocking is initiated. At high velocities the packing density may be less than at low velocities. It may also be a result of experimental uncertainties. For instance, two tests where carried out at ϕ_p =0.50 and U_{piston} = 25 mm/min for the glass beads suspensions (see Figure C.1). The results showed a variation in the maximum travel length of 40 mm.

For the non blocking curves it is observed that these retain an almost constant load level but for the lowest velocity of $U_{piston} = 5$ mm/min at $\phi_p = 38.5$, the load curve starts to increase slightly indicating heterogenous flow but without this causing blocking of the system at the end of the test.

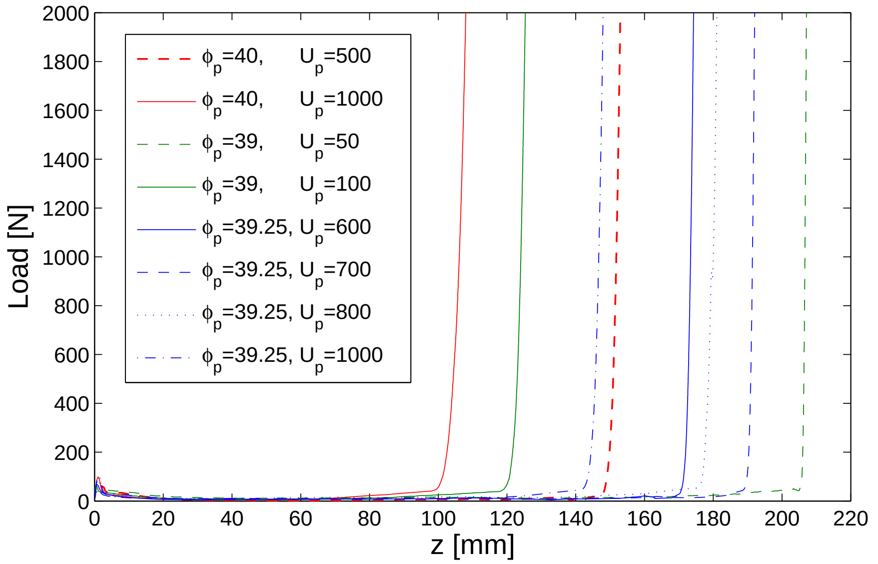

(a)

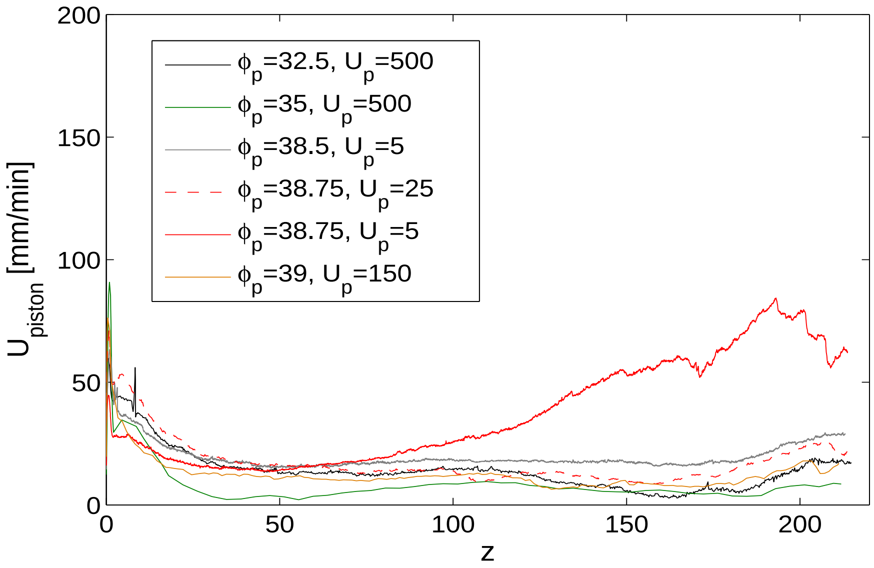

(b)

Figure C.3 *Blocking results showing piston load F_L versus piston travel length z for aluminium box suspensions at different particle volume fractions ϕ_p. Tests are carried out with tube B corresponding to a confinement ratio of $\alpha = 3.11$ and 4.41 according to model 1 and 2 in Table 6.3. At $F_L = 2000$ N complete consolidation is obtained.*

Figure C.4 shows piston load F_L versus piston travel length z for glass bead suspensions at $\phi_p = 0.39$ and 0.375. Tests are carried out with tube C corresponding to a confinement ratio of $\alpha = 2.72$. If complete heterogenous flow occurs, the maximum travel length for particle volume fraction of 0.39 and 0.375 is 75 mm and 80 mm according to Equation C.1. At ϕ_p =0.39 it is observed that complete heterogeneous flow occurs.

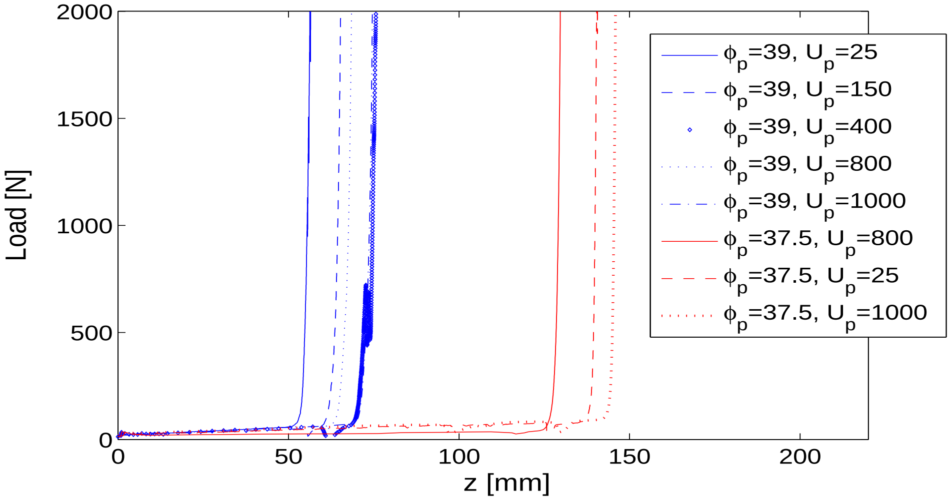

Figure C.4 *Blocking results showing piston load F_L versus piston travel length z for glass bead suspensions at different particle volume fractions ϕ_p of 0.39 and 0.375. Tests are carried out with tube C corresponding to a confinement ratio of $\alpha =$ 2.72. At F_L = 2000 N, complete consolidation is obtained.*

Figure C.5 and C.6 show piston load F_L versus piston travel length z for glass bead suspensions. Tests are carried out with tube D corresponding to a confinement ratio of $\alpha = 4.09$. One example of flow rate dependency is shown in Figure C.5 (a) where blocking was obtained at U_{piston} = 25 mm/min and not at 1000 mm/min. The tests were repeated twice and the same result was obtained.

Figure C.7 shows piston load F_L versus piston travel length z for aluminium box suspensions at ϕ_p of 0.20, 0.34 and 0.36. Tests are carried out with tube D corresponding to $\alpha = 2.33$ or 3.31 according to model 1 and 2 in Table 6.3.

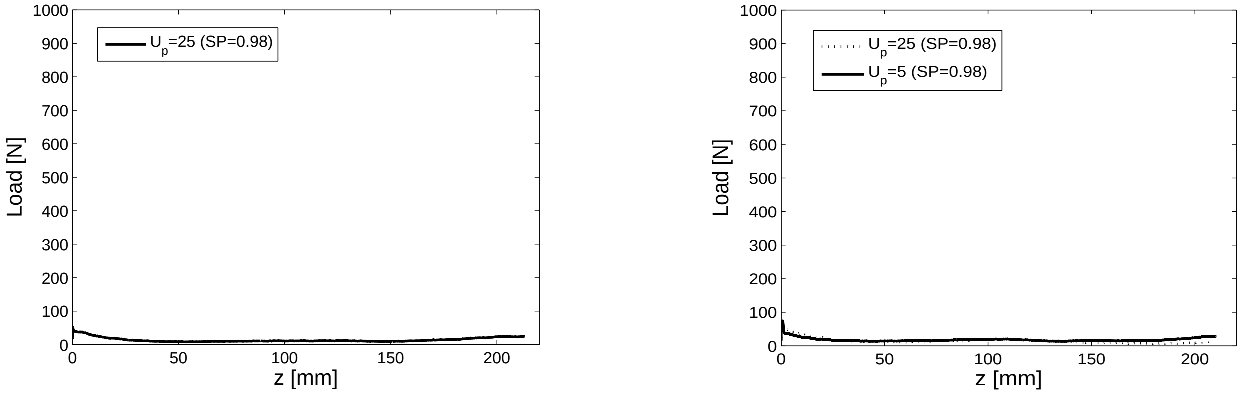

(a) ϕ_p= 38 %

(b) ϕ_p= 39 %

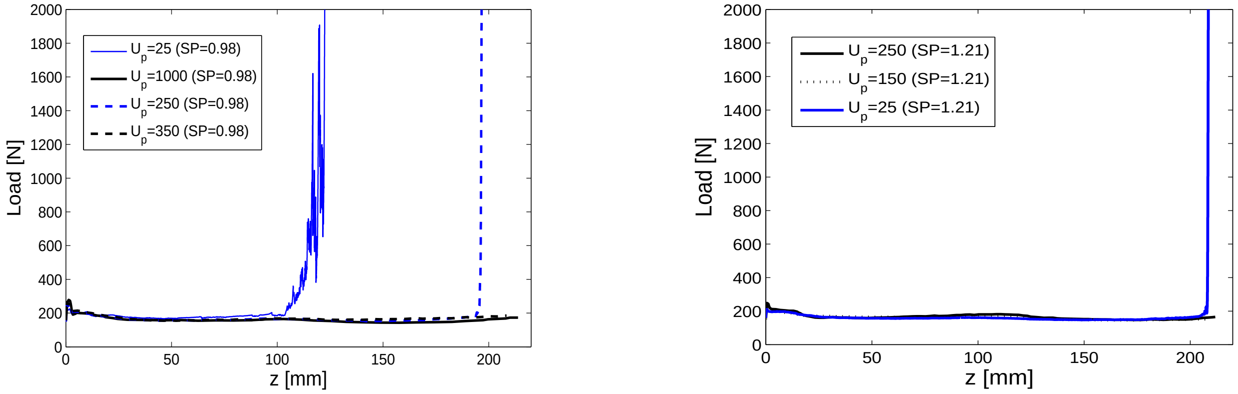

(c) ϕ_p= 40.3 %

(d) ϕ_p= 40.3 %

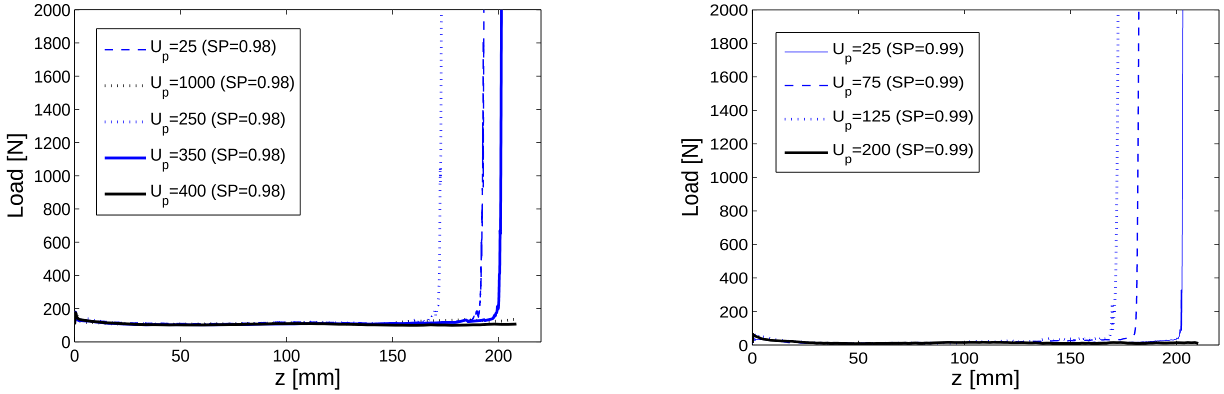

(e) ϕ_p= 40.3 %

(f) ϕ_p= 40.3 %

Figure C.5 *Blocking results showing piston load F_L vs. travel length z for glass bead suspensions. Tests are carried out with tube D corresponding to a confinement ratio of $\alpha = 4.09$. At $F_L = 2000$ N, complete consolidation is obtained.*

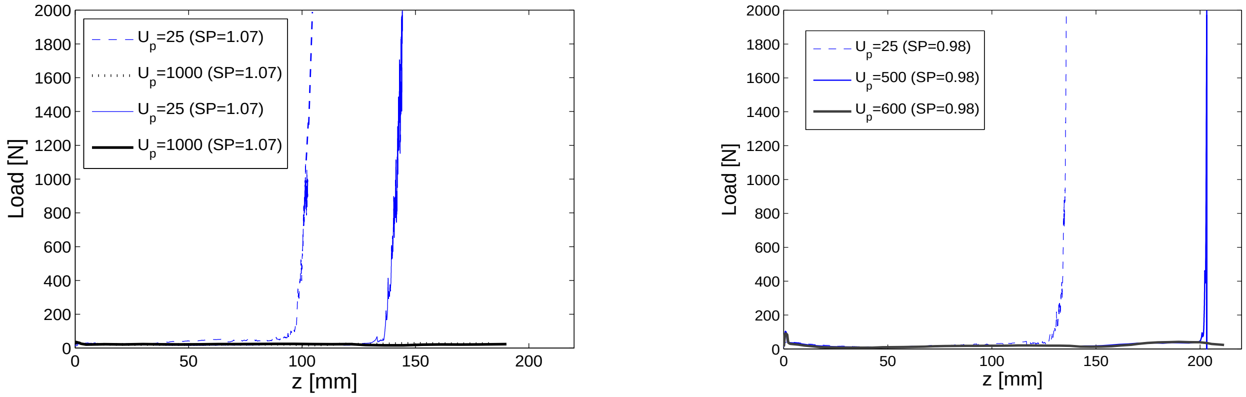

(a) ϕ_p= 41 % (b) ϕ_p= 41 %

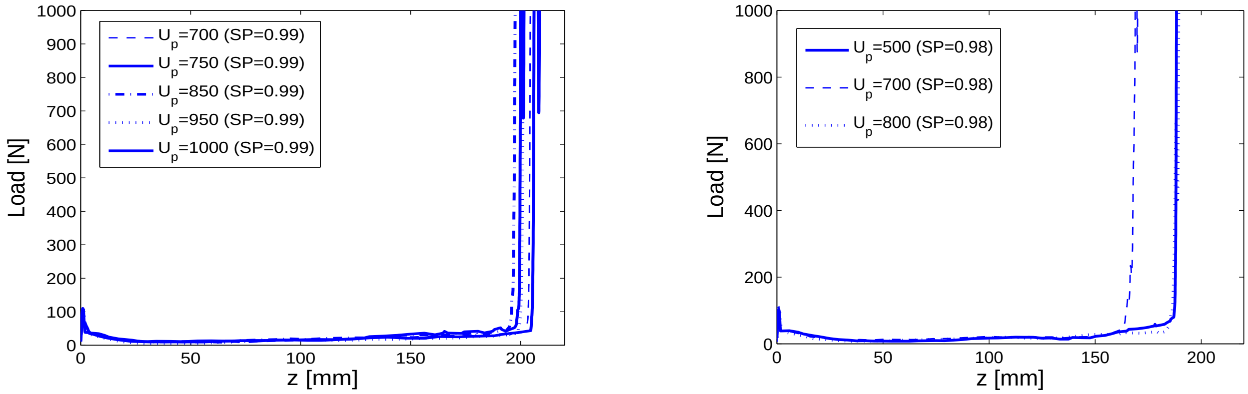

(c) ϕ_p=41.25 % (d) ϕ_p= 42 %

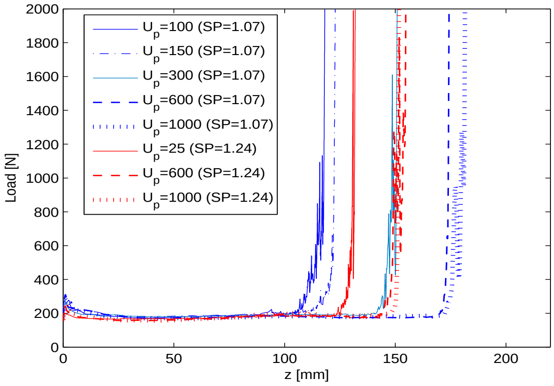

(e) ϕ_p= 45 %

Figure C.6 *Blocking results showing piston load* F_L *vs. travel length* z *for glass bead suspensions. Tests are carried out with tube D corresponding to a confinement ratio of* $\alpha = 4.09$. *At* $F_L = 2000$ *N, complete consolidation is obtained.*

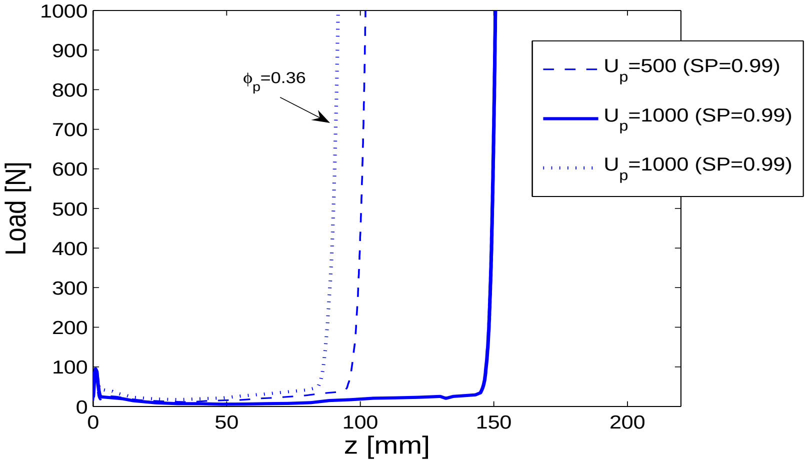

(a) ϕ_p= 34 and 36 %

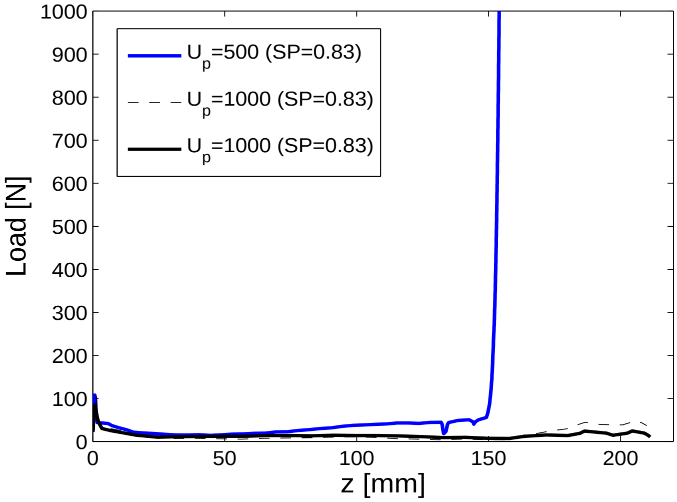

(b) ϕ_p= 20 %

Figure C.7 *Blocking results showing piston load F_L versus piston travel length z for aluminium box suspensions at ϕ_p of 0.20, 0.34 and 0.36. Tests are carried out with tube D corresponding to* $\alpha = 2.33$ *or* 3.31 *according to model 1 and 2 in Table 6.3. At F_L = 2000 N, complete consolidation is obtained.*

Appendix D

Detection of Free Surface Using Temperature Gauges

In form filling test FF2 temperature gauges were placed on the one side of the form. By measuring the temperature it was possible to detect the location of the free surface during filling. Figure D.1 shows the placement of these temperature gauges. The color and shape of a specific point represents the time interval in which the concrete passed that point. As shown in Section 7.4.3 the concrete builded up in front of the reinforcement. The reinforcement was placed from $x = 70$ to 145 cm. This is also captured in Figure D.1.

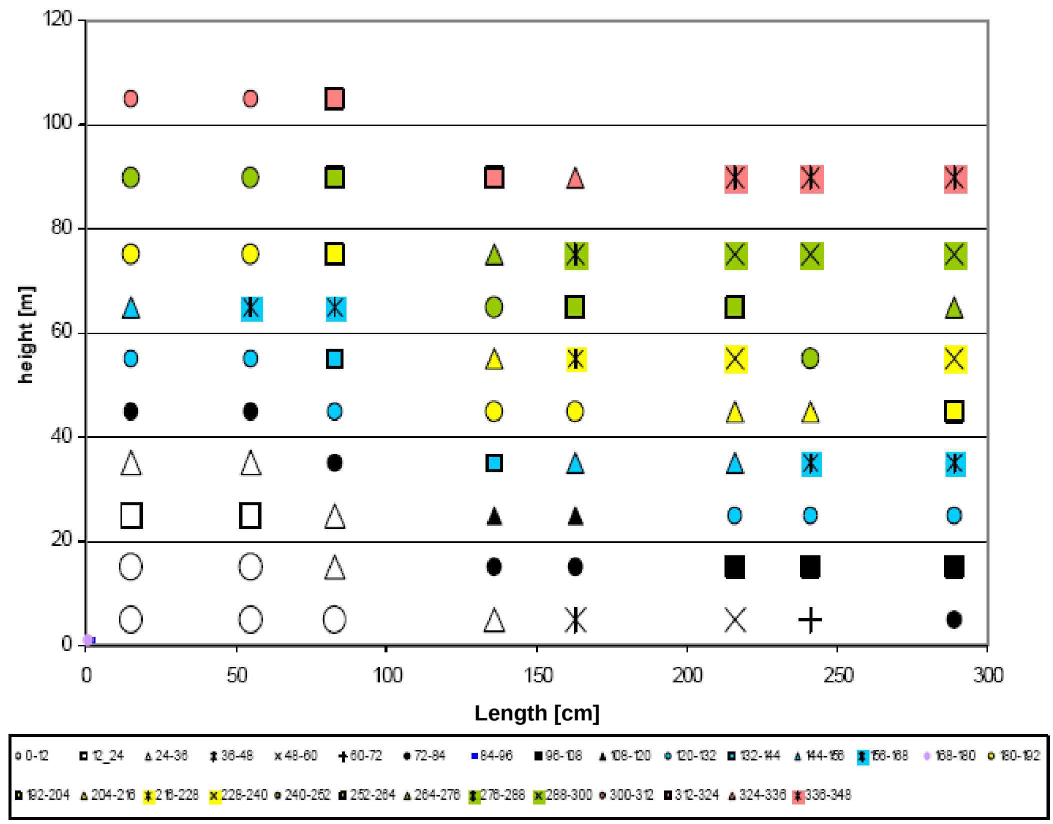

Figure D.1 *Measurement of the free surface in form filling test FF2 when using 80 temperature gauges. The color and shape of a specific point represents a given time interval during form filling)*

List of Figures

List of Tables

Report no R-172
ISSN 1602-2917
ISBN 978-87-7877-247-3